Neutron radiative capture on ^{242}Pu: addressing the target accuracies for innovative nuclear systems

Cross section measurements at the CERN n_TOF and BRR neutron beams from thermal to 500 keV

Jorge Lerendegui Marco

Departamento de Física Atómica, Molecular y Nuclear
Universidad de Sevilla

PhD Thesis

2018

Supervisor
Dr. Carlos Guerrero Sánchez

PhD tutor
Dr. José Manuel Quesada Molina

A mi gente, por hacerme creer en mí mismo

Agradecimientos
Acknowledgements

El tiempo desde que comencé esta aventura llamada tesis ha ido pasando y ha llegado el día de ver terminado el trabajo. Sin embargo, si dijera que de estos años sólo me llevo el trabajo y aprendizaje que se reflejan en esta memoria, os estaría engañando. Este periodo de mi vida ha sido rico en experiencias vividas con muchas personas a las que quiero agradecer su ayuda y compañía.

Empezaré por la gente que me ha rodeado en mi día a día en el trabajo y entre ellos por mi director, Carlos. Gracias por darme la oportunidad, por enseñarme tanto, por tu actitud crítica a la vez que motivadora y por tu supervisión detallada del trabajo y artículos. También tengo que agradecerte tu buen rollo y momentos divertidos que han hecho los días de trabajo más amenos y las facilidades que me has dado para compatibilizar mis *findes* estirados en el norte con mi trabajo en el sur. No me puedo olvidar de José Manuel, siempre dispuesto a poner su ojo crtico en el trabajo, solucionar las burocracias (aunque no sean precisamente de su gusto) o charlar un rato sobre sus tiempos por Ruesta. También quiero dar las gracias a Miguel por todo lo que me enseñó y ayudó en el periodo más *MonteCarlero* de mi tesis.

Sin salir de la Facultad de Física quiero agradecer a todos los compañeros de risas en el despacho, comidas y charlas de *cafelito*. En primer lugar a Mario, amigo desde el máster más viajero y compañero de aventuras no sólo dentro de la facultad. También quiero acordarme de Guille, al que le deseo mucha suerte en su periplo postdoc, y de Raúl, que seguro que se asienta felizmente en su regreso a Madrid. Quiero agradecer todo lo que he aprendido en el aspecto docente de todos los compañeros que he tenido en las prácticas de las distintas asignaturas y también a los alumnos por sus preguntas inquietas que siempre te hacen mejorar. Por último, y sin salir de la sexta planta de la facultad, quiero dar las gracias a todos los compañeros de departamento de FAMN por haberme hecho sentir como en casa desde el primer día y por general el buen ambiente que se respira. Quiero agradecer el trabajo de Pepe Diaz, siempre disponible a echar un cable en el laboratorio, junto con el de Nadia y Ento, una gran ayuda en aquello que más nos aborrece: los *papeleos*. Quiero dar las gracias por traer energías renovadas a las últimas incorporaciones jóvenes, Llanlle, Damián y Tere. No puedo salir de FAMN sin bajar a la quinta para dar las gracias a Carlos Plata, amigo y casi de la familia del máster, por la alegría que transmite cada día y por hacerme descubrir dónde se comen buenos molletes y churros en Reina Mercedes.

I could not forget to thank the n_TOF *gang*. You were since the very beginning of this trip, even before I enrolled the PhD in Sevilla. During my stays at CERN, I discovered how a working group can become something close to a family. I could devote many lines to thank you all, but I will restrict myself to the young members that have been always around or arrived when I was alreday an *n_TOFer*: Marta, Javi, Massimo, Federica, Toby, Petar, Mario, Michi, Adrià, Mirko, Víctor,... and many others. To you all: thank you for showing me the best part of research! I would also like to thank many other members of this big

family for sharing their expertise, starting interesting discussions during the meetings. All your efforts have improved this PhD work. Gracias al *Spanish team* por el apoyo en los meetings y por ser una piña dentro de este experimento.

Más allá de la gente de la facultad y n_TOF, querría terminar el capítulo profesional agradeciendo en particular a aquellos que han ayudado especialmente en este trabajo. Querría agradecer a Emilio, por su punto de vista crítico, sus dudas fundamentadas sobre los puntos débiles del análisis y sus propuestas de mejora. I would also like to thank Klaus and Arnd for their key role in the ^{242}Pu sample production and characterization. Last, thank you Tamas and your team for your hospitality during the nice stays in Budapest and for your crucial help during the measurements and analysis, that have led to nice results included in this work.

Debo pasar ahora a agradecer a la gente que me ha cuidado en estos años en Sevilla. En primer lugar, a mis compis de piso más duraderos, Jesús, Rocío y Juanan, y a la recién llegada Bea. Gracias a todos vosotros por interesaros por lo que hago, por mis viajes, por haber aguantado alguna chapa hablando de mi trabajo y por ayudarme a despejarme al llegar a casa en los días de más estrés. Gracias a mis grandes apoyos en Hispalis, el club de la Mongolfiera. Todo esto surgió de ese máster de Nuclear con derecho a ruta turística y ha terminado siendo un grupo de amigos cojonudo que ha ido creciendo con el tiempo. Joaquín, Anna, Cristina, Andrés, José, Llanlle, Laura, Migue, Mercedes, Carlos (el de los molletes de arriba), Mario (cómo no te iba a nombrar otra vez aquí) y Charles *Murcianito*, gracias por las tardes y noches de Alameda, por las cervecitas que te sacan los agobios, por los descubrimientos del tapeo Sevillano, por las barbacoas en Mordor, por las aventuras en Bienales y CPANes, por las Ferias de Abril, de Córdoba, Velás y muchas otras vivencias. Gracias también a Leti, fue un placer volver a coincidir en Sevilla; a Elena, a la que vemos poco pero nunca defrauda, y a Stefano, que paso sólo un año pero puso Bronte y su pistacho en un rinconcito de nuesto corazón. También quiero agradecer todos los alegres reencuentros que me ha traído Sevilla, como Itzi, María y Cid (Erasmus Oldenburg 2011/12) y Marta (Voluntariado Turquía 2013). Por último, no me puedo olvidar de los descubrimientos buenrolleros de Alba, Manoli y posteriormente todo su club: Nos quedan todavía km de Alameda que recorrer!

Toca subir de despeñaperros pa' arriba, para centrarme en dar las gracias a mi gente, a los de siempre. Al grupo de la TNH (sois muchos y no puedo nombraros a todos) os tengo que pedir disculpas por haber estado poco con vosotros estos años, mucho menos de lo que habría querido y agradeceros el hacerme sentir como si no me hubiera ido cada vez que nos vemos. Os quiero dar las gracias por mostrar siempre interés en mi trabajo, el avance de mi tesis, mis planes de futuro, etc... Tampoco puedo olvidarme del relax y desconexión de los que he disfrutado con vosotros en mis vueltas a Zaragoza. Han sido pocos momentos, pero muy intensos! Quiero agradecer en especial, por la conexión con esta tesis, a Huete, Peli (por aquel entonces perdido en los bosques de Chamonix), Juan y su esterilla autohinchable por la visita durante mi primera estancia en el CERN y las fuerzas que me distéis para seguir soplando neutrones por un tubo.

Toca acordarme también de mis amigos de pueblo, *lagunaks*, *estacazos*, *viñarockeros* y *solarpunkis*. Con vosotros he aprendido lo bonito que es tener un grupo de amigos diverso,

con rutinas diarias muy diferentes, pero que encajan como un puzzle que se mantiene unido con el paso de los años. Muchas gracias porque, aunque estos años haya podido ir menos, hacéis que me siga sintiendo como si hubiera nacido allí. Gracias a los que me habéis puesto en aprietos con preguntas sobre *qué leches* hago en mi trabajo durante una comida de cuadrilla, o con unos litros en el solar. Sos, mi pueblo y su gente, se merece un agradecimiento especial porque allí se empezó a fraguar este documento el pasado verano. Sin prisa pero sin pausa, y con la alegría de tener cerca a amigos con los que despejarte con una sesión de *charrada y pote*. De este pueblo y de esta cuadrilla salió también Bea, mi apoyo más continuo y sincero en estos últimos años, además de la persona que más rollos de particulitas, simulaciones, artículos y presentaciones se habrá tragado, con diferencia. Has sido una gran compañera de viaje, me has demostrado que al lado de tu MIR, esto de escribir la tesis parece casi un camino de rosas, y en el futuro me vas a evitar muchos malos tragos cuando pregunten angustiados si hay un doctor en la sala. Gracias por todo!

Acabo con mi familia, los que siempre (de forma literal) estuvieron ahí. Gracias a mis tíos, primos y abuelos: todos me habéis apoyado al 100% y animado a luchar por mis sueños. En cada momento importante de mi vida me habéis motivado y con mucha paciencia habéis aguantado con interés (o al menos cara de ello) mis parrafadas infinitas sobre casi cualquier tema, también sobre ciencia y sobre el trabajo que recoge esta tesis. No os voy a pedir que os la leáis más allá de los agradecimientos, simplemente quiero que sigáis apoyando como hasta ahora. Dejo para el final a mi padres, a los que debo principalmente el haber llegado hasta aquí. Por su culpa estoy en este mundo y soy como soy. Vosotros me enseñastéis desde pequeño a ser crítico, tenaz y a confiar en mi. Vuestro apoyo en todos los sentidos ha sido clave, os lo debo todo.

Contents

List of Figures

List of Tables

Abstract

A low-carbon energy oulook to mitigate the impact of the climate change requires the progressive replacement of fossil fuel technologies by sources with low CO_2 emissions. In this context, nuclear energy is expected to play a relevant role. Ensuring the long-term sustainability of nuclear energy points to the use of innovative nuclear systems, such as Accelerator Driven Systems and Generation-IV reactors and new fuel compositions, such MOX fuels aimed at the reduction of the nuclear waste.

The design and operation of these nuclear innovative systems requires a better knowledge of the capture and fission cross sections of the Pu isotopes. For the case of ^{242}Pu, a reduction of the uncertainty in the fast region (2-500 keV) from the current 35% down to 8-12% is required. Moreover, aiming at improving the evaluation of the fast energy range in terms of average parameters, the OECD NEA High Priority Request List, requests high-resolution capture measurements with improved accuracy below 2 keV. The uncertainties also affect the thermal point, where previous experimental results deviate from each other by 20%. In this context a series of experimental campaigns were proposed to improve the accuracy of the ^{242}Pu(n,γ) cross section in the different neutron energy ranges. This thesis presents the new measurement of the ^{242}Pu(n,γ) cross section from thermal to 500 keV combining different neutron beams and techniques.

In collaboration with JGU Mainz and HZ Dresden-Rossendorf, we produced a sample consisting of a stack of seven fission-like targets making a total of 95(4) mg of 99.95% pure ^{242}Pu electrodeposited on thin (11.5 μm) aluminium backings. The high quality in terms of actinide to backing mass ration, large surface and thickness have been crucial to overcome the limitations of previous similar capture experiments. The radiative capture on this ^{242}Pu sample has been measured using two complementary neutron beam facilities and different experimental techniques.

The thermal point of the cross section was determined from a measurement carried out at the Budapest Research Reactor, where four out of the seven ^{242}Pu targets were irradiated in the cold neutron beam of the PGAA facility. From this measurement, the thermal capture cross section was determined from the direct detection of the prompt γ-rays, the so-called Prompt Gamma Activation Analysis; and by means of Activation Analysis, i.e. the detection of the number of neutron captures produced in the sample from the detection of the subsequent decay of the product nuclei. The experimental set-ups for both techniques consist of high resolution HPGe detectors.

A second measured was carried out at the CERN n_TOF facility, featuring a spallation-based pulsed neutron source with a white spectrum. In this experiment, the cross section was determined by means of the time-of-flight technique at the EAR1 measuring station

(flightpath of 184 m) using a set of four C_6D_6 Total Energy detectors. The experimental set-up, data acquistion and analysis are described in detailed throughout this manuscript, focusing on the innovative methods developed in this work. From this measurement, the individual resonance parameters of 251 resonances have been extracted from the R-Matrix analysis of the Resolved Resonance Region (RRR) (1 eV - 4 keV), and the averaged cross section in the Unresolved Resonance (URR) Regions (1 - 500 keV) has been described in terms of average resonance parameters by means of a Hauser-Feshbach calculation allowing width fluctuations.

This manuscript deals with a detailed discussion on the final results and the comparison with the previous experiments and current evaluations, with special emphasis on the achieved accuracies in each energy region. In summary, the measurements presented in this work improve the knowledge of the ^{242}Pu(n,γ) cross section, reduce the current uncertainties and should help to clarify previous discrepancies among the experimental data. The work aims at contributing to the global effort to narrow the gap between the current status of nuclear data and the target accuracies required to design and operate nuclear innovative systems.

Part I

Introduction

Chapter 1

Motivations and goals

This chapter gives a brief introduction to the world energy supply and the necessary reduction of CO_2 emissions to prevent the impact of Climate Change, focusing on relevance of nuclear energy in a low-carbon energy future. A sustainable future for nuclear energy will be based in innovative systems, aiming at overcoming the current limitations and challenges. The design and operation of such systems requires nuclear data with improved accuracies, in particular neutron cross section of many isotopes. The current uncertainties of the radiative capture cross section of ^{242}Pu, related to the previous experimental data, call for new measurements with improved accuracy. This is the goal of experiments carried out in this thesis.

1.1 Status and outlook of world energy supply

1.1.1 World energy supply: sources and CO_2 emissions

The world energy consumption, defined as total energy used by the world citizens, has been continuously increasing since the beginning of theindustralization of the western countries in the late XIX century. A good estimator of the total energy consumption is the total primary energy supply (TPES), which includes all the energy production with the exception of the changes in storage capabilities. The world energy supply statistics are studied and published by the International Energy Agency (IEA) [1].

The evolution of the TPES in the last 45 years is shown in Figure 1.1, indicating that the total amount of consumed energy has doubled in this period. The energy unit in this plot are Mtoe (amount of energy released by burning one tonne of crude oil is equivalent to $\sim$42 GJ). The bottom panel of Figure 1.1 shows a quantitative study of the primary energy share by sources [1], illustrating te fact that fosil fuels dominate the energy mix nowadays, having reduced their share only from 87% to 82% in the last 40 years.

Focusing on the electricity sector, Figure 1.2 shows the increase in a factor 4 in the total electricity production from 1971 to 2015. This reflects the electrification of the primary

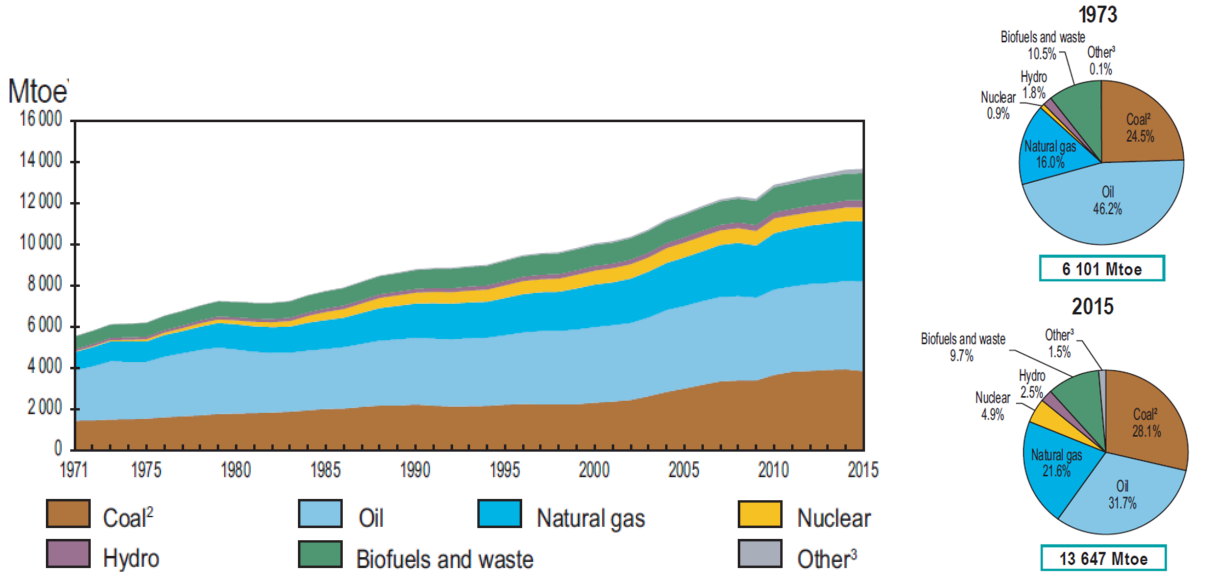

Figure 1.1: *Evolution of the primary energy supply from different sources between 1971 and 2015 (left). Share of the TPES in 1973 and 2015 (right). 2) Peat and oil shale are aggregated with coal. 3) Includes geothermal, solar, wind, tide/wave/ocean, heat and other. Source: Key World Statistics 2017 [1].*

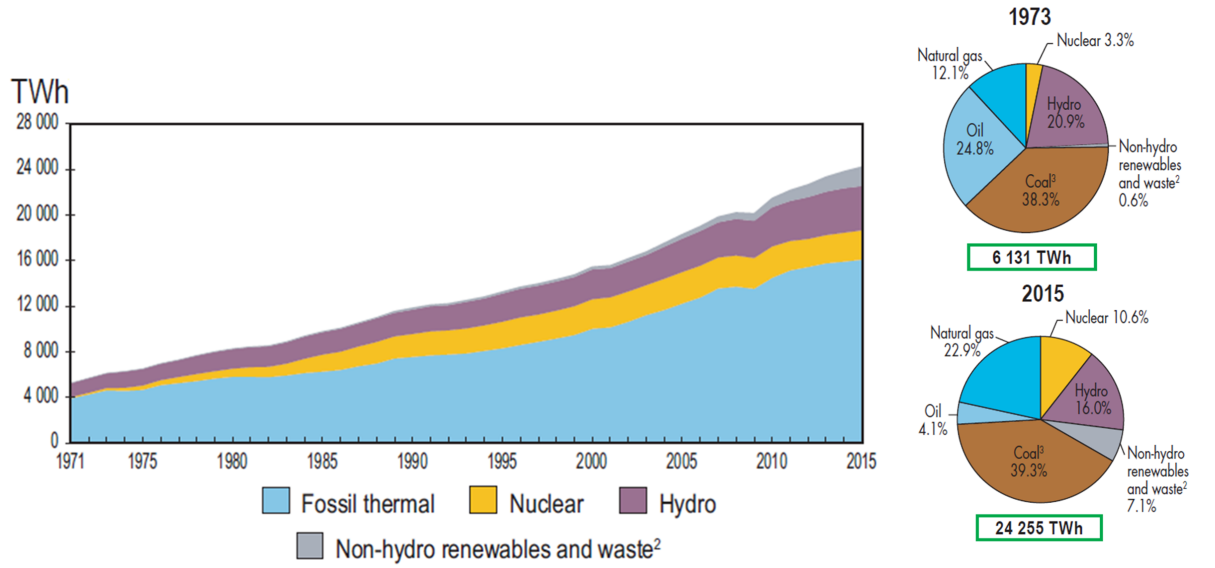

Figure 1.2: *Evolution of the electricity energy supply from different sources between 1971 and 2015 (left). Electricity share among the different sources in 1973 and 2015 (right). 2) and 3) are interchanged from Figure 1.1. Source: Key World Statistics 2017 [1].*

energy when compared to the growth of the TPES in the same period. Nowadays, the dominant contribution (66%) is still from fossile fuels, but both nuclear and renewable energies have increased significantly in the last 40 years.

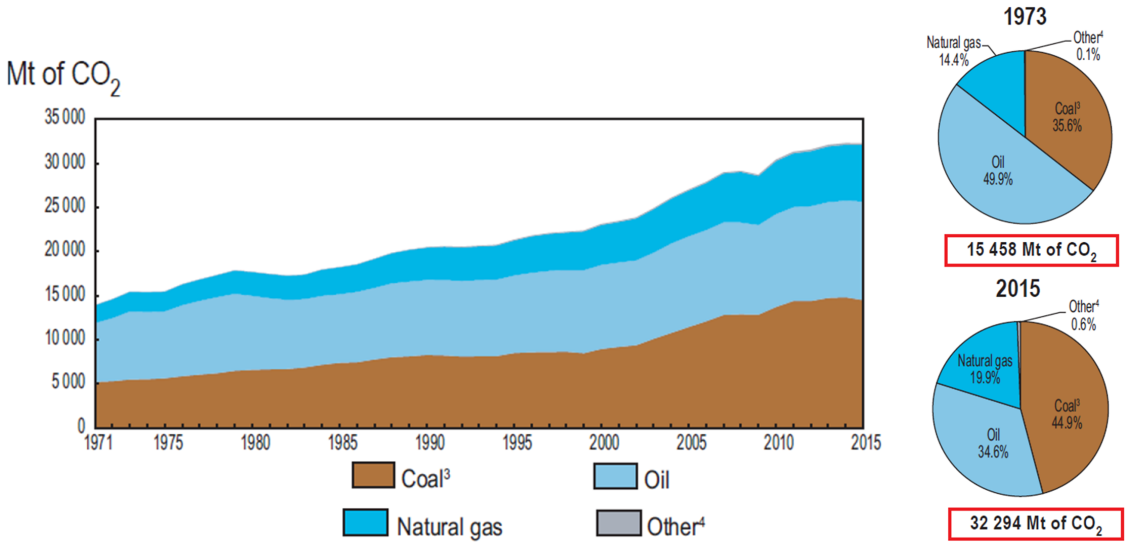

Figure 1.3: *Evolution of the CO_2 emmissions from different fossil fuels between 1971 and 2015 (left). Relative contribution of each fossil fuel to the total CO_2 emmissions in 1973 and 2015 (right). 3) see Figure 1.2. 4) Includes industrial and non-renewable municipal waste. Source: Key World Statistics 2017 [1].*

The world energy consumption has grown so far coupled to the GDP and, due to the extensive use of fossile fuels, the CO_2 emissions have increased accordingly (see Figure 1.3); despite the concerns for climate change.

The impact of CO_2 emissions and other Green House Gases (GHG) in the temperature rise in the following decades has been quantified in many works. The climate change report of 2014 [2] concluded that without additional efforts to reduce GHG emissions beyond those in place today (baseline scenario), the increase in emissions will lead to surface temperature increases in 2100 from 3.7°C to 4.8°C above the average for 1850-1900, according to different models. This will lead to climate change effects [2] by 2100, such as:

- Heat waves with a higher frequency and longer duration.
- Precipitation decrease in subtropical dry regions and extreme precipitation more intense and frequent.
- Glacier volume decrease by 35 to 85%.
- Average rise of the sea level between 0.5 and 0.7 m.
- Ocean acidification: decrease in surface ocean pH of 0.20-0.32 (60 to 109%).

To mitigate these effects, the IEA has proposed possible paths towards the decarbonisation of the primary energy sources. In particular, a strong reduction in GHG emissions in the electricity production compared to the current level is assumed to be mandatory. Figure 1.4 shows the the expected evolution of the global temperature increase with the cummulative emission of CO_2. In this figure the predicted situation in the baseline scenario is compated to different CO_2 mitigation scenarios (colored ellipses), where the values

correspond to the atmospheric concentration of CO_2 by 2100 (in ppm). According to Figure 1.4, some risks of climate change, such as risks to unique and threatened systems and risks associated with extreme weather events, are moderate to high at temperatures 1°C to 2°C above pre-industrial levels [2]. An increase below 2°C by 2100 would be achieved with an atmospheric concentration of GHG of about (450 ppm CO_2-equivalent).

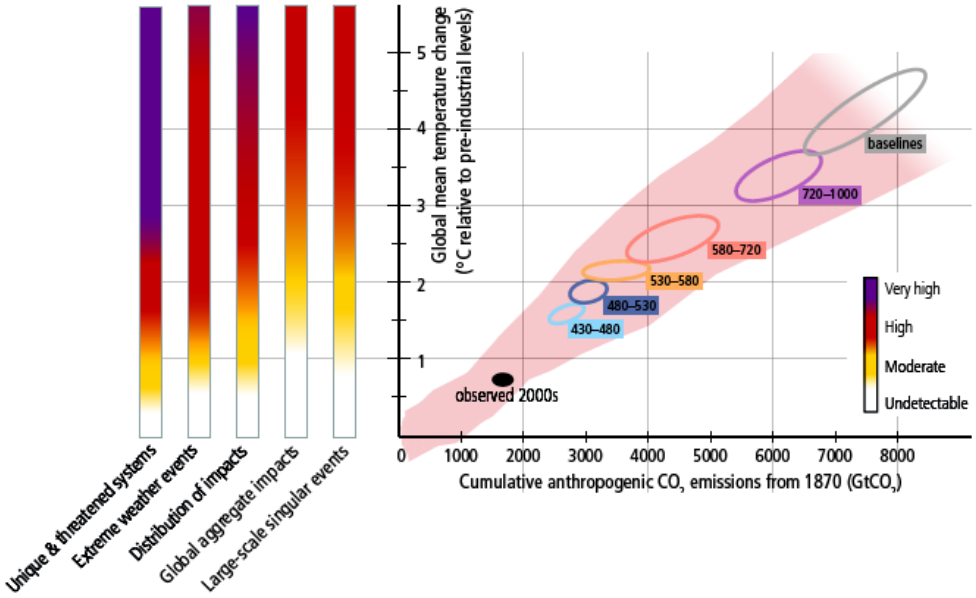

Figure 1.4: *Correlation between the predicted average temperature increase and the cummulative CO_2 emmissions. The circles indicated the expected results of different CO_2 mitigation scenarios (see text for details). From Ref. [2].*

1.1.2 Low-carbon energy future and nuclear energy

The required transformation of the energy sector in different CO_2 emissions scenarios has been studied in the recent years. In this section we will follow the *Energy Technology Perspectives 2017 (ETP)* report [3], covering the period to 2060. Similar scenarios are discussed in the *World Energy Outlook* (WEO) [4].

The **Reference Technology Scenario (RTS)** (aligned with the New Policies Scenario in WEO 2016 [4]) considers the actual commitments of countries against climate change. The RTS already requires significant changes in policy and technologies in the following 40 years that will lead to substantial additional cuts in emissions thereafter. The predicted increase in average temperature within the RTS is 2.7°C by 2100, but temperatures would likely keep increasing in the XXII century. In this scenario, the CO_2 emissions per year increase until they stabilize at 40 $GtCO_2$ by 2045 (see Figure 1.5),

The **2°C Scenario (2DS)**, very close to the 450 Scenario (450S) [4] and the Sustainable Development Scenario (SDS) [5], acomplishes a reduction of the CO_2 emissions consistent with a probability higher than 50% of limiting the global temperature rise by 2100 to

2°C. The CO_2 emissions of the energy sector are reduced to 30% of current levels by 2060 (see Figure 1.5) and zero-carbon (carbon neutrality) energy production should be reached by the end of the century. This scenario already represents a challenging modification of the current energy share and requires significantly stronger policies compared with the commitments to date.

The **Beyond 2°C Scenario (B2DS)** explores the limit of the current and innovative technologies to push the energy sector to achieve net-zero emissions by 2060 (see Figure 1.5). This would be consistent with a 50% chance of limiting the temperature increase to 1.75°C.

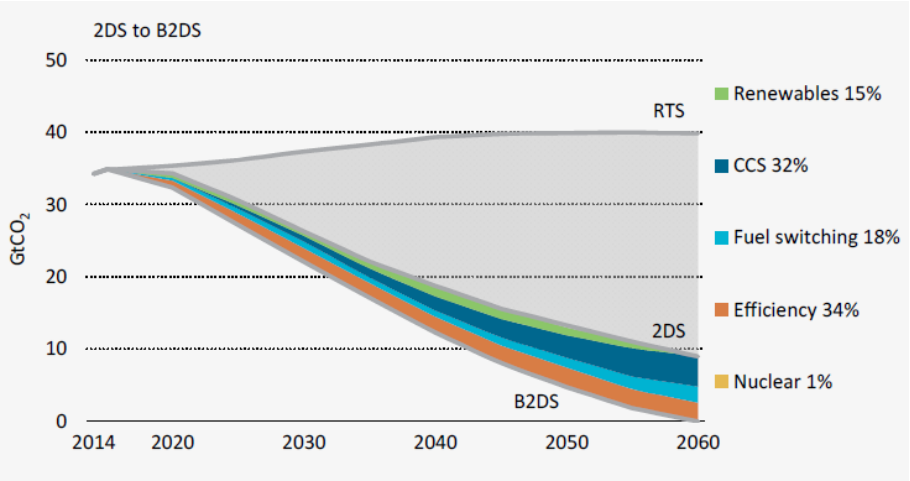

Figure 1.5: *Evolution of the CO_2 emissions per year from 2014 to 2060 in different CO_2 mitigation scenarios. Source: Ref. [3].*

The decarbonisation of the energy sector requires a strengthened impulse of the low-carbon technologies in the energy share. To illustrate the impact of each energy source in the CO_2 inventory we present the results of review carried out by the World Nuclear Association (WNA) in 2011 based on over 20 studies published worldwide [6]. The results, presented in Table 1.1, indicate a clear division in terms of GHG emissions between the fossil-fuel-burning technologies, with levels between 500 and 1000 tones CO_2 eq/Gwh, and the nuclear/renwable group, featuring GHG levels a factor 10-20 below.

The proposed evolution to 2060 of the primary energy shares to acomplish the CO_2 emmisions of Figure 1.5 in the the RTS and 2DS is shown in Figure 1.6. From this figure one concludes:

- **Total energy demand**: the RTS allows an increase of 48% compared to the level of 2014, which is only 17% in the 2D Scenario.
- **Fossil fuels**: The current share of 82% should be reduced to a value that ranges from 67% (RTS) to only 35% (2DS).
- **Renewable energies**: They should at least double their relative contribution from the current 13% (RTS) or become the main source in the 2D Scenario, where they are responsible for 53% of the electricity mix.

Table 1.1: *Range of GHG emissions from different electricity generation technologies according to a rewiew by the WNA (2011). Source: Ref. [6].*

	GHG emission (tones CO_2 eq/Gwh)		
Technology	Mean	Min.	Max
Coal	888	756	1310
Oil	733	547	935
Natural Gas	499	362	891
Solar PV	85	13	731
Biomass	45	10	101
Nuclear	29	2	130
Hydroelectric	26	2	237
Wind	26	6	124

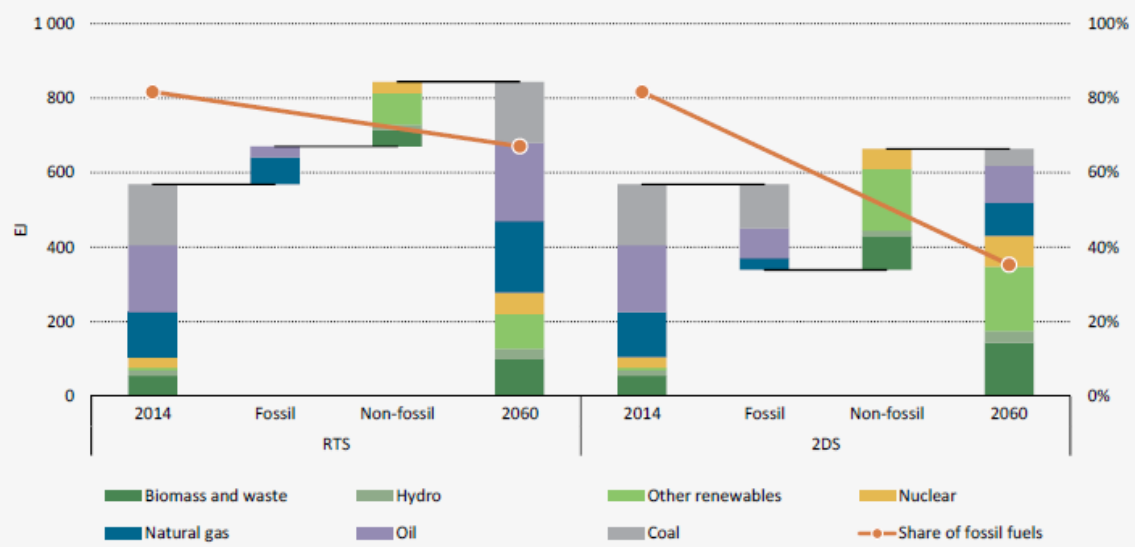

Figure 1.6: *Source: Comparison of the current primary energy demand and share and the predictions for 2060 according to different CO_2 reduction scenarios. The reduction of the fossil-fuel-based contribution (in percent in the right y-axis) is indicated with orange arrows. From Ref. [3].*

- **Nuclear energy**: Its share would increase from 5% to 7% in the conservative RTSm and should be multiplied by a factor 2.5 according to the 2DS.
- **Electrification:** The extreme reduction of the fossil fuel share in the 2DS requires doubling the electrification of the TPES.

The electricity share by 2060 in the three presented scenarios is shown in Figure 1.7. In the 2DS, 98% of the electricity production should be from low-carbon sources by 2060, which requires, among others, an increase up to 16% of the share of nuclear energy. This implies that over 20 GW of nuclear power should be installed per year by 2025, compared to the average 8.5 GW per year in the last decade. Therefore, the experts request the policy makers to provide clear and consistent policy support for existing nuclear power and encourage its further development [3].

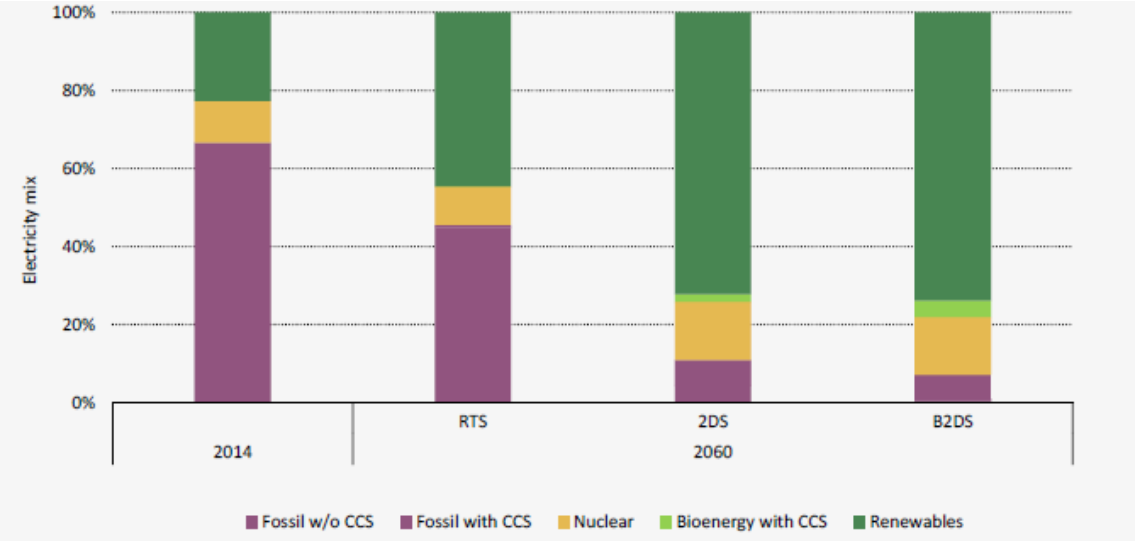

Figure 1.7: *Expected share of the electricity sector by 2060 in the different studided scenarios compared to the situation in 2014. Source: Ref. [3].*

In this context, innovative nuclear systems are being designed nowadays and this thesis aims at contributing to this endavour by suppliying part of the nuclear data required to design and operate such systems.

1.2 Nuclear energy production

1.2.1 Nuclear fission and chain reaction

The neutron-induced nuclear fission process consists in the division of a heavy nucleus in two lighter fragments when it absorbs a neutron. In each fission reaction, 2-3 neutrons and several γ-rays are emmited and an energy of about 200 MeV is released.

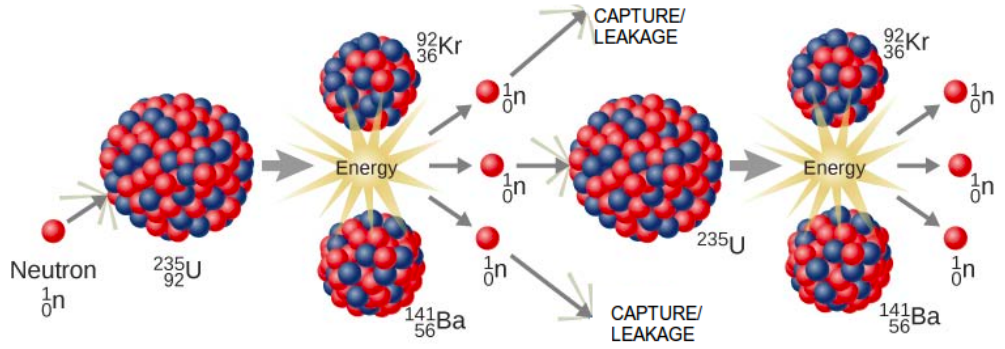

Figure 1.8: *Sketch of the self-sustaining (or chain) fission reaction on ^{235}U nuclei.*

The idea behind any nuclear reactor is the establishment of self-sustaining chain of fission reactions. As an example, a neutron induced fission on ^{235}U produces 3 neutrons, and two of them are lost through leakage or capture, only one neutron remains to carry on with the fission chain. In this case, sketched in Figure 1.8, the neutron multiplication factor k_{eff} is exactly one (critical system) and the chain reaction is self-sustained. On the other hand, if fewer neutrons are produced than lost ($k_{eff} < 1$, i.e. subcritical system) the chain reaction eventually stops, and if more neutrons are produced than lost ($k_{eff} > 1$, i.e. a supercritical system) the number of fissions grows rapidly after a few generations.

The Italian-born physicist Enrico Fermi and his coworkers achieved the first self-sustaining fission chain reaction in 1942 using natural uranium and a graphite moderator (Chicago Pile-1 experiment). Two years later, E. Fermi and L. Szilard applied for a patent with the name of *Neutronic Reactor* [7], that is considered the first design of a nuclear reactor.

1.2.2 Nuclear power plants

A nuclear power plant is an electricity production system which is based on using the large amounts of energy released in the self-sustained chain fission process to heat a fluid and generate electricity.

Nuclear power plants have been deployed since the 1950's. The evolution of the reactor designs is usually splitted into different generations (see Table 1.2). Most of current large power plants are Light Water Reactors with Pressurized Water Reactors (PWR) or Boiling Water Reactors (BWR), belonging to the second generation of reactors, deployed from 1970 to 1990. In the last two decades, advanced Light Water Reactors with enhanced efficiency and safety features have been deployed (Generations III and III+). Looking to future, the fourth generation of nuclear reactors shall overcome many of the limitations of nuclear energy sustainability with the inclusion of different fast reactor designs (see Section 1.3.2).

Table 1.2: *Summary of the nuclear reactor generations [8].*

	Gen-I	**Gen-II**	**Gen-III**	**Gen-III+**	**Gen-IV**
Deployment	50-60's	70-90's	90's	>2000	$\sim$ 2030
Designs	Shippingport, Dresden	PWR, BWR, CANDU	ABWR, AES-92, AP1000, EPR		Section 1.3.2
Features	Early protypes	Current large power plants	Advanced LWR	+efficiency +safety	Section 1.3.2

The major limitations of current thermal power reactors are the low fraction of burned fuel (0.5%) and the production of long-lived radioactive waste produced. This issues are described in the following section and possible solutions including Gen-IV reactors are presented in Section 1.3.

1.2.3 Current challenges: nuclear waste

The main challenges of nuclear energy are the safety during operation and in particular the waste disposal at the end of a burn-up cycle. The safety features of nuclear reactors has progressively improved with the different generations and in spite of the social concern, only a few sever accidents have occured in more than 60 years of operation of nuclear power reactors.

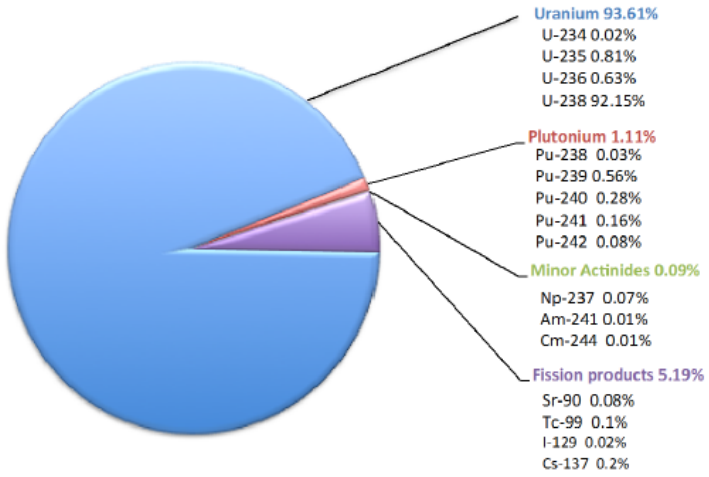

Figure 1.9: *Istopic composition of the burned fuel from a PWR with initial enrichment of 4.5 wt% after a 45 GWd/MTU burn-up: Ref. [9].*

The nuclear fuel of current reactors is usually made of slightly enriched (3-5% of ^{235}U) uranium oxide (UOX). During the burn-up of the UOX fuels in current thermal reactors, transuranium (TRU) isotopes such as Pu and other minor actinides (MA) (Np, Am, Cm, Cf), are built-up by means of neutron capture reactions which competes with the desired fisssion reaction. In addittion, fission generates a wide variety of radioctive isotopes around A = 95 and A = 137 (for ^{235}U(n_{th},f)). This is summarized in Figure 1.9, which sketches the isotopic composition of the discharged nuclear fuel of a LWR.

From the isotopes presented in Figure 1.9, most of the hazard is caused by Pu, Np, Am and Cm and a few long-lived fission products. A measure of the hazard of these elements is provided by the radiotoxicity arising from their radioactive nature. The evolution in time of the radiotoxicity of the spent fuel and its components is diplayed in Figure 1.10. This illustrates that the level of radiotoxicity is higher that of the Uranium ore, used as a reference, during 100000 yeard, hence the problem of storing the spent fuel. This long-term radiotoxicity (times larger than 100 years) is always dominated by Pu, followed by minor actinides.

A possible solution to the radioactive hazard of the spent fuel is its isolated disposal in stable deep geological formations (known as deep geological repositories) for a long period of time (10^5 years). The main problem to this solution is the lack of enough suitable spaces to store permanently the increasing cummulative radioactive waste and the difficulties to

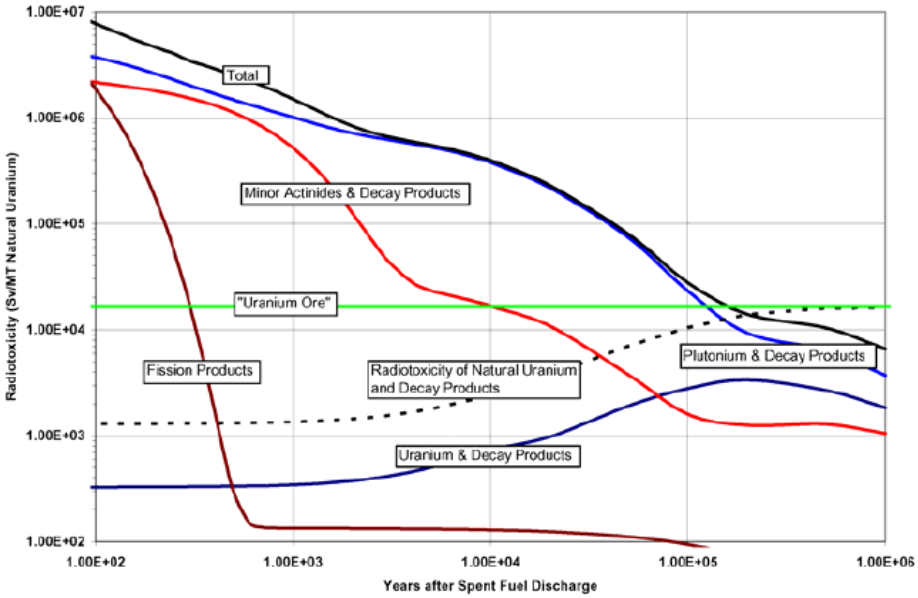

Figure 1.10: *Evolution of the total radiotoxicity of the burned nuclear fuel from a LWR as a function of the years after discharge. The contribution of the different components is compared to the radiotoxicity associated with the raw material used to fabricate 1 tonne of enriched uranium. Source: Ref. [10].*

predict the long-terms risks of the geological disposal. Hence, fifferent complementary solutions to the long-term radiotoxicity of nuclear waste have been discussed in the last decades. This solutions aim at:

- Reduce the total amount of waste to reduce the volume, residual heat and as a consequence the cost of its storage.
- Reduce the long-term radiotoxicity, mainly produced by Pu isotopes, by partitioning the burned fuel to separate the Pu an recylcle it to make Mixed Oxide Fuels (MOX) to allow fissioning the Pu isotopes (see Section 1.3.1) in a special type of reactor.
- Reduce the minor actinide (MA) component by transmutation in Accelerator-Driven Systems (ADS) (see Section 1.3.3).
- Design new fast reactors (Gen-IV) which enhance the burn-up and complement thermal reactors in closed fuel cycles to reduce the final amount of waste (see Section 1.3.2).

1.3 Innovative systems and fuel cycles

1.3.1 MOX fuels

Today, most countries use the once-through fuel cycle, meaning that the fuel is used only once and the spent fuel is directly stored. A good option to reduce the amount, activity and long-term radiotoxicity of the spent fuel is to introduce a closed fuel cycle including recycling (i.e. recovery of uranium, plutonium, and other transuranics from the spent fuel). The recycled elements are used to make new fuel, thereby producing more energy and reducing the need for enrichment and mining.

As mentioned before, the long-term radiotoxicity of nuclear waste is mainly associated to the presence of ∼1% of plutonium containing 66% of ^{239}Pu and ^{241}Pu. These are fissile isotopes and can be separated and reprocessed to combine them with depleted uranium (^{238}U) to make what is known as MOX (mixed oxide) fuel. In this way the Pu from spent fuel and the depleted uranium, otherwise considered as waste, are used in a new reactor cycle, contributing in this way to the long-term sustainability of nuclear energy. In addittion, the use of Pu as nuclear fuel is key to avoid the nuclear proliferation by increasing the safeguardability of the plutonium.

Currently, the use of MOX fuel has been established on an industrial scale in a number of countries for more than 30 years. In Belgium, France, Germany, Japan and Switzerland, there are a considerable number of thermal power reactors (LWRs) using MOX fuels to load 30% or more of the reactor core. However, the utilization of MOX fuel only in thermal power reactors will not completely solve the accumulation of Pu from the spent fuel, thus requiring it to be partially stored. A more efficient use of plutonium will ultimately be made in fast reactors, where multiple recycling is possible and has been demonstrated. Therefore the long term need for this reactor technology is recognized.

The oulook of MOX fuels can be divided in three phases [13]:

1. **Current status**: Gradual introduction of MOX fuels in LWRs in the past three decades. The current inventory of Pu has still to be recycled.
2. **Before 2030**: Expansion of MOX recycling with more power plants licensed for MOX fuels. This includes not only LWR but also advanced systems such as fast BWR's with 100% MOX cores.
3. **After 2030**: This phase will be reached only if a greater public acceptance of plutonium fuel technology is achieved and plutonium fuels become competitive and efficient. In this phase, advanced thermal and fast reactors working as breeders (i.e. producers of fissile isotopes) or burners would be deployed. The final goal will be removing completely the Pu form the final waste disposals.

1.3.2 Gen-IV reactors

The current challenges of nuclear energy have been adressed by the Generation-IV International Forum (GIF) [14, 8], which aims at developing the upcoming generation of nuclear reactors that can be supplementary to current systems and make the transition to the future of nuclear energy. The main goals defined in the original GIF Charter [8] are:

- **Sustainability**: Ensure long-term availability of resources and minimize the waste.
- **Safety**: Reduce the probability of core damage, become independent of off-site response, improve the heat removal capabilities and minimize the off-site releases in case of a severe accident. The two last features have been required after the Fukushima Daiichi accident.
- **Proliferation resistence**: Become very unatractive for theft of weapon-usable materials.

Table 1.3: *Summary of the main features of the preferred innovative systems for the Generation-IV of nuclear reactors [14].*

Reactor	**Spectrum**	**Coolant**	**T(°C)**	**Cycle**	**Power (MW_e)**
VHTR	Thermal	Helium	900-1000	Open	250-300
SCWR	Thermal/Fast	Water	510-625	Open/closed	300-1500
MSR	Fast/Thermal	F salts	700-800	Open/closed	1000
LFR	Fast	Lead	480-800	Closed	20-1000
SFR	Fast	Sodium	550	Closed	30-2000
GFR	Fast	Gas	850	Closed	1200

In 2002, GIF selected six systems from nearly 100 concepts as Generation IV technologies [8]:

1. Sodium-cooled fast reactor (SFR)
2. Gas-cooled fast reactor (GFR)
3. Lead-cooled fast reactor (LFR)
4. Molten salt reactor (MSR)
5. Supercritical-water-cooled reactor (SCWR)
6. Very-high-temperature reactor (VHTR)

As summarized in Table 1.3, the first three are fast reactors, while the MSR and SCWR can be operated as both fast and thermal reactors. The last type, the VHTR, has the special feature of aiming at the cogeneration of electricity, hydrogen and heat for industry. More details on these systems can be found in Refs. [14, 8]. The original (2002) and updated (2014) technology timelines for each of these systems is presented in Figure 1.11, indicating that validation of their viability and performance should finish between 2025 and 2030 for most systems.

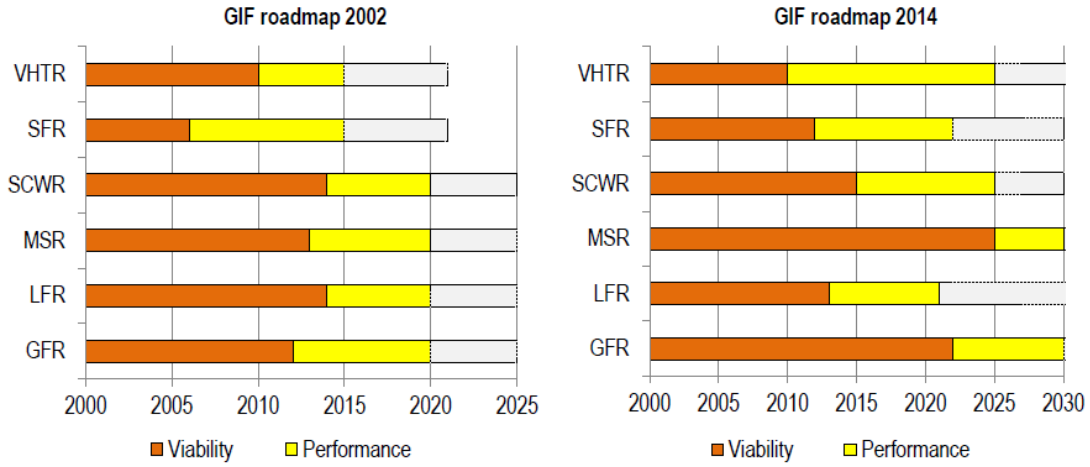

Figure 1.11: *Expected timeline as of 2002 and after the update in 2014 for the viability and industrial implementation of the different Gen-IV reactor designs (from Ref. [8].).*

Gen-IV reactors are among the energy technologies included in *The European Strategic Energy Technology Plan Towards a low carbon future* (SET-Plan) [15], which discusses the need of the design and construction of demonstration SFR reactors and alternative designs (LFR, GFR) and the the start of operation of the demonstration plants.

1.3.3 Transmutation and Accelerator Driven Systems

A significant reduction of the long-term radiotoxicity in the final waste disposal can be achieved by *transmutation*, i.e. the transformation of Pu and MA into less harmful and shorter lived-fission fragments via neutron induced fission of the target isotopes. According to Figure 1.10, the total radiotoxicity could be reduced in a factor 10 if all the Pu is separated and fissioned and a further reduction down to 1/100 would be reached if, in addition, the minor actinides (MAs) are burned.

Different reactor systems have been proposed to carry out transmutation [10]. Transuranic isotopes (TRU) (i.e. mixing Pu and MA) can be transmuted in MOX-LWR, but more efficiently in fast reactor systems. On the other hand, pure minor actinide burners must be designed as fast reactors since no feasible option is found with thermal reactors. In addition, critical fast reactors with high MA content are difficult to control due to the fuel heterogeneity. Aiming at solving these limitations, sub-critical systems with a fast neutron spectrum seem the best solution. This is the idea behind the Accelerator Driven System (ADS).

An Accelerator Driven System (ADS), sketched in Figure 1.12, consists of a subcritical core combined with an external neutron source based on spallation reactions induced on a heavy target (lead, tungsted, tantalum, ...) by a high-current and high-energy (>500 MeV) proton beam. The subcriticality condition means that an ADS can only run when neutrons are supplied to it because its fuel does not have a high enough fission-to-capture ratio for

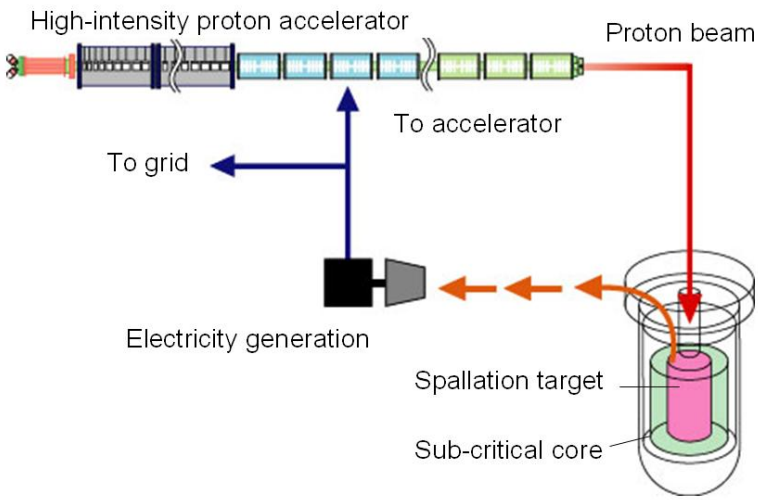

Figure 1.12: *Sketch of the main components of an Accelerator Driven System for nuclear waste transmutation. Source: Ref. [12].*

neutrons to maintain a fission chain reaction. These systems follow a very similar electricity generation system than normal critical reactors and a fraction of the produced electricity is dedicated to feed the accelerator (see Figure 1.12).

In the context of transmutation, ADS present the following advantages compared to critical reactors:

- Fuel flexibility (e.g. pure TRU or MA fuel) related to the removal of criticality.
- New reactor core designs which are not feasible in critical reactors.
- Safer system due to the direct proportionality of the reactor power and the accelerator current.

A review of the European R&D strategy for ADS design, fuel development and industrial demonstration can be found in Ref. [11].

1.4 The role of nuclear data in advanced nuclear technology

1.4.1 Introduction to nuclear data

Nuclear data (ND) includes all the measured or evaluated observables related to the interaction of particles with atomic nuclei. Nuclear data is of key importances for many applications of nuclear physics [16]: Nuclear technology, astrophysics, medical physics, basic nuclear physics, industrial applications and security.

A general division of nuclear data is made into:

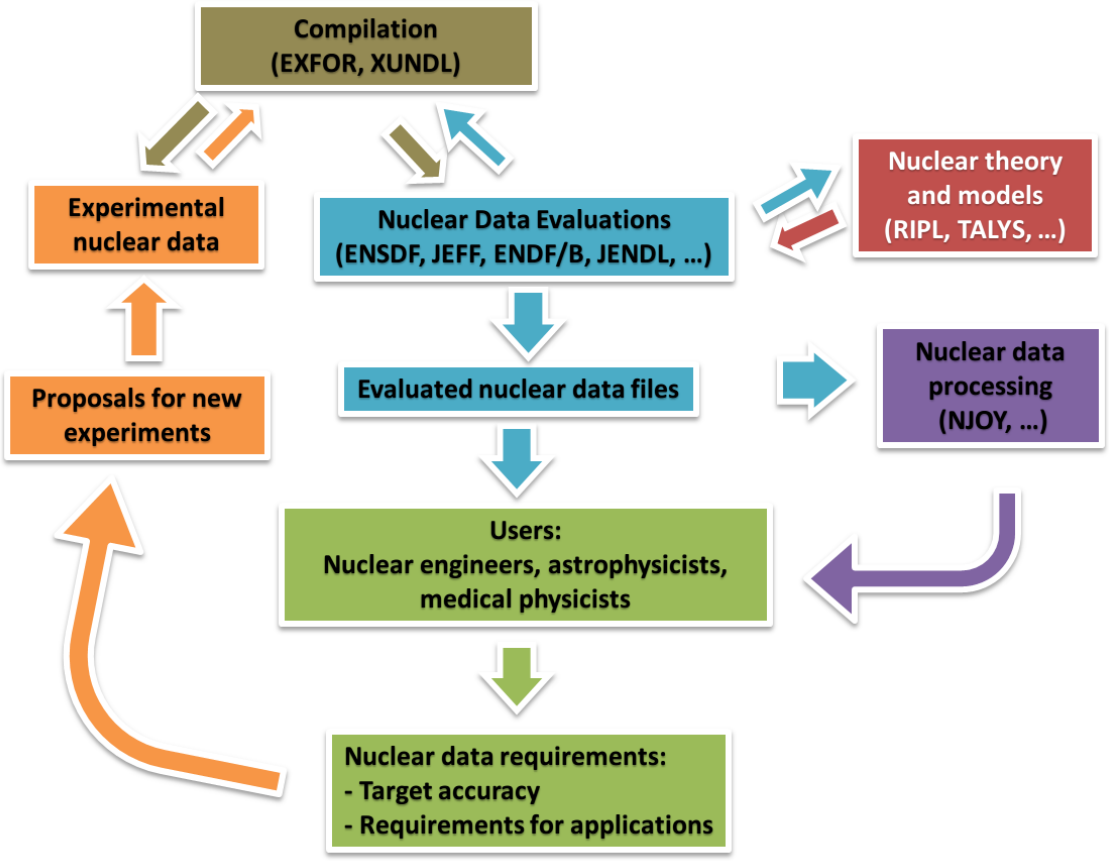

Figure 1.13: *Nuclear data cycle showing all the steps involved from the experimental determination of nuclear data to its dissemination for applications.*

1. **Nuclear structure**: nuclear masses, nuclear levels (energy, spins and parities, half-lives), decay modes, branching rations, conversion coefficients, etc...
2. **Nuclear reactions**: Energy-dependent reaction cross sections, energy and angular distributions of reaction products, resonance parameters, etc...

The different steps involved in the development of nuclear data for applications are illustrated in the flowchart of Figure 1.13. The nuclear data *cycle* starts with the **nuclear data experiments**, wich are proposed targeting specific needs in any of the applications of nuclear data. The experimental data measured to date must be collected in a continuous process known as **compilation**. This step is the groundwork for any evaluation and helps to preserve investments by avoiding the repetition of experiments. The main compilation databases are:

- Nuclear structure: *Experimental Unevaluated Nuclear Data List* (XUNDL) [17] (~6000 data sets).
- Nuclear reactions: *Experimental Nuclear Reaction Data* (EXFOR)[18] (~22300 data sets).

The **evaluation** process combines the compiled experimental ND with theory, including modeling and covariances. The evaluated libraries also keep the division between nuclear reaction and structure data:

- Nuclear structure: *Evaluated Nuclear Structure Data File Search and Retrieval* (ENSDF) [19].
- Nuclear reactions: Several evaluated libraries for nuclear reactions or only neutron induced reactions are currently present, such as JEFF (Europe) [20], ENDF/B (USA) [21], JENDL (Japan) [22], RUSFOND (Russia) [23], CENDL (China) [24].

Nuclear theory plays a major role in the ND evaluation since it is able of filling the gaps in experimental data, extrapolating to the ranges where no data is available, ensuring the consistency of the evaluation, helping to reject data sets, and imposing physical constraints. Among the nuclear theory tools extensively used by the nuclear data community one can highlight:

- TALYS [25] is a software package for the generation of nuclear reaction observables in the 1 keV - 200 MeV energy range.
- The *Reference Input Parameter Library* (RIPL) [26] is devoted to input parameters needed in calculations of nuclear reactions and nuclear data evaluations.

The last steps in the ND cycle are its **dissemination and processing**. The dissemination consists on a cost-free and convenient access to numerical data needed for their applications. Most of the data can be retrieved online from the websites of the nuclear evaluations. Some applications require a processing of the ENDF format used in the evaluations into libraries useful for applications calculations (Monte Carlo codes, deterministic transport codes, reactor codes, etc...), which can be done with software such as *Nuclear Data Processing System* (NJOY) [27].

Once the users of ND can study the impact of the nuclear data quality in their applications, they can establish target accuracies and request improved experimental data. The accuracy assesing process is explained for the case of nuclear innovative systems in the next section and the specific requests and status of the current data that motivate the new experiments in this thesis are presented in Section 1.5.2.

1.4.2 Nuclear data needs for nuclear innovative systems

High accuracy measurement of fission and capture cross sections are a basic groundwork for the design and operation of current and future nuclear systems such as Accelerator Driven Systems and Gen-IV reactors aimed at the reduction of the nuclear waste and the long-term sustainabity of nuclear energy [28].

Following the steps sketched in the Nuclear Data cycle of Figure 1.13, the nuclear data needs for the design and operation of several innovative nuclear systems (the preferred Generation-IV reactors [14, 8] and others systems) have been systematically studied by the Subgroup 26 of the Working Party on International Nuclear Data Evaluation Co-operation (WPEC) of the Nuclear Energy Agency (NEA) [29].

The study consisted on the study on a quantitative evaluation of the target accuracies by isotope, energy range and neutron induced reaction required to meet the design accuracies of the different systems. Among the studied systems we find:

- **Fast reactors**: Three Sodium-cooled fast reactors, including a general design (SFR), the Advanced breeder test reactor (ABTR) and the European fast reactor (EFR) and Gen-IV reactors using other coolants, such as GFR, LFR (see Section 1.3.3).
- **Accelerator-driven systems**: Accelerator-driven minor actinide burner (ADMAB)
- **Thermal reactors**: The pressurised water reactor with extended burn-up (PWR), and the Very high-temperature reactor (VHTR).

In this list, all the systems are based in the uranium cycle, with differerent fuel types, coolant, enrichments and concentration of minor actinides (MA) and transuranic elements (TRU). Table 1.4 summarizes the main features of the studied fast reactors.

The analysis procedure is based on studing the sensitivity of critical parameters of the reactor design to the present uncertainties in the cross sections. Among the studied integral parameters we find the reactor criticality, the power peak value or the changes in reactivity along the burn-up. The conclusions of this work highlight three major sources for the overall uncertainty:

1. Capture, fission cross section and $\bar{\nu}$ (average number of neutrons per fission) of plutonium isotopes with the exception of ^{239}Pu.
2. Fission cross-sections of some minor actinides for TRU burner reactors, such as the SFR and ADMAB.
3. Inelastic cross sections, being ^{238}U, ^{56}Fe and ^{23}Na (just for sodium cooled systems).

The most relevant requests are included by the Nuclear Energy Agency in its *High Priority Request List* (HPRL) [30].

Table 1.4: *Main features of the fast reactor studied in the WPEC-26 report [29].*

Reactor	**Fuel/Coolant**	**Enrichment(%)**	**TRU/(U+TRU)(%)**	**MA/(U+TRU)(%)**
ABTR	Metal/Na	17	16	0
SFR	Metal/Na	56	60	11
EFR	MOX/Na	22	24	1.2
GFR	Carbide/He	17	21	5.0
LFR	Metal/Pb	21	23	2.4
ADMAB	Nitride/Pb-Bi	32	100	68

1.5 ^{242}Pu(n,γ) cross sections: sstatus of nuclear data and requirements

1.5.1 Status of the ^{242}Pu(n,γ) experimental data

The review of the current status of the ^{242}Pu(n,γ) experimental data sets in this section is divided in the three energy regions were new capture data on this isotope are reported in this thesis.

1.5.1.1 Thermal cross section

The discrepancies among the experimental results of this cross section begin with its thermal point. In Figure 1.14 we summarize the thermal cross section values available in EXFOR [18] in chronological order and we compare them to the values present in the current evaluated libraries, which differ from each other by up to 15%. The main features of the previous measurements are presented in Table 1.5.

The first direct measurements of the thermal capture cross section of this isotope were carried out in the National Research Experimental (NRX) Heavy Water Moderated Reactor at the Chalk River Laboratories (Canada). Fields et al. [31] carried out a pile oscillation experiment on a sample containing several heavy Pu isotopes (A >239) and extracted a value 30(10) b for the thermal cross section of ^{242}Pu relative to that of ^{239}Pu. This value has not been included in Figure 1.14 due to its 30% uncertainty. One year after, Butler et al. [32], carried out an activation measurement relative to the ^{59}Co(n,γ) cross section and reported a significantly smaller value 18.6(8) b, from alpha spectrum analysis and total alpha counting of the generated ^{243}Am (the daughter of ^{243}Pu).

Table 1.5: *Main features of the previous measurements of the ^{242}Pu σ_{th}(n,γ) compiled in EXFOR [18].*

	Reactor	Technique	Monitor
Fields et al. (1956)	NRX (Can)	Pile oscillation	^{239}Pu(n,γ)
Butler et al. (1957)	NRX (Can)	Act. + α-spect	^{59}Co(n,γ)
Durham et al. (1970)	NRU (Can)	Act. + Chem. + α-spect.	-
Bendt & J. (1979)	OWR (USA)	PGAA (weighted sum)	^{1}H(n,γ) (CH_2)
Marie (2006)	HFR-ILL(Fr)	Act. + α-spect	^{59}Co(n,γ)
Genreith (2012)	BRR (Hun)	PGAA (single line) & act.	^{197}Au(n,γ)
Genreith (2012)	FRM II(Ger)	PGAA (single line)	^{197}Au(n,γ)

Two results consistent to that of Butler et al. were obtained in the 1970's using two different experimental techniques. First, Durham et al. [33] extracted a thermal cross section of 18.7(7) b by means of neutron activation in the NRU reactor, followed by chemical separation of the Am and Pu and alpha counting of the ^{243}Am and ^{242}Pu present in the

sample. In 1979, a Prompt Gamma Activation (PGAA) measurement of the ^{242}Pu(n,γ) reaction was performed by Bendt and Journey in the Omega West Reactor at Los Alamos Nat. Lab. (USA). From this experiment, a thermal cross section value 18.5(10) b was extracted from the the weighted sum of the partial γ-ray production cross section of 407 prompt γ-ray lines.

The largest value in Figure 1.14, 22.5(11) b, was obtained by Marie et al [35] through activation of ^{242}Pu in the High Flux Reactor of ILL and alpha spectroscopy on ^{243}Am, and disagreed by 20% with the previous measurements.

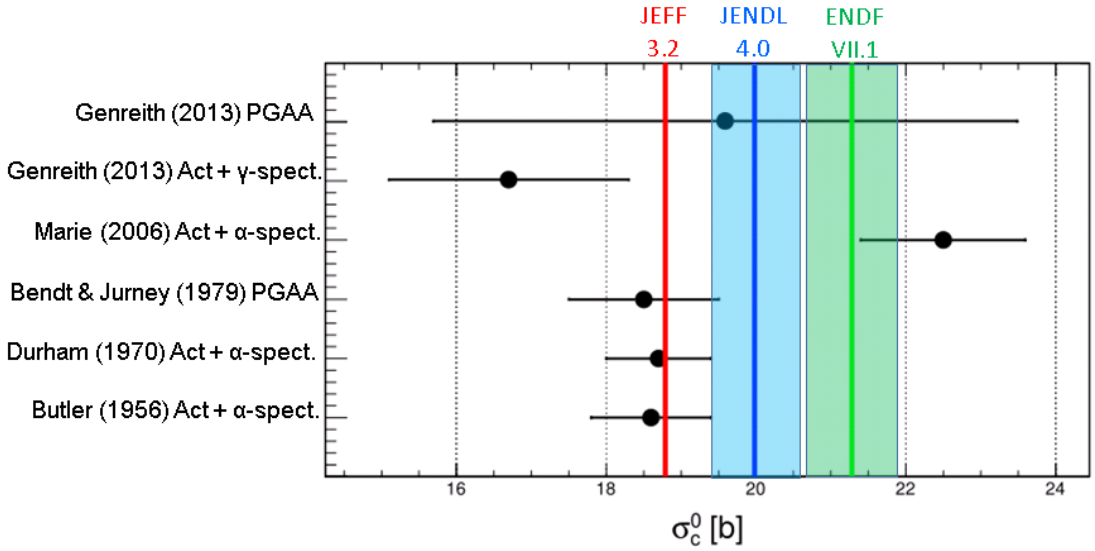

Figure 1.14: ^{242}*Pu thermal neutron capture cross section: Experimental results in chronological order compared to the values included in the latest evaluated libraries.*

On the view of this disagreement, two new measurements by Genreith et al. [36, 37] were carried out at the FRM II research reactor of the Garching Forzungszentrum and the Budapest Research Reactor by means of the Prompt Gamma Activation Analysis (PGAA) technique. However, their results 19.6(39) b (BRR) and 19.9(40) b (Garching) did not succeed to clarify the situation due to their 20% uncertainy, related to the intensity I = 0.39(8) [38, 39] of the 287.65 keV prompt gamma line. Figure 1.14 includes only the result from the measurement at BRR since both are very close and present the same limitation in accuracy. The measurement by Bendt and Jurney [34], the only previous prompt gamma measurement, did not suffer from this uncertainty since they considered the integral γ-ray spectra and not an individual γ-ray line.

In the same work, Genreith et al. looked at the decay of ^{243}Pu ($T_{1/2}$ = 4.956 h) via the most intense (I = 0.23(2)) γ-ray transition of 83.56 keV. The corresponding result of 16.7(16) b was not far from the old measurements but was discarded by the authors because of the large correction factor (47%) needed for the self-attenuation of the 83.56 keV γ-rays in the 0.75 mm thick quartz ampule and the PuO_2 pellet, a cylinder of 1.5 mm diam x 3 mm tall.

Table 1.6: *Main features of the previous time-of-flight measurements of the ^{242}Pu(n,γ) cross-section in the RRR compiled in EXFOR [18].*

	Facility/Detector	**Reported data**	E_n **(eV)**
Poortmans et al. (1973)	CNMB/Moxon-Rae	RP	1-130
Buckner et al. (2016)	LANSCE/Tot. abs.	σ(n,γ) and RP	1-500

1.5.1.2 Resonance region and resonance parameters

The first attempt to measure the ^{242}Pu(n,γ) reaction in its resonance regions was made in 1973, when Poortmans et al. [40] used Moxon-Rae-like detectors to measure the point-wise cross section below 1.3 keV at the 60 m flight path of the CBNM e$^-$ linear accelerator neutron time-of-flight spectrometer (Geel, Belgium). In this work, the R-Matrix description of the resonant cross section (see Section 2.2) in terms of resonance parameters was carried out up to 1300 keV from the combined analysis of capture, fission and total cross section data sets but radiative widths Γ_γ were only reported up to 920 eV.

A recent time-of-flight measurement was carried out with the DANCE Total Absorption detector at LANSCE by Buckner et al. [41]. In this measurement, the capture cross section of ^{242}Pu normalized to ^{239}Puσ(n,f) was determined in the energy region from thermal to 40 keV but resonances were resolved only up to 500 eV due to the limited neutron energy resolution of the DANCE facility related to its short flightpath (21 m). Their results, with a final systematic uncertainty around 6%, show a fairly good agreement with the evaluations in the resonance region.

The resonance parameters reported in the ENDF/B-VII.1 [21] and JEFF-3.2 [20] are basically those reported in Poortmans' work. The current high energy limits of the RRR in the evaluations are those of the Poortmans measurement: ENDF/B-VII.1 [21] reports parameters up to 920 eV, while JEFF-3.2 [20] expands the energy up to 1.3 keV.

The lack of high resolution data up to higher neutron energies limits the possibility of extracting accurate resonance parameters for a large set of resonances. This affects severely the uncertainty of the average resonance parameters extracted from the statistical analysis of individual resonances (see Section 2.2.4), as it is reflected in the present large discrepancies among average resonance parameters in the literature (see Table 7.7).

Table 1.7: *Average resonance parameters in the literature showing discrepancies around 10%.*

	ENDF [21]	**JEFF [20]**	**JENDL [22]**	**RIPL [26]**	**Rich et al.**[42]
S_0 (10^{-4})	1.02	1.00	0.98	0.98(8)	0.91(20)
D_0 (eV)	13.6	15.3	-	13.50(15)	16.8(5)
$<\Gamma_\gamma>$ (meV)	22.27	24.2	23.4	23(2)	22(1)

1.5.1.3 Fast region (>1 keV)

The first attempts to measure the ^{242}Pu(n,γ) reaction in the keV region, also known as unresolved resonance region (URR) (see Section 2.1.1), were made in 1975 when Hockenbury et al. [43] carried out a time-of-flight measurement (6-87 keV) at the Rensselaer Polytechnic Institute (RPI) (Troy, USA). In this work, the point-wise capture cross section was determined at the Gaerttner Linear Accelerator (e^- LINAC) using organic liquid scintillators to detect the capture γ-rays and a NaI(Tl) detector to monitor the neutron flux.

A few years later, Wisshak and Kaeppeler [44, 45] measured the ^{242}Pu capture cross section relative to that of ^{197}Au in the unresolved resonance region in two energy intervals, 10 to 90 keV and 50 to 250 keV. Neutrons were produced via the ^{7}Li(p,n) (10 to 90 keV) and T(p,n) reaction (50 to 250 keV) with the Karlsruhe 3-MV pulsed Van de Graaff accelerator and a neutron time-of-flight distance of 10 and 66 cm was used, respectively. Capture γ-rays were detected in both cases by a Moxon-Rae detector. The results of both measurements, with uncertainties in the 6-20% range, are consistent in the overlapping energy region.

Recently, another time-of-flight measurement was carried out with the DANCE detector at LANSCE by Buckner et al. [41], covering the region from thermal to 40 keV. Their result suggests a systematic reduction of 20-30% in the URR (above 1 keV) compared to ENDF/B-VII.1. The summary of the main features of these measurements is presented in Table 1.8.

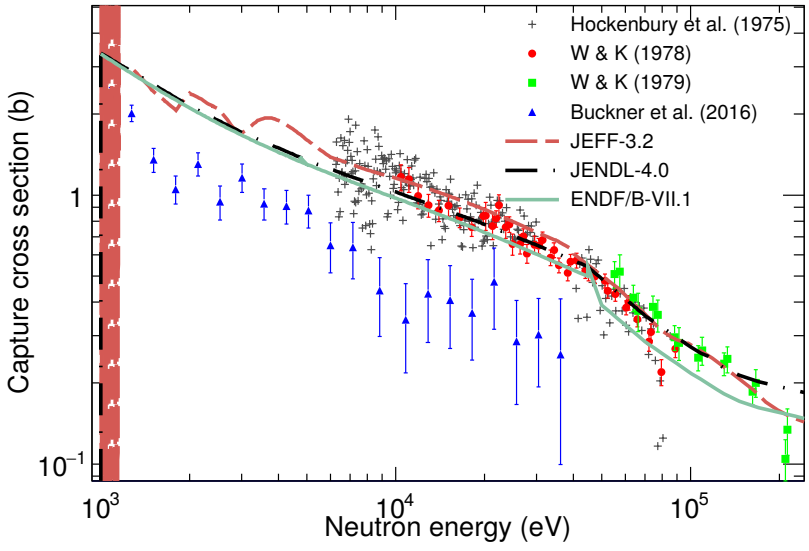

Figure 1.15: *Capture cross section of ^{242}Pu in the fast energy region. The previous experimental data sets available in EXFOR are compared to the cross section reported in the main evaluated files.*

Among the evaluations, JEFF-3.2 is in agreement with ENDF/B-VII.1 around 1 keV but 10-20% above the latter at ~10 keV and JENDL 4.0 falls in between JEFF and ENDF

up to 50 keV and is in agreement or above JEFF beyond this energy. Figure 1.15 illustrates the current status of the ^{242}Pu(n,γ) cross section in terms of evaluations and experimental data in the URR (1 - 250 keV).

Table 1.8: *Main features of the previous time-of-flight measurements of the ^{242}Pu(n,γ) cross-section in the URR compiled in EXFOR [18].*

	Facility/Detector	**Final data**	E_n **(keV)**	**Unc. (%)**
Hockenbury et al. (1975)	RPI/Liq. scint.	^{242}Pu cross section	6-87	n.a.
W. and K.(1978)	FZK/Moxon-Rae	Ratio to ^{197}Au(n,γ)	10-90	6-12
W. and K. (1979)	FZK/Moxon-Rae	Ratio to ^{197}Au(n,γ)	50-250	10-20
Buckner et al. (2016)	LANSCE/Tot. abs.	^{242}Pu cross section	1-40	6-61

1.5.2 Nuclear data requirements for the ^{242}Pu(n,γ) reaction

As we presented in Section 1.4.2, the design and operation of these innovative systems require improved knowledge of the neutron cross sections of some of the isotopes present in the new fuel compositions such as the MOX [28]. Among the neutron cross sections that need to be improved in terms of accuracy, the NEA Subgroup WPEC-26 recommends in its report *Uncertainty and target accuracy assessment for innovative system using recent covariance data evaluations* [29] that the capture cross section of ^{242}Pu should be measured with an accuracy of 8-10% in the energy range between 2 keV and 500 keV (see Table 1.9).

Table 1.9 presents only a summary of the target accuracies for each of the studied nuclear systems. From the results in this table, one concludes that relevant energy range and the target accuracy vary significantly depending on the specific nuclear system. This result is related to the different sensitivity of each of the integral parameters in each system to the capture cross section of ^{242}Pu.

Table 1.9: *Current and required accuracy of ^{242}Puσ(n,γ) for nuclear innovative systems (fast reactors) according to the NEA-WPEC26 [29] and the requested in the HPRL [30]. The uncertainty ranges represent the maximum and minimum values among the different energy groups.*

		Accuracy(%)	
	Energy Range	**Current**	**Required**
SFR	2-500 keV	24-39	8-12
EFR	2-183 keV	∼35	25-32
GFR	2-183 keV	∼35	8-13
LFR	9-183 keV	∼35	11-12
ADMAB(ADS)	9-25 keV	∼35	10
All Combined	2-183 keV	∼35	8-12
HPRL	0.5 eV-2 keV	14[a]	8

a) From the overestimation of ^{242}Puσ(n,γ) cross section in JEFF observed in the PROFIL experiments.

An additional motivation to improve the accuracy of this cross section, is related to the results of the PROFIL and PROFIL-2 experiments, carried out in Phénix demonstration fast reactor between 1975 and 1980. These experiments consisted of the irradiation of isotopically pure samples in a well charaterized neutron flux followed by a measurement of the isotopical composition of the irradiated samples by means of mass spectrometry. In particular, three to four independent ^{242}Pu samples were irradiated in the PROFIL and PROFIL-2 experiments to reduce the possible experimental uncertainties. The experimental results were compared to the burn-up calculation based on the evaluated libraries, in particular JEFF-3.1 (=JEFF-3.2). The experimental details and analysis techniques can be found in Ref. [47].

The ratios between the calculated and experimental result, usually noted as C/E, showed for the case of ^{242}Pu capture the largest deviation among the studied actinides. In particular, the interpretation of this experiments with JEFF-3.1 resulted in a a $C/E = 1.165(12)$ for PROFIL and $C/E = 1.120(20)$ for PROFIL-2. The average of the two experiments indicates an overestimation of about 14% of the ^{242}Pu integral capture cross section for the spectrum of the Phénix Reactor. Although the reactor neutron spectrum convers the energy range between 1 keV and 10 MeV [48], the maximum sensitivity of the C/E value for ^{242}Pu(n,γ) corresponds to a neutron energy of about 40 keV [46].

The reduction of the capture cross section from JEFF suggested by the PROFIL and PROFIL 2 experiments seems to agree with the trend of the data by Whissak et al. and Hockenbury et al., significantly below the JEFF-3.2 cross section (see Figure 1.15). This result is surprising since the modeling of the average capture cross section in JEFF-3.2 was performed on these data sets and confirmed the need of an improved consistency between the parameters from the resonance region and the fast region, described in terms of optical model calculations [46].

Aiming at improving the evaluation of the fast energy range in terms of average parameters, the NEA, in its *Nuclear Data High Priority Request List* (HPRL) [30], requests high-resolution capture measurements with improved accuracy below 2 keV. A new large set of accurate individual resonance parameters should solve the above mentioned inconsistencies. This should also also allow to solve the present discrepancies in the average resonance parameters in the literature (see Table 7.7).

Last, as we discussed in the previous section, the discrepancies between experimental values affect the thermal cross section as well (see Figure 1.14), leading to differences of up to 15% among the evaluated libraries. This situation calls for a new accurate measurement of the thermal point of the ^{242}Pu(n,γ) cross section as well.

Chapter 2

Neutron cross sections: theory and experiment

In this chapter, a brief introduction to neutron cross section is given, from both the theoretical and experimental points of view. Neutron cross sections in the Resolved and Unresolved Resonance Regions are theoretically described by means of the R-Matrix theory and the Hauser-Feshbach formalism or Optical Models, respectively. The different neutron beam facilities and experimental techniques available to date to carry out neutron cross section measurements, in particular radiative capture measurements, are also introduced in this chapter. Last, we present the complementary use of different neutron beams, measuring techniques and theoretical approaches used in this work for a a comprehensive measurement of the radiative capture cross section of ^{242}Pu.

2.1 Introduction to neutron cross sections

2.1.1 Neutron-nucleus interactions and neutron cross section

Cross sections are, in general, described as the effective area of an object that quantifies the probability of a certain interaction between an incident projectile and the target object. In Nuclear Physics, cross sections characterize the probability that a certain nuclear reaction will occur and are measured in units of surface, as it is illustrated inFigure 2.1. The standard units for measuring nuclear cross sections is the barn (b) (1 b = 10^{-28} m^2), since this is the order of magnitude of the cross-sectional area of the atomic nucleus.

Focusing on the neutron-nucleus reactions, a large variety of nuclear processes may arise when a neutron interacts with a target nucleus. The microscopic neutron cross section (hereafter denoted σ) can reflect the total interaction probability, σ_{tot}, which is defined as the sum of the partial contributions of each reaction channel

$$\sigma_{tot} = \sigma_n + \sigma_\gamma + \sigma_f + ..., \tag{2.1}$$

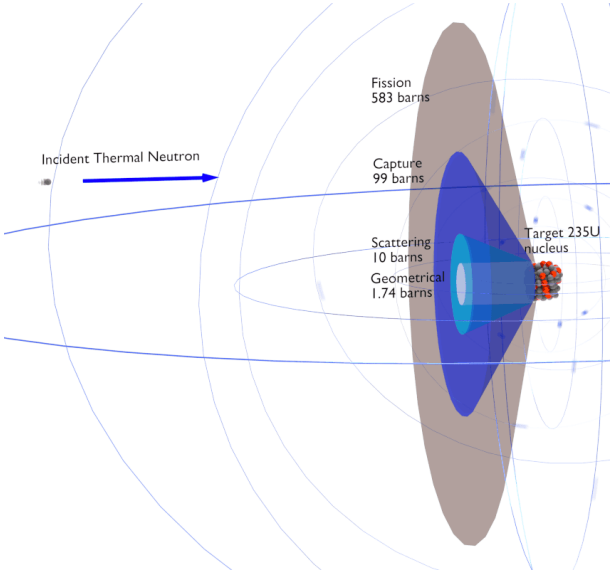

Figure 2.1: *Graphical interpretation of the neutron cross section illustrated with the case of a thermal (25.3 meV) neutron interacting with a* ^{235}U *nucleus. Source: Ref. [49].*

where n, γ and f is the common nomenclature for the neutron scattering, radiative capture and neutron-induced fission, respectively.

The reaction rate (i.e. number of reactions per unit time) induced by a neutron beam with a flux ϕ(n/cm^2/s) that impinges an isotopically-pure thin film with surface S(cm^2), areal density n(atoms/b), is directly proportional to the total neutron cross section σ_{tot}(b) by

$$R = \sigma_{tot} \cdot \phi \cdot S \cdot n. \tag{2.2}$$

The theoretical description of neutron cross sections varies depending on the time scale of the interaction within the nucleus, related to the neutron energy. According to this magnitude, neutron-nucleus reactions can be classified:

- **Direct reactions**: A neutron and a target nucleus interact for a very short time ($\tau \sim 10^{-22}$ s) allowing for an interaction with a single nucleon. This reactions require minimum neutron energies of $\sim$5 MeV/A and are characterized by anisotropical distributions of the outgoing particles. These reactions will not be addressed by theoretical description in the following.
- **Compound Nucleus reactions**: The neutron and the nucleus are within the range of nuclear forces for a suffiently long time (10^{-16}-10^{-18} s), allowing the creation of a relatively long-lived intermediate state called the Compound Nucleus. This kind of reactions are usually created by neutrons in the energy range studied in this work and are described in more detail in the following.

Among the Compound Nucleus reactions, different reaction channels can be distinghished:

- Elastic scattering (n,n): the neutron is emitted with the same energy.

- Radiative capture (n,γ): the neutron is absorbed and the Compound Nucleus decays to its ground state by multiple γ-ray emission (capture cascade).
- Fission (n,f): the Compound Nucleus splits into lighter nuclei, emitting as well photons a neutrons.
- Inelastic (n,n'): some energy of the incident neutron is absorbed by the nucleus and, as a consequence, the recoil nucleus is left in an excited state and the emitted neutron has less energy.
- Charged particle (n,α), (n,p), ...: the Compound Nucleus has sufficient excitation energy to overcome the coulomb barrier and eject a proton or a cluster of nucleons.

The partial cross sections change significantly for different neutron-induced reactions and the neutron energies. As an example, Figure 2.2 shows the capture and fission cross sections of ^{239}Pu and ^{242}Pu as a function of the neutron energy. From this figure one can appreciate the wide range between the minimum and maximum values of the cross sections and the very different dependence of the partial cross sections with the neutron energy. The neutron cross section are different for each isotope owing to the sensitivity of neutrons to the nuclear structure, as it is illustrated in Figure 2.2 for two different isotopes of plutonium (A=239 and 242).

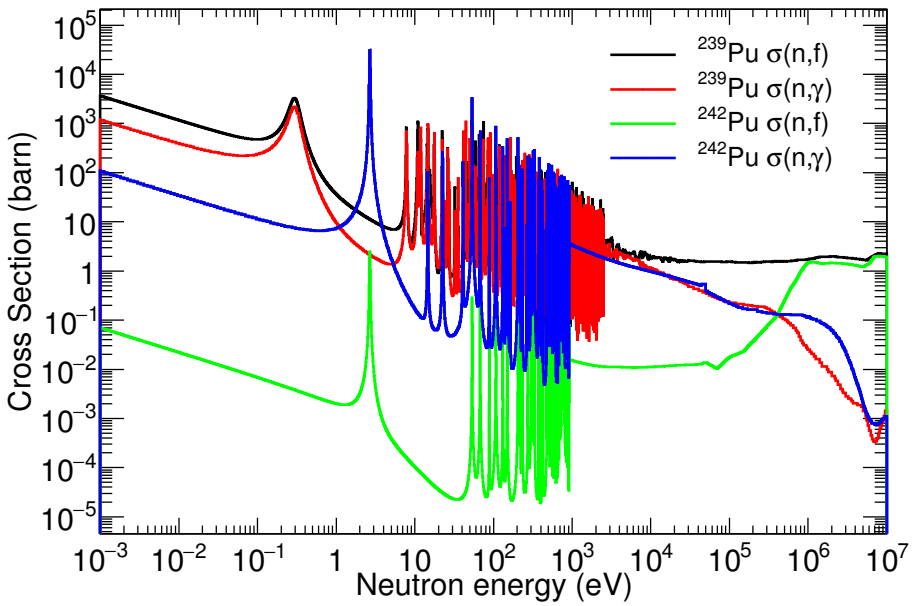

Figure 2.2: *Capture and fission cross sections of ^{239}Pu and ^{242}Pu extracted from the ENDF/B-VII.1 evaluation [21].*

The following energy regions can be indentified according to the structures observed in the cross sections shown in Figure 2.2:

- **Thermal region**: the cross section for neutron energies below the first resonance is inversely proportional to the time that the neutron spends in the proximity of

the nucleus or equivalently inversely proportional to the velocity of the neutron ($\sigma \sim 1/v \sim 1/\sqrt{E}$). This region includes the so-called thermal point at 25.3 meV, corresponding to the energy of a neutron in thermal equilibrium with water at 20°.

- **Resolved Resonance Region (RRR)**: neutron cross sections present resonant structures in an energy region which varies depending on the isotope, for instance in Figure 2.2 between a few tenths of eV and several keV. The resonances are the signature of quasi-stationary states in the Compound Nucleus above the neutron separation energy, as it is described Section 2.1.2. Resonances are assumed to be resolved when their intrinsic widths are smaller than the average distance between them. The description of the resonance region is based on a parameterization of the resonances in the framework of the R-Matrix formalim, described in Sections 2.2.1 and 2.2.3. The statistical properties of the resonance parameters serves to define the average resonance parameters (see Section 2.2.4), that help describing the cross section at higher energies.
- **Unresolved Resonance Region (URR)**: the level density increases with energy and the spacing between consecutive resonances becomes smaller, and the resonances begin to overlap. In this energy region the cross section cannot be described in terms of individual resonances. However, the smooth cross section can still be described in terms of an overlap of statistically distributed resonances following the average resonance parameters mentioned before, as it is described in Section 2.3.
- **Continuum/high energy region**: At higher energies the distance between consecutive levels is so small than it can actually be considered a continuum. In this neutron energy region new threshold reaction channels open up and direct reactions start to become relevant.

2.1.2 Compound Nucleus theory

The resonant structures observed in the neutron cross sections (see Figure 2.2) can be understood following the description of the compound neutron-nucleus reactions, introduced before in this section. The idea of the Compound Nucleus formation, known as Compound Nucleus Theory, was first proposed by Niels Bohr in 1936 [50] and extended to all the reaction channels including fission in 1940 [51]. This model, sketched in Figure 2.3, explains the neutron induced reactions as a two-step process:

1. The incident particle (neutrons in our case) and the target nucleus become indistinguishable after the collision and together constitute the Compound Nucleus (CN), which is left at an high excitation energy above the neutron bounding energy S_n, typically in the 5-10 MeV range. The total excitation energy is approximately given by $E = S_n + \frac{A}{A+1}E_n$. The excitation energy is distributed among all the nucleons (they reach thermal equilibrium) and for some specific energies of the incident neutrons, a quasi-stationary level or resonance of the Compound Nucleus is populated. The total cross section is proportional to the probability of formation of the Compound Nucleus.

2. The Compound Nucleus decays with a half-life τ corresponding to a resonance width $\Gamma = h/\tau$, through one of the open channels: emission of γ-rays (n,γ), re-emission of a neutron with the same (n,n) or lower energy (n,n'), fission of the nucleus (n,f), etc. The total resonance width Γ is the sum of the partial contributions of each open channel.

$$\Gamma = \Gamma_\gamma + \Gamma_n + \Gamma_f + ... \tag{2.3}$$

The probability of decaying via each of the open channels is proportional to the corresponding partial width.

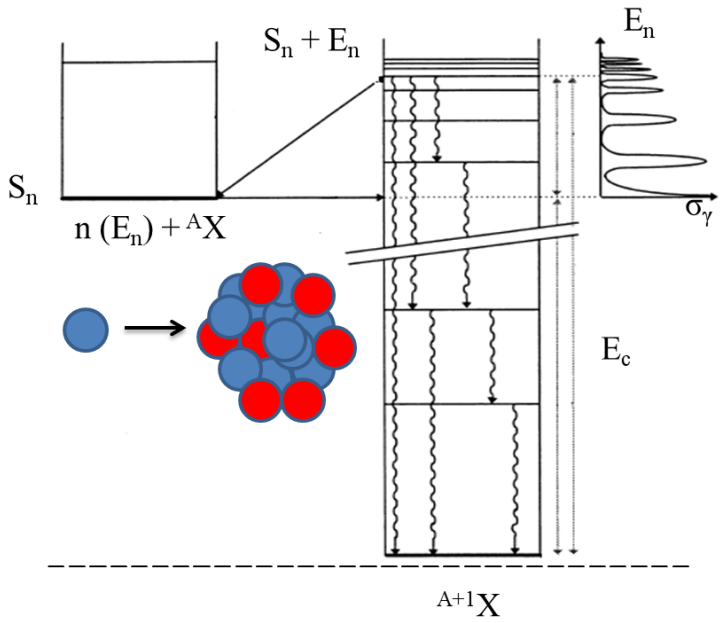

Figure 2.3: *Sketch of the Compound Nucleus formation when a neutron of energy E_n interacts with ${}^{A}X$ nucleus. The quasi-stationary states on the Compound Nucleus above the neutron separation energy S_n lead to resonances in the cross section. The total excitation energy to be released in the decay of the compound nucleus is noted as $E_c = S_n + E_n$.*

The sketch shown in Figure 2.3, corresponds to the Compound Nucleus formation and the subsequent decay via γ-ray emission which characterizes the radiative neutron capture studied in this work. In this figure, one observes that the level density increases with energy, being the usual level spacings ~100 keV near the ground state and ~10 eV in the vicinity of S_n (for heavy nuclei).

The mathematical description of the Compound Nucleus Theory in the framework of the scattering theory is carried out with the R-matrix formalism, described in the following section.

2.2 Neutron cross section in the RRR

2.2.1 Theoretical description: R-Matrix formalism

The R-matrix formalism is the most convenient description for the Resolved resonances in the context of the Compound Nucleus. It was first proposed by Wigner and Eisenbud in Ref. [53, 54] but achieved its current standard formulation after with the comprehensive review article of Lane and Thomas in the late 50' [55]. The latest review of theory was carried out by Fröhener in the JEFF Report 18 [57].

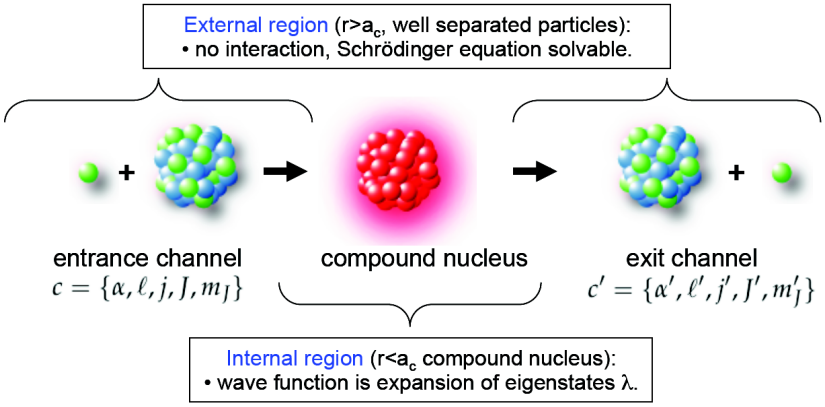

Figure 2.4: *Scheme of the basic principles of the R-Matrix theory (see text for the details). From Ref. [56].*

The main principles of the R-matrix theory are illustrated in Figure 2.4 can be summarized as:

1. All collisions are considered as an ingoing wave function describing the two incident particles, an outgoing wave function the two ejected reaction products.
2. The space is divided in two regions, using as a boundary the so-called channel radius $a_c \propto A^{1/3}$:
   - An external region ($r > a_c$) where the particles are considered separated and non interacting and are described with the well known wave functions.
   - An internal region ($r < a_c$) dominated by the nuclear forces where the incident particles interact to form the Compound Nucleus. Although the wave function is unwknown in this region, it can be expressed as an expansion in terms of eigenstates λ of the CN that satisfy the boundary conditions at $r = a_c$ to match the external wave functions.
3. As a result, one finds that for any ingoing wave, all the outgoing waves contain the properties of a quasi-stationary level λ of the CN, characterized by a given energy E_λ, spin and parity J^Π, and partial decay widths $\gamma_{\lambda,c'}$ corresponding to the decay channel c'

In general, in nuclear scattering theory one talks about reaction channels, each of them being fully defined by $c = (\alpha, l, s, J)$ where

- α represents the two particles making up the channel and includes mass (m and M), charge (z and Z), spin (i and I) with associated parities, and all other quantum numbers for each of the two particles,
- l is the relative orbital angular momentum of the two particles in the channel, and the associated parity is given by (-1)^l.
- s represents the channel spin (including the associated parity) and is defined as the quantized vector sum of the spins of the two particles of the pair $\vec{s} = \vec{i} + \vec{I}$ and satisfies $|I - i| \leq s \leq I + i$, and
- J is the total angular momentum (and associated parity), calculated from the vector sum of l and s: $\vec{J} = \vec{s} + \vec{l}$ and satisfies $|l - s| \leq J \leq l + s$.

For the simplest case of spinless, neutral particles, one can solve the non-relativistic Schrödinger equation for the boundary conditions: Stationary plane wave in the entrance channel + Stationary spherical wave in the exit channel, results in the following differential cross section

$$d\sigma_{cc'} = \pi\bar{\lambda}_c^2 | \sum_{l=0}^{\infty} (2l+1)(1 - U_l) P_l(cos\theta)|^2 \frac{d\Omega}{4\pi}, \tag{2.4}$$

where

- c and c' denote the entrance and exit channel, respectively.
- The de Broglie wave lenght $2\pi\bar{\lambda}_c^2 = \frac{\hbar}{\mu_c v_{rel}}$ is the kinematic factor related to the relative motion of the collision partners with reduced mass μ_c and relative velocity v_{rel}. This factor relates probability and cross section.
- P_l, the angular momentum eigenfunctions, are Legendre polynomials of order l, dependent on the scattering angle θ.
- U_l is known as the collision function and describes the modification of the l^{th} outgoing partial wave with respect to the zero-interaction case.
- $d\Omega$ is the differential solid angle.

Blatt and Biedenharn generalized the previous expresision for particles with spin and for partition changing collisions [58]. For zero Coulomb interaction (i.e. neutral particles) they obtained the following expression for the angle-integrated cross section

$$\sigma_{cc'} = \pi\bar{\lambda}_c^2 \sum_J g_J \sum_{l,l'} \sum_{s,s'} |\delta_{\alpha\alpha'}\delta_{ll'}\delta_{ss'} - U^J_{ll'ss'}|^2 \tag{2.5}$$

where $U^J_{ll'ss'}$, hereafter written in the compact notation $U_{cc'}$, represent the collision matrix elements. In the same way, the $\delta_{\alpha\alpha'}\delta_{ll'}\delta_{ss'} = \delta_{cc'}$ is the Kroeneker symbol that arises due to the fact that ingoing and outgoing particles are undistinguishable if $c = c'$. In the previous

expression, g_J are the so-called spin factors given by

$$g_J = \frac{(2J+1)}{(2I+1)(2i+1)}, \tag{2.6}$$

J, I and $i = 1/2$ are the spins of the resonance in the Compound Nucleus, target nucleus and neutron, respectively.

Following the compact notation that groups all the angular momentand nature of the channels [57], Eq. (2.5) can be written as

$$\sigma_{cc'} = \pi\bar{\lambda}_c^2 g_c |\delta_{cc'} - U_{cc'}|^2, \tag{2.7}$$

The previous expression is simplified if $c \neq c'$ (i.e. everything but (n,n)), and the partial cross section becomes proportional to $|U_{cc'}|^2$, the probability of transition from channel c to channel c', and to g_c, the probability of summing the correct angular momentum J from the spins of the collision partners.

Resonances are introduced by the R-matrix theory, which allows us to express the collision matrix **U** as a function of the channel matrix **R**

$$R_{cc'} = \sum_{\lambda} \frac{\gamma_{\lambda c}\gamma_{\lambda c'}}{E_\lambda - E}. \tag{2.8}$$

This description is given in Refs. [55, 59]. Alternatively, **U** can be expressed a function of the level matrix **A**

$$\begin{aligned} U_{cc'} &= e^{-i(\varphi_c+\varphi_{c'})}\left(\delta_{cc'} + i\sum_{\lambda,\mu}\Gamma_{\lambda c}^{1/2} A_{\lambda\mu}\Gamma_{\mu c'}^{1/2}\right), \\ \Gamma_{\lambda c}^{1/2} &\equiv \gamma_{\lambda c}\sqrt{2P_c}, \\ (\mathbf{A}^{-1})_{\lambda\mu} &= (E_\lambda - E)\delta_{\lambda\mu} - \sum_c \gamma_{\lambda c} L_c^\circ \gamma_{\mu c}, \end{aligned} \tag{2.9}$$

where Greek subscripts (λ, μ) refer to levels of the Compound Nucleus and c and c' represent generic entrance and exit channels. In Eq. (2.9), a first group of variables is found, which characterize a resonance in the Compound Nucleus:

- E_λ and E are the resonance and neutron energies, respectively.
- $\gamma_{\lambda c}$ are the probability amplitudes of formation of a state λ in the Compound Nucleus from the entrance channel c or decay from that state to the exit channel c'.
- $\Gamma_{\lambda c}$ are the partial decay widths, frow which the total widths are defined as $\Gamma_\lambda \equiv \sum_c \Gamma_{\lambda c}$. Cross sections are more commonly expressed in terms of $\Gamma_{\lambda c}$ rather than $\gamma_{\lambda c}$.
- P_c are the centrifugal barrier penetrabilities and relate the partial widths with the probability amplitudes, and are a function of αm E, and l.

In addition, one finds a second group of variables which consists of hard-sphere phases φ_c and logarithmic derivatives L_c, that dependend only on the in- and outgoing radial

wave functions I_c and O_c at the channel radius a_c. The general expressions for φ_c and L_c can be found in Ref. [57]. For neutral projectiles, the outgoing radial wave functions are proportional to spherical Hankel functions of the first kind, $h_l^{(1)}$,

$$O_c = I_c^* = ik_c r_c h_l^{(1)}(k_c r_c) \quad (\simeq i^l e^{ik_c r_c} \quad if \quad k_c r_c \gg \sqrt{l(l+1)} \ ), \tag{2.10}$$

where r_c is the distance between the collision partners and $k_c = 1/\bar{\lambda}_c = \sqrt{2M_\alpha E/\hbar^2}$. As a consequence, L_c can be expressed as recursion relations of the form

$$L_0 = ik_c a_c = iP_0, \qquad L_l = -l - \frac{(k_c a_c)^2}{L_{l-1} - l}, \tag{2.11}$$

The shift factor S_c and the centrifugal barrier penetrabilites P_c that appeared in Eq. (2.9), are defined as the real and imaginary parts of L_c:

$$\begin{aligned} S_c &\equiv ReL_c \\ P_c &\equiv ImL_c \end{aligned} \tag{2.12}$$

For the case of the hard sphere phases φ_c one obtains

$$\varphi_0 = k_c a_c, \qquad \varphi_l = \varphi_{l-1} + arg(l - L_{l-1}). \tag{2.13}$$

The explicit expressions of O_c, φ_c, S_c, P_c for each partial wave are given in Table 3 of Ref. [57]. Figure 2.5 illustrates the dependency of the S_c, P_c parameters as a function of the dimensionless $k_c r_c$ and the corresponding neutron energy for A=238 for different angular momenta.

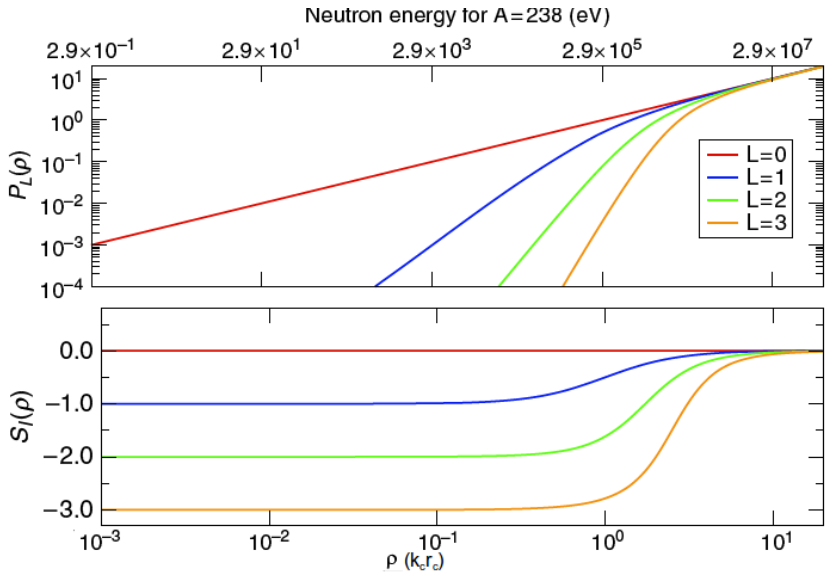

Figure 2.5: *R-Matrix parameters for the neutron exit channel as a function of the angular momentum $L \equiv l$ and $k_c r_c$. The equivalent neutron energy (for A=238) is shown in the upper x-axis. From Ref. [56].*

Several relevant results can be noted at this point:

- The channel radius is usually taken to be $a_c = (A^{1/3} + 0.8)fm$.
- Figure 2.5 shows that $S_c \to -l$ at low energies (good choice for the RRR), and therefore $S_0 = 0$ ($l = 0$), meaning that the resonances are not shifted and their peaks are located at E_λ.
- P_c is usually assumed to be constant for (n,γ) and (n,f). The, according to Eq. (2.9) $\Gamma_{\lambda\gamma}$ and $\Gamma_{\lambda f}$ are also constant.
- P_c for the neutron exit channel and s-waves $P_0 = k_c a_c \propto \sqrt{E}$ (see Figure 2.5) and the corresponding partial width is

$$\Gamma_{\lambda n}(E) = 2a_c \sqrt{\frac{2M_\alpha E}{\hbar^2}} \gamma_{\lambda n}^2 \propto \sqrt{E}\gamma_{\lambda n}^2. \tag{2.14}$$

- The resonance parameters E_λ, $\gamma_{\lambda,c}$ depend on the unknown nuclear interaction and cannot be calculated except for very simple models. In typical applications of the R-matrix theory, such as for the parameterization of the resonance cross sections from the experimental data in this work (see Section 7.1), they are considered just fit parameters.

2.2.2 Approximations to the R-Matrix formalism

The basic principles and expressions of the R-matrix theory have been reviewed so far in the previous section and provide all what is needed for the application of this formalism. However, in order to practically apply this theory, several representations or approximations are usually introduced for the inversion of the **A** matrix in Eq. (2.9). In the following, we will describe the most extensively used approximations, included in the R-Matrix code SAMMY [62], described later in Section 7.1.1.

One option is to consider only one level, while the others are neglected. This is the so-called **Single Level Breit-Wigner approximation (SLBW)**:

$$(\mathbf{A}^{-1})_{\lambda\mu} \to E_0 - E - \sum_c L_c^\circ \gamma_c^2 \equiv E_0 + \Delta - E - \frac{i}{2}\Gamma, \tag{2.15}$$

where the level shift Δ and the total level width $\Gamma = \sum_c \Gamma_c$ are real and with explicitely known energy dependences. This approximation is the least accurate one but provides the simplest expressions to derive the cross section expressions as a function of the resonance parameters. Replacing the approximated inverse level matrix of Eq. (2.15), the collission matrix in Eq. (2.9) yields

$$U_{cc'} = e^{-i(\varphi_c + \varphi_{c'})} \left(\delta_{cc'} + \frac{i\sqrt{\Gamma_c \Gamma_{c'}}}{(E_0 - E) - \frac{i}{2}\Gamma} \right). \tag{2.16}$$

For neutrons as incident particle and choosing boundary conditions so that the level shift is zero (i.e. resonance energy is exactly the energy of the λ compound level), the previous

expression is simplified to

$$U_{nc'} = e^{-2ik_cR}\left(\delta_{nc'} + \frac{i\sqrt{\Gamma_c\Gamma_{c'}}}{(E_0 - E)^2 + \Delta - \frac{i}{2}\Gamma}\right), \tag{2.17}$$

$R = a_c$ being the effective radius of the Compound Nucleus. Last, for s-wave resonances of spin J and with $k_cR \ll 1$ (see Figure 2.5), the expression for the total cross section is given by

$$\sigma_n^J = 4\pi g_J R_J^2 + 4\pi\bar{\lambda}^2 g_J\left(\frac{\Gamma_n\Gamma}{\Gamma^2 + 4(E_0 - E)^2} + 4k_cR_J\frac{\Gamma_n(E_0 - E)}{\Gamma^2 + 4(E_0 - E)^2}\right). \tag{2.18}$$

The different terms in this expression are illustrated with the ^{56}Fe 28 keV resonance in Figure 2.6, where the different contributions to the total cross section $\sigma_{tot} \equiv \sigma_n^J$ are plotted separately:

- $4\pi g_J R_J^2$: Potential neutron scattering (σ_{pot} in Figure 2.6), proportional to the square of the effective scattering radius of the Compound Nucleus R_J^2.
- Second term: Resonant term (σ_{res}) with a maximum at the resonance energy E_0 and symmetric in energy.
- Third term: Interference term (σ_{int}) assymetric on both sides of the resonance energy E_0.

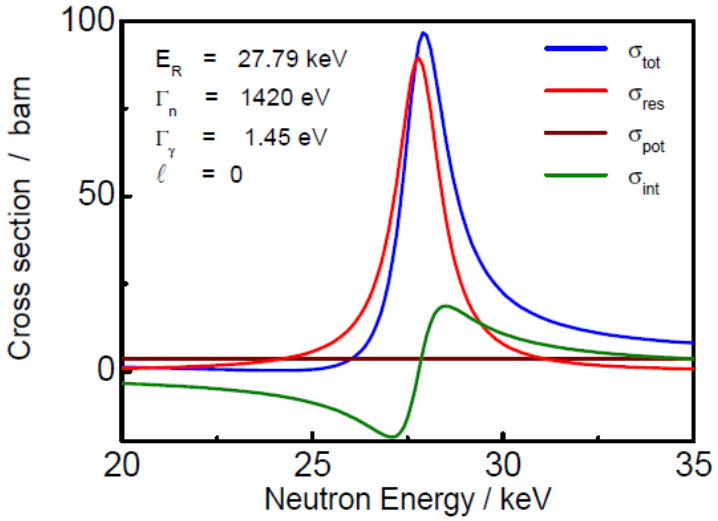

Figure 2.6: *Total cross section of ^{56}Fe showing the s-wave resonance at 28 keV calculated with the SLBW approximation. The different terms contributing to the total cross section are plotted separately. From Ref. [63].*

Following with the s-wave case, the resulting expression for the partial cross sections are

$$\begin{aligned}\sigma_{nc}^J &= 4\pi\bar{\lambda}^2 g_J\frac{\Gamma_n\Gamma_c}{\Gamma^2 + 4(E_0 - E)^2},\\ \sigma_{nn}^J &= \sigma_n^J - \sum_c \sigma_{nc}^J\end{aligned} \tag{2.19}$$

where ($c \neq n$) in both expressions and σ_{nc}^{J}, symmetric in energy is known as the Breit-Wigner formula [52].

More accurate approximations of the inverse level matrix are the Multi Level Breit-Wigner approximation (MLBW) and, in particular, the Reich-Moore approximation. The **Multi Level Breit-Wigner approximation (MLBW)** consists in neglecting all the offdiagonal terms of $\mathbf{A}^{-1}$ (i.e. assuming non-correlated levels):

$$(\mathbf{A}^{-1})_{\lambda\mu} = (E_\lambda - E - \sum_c L_c^\circ \gamma_{\lambda c}^2)\delta_{\lambda\mu} \equiv (E_\lambda + \Delta_\lambda - E - \frac{i}{2}\Gamma_\lambda)\delta_{\lambda\mu}, \tag{2.20}$$

where the level shift Δ_λ and the total level width $\Gamma_\lambda = \sum_c \Gamma_{\lambda c}$. Last, the most accurate approximation is the **Reich-Moore approximation**, which neglects only the off-diagonal terms for the γ exit channels $c = \gamma$.

$$(\mathbf{A}^{-1})_{\lambda\mu} = (E_\lambda + \Delta_{\lambda\gamma} - E - \frac{i}{2}\Gamma_{\lambda\gamma})\delta_{\lambda\mu} - \sum_{c\neq\gamma} \gamma_{\lambda c} L_c^\circ \gamma_{\mu c}, \tag{2.21}$$

where the real $\Delta_{\lambda,\gamma}$ level shifts are usually absorbed in the constant E_λ and the total radiation width $\Gamma_{\lambda\gamma} = \sum_{c=\gamma} \Gamma_{\lambda c}$ are usually taken as constant.

Some exact representations of the inverse level matrix are are the Wigner-Eisenbud representation [54] and the Kapur-Peierls representation [60]. Further approximations are also available in the literature, such as the Adler-Adler approximation [61].

2.2.3 Analysis of the resonances

The resonance parameters of the R-Matrix formalism provide a description of each resonance in the cross section. This parameters are the resonance energy E_0 and the resonance widths with $\Gamma = \sum_c \Gamma_c$, where the sum runs in c runs over all the open reaction channels.

These parameters can be extracted from the analysis of total and partial cross section measurements, which provide transmission coefficients $T(E_n)$, given by Eq.(2.51), and reaction yields $Y_r(E_n)$, defined in Eq.(2.48) using two different methods:

1. **Resonance Area Analysis**: allows to extract the resonance parameters from the analysis of the resonance areas.
2. **Resonance fitting**: more accurate method to calculate the parameters by fitting the shape of the experimental data.

From the analysis of the resonance areas, one can obtain different information depending on the type of cross section. In the case of transmission measurements the resonance area

$$A_t = \int (1 - T(E_n) dE_n = 2\pi^2 n \bar{\lambda_0} g_J \Gamma_n, \tag{2.22}$$

is proportional to the neutron width Γ_n. In the previous expression $\bar{\lambda_0}$ is the reduced wave lenght of a neutron with the energy of the resonance.

In the case of partial cross section measurements, the area of the resonances in the obtained reaction yields

$$A_r = \int \sigma_r(E_n) dE_n = 2\pi^2 n \bar{\lambda_0} g_J \frac{\Gamma_n \Gamma_r}{\Gamma}, \tag{2.23}$$

is proportional to the so-called Reaction Kernel, defined as:

$$K_r = g_J \frac{\Gamma_r \Gamma_n}{\Gamma}, \tag{2.24}$$

where g_J is the spin factor defined in Eq. (2.6). In some cases the resonance width is dominated by a given channel and the Reaction Kernel becomes proportional to one of partial widths

$$\begin{aligned} \Gamma_r \ll \Gamma_n : R_K \rightarrow g_J \Gamma_r \\ \Gamma_r \gg \Gamma_n : R_K \rightarrow g_J \Gamma_n \end{aligned} \tag{2.25}$$

While the Resonance Area Analysis analysis works in most cases, if measurements have sufficient statistics and energy resolution, a better result (in particular more information on Γ_r), is obtained by directly fitting the experimental data (reaction yields or transmission coefficients) with and R-Matrix Analysis code to extract the resonance parameters. Together with the SAMMY code used in this work, REFIT [64] is also available for this purpose. The former is based on a Bayesian approach while the latter uses Least-Squares fitting procedures.

More details on the SAMMY code, the experimental corrections included in the calculation, the initial parameters, fitting procedure and uncertainty estimation for the fitted parameters are given in Section 7.1.

2.2.4 Average resonance parameters and statistical properties

The statistical properties of the resonance parameters extracted from the R-Matrix analysis of the experimental data in the RRR can be studied in terms of the corresponding average parameters, and the statistical properties. This analysis is very relevant for:

1. Testing the consistency of the resonance parameters distribution with the expected behaviour.
2. Describing the cross section in the URR with the mentioned average resonance parameters (see Section 2.3).
3. Providing a key input for the Optical Model (OM) calculations of neutron cross sections in the URR and beyond.

The statistical model of nuclear resonance reactions emerged in the 50's. In particular, the Compound Nucleus at energies around S_n can be statistically described by the Gaussian Orthogonal Ensemble (GOE). The main works introducing this model are included in a

review by C.E. Porter (1965) [65]. According to this model, the matrix elements $\gamma_{\lambda\mu}$ governing the nuclear transtions are random variables following Gaussian distributions of zero mean. This implies several theoretical distributions for the partial widths and level spacing defined within the R-Matrix formalism. In this context, the following section aims at briefly introducing the statistical distributions of resonance parameters.

2.2.4.1 Distribution of resonance spacings

The distribution of levels in the Compound Nucleus is derived from the level density, which is in general a function of the energy E, spin J and parity P

$$\rho(E, J, P) = \rho_E(E)\ \rho_J(J)\ \rho_P(P), \tag{2.26}$$

where the individual factors are the energy, spin and parity distribution of levels, respectively. Many models for density distributions are available; in particular, its dependence with the excitation energy is described by models such as the Fermi Gas Model [67] or the Constant Temperature Model [66].

In neutron cross section measurements, the level density of the Compound Nucleus in the proximity of the neutron binding energy can be directly calculated from the number of observed levels N^J (i.e. number of resonance resonances) with the same spin and parity J^P in a given neutron energy range ΔE_n.

$$\rho^J = \frac{N^J}{\Delta E_n}. \tag{2.27}$$

From the previous expression, we can define the **average level spacing** $\langle D^J \rangle$, the first average resonance parameter, as

$$\langle D^J \rangle = \frac{1}{\rho^J}, \tag{2.28}$$

which is experimentally calculated from the inverse slope of the cumulative distribution of observed resonances,

$$N^J(E_n) = N^J(0) + \frac{1}{\langle D^J \rangle} E_n. \tag{2.29}$$

According to the GOE of real symmetric matrices, the theoretical distribution of next-nearest neighbour spacings is given by the Wigner law [68]

$$p(x)dx = \frac{\pi x}{2} e^{-\frac{\pi x^2}{4}} dx, \tag{2.30}$$

where $x = D_i^J / \langle D^J \rangle$ with $D_i^J = E_{i+1} - E_i$ being the distance between consecutive resonances with a certain J^P and $\langle D^J \rangle$ its average value. The statistical uncertainty of the average level spacing $\langle \Delta D^J \rangle$, assuming the Wigner distribution of Eq. (2.30) for the next neighbour level spacings, is given by

$$\frac{\Delta \langle D^J \rangle}{\langle D^J \rangle} = \sqrt{\frac{1}{N^J}(\frac{4}{\pi} - 1)}. \tag{2.31}$$

For the analysis of the experimental distribution of spacings for s-wave resonances of ^{242}Pu (see Section 7.4.1), the average level spacing will be noted as $D_l \rightarrow D_0 \equiv \langle D^{1/2+} \rangle$, since all the s-wave resonances in the Compound Nucleus ($^{242}Pu + n$) have $J^P = 1/2^+$. The D_l notation is also used for the description of the average cross section in the URR (see Section 2.3).

2.2.4.2 Distributions of resonance widths

Partial resonance widths $\Gamma_{\lambda c}$ for each level in the Compound Nucleus are defined in Eq. (2.9) as a function of the penetrability P_c amplitude probabilities $\gamma_{\lambda c}$. In reality, the partial width of the CN level λ for the exit channel c contains the contribution of the ν possible de-excitation modes

$$\Gamma_{\lambda c} = \sum_{\alpha=1}^{\nu} 2P_\alpha \gamma_{\lambda\alpha}^2, \tag{2.32}$$

where the amplitude probabilities $\gamma_{\lambda\alpha}$ fluctuate following a Gaussian distribution. Two particular cases can be found from this general expression:

1. $c \neq n$: For photon and fission channels the penetrability factors can be assumed to be almost constant in energy in the RRR.
2. $c = n$: For the case of the neutron channel, the penetrabilities are strongly dependent with energy. For s-waves, $P_\alpha \propto \sqrt{E}$ (see Eq. (2.14)).

For the case ($c \neq n$), the general distribution of partial widths $\Gamma_{\lambda c}$ is given, according to Ref. [69], by

$$\begin{aligned} p(x,\nu)dx &= \frac{\frac{\nu}{2}}{\Gamma(\frac{\nu}{2})}(\frac{\nu}{2}x)^{\frac{\nu}{2}-1}e^{-\frac{\nu}{2}x}dx, \\ x &= \frac{\gamma_{\lambda c}^2}{\langle \gamma_{\lambda c}^2 \rangle} = \frac{\Gamma_{\lambda c}}{\langle \Gamma_{\lambda c} \rangle}, \end{aligned} \tag{2.33}$$

which corresponds to a χ^2 distribution with ν degrees of freedom, average value $x = 1$ and variance $2/\nu$. This expression applies for the distribution of fission $\Gamma_{\lambda f}$ and radiative $\Gamma_{\gamma f}$ widths.

For the case of the radiative width $\Gamma_{\lambda\gamma}$, the total width is expected to be the sum of many partial contributions due to the large number of available levels below S_n, especially for heavy nuclei. If we assume that $\nu \rightarrow \infty$, the distribution given by Eq. (2.33) turns in to Dirac Delta, and Eq. (2.32) becomes

$$\Gamma_{\lambda\gamma} = \sum_{i=1}^{\nu \gg 1} \Gamma_{\lambda\gamma_i} = \Gamma_{\mu\gamma} = \langle \Gamma_\gamma \rangle, \tag{2.34}$$

where λ and μ represent two different CN levels, meaning that the radiative width features a constant value. The **average radiative width** $\langle \Gamma_\gamma \rangle$ is the second average parameter.

At this point we have to remark that the assumption of infinite degrees of freedom is just an approximation. Realistic results of the fluctuations of radiative widths based on

statistical model simulations will be discussed in the analysis of resonances parameters in Sections 7.1.2 and 7.4.2.

Fission widths can not be approximated to either 1 or infinite degrees of freedom, and the value of ν is extracted from the fit of the general expression in Eq. (2.33) to the experimental data (for instance, in Ref. [69], a value $\nu = 2.3$ is reported for the fission widths of ^{238}U).

On the other hand, for the neutron exit channel (i.e. $c = n$ in Eq (2.32)), the energy dependency of the penetrability factors can be removed if one defines a reduced neutron width

$$\Gamma_n^0 = \frac{\Gamma_n}{\sqrt{E_n}}, \tag{2.35}$$

independent of the energy and directly proportional to the amplitude probability. The neutron scattering reaction has just one decay channel ($\nu = 1$) and the general probability of finding a certain reduced neutron width (Eq. (2.33)) simplifies to

$$\begin{aligned} p(x)dx &= \frac{1}{\sqrt{(2\pi c)}} x e^{-\frac{x}{2}} dx, \\ x &= \Gamma_n^0 / \langle \Gamma_n^0 \rangle, \end{aligned} \tag{2.36}$$

known as the Porter-Thomas (PT) distribution [69].

2.2.4.3 Neutron strength function

The last average parameter, together with the average level spacing $\langle D^J \rangle$ and the average radiative width $\langle \Gamma_\gamma \rangle$ is the so-called **neutron strength function** S_l. The neutron strength function for a given angular momentum l is defined as the ratio of the average reduced neutron width and the average level spacing

$$S_l = \frac{\langle g_J \Gamma_{\lambda n}^{0,J} \rangle}{\langle D^J \rangle}, \tag{2.37}$$

where $\Gamma_{\lambda n}^{0,J}$, g_J and $\langle D^J \rangle$ are the reduced neutron widths, spin factors and average levels spacings for all the resonances with J compatible with l. An equivalent expression is used to actually calculate S_l from the sum of the reduced neutron widths of resonances with angular momentum l in a given energy interval ΔE_n

$$S_l = \frac{1}{\Delta E_n} \sum_J \sum_\lambda g_J \Gamma_n^{0,J}, \tag{2.38}$$

where the sum runs over all the levels (resonances) λ with J compatible with l. The uncertainty in S_l, labeled as ΔS_l, is based on the variation of the sum of neutron widths distributed in accordance with the Porter-Thomas law [69] and is commonly calculated as

$$\frac{\Delta S_l}{S_l} = \sqrt{\frac{1}{N_l}(\frac{4}{\pi} + 1)}, \tag{2.39}$$

being N_l the total number of resonances considered in the sum of Eq. (2.38).

2.3 Neutron cross section in the URR

2.3.1 Theoretical description: Hauser-Feshbach formalism

As the neutron energy increases, the increasing level density combined with the increase of the intrinsic resonance widths and the enhanced resolution broadening lead to the overlap of resonances beyond a given neutron energy (see Figure 2.2). As soon as one can not identify individual resonances anymore, we enter in the Unresolved Resonance Region, where only resonance-average, seemingly smooth cross sections, can be considered. The description of the smooth cross sections in the URR is usually carried by one of the following methods:

1. **Hauser-Feshbach (HF) calculation with width fluctuations** [70, 71]: This method, based on the R-Matrix theory, describes the average cross section in the URR as the overlap of ficticious resonances generated with spacings and widths distributions fluctuating around their average values according to the statistical properties described in Section 2.2.4.
2. **Optical Model calculations** [72, 73]: Neutron total and elastic cross sections can be well fitted by the optical model with a complex potential with suitably adjusted parameters to match the experimental data. The parameters given by the optical model calculations can be connected to the average R-Matrix parameters to provide a consistent description in the overlap between the URR and the continuum [74].

In this work, the analysis of the URR was performed using the HF formalism with width fluctations, which will be briefly presented and connected to the R-Matrix theory for the analysis of resolved resonances.

The HF formalism is based on a description of the cross section averages in the URR by means of statistically generated overlapping resonances, distributed according the average resonance parameters. In order to account for the statitiscal properties of the resonance parameters, width fluctuations are added to the HF theory. The description in terms of resonances is specially relevant since it is the usual approach to generate resonances in the calculation of self-shielding factors or probability tables.

Following the most general definition of the cross section in the R-Matrix formalism, given by Eq. (2.7), the average partial cross section in the URR for a reaction from the entry channel c to the outgoing channel c' $\langle\sigma_{cc'}\rangle$ is related to the averaged collision matrix $U_{cc'}$ by

$$\langle\sigma_{cc'}\rangle = pi\bar{\lambda}_c^{-2} g_c \langle(\delta_{cc'} - U_{cc'})^2\rangle, \tag{2.40}$$

where the collission matrix elements $U_{cc'}$, containing all the information related to the R-Matrix (i. e. CN level energies and amplitude probabilities), are defined in the general formulation of the R-Matrix in Eq. (2.9) and explicitely given for the simple SLBW approximation in Eq. (2.16). The analogous expression to Eq. (2.40) for the total cross section is given by

$$\langle\sigma_c\rangle = 2pi\bar{\lambda}_c^{-2} g_c (1 - Re\langle U_{cc'}\rangle), \tag{2.41}$$

The different dependencies of the averaged collission matrix in the previous expressions are not always easy to calculate. To solve this problem, transmission coefficients T_c, calculated with optical model calculations, are introduced:

$$T_c = 1 - \langle U_{cc'} \rangle^2. \tag{2.42}$$

Tranmission coefficients are also used in the Hauser-Feshbach formalism for the description of the average cross sections. According to the HF theory, transmission coefficients are related to the average parameters $\langle D \rangle$ and $\langle \Gamma_c \rangle$ for a given channel c by

$$T_c = 2\pi \frac{\langle \Gamma_c \rangle}{\langle D \rangle}. \tag{2.43}$$

The statistical distribution of the ficticious resonances is added to the HF theory by defining a width fluctuation correction factor $W_{cc'}$, defined as

$$W_{cc'} = \left\langle \left(\frac{\Gamma_c \Gamma_{c'}}{\Gamma} \right) \right\rangle \frac{\langle \Gamma \rangle}{\langle \Gamma_c \rangle \langle \Gamma_{c'} \rangle} \tag{2.44}$$

With these two ingredients, the total cross section is described in this formalism as

$$\langle \sigma_{cc'} \rangle = \pi \bar{\lambda}_c^{\,2} g_c \frac{T_c T_c'}{\sum_c T_c} W_{cc'} \tag{2.45}$$

2.3.2 Analysis of the URR

In the Unresolved Resonance Region, resonances are overlapping and one measures average reation yields $\langle Y_r(E_n) \rangle$ or the average transmission coefficients $\langle T(E_n) \rangle$, which are related to the average partial and total cross sections via Eqs. (2.49) and (2.52), respectively.

The HF formalism with width fluctuations described in the previous section, allows describing the average partial and total cross section in the URR for each partial wave (i.e. each angular momentum) from the average level spacing (D_l), average radiation width ($\langle \Gamma_\gamma \rangle_l$) and the neutron strength function (S_l).

In this work, the description of the capture cross section of ^{242}Pu in the URR in terms of average resonance parameters has been carried out by means of HF calculations with width fluctuations using the FITACS code [75], as included in SAMMY [62]. The details on the code are described in Section 8.4.1.

2.4 Experimental determination of neutron cross sections

This section aims at providing a comprehensive overview of the different neutron beams and techniques available to measure neutron cross sections to date, with special emphasis given to radiative capture measurements.

2.4.1 Neutron beam facilities

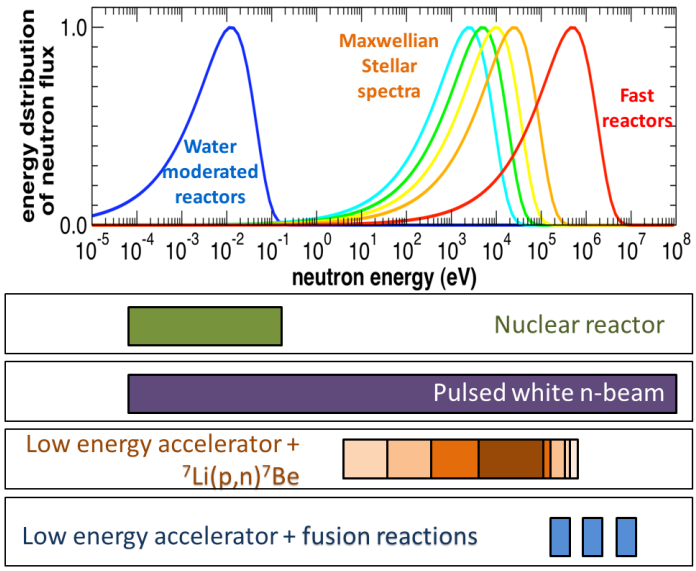

Figure 2.7: *Neutron energy spectra of relevance in different applications of neutron cross sections compared to the energy range covered by different types of neutron beam facilities. By courtesy of F. Gunsing.*

The need of different neutron beam facilities is motivated by the wide range of neutron energies of interest in different applications of neutron cross section. Typical energy distributions of neutrons in different fields of interest are shown in Figure 2.7 together with the energy ranges covered by different neutron facilities. The applications of neutron cross sections range from nuclear technologies [76, 77], either thermal power reactors, characterized by a Maxwell-Bolztmann (MB) distribution of neutrons at kT=25.3 meV, or fast reactors with a neutron sprectum in the 10 keV-10 MeV range. Moreover, nuclear astrophysics, in particular the slow neutron capture (s-) process of the stellar nucleosynthesis [78, 79], requires a good knowledge of the capture cross section of certain isotopes at neutron energies in the 5-90 keV region, typical of the neutron field of the stellar sites where the s-process occurs.

The classification of neutron facilities in this work will be carried out following the scheme of Figure 2.8, which classifies the facilities according to the neutron production method. Neutrons beams can be generated using a wide variety of systems [80].

Nuclear Research Reactors (RR) produce the highes neutron fluxes (up to 10^{14} n/cm^2/s) via neutron induced fission. External cold and thermal neutron beams are usually extracted from RRs to carry out (mainly) neutron scattering or radiography experiments with applications for industry, material science and biology. This work includes measurements carried out at the BRR, which deserves a more detailed description given in Section 3.1.

Neutron beams are also extensively produced using **low energy (<15 MV) accelerators of light charged particles**. Neutron sources are usually located in Tandem

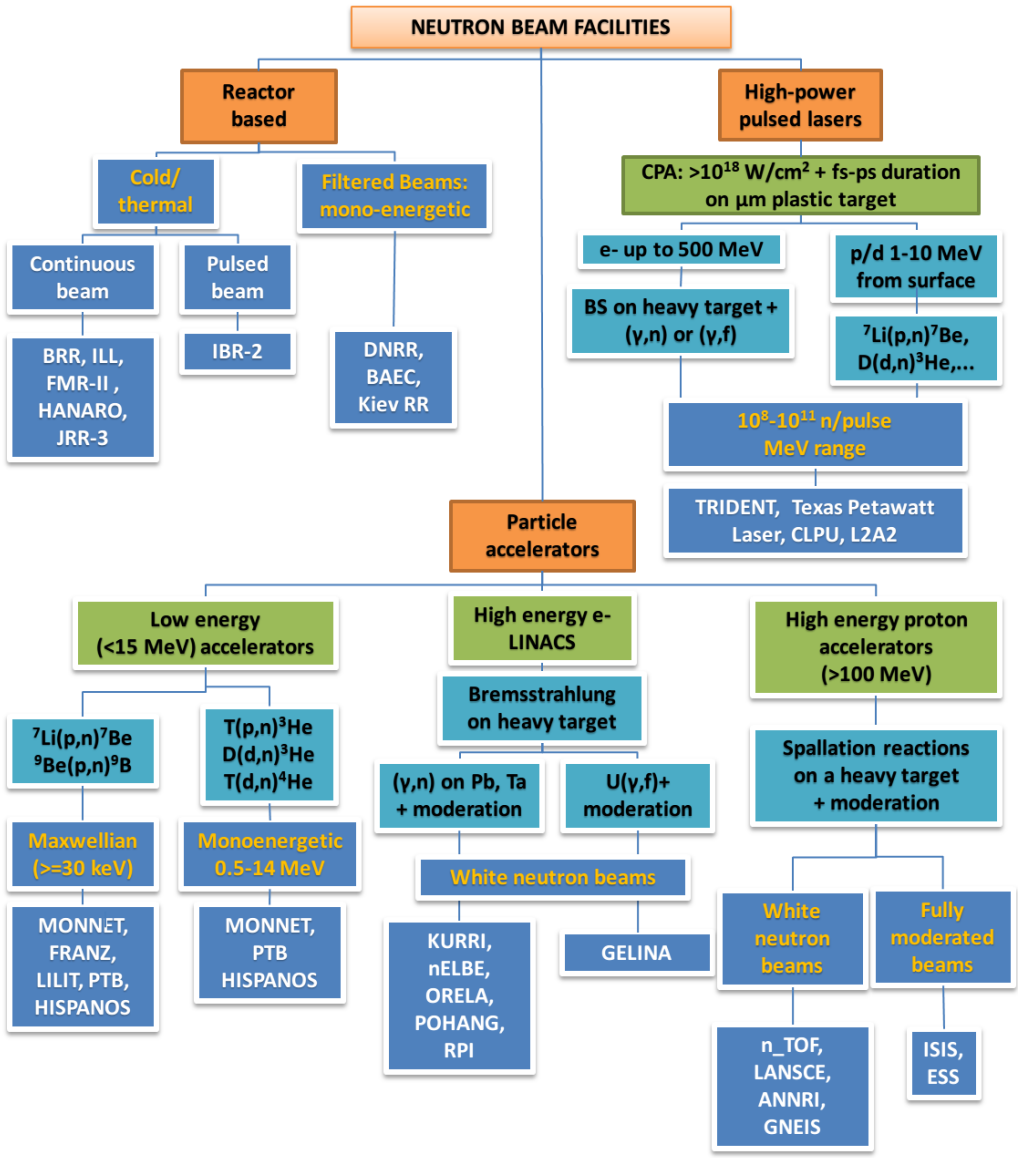

Figure 2.8: *Scheme of neutron beam facilities according to the energy distribution of the neutron beam.*

accelerators like the recient HispaNoS Facility at CNA (Seville, Spain) [86], Van-der-Graff accelerators, such as one at the JRC Monnet facility (Geel, Belgium) [87], and more reciently in high-current accelerators based on the radiofrequency quadrupole (RFQ) design such as the LiLiT facility at SARAF (Soreq, Israel) [88] or the upcoming Frankfurt Neutron Source (FRANZ) (Germany) [89]. The neutron beams produced in these facilities can be separated in two groups:

- **Mono-energetic MeV neutrons**: Mono-energetic or quasi-monoenergetic neutrons of energies ranging from 0.5 to 24 MeV (shown in Figure 2.7) are produced by means of high Q-value fusion reactions induced by proton or deuterium beams: $\mathrm{T}(p,n)^3\mathrm{He}$,

$D(d,n)^3He$, $T(d,n)^4He$.

- **Quasi-stellar neutron beams in the keV range**: Generated using proton beams impinging on ^7Li or ^9Be target at energies just above the threshold of the $^7Li(p,n)^7Be$ and $^9Be(p,n)^9B$, respectively. The angle integrated neutron energy distributions present an almost MB distribution at energies around 30 keV, which resembles the neutron spectrum at the s-process stellar sites (see Figure 2.7). These facilities allow a determining the so-called Maxwellian Averaged Cross sections (MACS) [90], defined in Eq. (2.53).

Pulsed **electron Linear accelerators (LINACS)** can be used to generate pulsed neutron beams by impinging an electron beam on a heavy target. Two different neutron-producing mechanisms are used in these facilities:

- The bremsstrahlung produced by slowing-down electrons induces (γ,n) reactions on non-fissile heavy metals (e.g. lead or tantalum).
- The bremstrahlung γ-rays can induced photo-fission in fissile targets, such as uranium.

The produced neutrons, emitted in 4π with a wide energy distribution can be partially moderated (i.e. slowed-down) by using a thin water layer as moderator. The energy spectrum of the resulting white neutron beam is measured by means the time-of-flight technique (see Section 2.4.2.1). Some examples of neutron facilities based in e^--LINACS are GELINA [91] at JRC (Geel, Belgium) and ORELA at the Oak Rigde National Laboratory (USA) [92].

High proton spallation sources are the second big group of facilities generating white neutron beams. In this case, neutron bunches are generated by spallation reactions induced by a high energy (100 MeV - 20 GeV) pulsed proton beam in a heavy target (Pb, Ta, W). The high energy neutron spectrum produced in spallation reactions (MeV-GeV) is partially moderated with hydrogen-based moderators. These facilities provide also a white neutron spectrum, where point-wise cross sections are measured by means of the time-of-flight technique (see Section 2.4.2.1). Among the neutron spallation sources devoted to nuclear data measurements (see Figure 2.8), we find n_TOF at CERN [93], which reciently opened a new experimental area (EAR2) [94]; DANCE [95] at Los Alamos National Laboratory (LANL) (USA) and ANNRI [96] at JPARC (Japan). Other spallation neutron facilities, such as the upcoming *European Spallation Source* (ESS) [97] (Lund, Sweden), use a fully moderated neutron beam for neutron science applications rather than nuclear data measurements.

Figure 2.9 compares the average flux per pulse (top) and per second (middle), and the instantaneous flux (bottom), of different facilities based in spallation sources and electron LINACS. In this figure one appreciaties that spallation sources with short flight paths (n_TOF-EAR2, ANNRI and DANCE) reach the highest fluxes per pulse. However, if one takes into account the high repetition rate of the pulses GELINA, this facility equals n_TOF-EAR1 in terms of average flux per unit time. Last, concerning instantaneous flux, what actually maximizes the neutron to background ratio, the new n_TOF-EAR2 facility features the highest instantaneous white neutron flux worldwide [98].

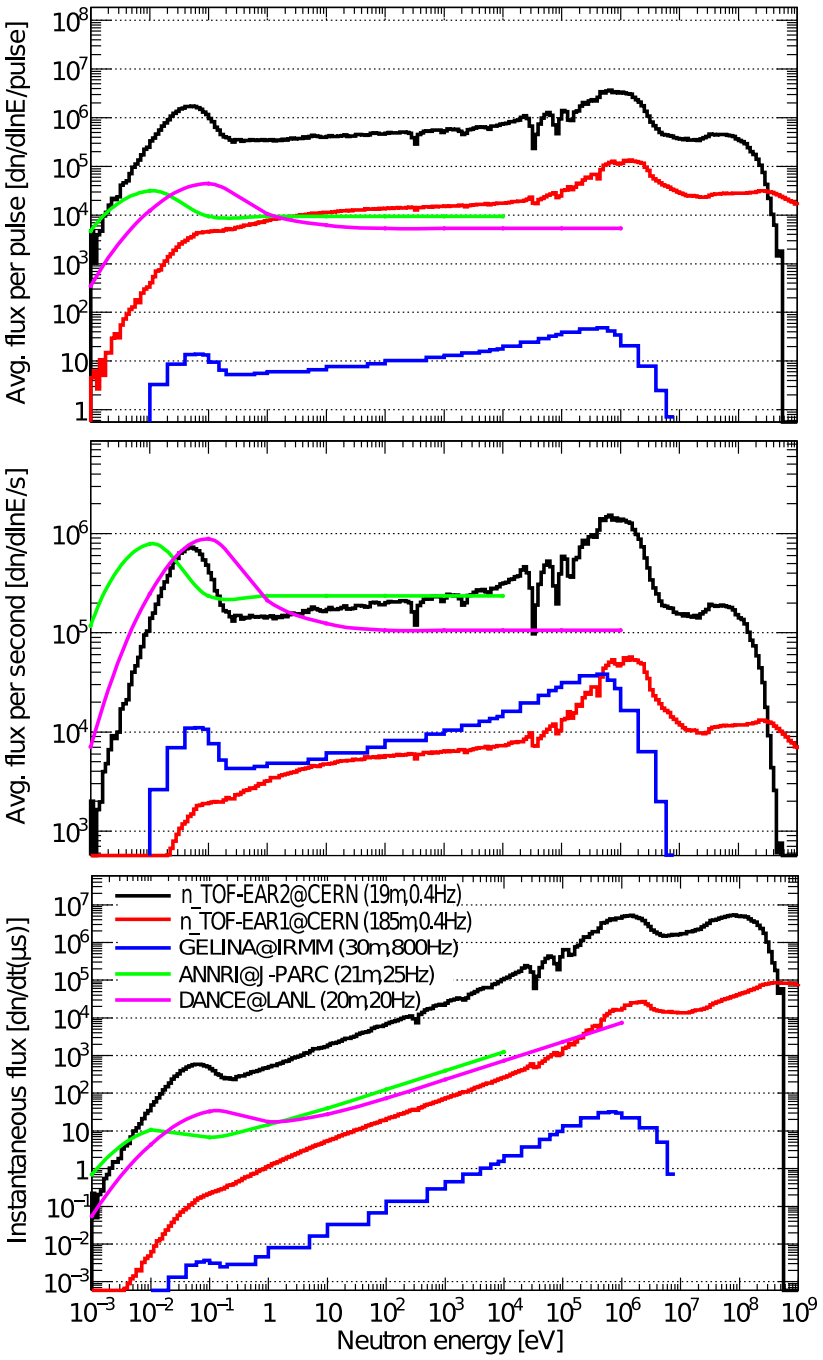

Figure 2.9: *The neutron flux at n_TOF-EAR2 compared to n_TOF-EAR1, GELINA, DANCE and ANNRI (flightpaths in the legend). The neutron flux is expressed in the form of average neutron flux per pulse (top), average neutron flux per second (middle) and instantaneous neutron flux per pulse (bottom) (see Ref. [98]).*

Last, it is worth mentioning the possibilities of using **high power lasers**. Neutron production has been based so far in particle accelerators. However, the use of high power (TW or even PW) fast-pulsed (ps or even fs) lasers based on the *Chirped Pulse Amplification* (CPA) for the production of neutrons has been already proofed and could become a

promising and compact option for future facilities and neutron applications. A complete review of the status of laser-driven neutron sources is given in Ref. [99]. This emerging technique shows promising results in terms of neutron flux per pulse. Calculations considering the features of upcoming high-power laser facilities, such as the European Extreme Light Infrastructure (ELI) [100], indicate that laser-driven neutron sources could provide higher energy fluxes in the fast energy region than currently existing facilities [101].

2.4.2 Experimental techniques for neutron cross section measurements

Different neutron techniques are available for the experimental determination of neutron cross sections. Figure 2.10 shows a classification of the different methods attending to the properties of the beam. According to the description in the previous section, neutron beams can be mono-energetic, from which the cross section value is extracted at the given neutron energy; quasi mono-energetic (QMN) or white neutron beams, which allow peforming both integral measurements or point-wise cross section measurements. Last, beams of other particles can be used for the indirect determination of the neutron cross section through surrogate reactions.

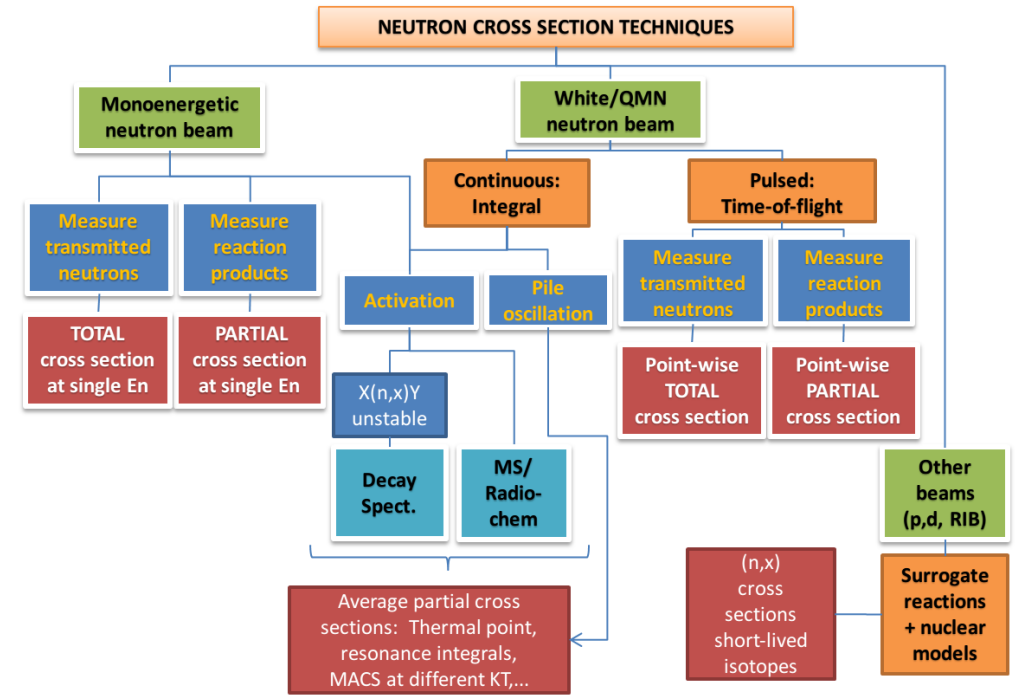

Figure 2.10: *Scheme of neutron beam facilities according to the energy distribution of the neutron beam.*

2.4.2.1 Point-wise cross sections

Neutron cross sections for a given energy can be extracted either using monoenergetic neutron beams or white neutron-beams combined with the neutron Time-of-Flight (TOF) method. This technique is used to assess the energy of the neutrons transmitted or inducing (n, x) reactions in a sample and is based on installing the measuring station at a distance L from the neutron source so that, from the measured neutron time-of-flight t (i.e. time it takes the neutron to fly over the distance L), the neutron energy is determined with the non-relativistic expression

$$E_n = \frac{1}{2} m_n \frac{L^2}{t^2}, \tag{2.46}$$

where m_n is the mass of the neutron. A more detailed description of this technique is provided for the case of the n_TOF facility in Section 5.1.3. This technique enables the measurement of total and partial point-wise cross sections in a wide energy range.

From the mesurement of partial reaction cross-sections, one experimentally determines the **reaction yield** $Y_r(E_n)$, defined as the probability of an incident neutron for undergoing a reaction or equivalently as the fraction of the neutrons of a given energy which induce a reaction while travelling through the sample. In general, reaction yields are calculated as

$$Y_r(E_n) = \frac{C_r(E_n)}{N(E_n)\varepsilon(E_n)}, \tag{2.47}$$

where $C_r(E_n)$ are the counts in the detector related to the reaction under study, $\varepsilon(E_n)$ is the detection efficiency for the reaction products and $N(E_n)$ is the total number of neutrons of a given energy impinging the sample. The reaction yield $Y_r(E_n)$ is related to the reaction $\sigma_r(E_n)$ and total cross sections $\sigma_{tot}(E_n)$ by

$$Y_r(E_n) = F_{ms}(E_n)(1 - e^{-n\sigma_{tot}(E_n)})\frac{\sigma_r(E_n)}{\sigma_{tot}(E_n)}, \tag{2.48}$$

where n is the areal density (at/b) of the sample and $F_{ms}(E_n)$ is the so-called multiple scattering correction, which accounts for the contribution to the yield of neutrons suffering one or more scatterings in the sample (see Section 7.1.1). In the URR, resonances are overlapping and one does not measure the yield for a given energy but an average value $\langle Y_r(E_n)\rangle$, which can be related to the average reaction cross section $\langle \sigma_r(E_n)\rangle$ by

$$\langle Y_r(E_n)\rangle = F_r(E_n) \cdot n \cdot \langle \sigma_r(E_n)\rangle, \tag{2.49}$$

where $F_r(E_n)$, is the correction that accounts for self shielding and multiple scattering effects, explained in Section 7.1.1.

Total cross section measurements are based in measuring the dimensionless **transmission coefficients** $T(E_n)$, defined as the fraction of neutrons of each energy travelling through the sample. Experimentally, $T(E_n)$ is calculated as the ratio of the number of neutrons counted in a detector placed behind the sample C_i with respect to the counts with the sample out of the beam C_o:

$$T(E_n) = \frac{N_o(E_n)}{N_i(E_n)}\frac{C_i(E_n)}{C_o(E_n)}, \tag{2.50}$$

where $N_{i/o}$ are the number of neutrons allocated to the measurements with the sample in and out of the beam. This method is independent of the neutron detection efficiency and the absolute number of neutrons (only the ratio N_o/N_i must be known). The relation of the transmission coefficients $T(E_n)$ with the total cross section $\sigma_{tot}(E_n)$ is given by

$$T(E_n) = e^{-n\sigma_{tot}(E_n)}. \tag{2.51}$$

In the same way than the reaction yields, in the URR only average transmission coefficients $\langle T(E_n)\rangle$ can be measured, which present the following relation to the average total cross section

$$\langle T(E_n)\rangle = e^{-n\langle\sigma_{tot}(E_n)\rangle}\langle e^{-n(\sigma_{tot}(E_n)-\langle\sigma_{tot}(E_n)\rangle)}\rangle = F_T(E_n)e^{-n\langle\sigma_{tot}(E_n)\rangle}, \tag{2.52}$$

$F_T(E_n)$ being the correction for multiple scattering and self-shielding, equivalent to $F_r(E_n)$ in Eq. (2.49).

2.4.2.2 Integral cross sections

Among the methods summarized in Figure 2.10, one also finds techniques that allow to extract energy averaged cross sections. This methods are typical of QMN beams. The main integral quantities of interest for applications in nuclear technology or astrophysics [102] are presented in this section.

A quantity of high importance, in particular in the field of nuclear astrophysics, is the **Maxwellian Averaged Cross Section (MACS)** $\langle\sigma\rangle_{kT}$ at a given temperature $kT = E_n$, defined as

$$\langle\sigma\rangle_{kT} = \frac{\sigma v}{\langle v\rangle_{kT}} = \frac{2}{\sqrt{\pi}(kT)^2}\int_0^\infty \sigma(E_n)E_n e^{-\frac{E_n}{kT}}dE_n, \tag{2.53}$$

where where v is the relative velocity of neutrons and a target nuclide, and $\langle v\rangle_{kT}$ is the mean thermal velocity given by $\langle v\rangle_{kT} = \sqrt{2kT/\mu}$, being μ the reduced neutron mass of the neutron-target system. This quantity is almost directly extracted from the measurements carried out in quasi-stellar beams and is key for the calculation of stellar neutron capture rates, a basic magnitude in the s-process nucleosynthesis models [79]. The reference value of the MACS for stellar calculations is given at kT=30 keV and a complete set of MACS can be found in Ref. [90].

A second relevant magnitude that is extracted from integral measurements is the **thermal cross section** σ_{th}, defined as the cross section at E_n=25.3 meV, corresponding to a temperature of 297 K or a neutron velocity of 2200 m/s. Measurements of σ_{th} are carried out in thermal reactors which feature a MB energy distribution $\phi_{th}(E_n)$ centered at E_n=25.3 meV. The direct measurement provides thus the MACS $\langle\sigma\rangle_{th} \equiv \langle\sigma\rangle_{25.3\ meV}$, which is related to thermal cross section by

$$\langle\sigma\rangle_{th} = \frac{\int \sigma(E_n)\phi_{th}(E_n)dE_n}{\int \sigma(E_n)(E_n)dE_n} = g_w\sigma_{th}, \tag{2.54}$$

where g_w is known as the Westcott g-factor and is close to unity for nuclei whose thermal cross section is $\sim 1/v$

2.4.2.3 Surrogate reactions

Another possibility to obtain neutron cross sections is to replace the original reaction ${}^{A}X + n \rightarrow {}^{(A+1)}X^*$ by the so-called surrogate reaction ${}^{A}Y + a \rightarrow {}^{(A+1)}X^* + b$ [103]. In this method, the decay of the ${}^{(A+1)}X^*$ CN state is measured and the second reaction product b is used to determine the excitation energy of the decaying CN, which can be related to the equivalent incident neutron energy in the original reaction. This approach to determine neutron cross sections is used for the case of highly radioactive or scarce isotopes, for which it is sometimes the only feasible method. Its main drawback is that the probability of formation of the CN through the original and surrogate reactions are different and the latter must be obtained from nuclear model predictions.

2.5 Neutron capture cross section measurements

Different techniques for radiative neutron capture measurements are currently available. In general, they can be grouped as follows (see Figure 2.11):

- The capture cross section can be determined from the **number of ${}^{(A+1)}X$ nuclei** produced after a neutron capture on a certain ${}^{A}X$ isotope.
- The measurement of the **prompt γ-rays** emited during the decay of the Compound Nucleus state (see Figure 2.3) allows extracting the cross sections.
- **Pile oscillation** method [104] are based on studing the changes in reactivity associated to the neutron captures on a sample oscillating inside a RR.

2.5.1 Measurements of the product nuclei

From the number of ${}^{(A+1)}X$ nuclei $N_{(A+1)}$ produced via (n,γ) reactions in a given sample one can extract the capture cross section σ_γ as

$$\sigma_\gamma = \frac{N_{(A+1)}}{n_A \ \phi \ t_{irrad} \ S}, \tag{2.55}$$

where n_A is the areal density of the target (at/b), ϕ is the neutron flux (n/cm^2/s), t_{irrad} is the neutron irradiation time and S is the irradiated surface (cm^2). In this expression σ_γ can represent either $\sigma_\gamma(E_n)$ in the case of mono-energetic neutron beams or $\langle\sigma_\gamma\rangle$ if the sample is irradiated in a QM or white neutron beam. The number of product nuclei of the neutron capture can be determined through different methods.

The **activation analysis** method [105] is based on counting the number of ${}^{(A+1)}X$ nuclei present in an irradiated sample from the measurement of characteristic lines (usually γ-rays or α-particles) of the decay. Therefore, this method only applies for the case where the product nucleus is unstable. This technique has been used in this work to determine the thermal capture cross section of ^{242}Pu at the BRR.

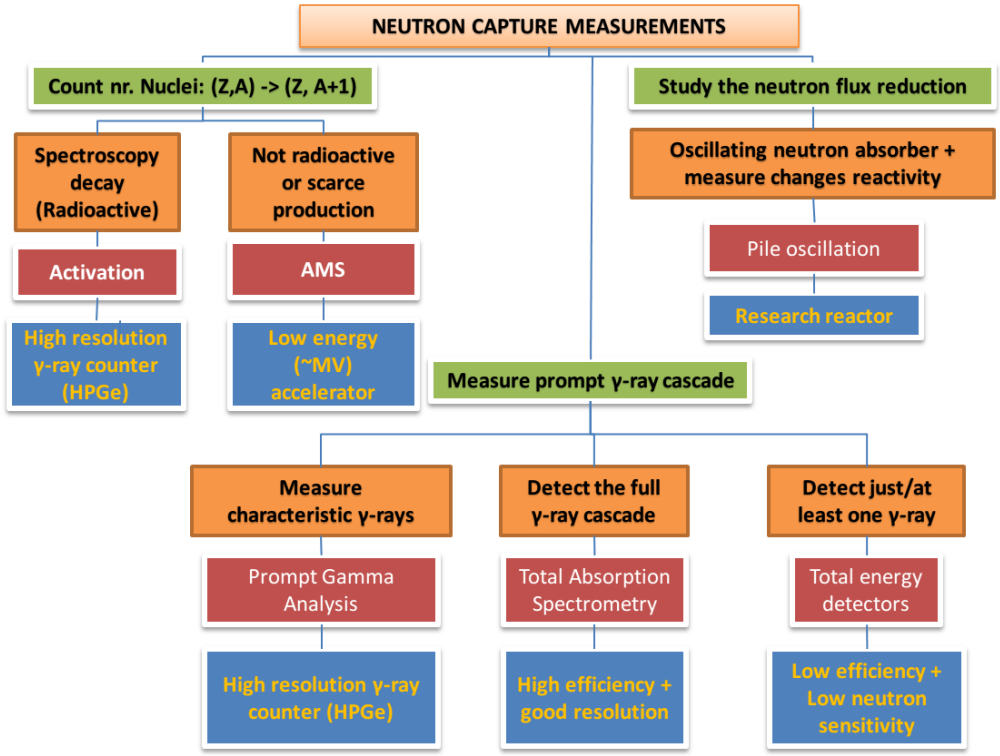

Figure 2.11: *Scheme of the existing techniques for (n,γ) measurements.*

If the $^{(A+1)}X$ isotope is stable, the activation method is not applicable and one can think of **radiochemical methods** or the more sensitive **mass spectroscopy** techniques (AMS or ICP-MS). Indeed, the high sensitivity of these techniques (10^{-15} for AMS and 10^{-6} for ICP-MS) opens the door to measurements of very small numbers of produced nuclei, such as in the case of double capture experiments [101].

2.5.2 Prompt γ-ray measurements

Radiative capture cross sections can be determined from the measurement of the multiple γ-rays, the so-called capture cascades, emitted during the de-excitation of the CN. The three techniques presented in Figure 2.11 are the most extensively used:

1. **Prompt Gamma Activation Analysis (PGAA)**: This technique is based on the detection of a single characteristic prompt γ-rays of the capture cascade with well known emission probability (i.e. fraction of the cascades that go through that transition). This experimental method requires high-resolution HPGe detectors and is commonly used for non-destructive analytical technique [108] but can also be used to determine thermal neutron capture cross sections. Indeed, this technique has been applied in this work to extract σ_{th}(n,γ) of ^{242}Pu from a measurement in the PGAA facility at the BRR. The key points of on this technique are described in Section 3.2.1.

2. **Total Energy Detection (TED)**: This method is based on having a detection

system that registers a capture event with an efficiency that is directly proportional to the total energy of the cascade (E_c in Figure 2.3). This condition is a priori not easy to achieve since the de-excitation of the Compound Nucleus can follow many different paths. Moxon-Rae detectors [109], introduced in the 1960's, were the first total energy detectors but were soon replaced by organic scintillators [110], such as C_6F_6 first and later C_6D_6. The latter are very well suited for neutron capture measurements due to their fast time response with low neutron sensitivity but require a mathematical manipulation of the response, the so-called *Pulse Height Weighting Technique* (PHWT) [110], to fulfill the required proportionality between detection efficiency. In this work, the point-wise ^{242}Pu(n,γ) cross section was determined at the n_TOF-EAR1 facility using a set of four C_6D_6 Total Energy Detectors.

3. **Total Absorption (TA) technique**: This method is based on the detection of the full γ-ray cascade following the neutron capture. Suitable detectors for this technique should have large solid angle coverage, high photopeak efficiency, good resolution, high segmentation, fast response and low neutron sensitivity. The high photopeak efficiency and segmentation enable powerful background rejection methods based on the capture and background characteristic total deposited energy and the multiplicity. Different Total Absorption detection systems are currently found in time-of-flight facilites such as the n_TOF TAC (40 BaF_2) [111] or DANCE (160 BaF_2) crystals [112] at LANL. More details on this technique, focusing on the neutron capture measurements with the n_TOF TAC, are given in Section 5.3.2.

2.5.3 Complementary beams and techniques to measure the ^{242}Pu(n,γ) cross section

The new measurement of the ^{242}Pu radiative capture cross section presented in this thesis combines different neutron beam facilities, experimental techniques and theoretical frameworks to provide a comprehensive understanding of this cross section. Figure 2.12 summarizes the different energy regions studied in this work and indicates the neutron beam, experimental technique, extracted type of data and theoretical formalism used for the analysis of each energy region.

1. **Thermal cross section**: The thermal capture cross section of ^{242}Pu was measured by means of **Activation Analysis** and **PGAA** in the **cold neutron beam** of the Budapest Resarch Reactor (BRR), providing the **cross section value at 25.3 meV**. The details on the facility, experimental technique and detection set-ups are described in Chapter 3, while Chapter 4 focuses on the analysis and results of this measurement.

2. **Resolved Resonance Region (RRR)**: The radiative capture cross section has been measured using **Total Energy Detectors** at the n_TOF-EAR1 facility. The combination a **white neutron beam** with the **time-of-flight technique**, has allowed us to extract the **point-wise** capture yield up to 4 keV. The cross section has been described in terms of individual resonance parameters extracted with an **R-Matrix** code. An introduction to the n_TOF Facility, focusing on the beam properties of

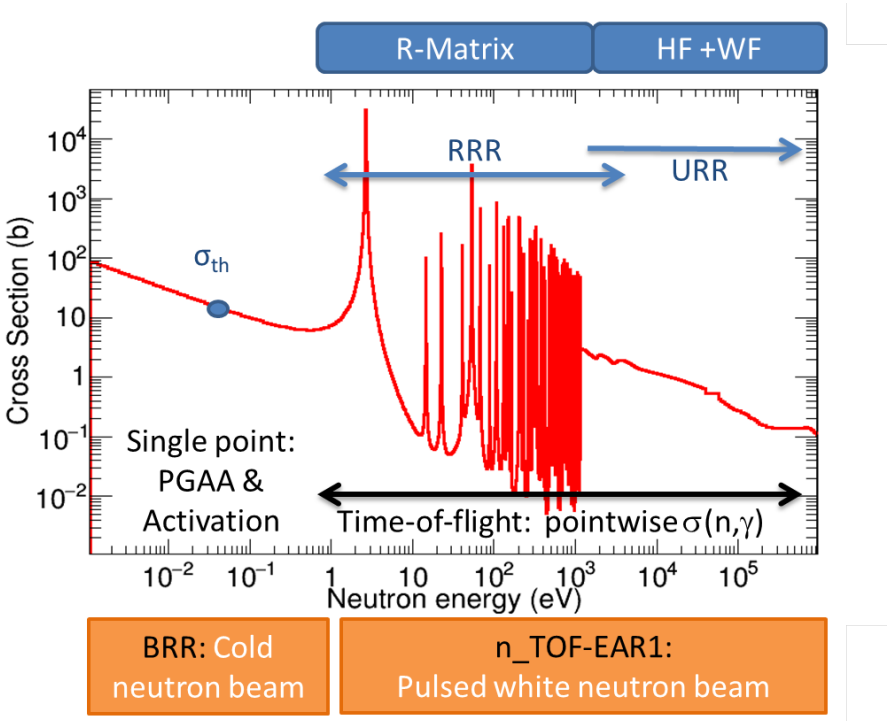

Figure 2.12: *Neutron capture cross section of* ^{242}*Pu showing the different facilities, experimental techniques and theoretical formalisms used in this work to determine this cross section in its different energy regions: Thermal point, RRR and URR.*

its first experimental area (EAR1) and the description of the experimental set-up is provided in Chapter 5. The details on the data reduction towards a capture yield are presented in Chapter 6, and Chapter 7 deals with the R-Matrix analysis of the cross section in the RRR and the results.

3. **Unresolved Resonance Region (URR)**: From the same measurement at n_TOF, the **averaged cross section** has been extracted between 1 and 500 keV and described according to the **Hauser-Feshbach theory with width fluctuations**. The results ^{242}Pu cross section in the URR are presented in Chapter 8.

Part II

Experiment at BRR (25 meV) and results

Chapter 3

Activation and PGAA mesurements at BRR

3.1 Budapest Research Reactor at the BNC

3.1.1 Research Reactor

The Budapest Research Reactor (BRR) is a VVR-type tank reactor, moderated and cooled by light water with a thermal power of 10 MW. The original Soviet designed and built reactor, with a power of 2 MW, went first critial on March 25, 1959. The thermal power was upgraded to 5 MW in 1967 and a major refurbishment was carried out from 1986 to 1990 supported by the International Atomic Energy Agency (IAEA) and the European Union. Following the commitment to join the Russian Research Reactor Fuel Return (RRRFR) programme, the BRR changed the core between 2007 and 2012. This conversion aimed at reducing the previous High Enriched Uranium (HEU) fuel (VVR-SM fuel with 36% enriched uranium) to a Low Enriched Uranium (LEU) fuel (VVR-M2 type with 20% enriched uranium). The main technical details of the current reactor are summarized in Table 3.1.

The reactor has been operated by the Centre for Energy Research (CER), one of the research centres of the Hungarian Academy of Sciences. In 1992, a consortium, named Budapest Neutron Centre (BNC), was formed as an association of the neutron-research based laboratories on the KFKI campus site. The general view of the Reactor Hall is shown in Figure 3.1.

The reactor cycle is about 10 effective days, which are followed by a two-day-long break. The BRR is known for its reliable operation, operating for more about 160 days per year. In the 50 years of operation of the BRR, this facility has become one of the leading research infrastructures in Hungary and in Central-Europe. The main Neutron Science activities at BRR are summarized in Section 3.1.2.

Table 3.1: *Main technical details of the Budapest Research Reactor.*

Thermal power	10 MW
Power density	39.7 kW/l
Neutron flux (max)	2.5 10^{14} n cm^{-2} s^{-1}
Temp. water cooling (max)	60°
Fuel assembly	VVR-M2
Fuel material	UO_2-Al
^{235}U enrichment	19.7%
Core height	600 mmr
Coolant	Demineralized water
Reflector	Beryllium
Control rods	B_4C

3.1.2 Beamlines and neutron science applications

The experimental facilities at the Budapest Research Reactor allow to perform a great variety of research activities with twelve experimental stations covering topics at the forefront of Nuclear Physics, Chemistry, Materials Science, Earth Science, Engineering, Biology and Archaeology.

The experimental facilities are located around the reactor vessel in the Reactor Hall or behind a shielding wall, in the Measuring Hall of the Center for Neutron Science (CNS). A sketch of the facility is shown in Figure 3.2. The main instruments in the BRR, dedicated to different applications of neutron science are:

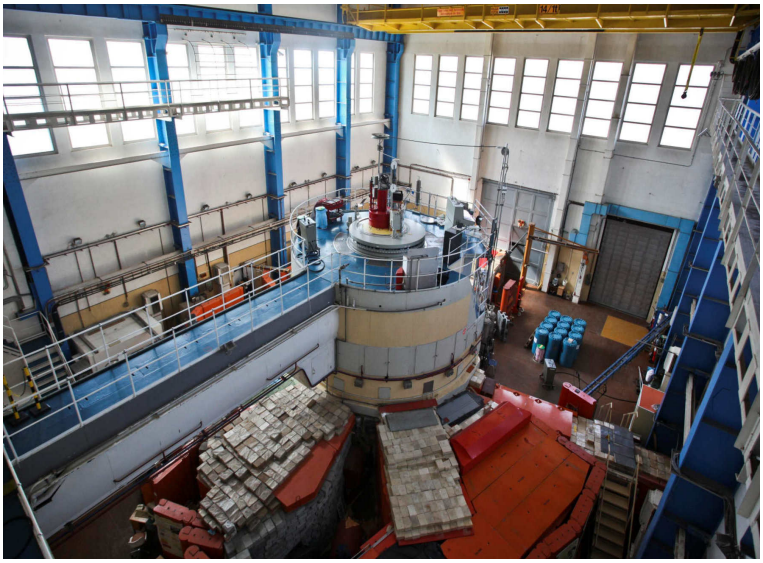

Figure 3.1: *General view of the 10 MW Budapest Research Reactor Hall. The experimental beamlines exit the reactor on the left side and go across a thick shielding wall that separates the reactor hall and CNS Measuring Hall, where the PGAA and NIPS facilities are found.*

- **BIO**: This facility is placed in the Reactor Hall at 3.1 meters from the detector core is dedicated to study the effects of the neutron and gamma radiation and high dose rate on the living animals, cells, etc..
- **MTEST**: The Material Test Diffractometer is a general-purpose powder diffractometer using neutron wave lengths around 0.130-0.145 nm and a neutron flux of 10^6 n cm^{-2} s^{-1}.
- **TAS and TASC**: These instruments are Three-Axis Neutron Spectrometers dedicated suited for the study of phonon and magnon dispersion curves in single crystals, phonon density of states for that large class of materials which contain hydrogen.
- **PSD**: The Position Sensitive Detector system on a neutron diffractometer is suitable for atomic structure investigations of amorphous materials, liquids and crystalline materials at different temperatures from 300 to 1200 K.
- **SNR and DNR**: The Static and Dynamic thermal-neutron radiography stations are two facilities placed at different positions along the neutron beam path. They make use of the transmission of neutrons through a given sample to obtain information of its composition and the processes ocurring inside it. Filters containing ^{10}B allow to change significantly the fast/thermal neutron flux ratio.
- **SANS**: The Small Angle Neutron Scattering Instrument is placed in neutron guide Nr. 2 of the CNS Measuring Hall and is suited for diffractometry studies able to probe crystal structures at the scale of 5 to 1500 $\mathring{A}$.
- **IBMS**: The In-Beam Mössbauer Spectrometer, uses a guided cold neutron beam of 10^9 n cm^{-2} s^{-1} to induce Mössbauer transitions. The applications of this technique range from the study of biological systems, geological samples and magnetic layers, to studies of chemical changes induced by radiation damage.

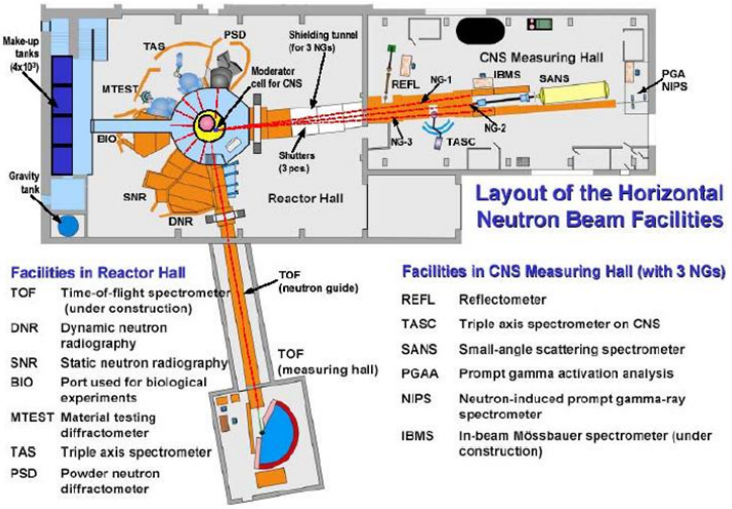

Figure 3.2: *Sketch of the BRR and all the Neutron Science instruments located in the Reactor Hall and the neighbouring BCN Measuring Hall.*

- **NIPS**: The NIPS is located at the end of the neutron guide Nr. 1 and is designed for a wide variety of experiments involving neutron-induced γ-ray emission.
- **PGAA**: The PGAA facility shares the neutron guide with the NIPS facility and is devoted to non-destructive elemental analysis of samples by detecting the characteristic prompt γ-rays following the neutron captures. More details on the PGAA facility are given in Section 3.2.

3.2 PGAA facility at the BRR

3.2.1 PGAA technique and capture cross section measurements

Prompt gamma activation analysis (PGAA) is a nuclear analytical method which makes use of the prompt gamma radiation released in the radiative neutron capture reaction to identify and quantify the elemental or isotopic content of samples. It is based on the fact that the γ-ray cascade emitted after a neutron capture on a given nuclei presents a characteristic energy distribution.

Due to the large penetrability of neutrons and γ-rays, this technique provides bulk analysis results for the major components of the irradiated volume of a given sample. For specific isotopes with very large thermal cross sections it can be used to identify them at trace levels (ppm). The sample can be in solid, powder, liquid or gaseous form and is placed with a minor or no sample preparation into the target chamber, where it is irradiated with the cold neutron beam (see Section 3.2.2).

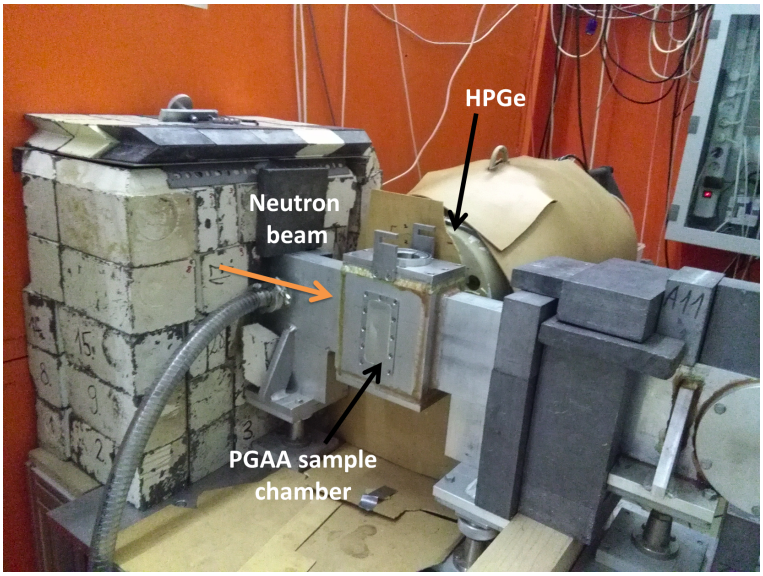

Figure 3.3: *Sketch of the BRR and all the Neutron Science instruments located in the Reactor Hall and the neighbouring BCN Measuring Hall. PGAA facility in one of the beamlines of the Budapest Research Reactor.*

The PGAA technique requires high intensity beams, being intense spallation sources or research reactors the best suited neutron facilities. At the Budapest Research Reactor, the PGAA facility is placed at the end of the neutron guide Nr. 1 that is connected to a liquid-helium-cooled neutron source in the reactor. The general view of the PGAA facility is shown in Figure 3.3. This cold neutron guide presents two spatially separated (upper and lower) beams and is shared with the NIPS facility. The PGAA irradiation chamber is installed close to the end of the neutron guide along the upper beam while the NIPS facility uses the lower beam and is placed 1 m dowstream from the former. A complete and updated review of the PGAA facility at the BRR can be found in Ref. [108].

In the analysis of the PGAA measurements, the area of a peak A_i in the prompt γ-ray spectrum emitted by a sample as a consequence of the neutron captures on it, is expressed in the following form

$$A_i = m\ t\ \frac{N_A}{M}\ \sigma_i\ \phi\ \varepsilon(E_\gamma), \tag{3.1}$$

where m the mass of the element Only for where the neutron capture was produced, t is the irradiation time, N_A the Avogadro number, M tge molar mass, ϕ the neutron flux, E_γ is the γ-ray energy, $\varepsilon(E_\gamma)$ the detection efficiency for that energy and σ_i the elemental partial γ-ray production cross section. The latter is related to the capture cross section of the isotope that emitted the γ-ray σ_γ by

$$\sigma_i = C_{isot}\ P_\gamma\ \sigma_\gamma, \tag{3.2}$$

being C_{isot} and P_γ, respectively, the isotopical concentration and the fraction of capture cascades where that γ-ray is emmitted. The values of σ_i are experimentally determined in the same facility and published in Refs. [113, 114].

Besides its main use for elemental analysis, the neutron irradiation chamber and the detection system in the PGAA facility can be also used to extract any of the quantities in Eqs. (3.1) and (3.2), and in particular to carry out thermal capture cross section measurements, as it was introduced in Section 2.5.2. Several neutron capture measurements had been carried out in the PGAA facility at the BRR (see for intance Refs. [115, 116, 117, 118, 36]). In this work, the thermal capture cross section point of ^{242}Pu was determined by irradiating the sample in the PGAA facility and analyzing the prompt *gamma*-rays and the decay γ-rays of the produced ^{243}Pu nuclei.

3.2.2 Neutron beam properties in the PGAA facility

The first PGAA facility at the Budapest Research Reactor featured a thermal neutron beam and was operating from 1996 to 2000 [119]. To increase the thermal equivalent neutron flux, which was rather low ($2{\cdot}10^6$ n cm^{-2} s^{-1}), a cold neutron source containing liquid hydrogen was installed in the reactor in 2001 and the neutron guide was also rebuilt. After these improvements, the thermal equivalent neutron flux increased up to $3{\cdot}10^7$ n cm^{-2} s^{-1} [120]. In 2003 a beam-chopper was added to the PGAA setup for studies on short-lived radionuclides produced during the irradiation. The last significant upgrade started in 2007, when the last

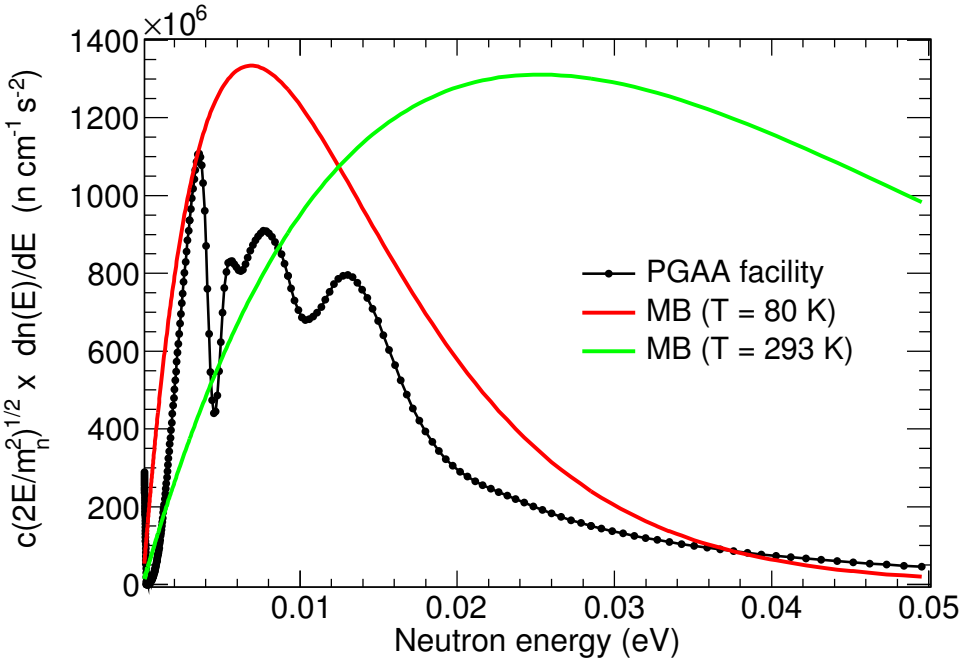

Figure 3.4: *Energy distribution of the cold neutron beam of the PGAA beamline at the Budapest Research reactor compared to two Maxwell Boltzmann distributions centered at T = 80 keV and T =293 keV.*

section of the neutron guide Nr. 1 was changed to $2\theta_c$ supermirror elements, increasing the thermal equivalent neutron flux to the current $1.2{\cdot}10^8$ n cm^{-2} s^{-1} at the PGAA irradiation chamber [121].

The energy distribution of the neutron flux at the PGAA chamber was measured with help of the chooper and the time-of-flight technique using an ^{3}He-filled Multiwire Proportional Chamber (MWPC). All the details on this measurement are found in Ref. [122]. The experimental energy distribution of the neutrons is shown in Figure 3.4 together with a Maxwell-Boltzmann distribution at T = 293 K (κT = 25.3 meV) and T = 80 K (κT = 6.9 meV) to illustrate the sub-thermal average energy. The cold neutron beam has an average neutron energy of 12 meV (140 K) and can be parametrized as a combination of three Maxwell-Boltzmann distributions at T_1 = 20 K (the temperature of the liquid hydrogen), T_2 = 80 K (due to incomplete moderation in the 5-cm-thick liquid volume) and T_3 = 320 K (the temperature of the reactor pool). Last, the neutron energy distribution presents some some dips related to monochromator crystals from other instruments located upstream in the same line (see Figure 3.4).

From the original size of the neutron guide of 100x25 mm^2, the beam is divided into two 20x20 mm^2 beams that irradiate the PGAA and NIPS chambers. These beam lines can be closed independently using two PC-controlled shutters coated with two neutron absorber layers (B_4C-loaded rubber plus a Cd sheet). The final beam size at the sample position is first adjusted with a remotely controlled far collimator that can reduce the beam size down to 10x10 mm. A set of manually placed ^{6}Li collimators and a borated paraffin block placed

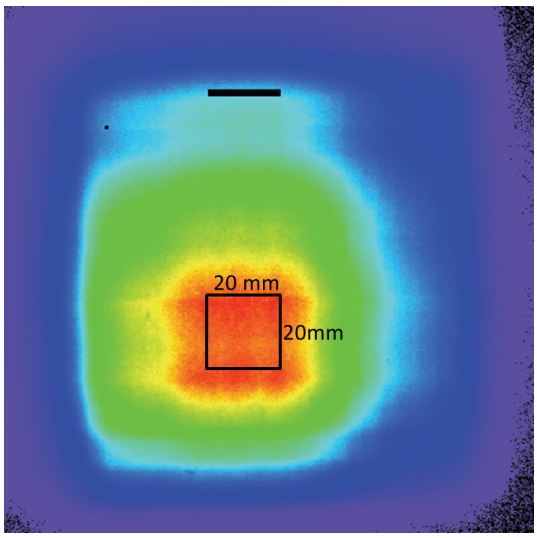

Figure 3.5: *Sketch of the BRR and all the Neutron Science instruments located in the Reactor Hall and the neighbouring BCN Measuring Hall.Spatial distribution of the neutron beam intensity without any collimators. The red colour (center) indicates the highest value. A size of 2 cm is shown by a horizontal black line as a reference. Extracted from Ref. [108].*

downstream in the neutron beamline filter the divergent or scattered neutrons before they reach the sample chamber. The final irradiated surface in the PGAA chamber ranges from 5 to 400 mm^2. Figure 3.5 shows the 2D profile of the beam measured by means of neutron radiography within the EU FP6 ANCIENT CHARM project, showing a nice homogeinity in the center where the samples are located.

3.3 Samples and irradiations at the BRR

3.3.1 ^{242}Pu fission-like targets

The two experiments described in this thesis have been succesfully carried out thanks to the high quality ^{242}Pu targets prepared within the EC CHANDA project [123] by the JGU University of Mainz and the HZDR research center in Germany. This collaborative work aimed at producing high quality targets that should match the following general conditions:

- **Target mass**: the higher the mass the better overall statistics and a higher capture-to-background ratio, excluding the background from the target activity (not especially harmful for the case of ^{242}Pu).
- **Target purity**: this is always desirable to avoid contributions from impurities in our measurements.
- **Target-to-backing mass ratio**: in general, the higher this ratio the better, but the choice of backing material plays an important role, hence the next parameter.

- **Capture in backing to target mass ratio**: reducing the captures requires not only thin backings but also as transparent as possible to neutrons. on the capture cross section of the backing material.
- **Target homogeinity**: the highest possible homogeinity of the deposit thickness is always desired.

Once this conditions are optimized one must think about the dimensions of the target. The design of the targets in this work is specially suited for the measurement at n_TOF (see Section 5.4.1). At the PGAA facility, the dimension of the beam can be adjusted and therefore the dimensions of the sample are not so critical. However, the use of thin ^{242}Pu deposits ($\lesssim$1 μm) and Al backings (20 μm per sample) presents also clear advantages for the PGAA and activation measurements carried out at the BRR since it has definitely reduced the γ-ray self-attenuation and neutron self-shielding corrections compared to a previous similar measurement by Genreith et al. [36, 37], as it is discussed in Section 4.3.2.

A total amount of 220 mg of PuO_2 highly enriched in ^{242}Pu were delivered from Oak Ridge National Laboratory (ORNL) (Oak Ridge, USA) to HZDR (Germany). The original isotopic composition (in wt %), certified in February of 1980, is summarized in Table 3.2. By the time the target was prepared, 84% of the the shortest-lived isotope, ^{241}Pu ($T_{1/2}$ = 14.3 y), had already decayed to ^{241}Am, which was removed from the Pu by anion exchange chromatography prior to deposition. The sucessful removal of the ^{241}Am was checked by α-particle spectroscopy.

Table 3.2: Isotopic composition of the original material delivered from ORNL compared to the final composition of the material in the ^{242}Pu targets.

	Isotopic compostion (% weight)
Sample	**Original material (1980)**
^{238}Pu	0.003
^{239}Pu	0.005
^{240}Pu	0.022
^{241}Pu	0.009
^{242}Pu	99.959
^{244}Pu	0.002

The targets were prepared by Molecular Plating (MP), a special type of Electrochemical Deposition. This method is based on depositing a material disolved in a small volume (5-20 μl) by appliying electric current densities in the mA/cm^2 range at voltages of hundreds of V. This technique is well stablished for cases where the target material is limited or highly radioactive and provides a high deposition yield and the capability of producing a target thickness of up $\sim$1 mg/cm^2. More details on the MP technique and its application for the production of large actinide targets can be found in Refs. [124, 125, 126]. The details on the production of the targets used in this work are given in Ref. [127].

A set of seven thin targets 45 mm in diameter were prepared by electrodeposition of 95 mg of ^{242}Pu on thin (10 μm) aluminum backings with a 50 nm Ti coating. Table 3.3 sum-

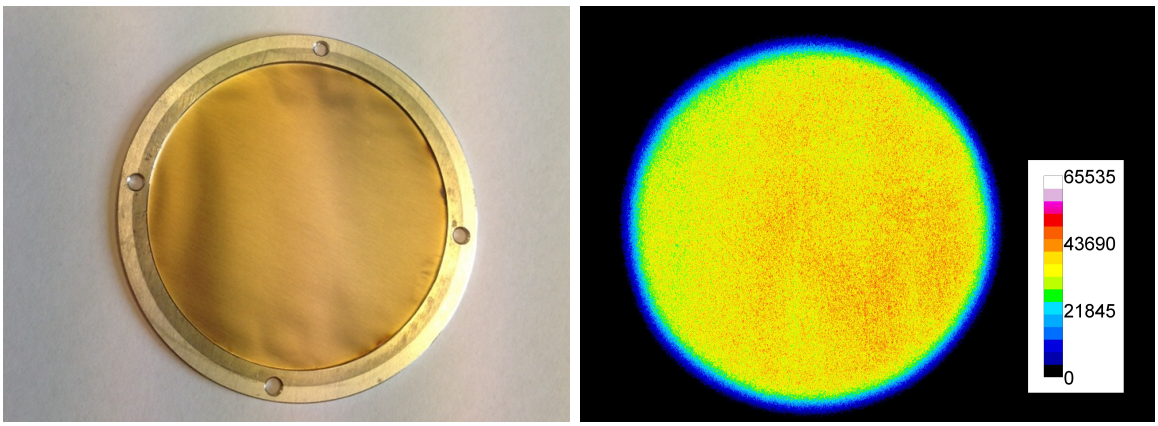

Figure 3.6: *Sketch of the BRR and all the Neutron Science instruments located in the Reactor Hall and the neighbouring BCN Measuring Hall.Left: Picture of ^{242}Pu target backing consisting on a 60 mm diameter and 10 μm thick aluminum foil coated with 50 nm of titanium and mounted on a 1 mm thick aluminum ring. Right: α-particle RI showing the homgeinity of the activity distribution of the deposited ^{242}Pu in one of the target backings.*

Table 3.3: *Sketch of the BRR and all the Neutron Science instruments located in the Reactor Hall and the neighbouring BCN Measuring Hall.Properties of the individual ^{242}Pu targets: Molecular Plating deposition yield, deposited ^{242}Pu mass and thickness for each target. The targets selected for their irradiation in the PGAA facility are marked with ^{a} and ^{b} superindex.*

Target #	**Deposition yield (%)**	**^{242}Pu mass (mg)**	**Thickness (μg/cm^2)**
1	98	13.4	842
2	98	13.1	826
3^a	98	14.3	896
4^a	97	15.1	947
5^b	99	14.7	923
6^b	98	15.5	976
7	99	8.9	562

a) Targets in Sample #1 in the experiments at the BRR.
b) Targets in Sample #2 in the experiments at the BRR.

marizes the deposition yield, ^{242}Pu mass and areal density of the seven individual targets. The average areal density is 850 μg/cm^2 of ^{242}Pu for the first six targets and only Target #7, where the remaining Pu material was electrodeposited, deviates significantly from this value. The masses of the ^{242}Pu deposits were determined by α-particle spectroscopy by comparing the ^{242}Pu content in the solution before and after the electrochemical deposition with an accuracy which is estimated to be 4%.

The target thickness homogenity was studied by means of radiographic imaging (RI) using a commercial RI system (FUJIFILM FLA 7000) equiped with imaging plates sensitive to α-particles. From the study of the activity distribution images, shown in Figure 3.6 the homogeinity was found to be 80%.

The ^{242}Pu samples irradiated in the PGAA facility (hereafer called Sample #1 and #2) consisted in two double-target sandwiches assembled using, in total, four out of the seven manufactured targets. The four selected ^{242}Pu targets are marked with the superscript ^{a} (Sample #1) or ^{b} (Sample #2) in Table 3.3. The total amount of ^{242}Pu in each of the samples was about 30 mg. The schematic sketch of the double-target assembly is shown together with its actual view in Figure 3.7. The inhomogeneity for each of the 2-target samples combined is estimated to be 4%, from the combination of two individual targets with a thickness inhomogeinity of about 20%.

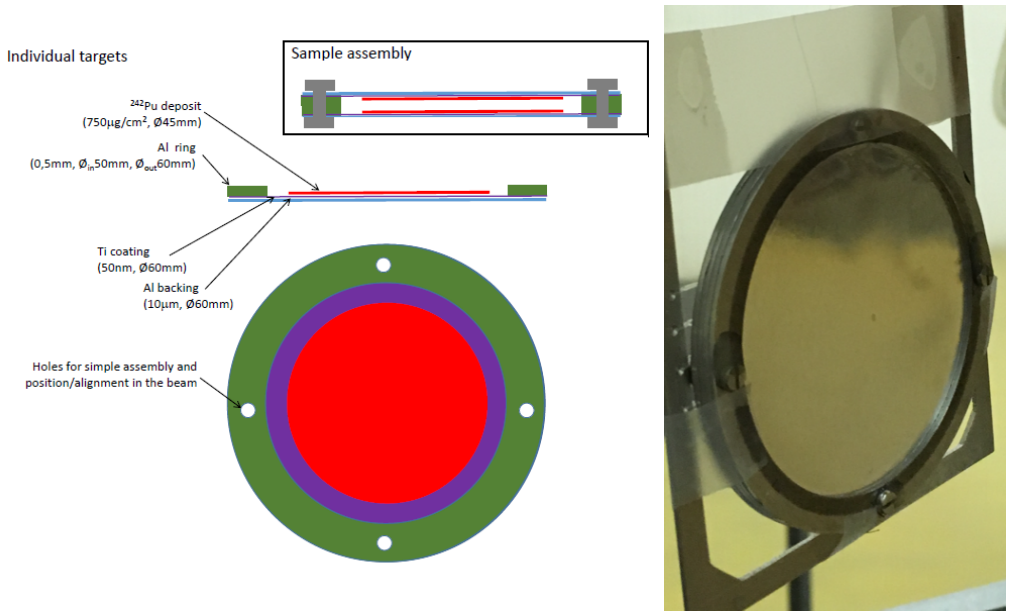

Figure 3.7: *Sketch of the BRR and all the Neutron Science instruments located in the Reactor Hall and the neighbouring BCN Measuring Hall.*^{242}*Pu target assembly and* ^{197}*Au reference sample of the same diameter placed in the PGAA sample holder. The* ^{197}*Au foil was placed downstream with respect to the* ^{242}*Pu target to avoid the absorption of low energy neutrons in the former.*

3.3.2 Neutron irradiations of ^{242}Pu and ancilliary measurements

The neutron irradiations in the PGAA facility are carried out inside the aluminum sample chamber shown in the left pad of Figure 3.8. The chamber is covered with a 2.4 mm thick sheet of enriched ^{6}Li-plastic on the inside to absorb the scattered neutrons. The last collimator made of the same neutron absorbing material is placed on the opening observed on the top side of the picture. For the irradiations in this work, two different collimators were used (10 x 10 mm^2 or 14 x 14 mm^2) depending on the γ-ray counting rate registered by the PGAA detector in each irradiation.

During the neutron irradiations, the flux evolution was monitored online using a gas neutron counter ORDELA Model 4511N with an active surface of 110x25 mm^2 and filled with a mixture of N_2 and CF_4 gases. Its counting efficiency was chosen to be as low as 10^{-6}, to provide a count rate of about 1000 cps. The monitor output is counted with a

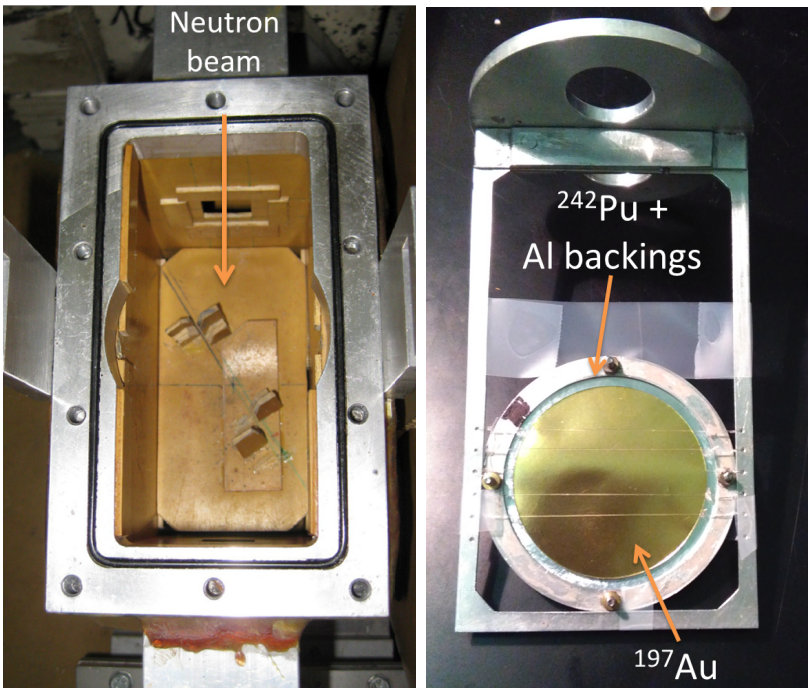

Figure 3.8: *Sketch of the BRR and all the Neutron Science instruments located in the Reactor Hall and the neighbouring BCN Measuring Hall.Left: Neutron irradiaton chamber covered with a ^{6}Li-plastic to absorb scattered neutrons. The tilted position of the sample is shown by the orientation of the slits on the chamber floor. Right: ^{242}Pu target assembly and ^{197}Au reference sample of the same diameter placed in the PGAA sample holder. The latter is placed downstream with respect to the direction of incidence of the neutron beam to avoid the absorption of low energy neutrons.*

NI-6601 PCI counter/timer card, and is displayed and recorded with a time-resolution of 1 sec over the whole 10-day long reactor cycle.

The samples are placed in a special holder which is installed inside this chamber using the slits observed at its bottom (see Figure 3.8). The sample holder is made out of aluminum and Teflon strings and accommodates objects with dimensions of about 70 x 70 x 5 mm^3. The right panel of Figure 3.8 shows the sample holder with the mounted ^{242}Pu Sample #2 and a gold sample of the same dimension used as a reference in the subsequent activation measurement (see Table 3.4). The frame is introduced into the sample chamber through the round cap visible on the image in Figure 3.8 and placed between the slits observed on the chamber floor.

The sample holder are placed in the irradiation chamber with an angle of 30° with respect to the neutron beam direction, which corresponds to 60° to the detector axis (see slits in Figure 3.8). By tilting the sample, a large irradiated area is ensured while the self-absorption of γ-rays in the direction of the PGAA detector (see Section 3.4 is reduced.

The experimental campaign at the PGAA facility, summarized in Table 3.4, included several irradiations aiming either at measuring the ^{242}Pu(n,γ) spectrum with the HPGe set-up described in Section 3.4 or at producing a significant amount of unstable nuclei

Table 3.4: *Summary of measurements carried out at the PGAA facility: sample thickness, irradiation time t, irradiated area (i.e. dimensions of close collimator) S and goal of the measurement.*

Sample	**Thickness(x 10^{19} at/cm^2)**	**t (min)**	**S (mm^2)**	**Goal**
^{242}Pu (#2) + Au	0.472(14) / 15.07(2)	1036.76	10 x 10	Activation
^{242}Pu (#1)	0.458(13)	1326.53	14 x 14	PGAA + Activation
Al	∼230 *	2.46	14 x 14	PGAA background
Ti	∼53 *	93.43	14 x 14	PGAA background
Glue	-	693.52	14 x 14	PGAA background
CH_2	-	11.62	14 x 14	PGAA background
Empty (Air + holder)	-	1014.48	14 x 14	PGAA background
^{242}Pu (#1) + Si	0.458(13) / 187.5(3)	110.64	14 x 14	PGAA normalization
^{242}Pu (#2) + Si	0.472(14) / 187.5(3)	77.42	14 x 14	PGAA normalization
Al + Si	23.16(3) / 187.5(3)	60.64	14 x 14	Mass Al backings

**) Accurate sample mass not required: spectrum normalized to the area of the main characteristic background peaks in the ^{242}Pu(n,γ) spectrum.*

(^{243}Pu) to subsequently measure their decay using a low background chamber described in Section 3.5. Some other measurements were carried out to assess the background in PGAA spectra or the absolute number of neutrons. The following list describes the different samples irradiated in the cold neutron beam of the PGAA facility:

1. Irradiation of ^{242}Pu sample #2 together with a ^{197}Au sample of the same dimension and 25 μm thick aiming at measuring the decay of the activated ^{242}Pu sample relative to Au. The prompt ^{242}Pu data of this measurement could not be analyzed due to the dominating prompt γ-ray spectrum from the Au(n,γ) reactions. Due to the large counting rate associated to the high ^{197}Au(n,γ) reaction rate, the far and both collimators were both set to 10 x 10 mm^2 to keep the dead time below 1%.

2. Irradiation of ^{242}Pu sample #1 for activation and prompt gamma analysis relative to the saturated decay of the activated ^{28}Al ($t_{1/2}$ = 2.45 min) from the target backings. For this irradiation the dimension of the PC-controlled far collimator was set to 20 x 20 mm^2 and a 14 x 14 mm^2 collimator was installed in the irradiation chamber. This configuration was left for the remaining irradiations.

3. The background assesment for the prompt gamma spectra measured during irradiation (2), required ancilliary irradiations of Al, Ti, glue, and polyethilene to determine the contribution of the capture reactions in the target backings. In addition, the background associated to neutron captures on the experimental set-up was determined with an irradiation of the empty sample chamber.

4. Additional irradiations of the ^{242}Pu samples combined with aluminum and silicon comparators served for validation and normalization purposes (see Section 4.2). The left panel of Figure 3.9 shows the sample holder for the PGAA sample containing the Al and Si comparators.

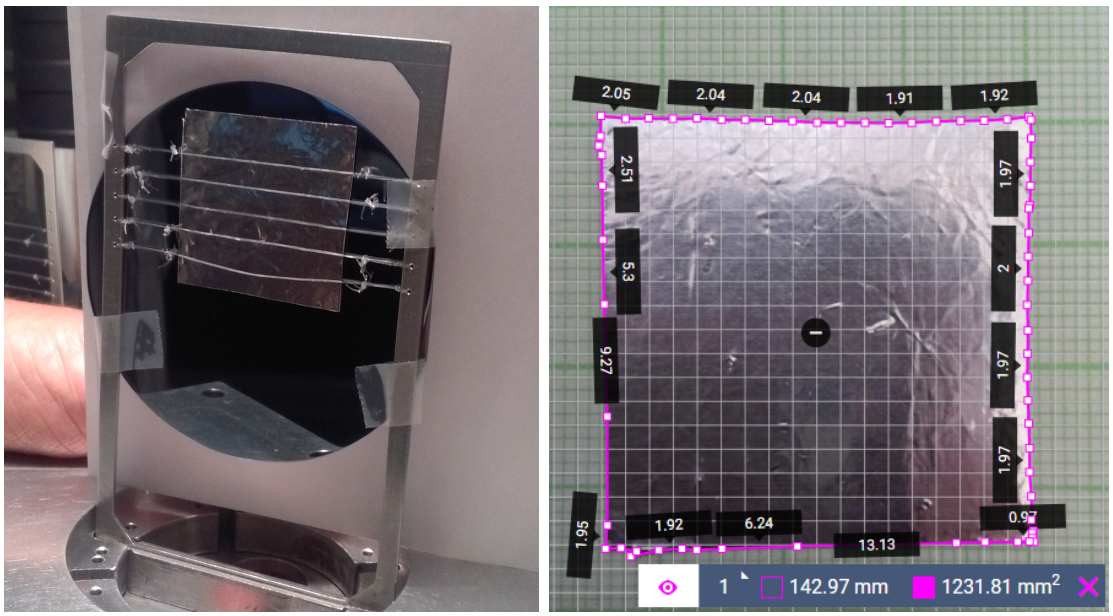

Figure 3.9: *Left: Sample holder prepared for the irradiation of the aluminum foil combined with a silicon wafer aiming at providing an absolute normalization to the number of neutrons. Right: Graphical determination of the surface of the aluminum foil using a commercial software [128].*

The target thickness for the aluminum and silicon comparators was precisely determined from the accurate measurement of their mass using a high-precision scale with an acurracy of 0.1 mg and the graphical calculation of the target area from the analysis of pictures on a millimeter graph paper (right panel of Figure 3.9). The resulting target thicknesses are included in Table 3.4.

In all the irradiations where two samples were placed in paralell, the one with higher neutron macroscopic cross section (i.e. nr of atoms x σ_{tot}) was placed downstream to minimize the neutron self-shielding and the neutron spectrum hardening. In particular, Au was placed downstream from the ^{242}Pu Sample #2 (Figure 3.8) and the Si comparator was placed upstream from both the ^{242}Pu Sample #1 and the Al comparator (Figure 3.9).

3.4 Prompt γ detection set-up

The prompt γ-rays generated as a result each neutron capture are partially detected a with a BGO guarded Compton-suppression n-type HPGe detector placed at 23.5 cm from the sample and perpendicular to the neutron beam axis (see Figure 3.3), hence looking at the sample with a 60° angle.

The spectrometer consists of a Canberra GR 2720/S coaxial n-type HPGe detector with 27% relative efficiency. The inner structure of the detector is illustrated in the X-ray image shown in the left panel of Figure 3.10. The HPGe detector is surrounded by an approximately 48 mm thick, eight segment, coaxial BGO scintillation detector that acts

as a Compton suppressor. In addition a 65 mm thick BGO scintillation detector, the so-called *back-catcher*, is placed in the opening behind the HPGe detector, closing the distance between the copper cold finger and the aluminum holder of the HPGe crystal. The detector is shielded from neutrons with enriched ^{6}Li-plastic layers and from γ-ray background from outside the sample chamber with a 11 cm thick lead shield with a circular collimator opening of 22 mm and an additional 10 mm thick tungsten collimator right in front of the BGO. A sketch of the full geomety of the detection set-up taken from the Geant4 geometry model developed in Ref. [129] is shown in the right panel of Figure 3.10.

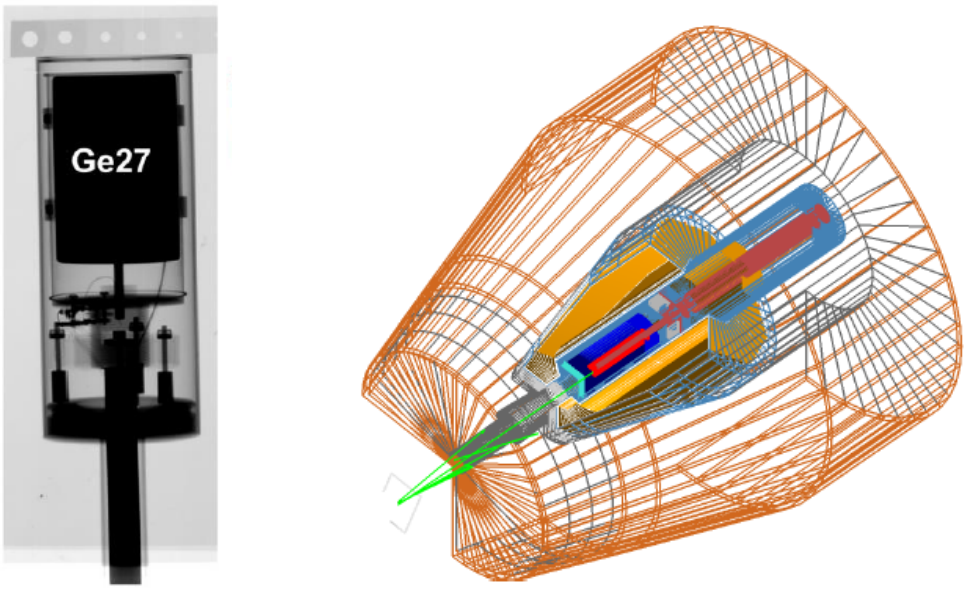

Figure 3.10: *Right: X-Ray image of the Canberra GR 2720/S coaxial n-type HPGe detector installed in the PGAA facility [130]. Left: Geant4 model of the full detection set-up at the PGAA station [129]. The solid volumes are the HPGe detector (blue) and the BGO Compton shield (orange) surrounding it. The shielding, sample and supporting parts are all drawn as wire-frame models.*

The processed and digitized pulse height signals are recorded in a PC-driven Multi Channel Analyzer (MCA) Canberra AIM 556. The prompt gamma spectra measured in this work were recorded without any Compton supression.

This set-up is periodically calibrated in energy and efficiency using a combination of radioactive samples (^{60}Co, ^{133}Ba, ^{152}Eu, ^{226}Ra, ^{241}Am) and characteristic γ-rays from the ^{35}Cl(n,γ) (PVC sample) and ^{14}N(n,γ) (urea sample) reactions with well known partial γ-ray production cross sections. The use of prompt γ-rays allows an extension of the calibrations up to 12 MeV.

The experimental efficiencies as a function of the γ-ray energy E_γ area fitted to an analytical function of the form

$$\varepsilon(E_\gamma) = exp\sum_{i=0}^{n}(lnE_\gamma)^i, \tag{3.3}$$

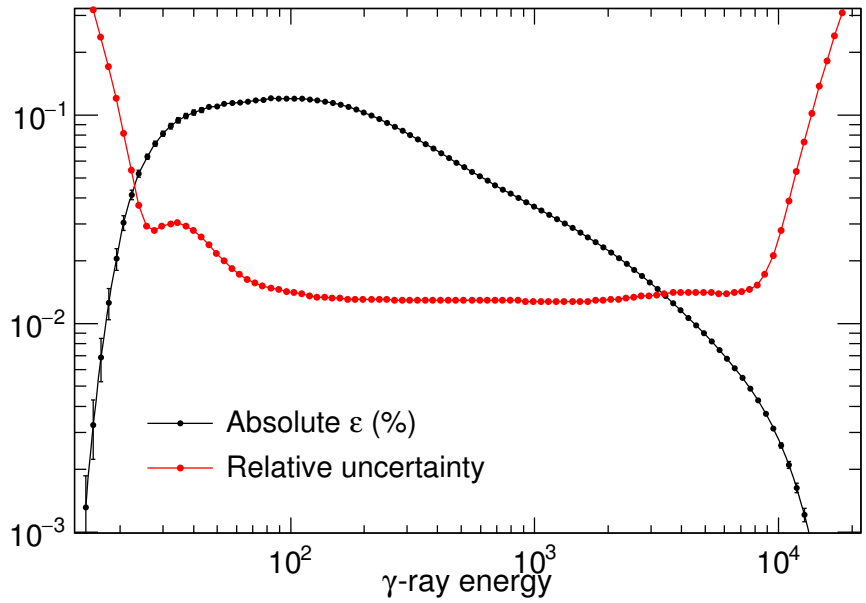

Figure 3.11: *Top: Absolute peak efficiency (%) as a function of the γ-ray energy (black) and its relative uncertainty (red) for the compton-unsupressed HPGe detection set-up of the PGAA facility.*

where the sum over i goes up to $n = 8$. The extracted efficiency curve for the prompt gamma detection set-up is shown in Figure 3.11. The red curve in the same plot corresponds to its relative uncertainty.

The energy deposited in the detector is represented by the channel number provided by the MCA. As several processes along the nuclear electronics chain such as the conversion from analog to digital signal, are not completely linear, the relation between channel and deposited γ-ray energy is not completely linear, either. The non-linear performance of this detection set-up causes a maximum deviation of 1 keV in the whole energy range. To assign the correct energies to all peaks a correction for the non-linearity needs to be applied. This correction is carried out using the HYPERMET software [131, 132, 133], which was specially developed in the Budapest Neutron Center for the analysis of spectra with thousand lines in a wide energy range (50 keV to 12 MeV). The correction for non-linearity is applied on channel units and then a linear fit of the corrected channel position of two peaks with well-known energies is applied to calibrate in energy.

3.5 Activation set-up

The decay of the activated ^{242}Pu and ^{197}Au samples was measured after they were removed from the irradiation station. The experimental set-up where the activation measurements take place is called DÖME, acronym for DÖgnehéz Mérö Eszköz or *damn heavy measuring tool* in Hungarian. It consists on a low background chamber with an internal dimension of

800 x 800 x 800 mm^3, with a HPGe installed inside. The wall of the chamber is 15.5 cm thick and has a graded shielding (148.5 mm Fe, 5 mm Pb and 1.5 mm Cu layers) that suppreses the ambient background from >200 cps outside the chamber down to only 1.4 cps. The iron in the chamber shielding is pre-WW2 (from the Elizabeth-bridge of Budapest, bombed in 1945) to avoid the presence of radionucleides produced in the weapon tests. A general view of the low background chamber from the outside is shown in Figure 3.12.

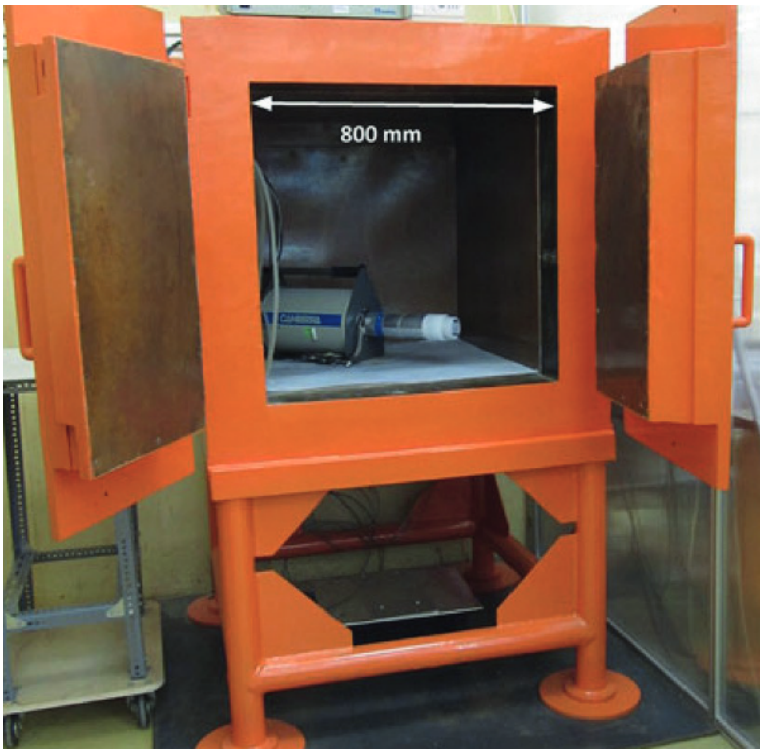

Figure 3.12: *General view of the DÖME set-up chamber from the outside (top) (Taken from Ref. [134]).*

The detection system inside the low-background chamber consists on a Canberra GR1319 HPGe detector of 13% relative efficiency with a BigMAC cryostat along the chamber's horizontal diagonal (See Figure 3.12). The cylindrical detector has dimensions of 46 mm in diameter and 41 mm in length and presents a low absorption 0.5 mm thin carbon epoxy endcap window that allows to measure from 7 to 3150 keV in γ-ray energy. For more details on this set-up the reader is referred to Ref. [134].

The efficiency calibration was assesed with ^{60}Co, ^{133}Ba, ^{152}Eu,^{226}Ra, ^{207}Bi and ^{241}Am sources and fitted to Eq. (3.3). Figure 3.14 shows the energy dependecy of the absolute peak efficiency of this set-up fitted to the function of Eq. (3.3). This curve was used to assess the detection efficiency for a given energy in the upcoming analysis. The relative uncertainty in the efficiency, also shown in Figure 3.14, is a smooth function of energy and was thus linearly interpolated.

The dimensions of the chamber allow sample-to-detector distances up to 250 mm. A precise distance from the detector is kept by using a special aluminum frame and aluminum

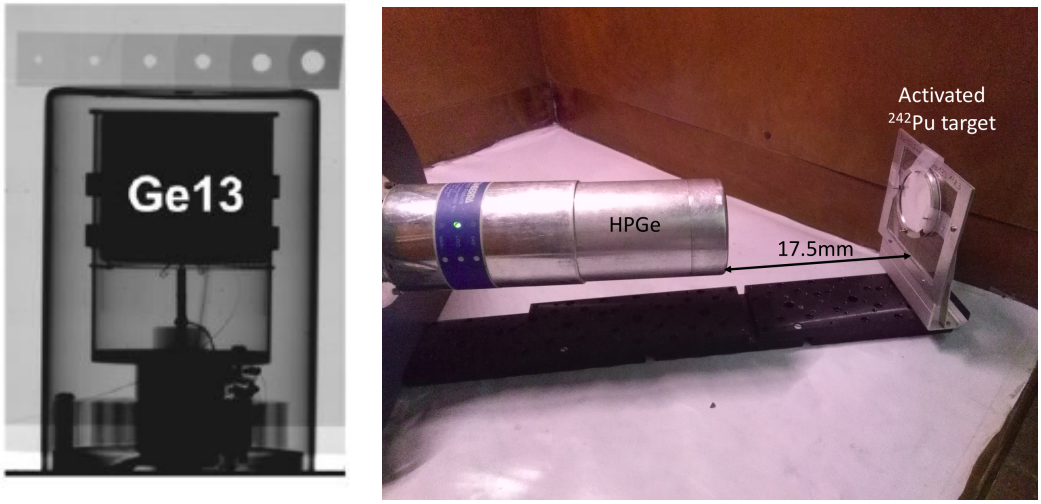

Figure 3.13: *Left: X-Ray image of the n-type Canberra Model GR1319 installed in the DÖME low-background chamber for activation mesurements (taken from Ref. [130]). A closer view detection setup showing the HPGe detector, the aluminum pieces that keep the sample at a fixed position and the sample frame holding the activated ^{242}Pu sample #2.*

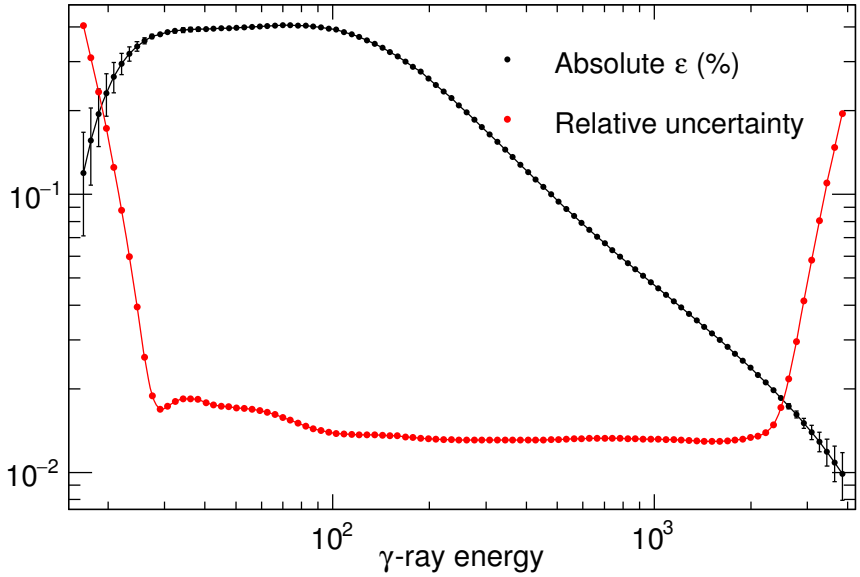

Figure 3.14: *Top: Absolute peak efficiency (black) and its relative uncertainty (red) of the DÖME low-background counter as a function of the γ-ray energy [134].*

distance pieces shown in the right panel of Figure 3.13. In our measurements, a distance of 176 mm from the sample holder to the detector window was used.

The decay γ-ray spectra emitted by the activated targets are acquired using a Canberra DSA-2000 acquisition system with 16000 channels and later evaluated with the HYPERMET software.

Chapter 4

Analysis and results of the measurements at the BRR

This chapter is devoted to the analysis of the measurements carried out at the BRR aiming at the experimental determination of the thermal capture cross section of ^{242}Pu. The experimental details of this experimental campaign were described in Chapter 3 The two first sections of this Chapter deal with the analysis of the measurements, each of them corresponding to a different experimental technique: Activation and Prompt Gamma Activation Analysis. Three compatible independent values for the thermal capture cross section have extracted in this work, which seem to clarify the previous experimental discrepancies and support the thermal cross section reported in the JEFF-3.2 evaluation, 15% below the value in ENDF/B-VII.1.

4.1 The ^{242}Pu activation analysis

4.1.1 ^{243}Pu and ^{198}Au decays

As it was introduced in Section 2.5.1, neutron capture cross sections can be determined by counting the number of nuclei produced in a given sample by means of (n,γ) reactions. In order to determine the number of neutron captures by means of the Activation method, the decay of the product nucleus is measured. This technique only applies when the nucleus produced via neutron capture is unstable, as it is the case for ^{243}Pu and ^{198}Au, products of the neutron captures in the ^{242}Pu and ^{197}Au samples irradiated in the PGAA facility.

The β^- decay of ^{243}Pu ($T_{1/2}$ = 4.956(3) h) populates eight excited states of ^{243}Am with a summed branching of 40% that decay to the ground state via emmission of γ-rays with energies ranging from 25 to 475 keV [19]. The decay scheme of this isotope is presented in Figure A.2 in Appendix A. The five main γ-ray transitions in this decay have been identified and analyzed in this work and their energies and absolute intensities per decay (i.e. per neutron capture) are presented in Table 4.1 [19]. Two different values for the

absolute intensity of the 84.0 keV reference line are found in the literature. The value of 0.23(2) [39], used in previous measurements, was obtained relative to the α-decay of ^{247}Cm to ^{243}Pu [135]. However, recently Leconte et al. [136] provided a more acurate value of 0.192(10) from a combination of activation and pile oscillation experiments and claimed that the 20% higher value used in revious works might be suffering from pandemounium effect. For this reason, the most recent value of Leconte et al. is used in our analysis.

Table 4.1: *Absolute intensities (I_γ) of the ^{243}Pu and ^{198}Au decay lines analyzed in this work, marked with blue arrows in Figure 4.1.*

Nucleus	**E$_\gamma$ (keV)**	**I$_\gamma$ (%) [19]**
^{243}Pu	41.8(2)	0.63(7)
	67(1)	0.19(10)
	84.0(2)	19.2(10)
	109.2(2)	0.134(15)
	381.6(2)	0.48(3)
^{198}Au	411.8020(2)	0.9562(6)

The neutron captures on the ^{197}Au produce ^{198}Au nuclei which decay by means of β^- ($T_{1/2}$ = 64.658(6) h) to ^{198}Hg. The simple decay scheme (see Figure A.1 in Appendix A), has a dominant β^- branching (98.99%) to a state with an excitation energy of 411.80 keV. The subsequent de-excitation to the ground state leads to the emission of a γ-ray of the same energy with an absolute intensity per neutron capture of 95.62(6)%. The β^- decay also populates an state of ^{198}Hg at 1087.68 keV that decays via emmission of two low intensity γ-rays (emitted in less than 1% of the decays) that were not considered in the analysis.

4.1.2 Analysis of the activation spectra

The activated samples were measured with a HPGe detector in the DÖME station (see Section 3.5) and the spectra were acquired with a 14-bits PC-driven MCA and calibrated in energy using several sources with well known γ-ray energies (see Section 3.5).

The full energy-calibrated γ-ray spectrum of the ^{242}Pu Sample #2 before (red) and after (black) the irradiation is shown in Figure 4.1. The background peaks characteristic the ^{242}Pu target activity are mainly low γ-ray transitions of ^{238}U (44.9, 103.5 and 159.0 keV) following the ^{242}Pu α-decay and U X-Ray lines (K between 13 and 20 keV and L between 94 and 114 keV). The the 59.5 keV γ-ray line from the ^{241}Am α-decay (coming from the traces of ^{241}Pu in the sample) is also visible in the spectrum of ^{242}Pu sample before activation. The ^{243}Pu peaks analyzed (see Table 4.1) are indicated with arrows.

The energy-calibrated γ-ray spectrum of the activated ^{197}Au comparator is shown in Figure 4.1. In this figure one can appreciated the simplicity of the γ-ray spectrum following the β-decay of ^{198}Au, dominated by the 411.8 keV line (blue arrow). The two remaining

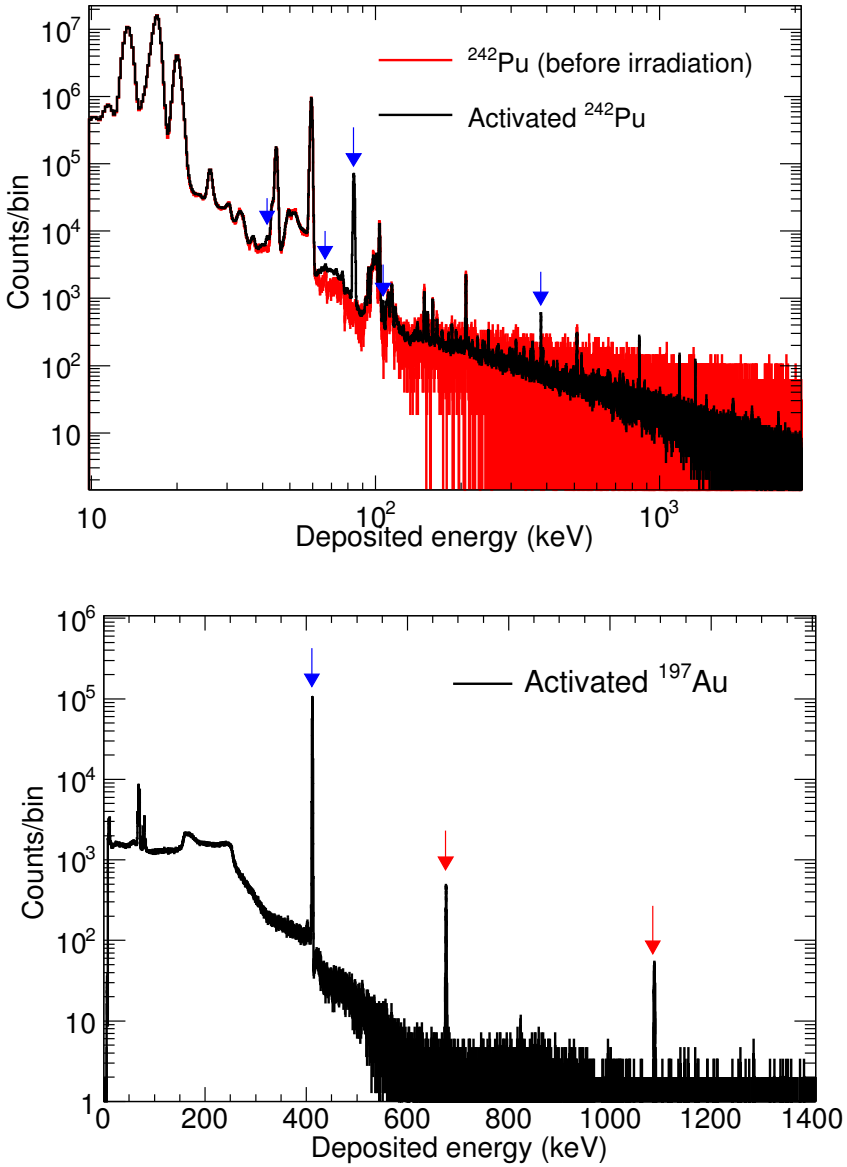

Figure 4.1: *Spectra of γ-ray energy deposition adquired with the HPGe detector in the activation station before (red) and after (black) activating the ^{242}Pu sample. The bottom panel shows the spectra of the activated ^{197}Au target. The analyzed lines are pointed with blue arrows.*

low-intensity ones are marked with red arrows. Since ^{197}Au is stable, the measurement of the activity background is not required in this case.

The decay of the activated ^{242}Pu sample #1 and #2 was measured over 25 and 20 hours, splitted into one-hour-long measurements (see Table 4.2), which allows validating the time evolution of the peak integrals. The activated ^{197}Au sample was measured for one hour at 25 and 56 hours after the end of the irradiation (EOI). In each analyzed spectrum, the number of counts associated to the decay lines summarized in Table 4.1 was extracted from

the fit of each peak to a Gaussian on top of a linear background, and, when necessary, an additional Gaussian corresponding to the neighbouring background peaks. The fits of the six peaks analyzed are displayed in Figure 4.2.

The ^{242}Pu data have been analyzed in two different ways:

1. *Decay Fit Method*: Each 1-hour-long measurement has been analyzed individually and the experimental decay rate has been compared with the half life of ^{243}Pu. This method serves as a validation of the peak fitting method.

2. *Integral Method*: Since the statistics available in the individual measurements is limited, the 1-hour-long are grouped together and the peak analysis is carried out on the time-integrated spectrum. Then, the number of activated nuclei at the EOI was estimated considering the half-life of ^{243}Pu.

The evolution with time of the 84.0 keV peak integrals is shown in Figure 4.3. In this plot, we show the perfect agreement within the uncertainties of the peak area obtained by numerical integration and from the fitted peak. The experimental decay rates for both ^{242}Pu show an excellent agreement with the theoretical value (see Table 4.2), thus validating the peak fitting method. In Table 4.2, the $T_{1/2}^{exp}$ value from sample #1 is more accurate due to the smaller statistical uncertainties and the larger number of fitted decay points than in the measurement of sample #2.

The first step to obtaine the number of nuclei produced by in the irradiated samples is the calculation of the counting rate at the EOI from the areas of the peaks in the spectrum. The peak integral C_j^{sum} extracted using the *Integral Method* from the fitted ^{243}Pu and ^{198}Au peaks shown Figure 4.2, is related to the counting rate at the end of the irradiation $R_j(EOI)$ by

$$C_j^{sum} = \int_{t_{start}}^{t_{stop}} R_j(EOI)\ e^{(-\lambda t_d)} dt_d, \tag{4.1}$$

where λ is the decay constant, t_d is the decay time and t_{start} and t_{stop} are the times after the end of the irradiation when the measurement started and finished, respectively. In our case, the measurement was not continuous in t_d and the integral in Eq. (4.1) leads to the following sum in each 1-hour-long i-measurement

$$C_j^{sum} = \ R_j(EOI)\ \frac{1}{\lambda}\ \sum_i e^{(-\lambda t_{start,i})} - e^{(-\lambda t_{stop,i})}, \tag{4.2}$$

Table 4.2: *Summary of the ^{243}Pu decay measurements: Start t_s and stop t_e times after the end of the irradiation (EOI), number of decay points NP (1-hour-long measurements) and fitted values for the half-lifes $T_{1/2}^{exp}$ compared to the evaluated values $T_{1/2}^{th}$. The last column shows the fraction of the activated nuclei that decayed during the activations measurements.*

Decay	t_s **(h)**	t_e **(h)**	**NP**	$T_{1/2}^{exp}$ **(h)**	$T_{1/2}^{th}$ **(h)**	F_m
^{243}Pu (#1)	1.57	26.58	25	4.948(10)	4.956(3)	0.78
^{243}Pu (#2)	3.00	24.28	20	4.98(3)	”	0.53

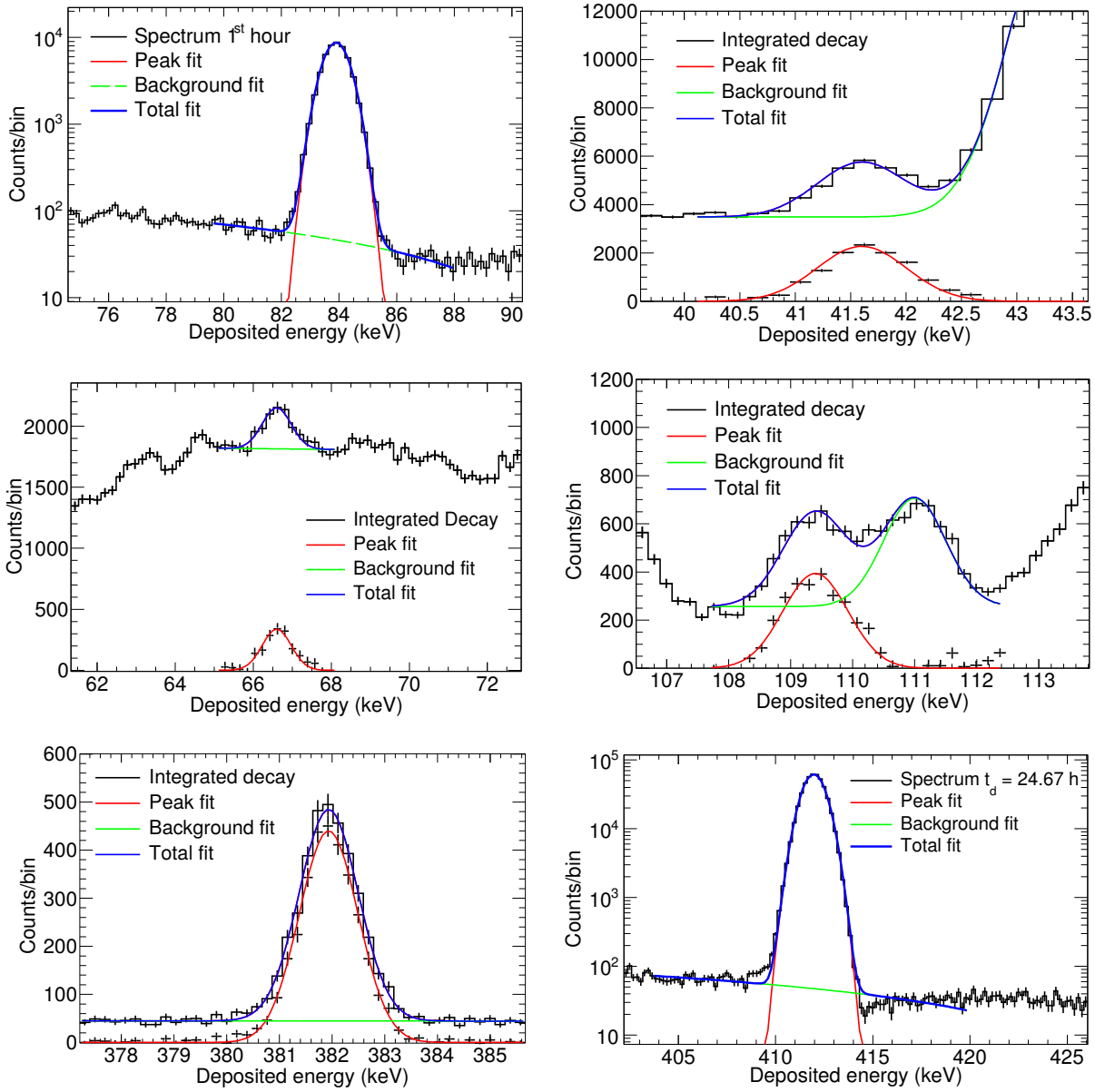

Figure 4.2: *Fitted peaks of the* ^{243}*Puγ-ray lines (42, 84, 109 and 382 keV) in sample* #1 *and the 411.8 keV* ^{198}*Auγ-ray line (bottom right).*

where $t_{start,i}$ and $t_{stop,i}$ are the start and stop times for each 1-hour-long measurements. The counting rates at the EOI, calculated with Eq. (4.2) for the five analyzed peaks of ^{243}Pu decay in the measurement of sample #1 are presented in Table 4.3. In the same table, we also present the counting rate at the EOI calculated from the two individual measurements of the activated ^{197}Au sample, which deviate to each other by 4.4%. The average has been taken for the calculation of the number of produced nuclei and a systematic uncertainty of 2.2% has been considered.

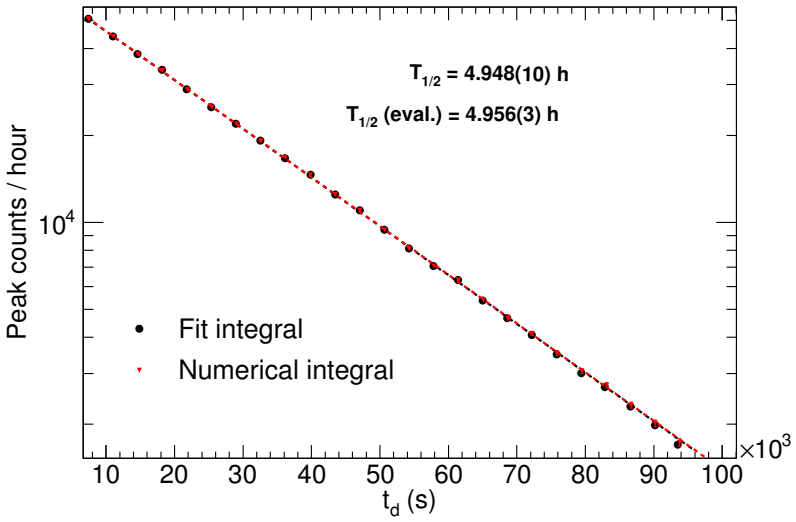

Figure 4.3: *Time evolution of the 84 keV peak area fitted to the expected exponential decay. The peak integral extracted from the fit peak (black) shows compatible results with the direct numerical integration on top of the background (red). The fitted half-life $T_{1/2}$ is compared to the evaluated one.*

Table 4.3: *Counting rate at the end of the irradiation $R_j(EOI)$ obtained with the Integral Method from the measurement of the activated ^{242}Pu sample #1 and the two measurements of the activated ^{197}Au sample.*

E_γ (keV)	**$R_j(EOI)$ (counts/s)**
67	0.082(8)
84	18.61(3)
109	0.133(4)
381.6	0.161(3)
411.8 (t_d=25 h)	165.8(3)
411.8 (t_d=56 h)	173.4(3)
411.8 (average)	169.62(19)

4.1.3 Calculation of the thermal capture cross section

The thermal capture cross section is defined, following the general definition of the thermal cross section in Eq. (2.54), as the value of the capture cross section for a neutron energy of 25.3 meV (equivalent to v = 2200 m/s or T = 300 K). However, the neutron flux in the PGAA facility has an average energy corresponding to a temperature of T = 120 K (Figure 3.4), well below the thermal energy. The integral experimental capture cross section $\langle\sigma_\gamma\rangle_{exp}$ extracted from the measurements in the PGAA facility is given by

$$\langle\sigma_\gamma\rangle_{exp} = \frac{\int \sigma_\gamma(E_n)\ \phi(E_n)\ dE_n}{\int \phi(E_n)\ dE_n}, \tag{4.3}$$

where $\phi(E_n)$ is the neutron flux of the PGAA facility shown in Figure 3.4 and $\sigma_\gamma(E_n)$ is the differential capture cross section.

Experimentally, the thermal capture cross section is calculated from the the number of captures (i.e. number of produced nuclei N) during the irradiation in the PGAA facility using the following expresion,

$$\sigma_{th} = F_{En}\ \frac{N}{n\ \phi_{int}}, \tag{4.4}$$

where n is the areal density of the sample, ϕ_{int} is the total number of neutrons impinging the sample during the irradiation and F_{En} is the factor that relates the thermal and experimental cross section (given by Eq. 4.10) and N is the number of nuclei produced in the sample:

$$N\ =\ \frac{N_0}{F_d}, \tag{4.5}$$

where N_0 represents the number of activated nuclei present in the sample at the EOI and F_d is the correction factor for the decaying nuclei during the irradiation. N_0 is calculated from the counting rate at the EOI $R_j(t_d = 0)$ for each of the decay lines as

$$N_0\ =\ \frac{R_j(t_d = 0)}{F_{geom}\ F_{abs}\ \varepsilon_j\ I_j}, \tag{4.6}$$

where I_j and ε_j are, respectively, the absolute intensity of the j-line (see Table 4.1) and the corresponding peak detection efficiency (Figure 3.14). F_{geom} and F_{abs} are correction factors of the detection efficiency. The calculation of all the correction factors is described in detail in Section 4.1.4.

In order to extract the thermal cross section of ^{242}Pu, the total number of neutrons incindent in our sample (ϕ_{int} in Eq. (4.4)) must be accurately determined. However, the neutron flux monitor (see Section 3.5) does not provide the absolute, but just a relative number of neutrons. Moreover, the size and profile of the neutron beam on our sample are not precisely known. For this reason, a Au sample of the same dimensions than the ^{242}Pu is irradiated in parallel to the sample of interest. Then, the absolute number of neutrons ϕ_{int} is determined from the the number of nuclei produced in the gold sample, calculated using Eq. (4.5), and the well-known thermal capture cross section of Au σ_{th}^{Au}

$$\phi_{int} = F_{E_n}^{Au}\frac{N^{^{198}Au}}{n_{^{197}Au}\ \sigma_{th}^{Au}}, \tag{4.7}$$

Replacing Eq. (4.7) in Eq. (4.4), the thermal capture cross section of ^{242}Pu yields

$$\sigma_{th}^{Pu} = \sigma_{th}^{Au}\ \frac{F_c^{^{242}Pu}}{F_c^{^{197}Au}}\ \frac{N_0^{^{243}Pu}}{N_0^{^{198}Au}}\ \frac{n^{^{197}Au}}{n^{^{242}Pu}}, \tag{4.8}$$

where $N_0^{^{243}Pu}$ and $N_0^{^{198}Au}$ are the number of activated nuclei present in the ^{242}Pu and ^{197}Au samples at the EOI (Eq. (4.6)). $n^{^{242}Pu}$ and $n^{^{197}Au}$ represent the number of atoms per barn

in the samples (see Table 3.4). F_c^{Pu} and F_c^{Au} have been introduced to group the different correction factors introduced above

$$F_c = \frac{F_{En}}{F_d\ F_{abs}\ F_{geom}}. \tag{4.9}$$

4.1.4 Correction factors in the activation analysis

Several correction factors, F_{En} in Eq. (4.4) and F_d in Eq. (4.5), F_{geom} and F_{abs} in Eq. (4.6), have been introduced in the calculation of the thermal capture cross section.

These correction factors account for the following effects:

- F_{En}: Ratio between the capture cross section at thermal energy and the experimental (integral) cross section in the cold neutron beam of the PGAA facility, calculated as:

$$F_{En} = \sigma_{th}\frac{\int \phi(E_n)dE_n}{\int\ \sigma_\gamma(E_n)\ \phi(E_n)\ dE_n}. \tag{4.10}$$

  The values of F_{En} for ^{242}Pu and ^{197}Au, presented in Table 4.4, have been calculated using the differential capture cross sections $\sigma_\gamma(E_n)$ in JEFF-3.2 [20] and ENDF/B-VII.1 [21], yielding similar results in both cases. According to the values in Table 4.4, the integral experimental cross section is about a factor two larger than the thermal one. This difference is illustrated in the right panel Figure 4.4, where we show the convolution of the capture cross sections of ^{242}Pu and ^{197}Au with the experimental flux of the PGAA facility compared to a Maxwellian thermal flux at kT = 25.3 meV. The value of the F_{En} factor for both isotopes is very similar since the cross section shape below thermal energies is very close to 1/v in both cases, as it is shown in the right panel of Figure 4.4. Consequently, the final correction in Eq. 4.8 (ratio of F_{En} factors of ^{242}Pu to ^{197}Au) turns out to be negligible.

- F_d: Fraction of activated nuclei that had not undergone decay at the EOI. This factor is defined as:

$$F_d(t_{irrad}) = \frac{N_d(t_{irrad})}{N_{tot}(t_{irrad})}, \tag{4.11}$$

  where t_{irrad} is the irradiation time, and N_d and N_{tot} are the number of product nuclei present in the sample at the EOI considering and neglecting the decay of the product nuclei, respectively. These quantities were caclulated by numerical integration of

$$\begin{aligned} \frac{dN_d(t)}{dt} &= n\ \langle\sigma_\gamma\rangle_{exp}\ \phi(t)\ -\ N_d(t)\ \lambda, \\ \frac{dN_{tot}(t)}{dt} &= n\ \langle\sigma_\gamma\rangle_{exp}\ \phi(t), \end{aligned} \tag{4.12}$$

  where $\phi(t)$ is the time evolution of the neutron flux given by the neutron monitor, and λ is their decay constant. The time evolution of N_d and N_{tot} during the irradiations of the ^{242}Pu sample #1 and the ^{197}Au sample are shown in Figure 4.5. F_d depends only

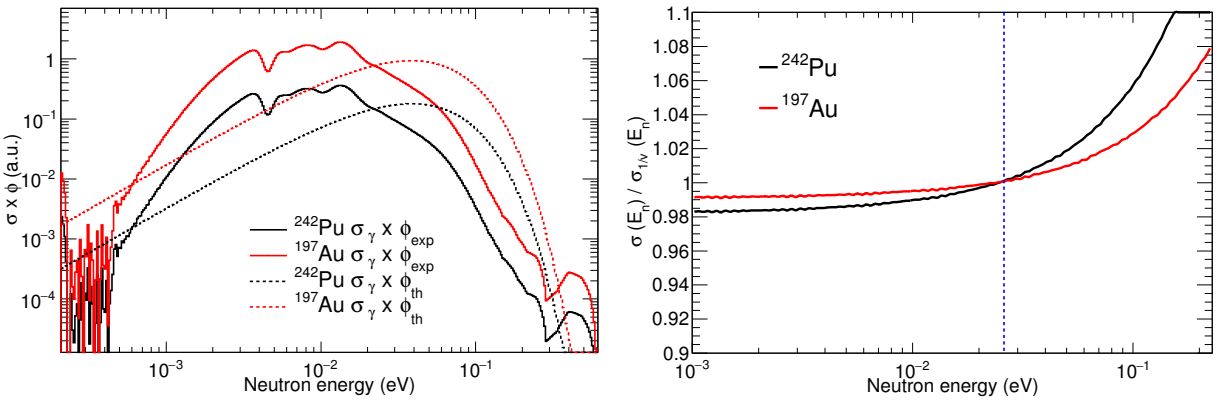

Figure 4.4: *Left: Comparison of the experimental cold neutron flux at the PGAA facility (solid line) and a Maxwellian thermal sprectum (T = 293 K) (dashed line) convoluted with the* $^{242}Pu(n,\gamma)$*(red) and* $^{197}Au(n,\gamma)$ *(red) cross sections. The experimental integral cross section* $\langle\sigma_\gamma\rangle_{exp}$ *corresponds to the integral of the solid curves. Right: Ratio of the differential cross sections in JEFF-3.2 with respect to the 1/v shape normalized to the cross section at 25.3 meV (blue dashed line).*

on the half-life of the produced nuclei, the irradiation time and the time evolution of the neutron flux but not on the absolute value of the latter or on the cross section. Table 4.4 presents the values of F_d.

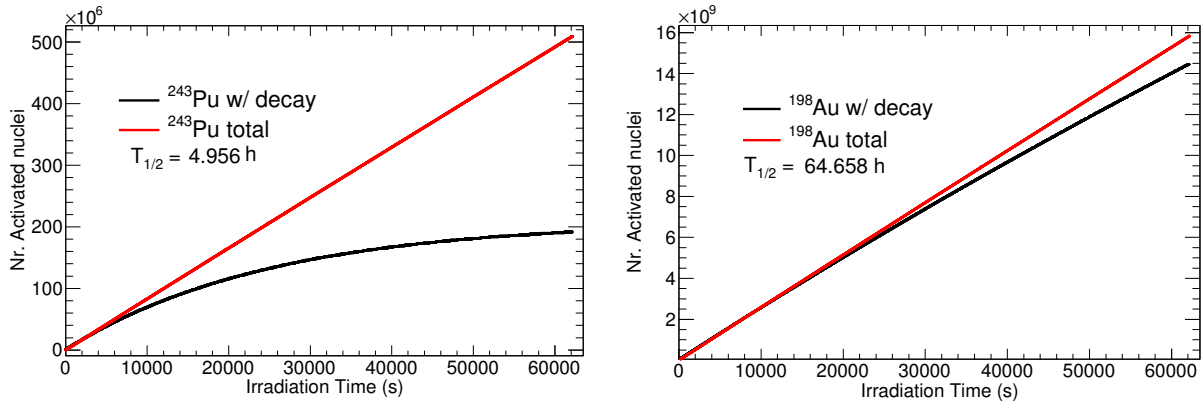

Figure 4.5: *Calculated number of nuclei produced via* $^{242}Pu(n,\gamma)$ *(left) and* $^{197}Au(n,\gamma)$ *(right) reactions as a function of the irradiation time (red dots). The black curve is obtained when we consider the decay of the produced* ^{243}Pu *(4.956(3) h) and* ^{198}Au *(64.658(5) h) nuclei and provides the number of surviving nuclei in the sample. The correction factor* F_d *(see Table 4.4) is obtained from these curves as the ratio of the surviving nuclei at the EOI to the total produced nuclei.*

- F_{abs}: Fraction of γ-rays escaping the target in the direction of the detector has been calculated by means of Monte Carlo simulations using the Geant4 toolkit [137, 138]. For these simulations, the details of the ^{242}Pu sample assembly (see Figure 3.7) were implemented in the Geant4 geometry model. The neutron self-shielding has been neglected (i.e. the γ-rays were emmited randomly along the sample thickness). The

value of the F_{abs} correction for all the analyzed lines, presented in Table 4.5, is lower than 1% except the lowest γ-ray emission at 41.8 keV.

- F_{geom}: Correction of the geometric efficiency for the deviation between a point source placed at 176 mm from the detector (efficiency calibrations) with respect to the actual γ-ray emission distribution (a square of 14x14 mm^2) in the irradiated targets. This factor was also calculated by means of Geant4 simulations where the neutron beam size was taken into account to simulate the distribution of emmited γ-rays and the neutron self-shielding was again neglected. The values of F_{geom} for ^{242}Pu and ^{197}Au were found to be independent of the γ-ray energy within the uncertainties and are presented in Table 4.5.

Table 4.4: *Correction factors not dependent on the γ-ray energy: Correction factor from the experimental average cross section and the thermal value for ^{242}Pu and ^{197}Au F_{E_n} using different evaluated cross sections. The last column corresponds to the fraction of activated nuclei that had not undergone decay at the EOI F_d.*

Sample	F_{E_n}	F_d
^{242}Pu (#1)	0.53	0.31
^{242}Pu (#2)	0.53	0.37
^{197}Au	0.53	0.92

Table 4.5: *Correction factors for the detection efficiency: Energy-dependent absorption in the sample F_{abs} and total correction and geometric efficiency correction with respect to a point source at the reference position for the calibrations (176 mm) F_{geom}. The uncertainties in this table are due to counting statistics in the simulations.*

Nucleus	**E$_\gamma$ (keV)**	F_{abs}	F_{geom}
^{243}Pu	41.8(2)	0.9812(6)	1.019(5)
	67(1)	0.9946(6)	
	84.0(2)	0.9969(6)	
	109.2(2)	0.9983(6)	
	381.6(2)	0.9995(6)	
^{198}Au	411.8020(2)	0.9954(7)	0.998(5)

Among the different corrections described in this Section, it is important to remark the small values of F$_{abs}$ related to the use of thin targets and backings. Even for a γ-ray energy as low as 42 keV, the correction does not exceed 2% and is below 0.5% for the main decay line of 84 keV. This improves significantly the situation with respect to 47% correction for the same line the activation measurement carried out by Genreith et al. [36].

4.1.5 Results and uncertainties in the activation analysis

The thermal capture cross section of ^{242}Pu was obtained relative to that of ^{197}Au using Eq. (4.8) for each of te different ^{243}Pu decay lines. (42, 67, 84, 109 and 382 keV). The

results summarized in Table 4.6 show and excelent agreement between the different lines studied, except for that of 67 keV, which affected by a 50% uncertainty due to the transition intensity, has been excluded from the weighted average. The individual sources contributing to the final uncertainties in Table 4.6 can be splitted into two groups: common to all the lines and γ-ray line dependent.

Table 4.6: *Values for the thermal capture cross section of ^{242}Pu obtained by means of activation using the new value for the reference line intensity 0.192(10), obtained by Leconte et al. [136].*

$\mathbf{E_\gamma}$ **(keV)**	σ_{th} **(b)**
41.8	17.9(21)
84	18.0(14)
109	21(3)
381.6	19.5(17)
Weighted Average[a]	**18.7(9)**

a) Line excluded from the average due to the large uncertainty in the decay intensity (50%).

The first group is dominated by the uncertainties in the ^{242}Pu mass (3%) and inhomogeneity (4%) (discussed in Section 3.3.1), and the 2.2% uncertainty in the normalization to Au associated to the difference between the results of the two measurements of the activated ^{197}Au target. The additional common sources of uncertainty are associated to the statistics in the analysis of the 411.8 keV line from ^{198}Au (0.15%), the uncertainty in its absolute intensity (0.06%), that of the efficiency (1.3%), and last the F_{abs} and F_{geom} corrections (0.5% combined) for both, the ^{242}Pu and ^{197}Au samples.

Table 4.7: *Individual sources contributing to the final uncertainty of the thermal cross section measured by means of activation analysis in this work. The uncertainties in this table are common to all the analyzed ^{243}Pu decay lines.*

Source of uncertainty	**Uncertainty (%)**
Peak integral Au	0.15
Peak intensity Au	0.06
Peak efficiency Au	1.3
Efficiency correction Au	0.5
Mass Au	0.10
Normalization Au	2.2
Efficiency correction Pu	0.5
Inhomog. Pu target	4.0
Mass Pu	3.0
Overall *common*	**6**

The energy-dependent uncertainties, presented in Table 4.8 are clearly dominated by the uncertainty on the decay intensities, which ranges from 5.2 to 11% (excluding the 67 keV line). The statistical uncertaintyis below 3% for all thelines and is only 0.5% for the

main one at 84 keV. Last, the uncertainty in the efficiency ranges from 1.3 to 1.8%. The overall uncertainty in the cross section for each line is also presented in Table 4.8.

Table 4.8: *Individual statistical and systematic uncertainties for the ^{243}Pu decay lines analyzed in the activation measurement.*

Relative uncertainties (%)					
E_γ (keV)	**Stat.**	**Intensity**	**Efficiency**	***Common***	**TOTAL***
41.8	1.9	10	1.8	6	12
84	0.5	5.2	1.5	6	7.9
109	2.9	11	1.4	6	13
381.6	2.0	6.6	1.3	6	9.0

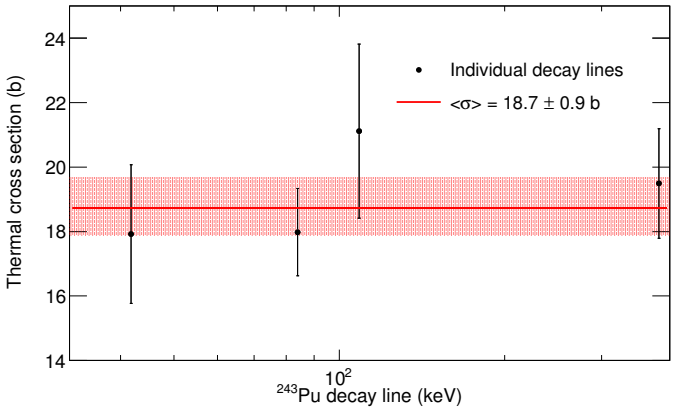

Figure 4.6: *Thermal capture cross section values obtained from the analysis of the four most intense lines of the produced^{243}Pu nuclei. The weighted average is indicated as a solid line and the shadowed corridor represents the standard deviation of the individual values, assumed as the final uncertainty.*

The four cross section values extracted using the lines with accurate relative intensities (42, 84, 109 and 381 keV), summarized in Table 4.8 and displayed in Figure 4.6, are in agreement within a standard deviation of 0.9 b, below the uncertainties of each line individually. Thus, this standard deviation can be assumed as the final uncertainty in the result. The weighted average of the four analyzed lines $\sigma_{th} = 18.7(9)\ b$, indicated with a solid line in Figure 4.6, is considered the final value for the activation measurement. It must be emphasized at this point that if the value for the intensity I_{84}= 0.230(20) reported in ENSDF [19] was used a 20% lower value would resul, which is significantly below all the previous experimental results and thus discarded.

4.2 The ^{242}Pu Prompt Gamma analysis

4.2.1 Spectrum analysis and background subtraction

As we introduced in Section 2.5.2, the capture cross section can be determined by detecting the γ-ray cascade emmited by the compound nucleus after a neutron capture. In particular, the same detection set-up used for PGAA measurements (see Section 3.4) can be used to carry out high-resolution measurements of the capture cascade spectrum aiming at determining the associated capture cross section.

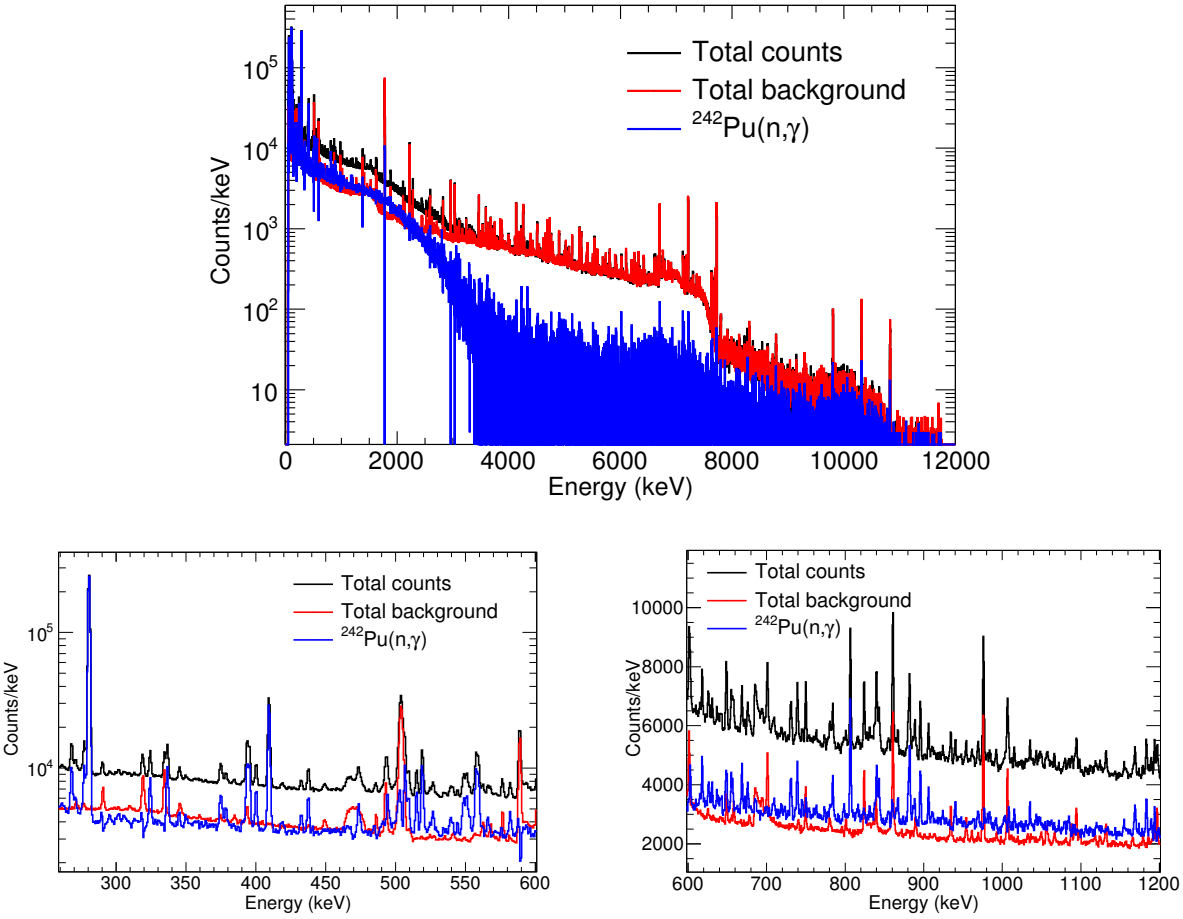

Figure 4.7: *Top left: Total counting rate (black) registered by the HPGe as a function of the deposited γ-ray energy in the full energy range up to 12 MeV. The red curve shows the total background while the blue line is the background-subtracted response to the ^{242}Pu(n,γ) cascade. The bottom panels zoom into different energy intervals to the enhancement of the peak to continuum ratio in the background-subtracted ^{242}Pu spectrum.*

In this work two ^{242}Pu samples and several ancilliary samples for background assesment purposes were irradiated in the PGAA beamline (see Table 3.4) and the compton-unsupressed prompt γ-ray spectra were recorded with the detection set-up described in

Section 3.4. The spectrum of the ^{242}Pu sample #2 was found to be completely dominated by the prompt γ-rays following the captures in the Au sample used as a neutron monitor for the activation analysis and hence it has not been considered in this analysis.

The pulse amplitude spectra obtained with the MCA are first corrected in channels for the small non-linearity of the system (see Section 3.4) and, in a second step, linearly calibrated in energy using two characteristic peaks of each spectrum with well known energies (e.g. Al: 1778, 7725 keV).

The top left panel of Figure 4.7 shows in black the total Compton-unsupressed counts as a function of the deposited energy during the irradiation of ^{242}Pu sample #1. The total measured counts include, together with the ^{242}Pu(n,γ) spectrum, several background contributions (red curve) related to neutron captures on the target backings (Al and Ti) and around the experimental set-up. This background was assesed with different ancilliary measurements summarized in Table 3.4, and the subtracted (see blue line). The lower pads of Figure 4.7 zoom into the energy ranges between 200 and 600 keV and 600 to 1200 keV to better appreciate the complete suppression of the background peaks and the ehancement of the ^{242}Pu(n,γ) peaks in the background-subtracted spectrum. From Figure 4.7 one concludes that the contribution of the ^{242}Pu(n,γ) is higher or at the same level of the background up to about 2000 keV, while beyond 3500 keV the data are completely dominated by the background.

The background in the PGAA measurement of ^{242}Pu Sample #1 presents different origins and for this reason different measurements were carried out to properly substract it from the histogram of total measured counts. The individual contribution of each background component is displayed in Figure 4.8 together with the total background in our measurement. The normalization factor for each background contribution was calculated to completely remove the main background peaks and achieve a flat counting rate fluctuating around zero above the neutron separation energy of ^{243}Pu (S_n = 5034 keV). In the bottom left panel of Figure 4.8 we zoom into the energy interval from 0 to 800 keV. In this energy range, the *Empty* background (i.e. related to neutron captures in the irradiation chamber and the experimental set-up) dominates the background. In the bottom right panel of Figure 4.8, we show the energy range from 1600 to 2400 keV, where most of the large peaks (up to 7 MeV) are prompt and decay γ-rays following the neutron captures in the Al backings. Above 7 MeV, the *Empty* dominates again, showing characteristic peaks of different elements such as N from air, Fe, Al and Ge, that expand up to 14 MeV. In Figure 4.8 we appreciate the presence of other relevant peaks coming from captures in the Ti coating. Last, a large 2.223 MeV peak associated to the neutron capture in H is also observed in the spectrum. Aiming at a complete subtraction of the latter, a polyethilene (CH_2) sample was measured.

The resulting background-subtracted response of the HPGe detectors to the ^{242}Pu(n,γ) cascades (blue curve in Figure 4.7) indicates that the major fraction of the capture cascade is below 3500 keV, as it is expected due to the small number of primary transitions. Above 4 MeV just a few weak primary transitions are observed, due to the fact that the initial state of the compound nucleus features a $J^P = 1/2^+$ while most of the low energy states of ^{243}Pu have high spins (7/2, 9/2, 11/2, 13/2, ...).

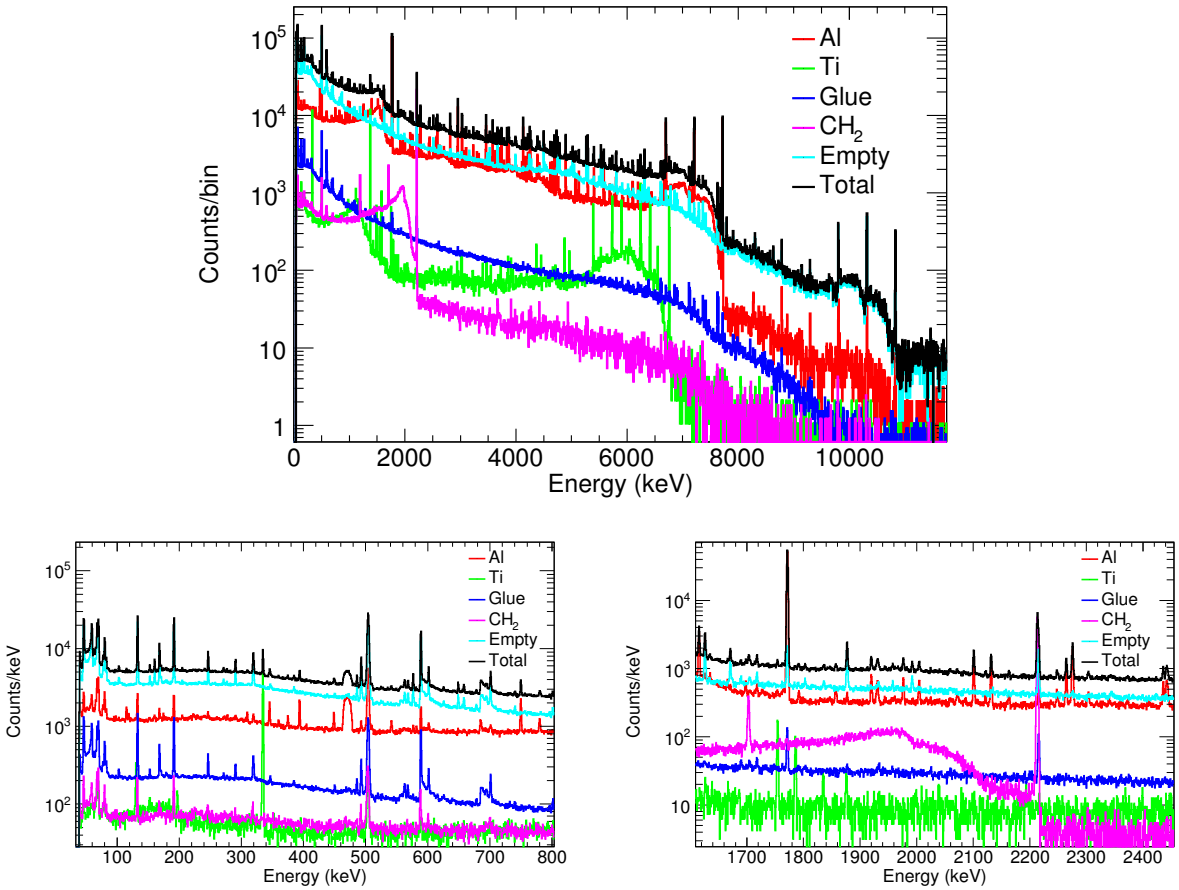

Figure 4.8: *Contribution of each ancilliary measurement to reproduce the total background in the PGAA measurement of the ^{242}Pu sample #1 (see Figure 4.7). The full spectrum is shown in the top pannel. The bottom pannels show different zooms into the energy ranges 0-800 keV and 1600-2400 keV.*

4.2.2 Partial γ-ray production cross section

The partial production cross section of a given γ-ray of the ^{242}Pu(n,γ) cascade, defined in Eq. (3.2), can be experimentally determined from the analysis of the spectrum of Figure 4.7. In this work, the partial production cross section for the main ^{242}Pu(n,γ) secondary γ-ray of 287 keV σ_{287} has been extracted with two different goals:

- Calculate the thermal capture cross section from the partial production cross section and its absolute intensity value per capture (see Section 4.2.3).
- Obtain the absolute normalization to cross section units for the calculation of the thermal capture cross section from the full γ-ray spectrum using the weighted sum rule (see Section 4.2.4) .

The peak areas in the background-subtracted prompt γ-ray spectrum of ^{242}Pu (Figure 4.7) were extracted usign the same fitting method than in the activation analysis.

From the extracted peak area A_i for a given line, the thermal partial γ-ray production cross section σ_i is given by

$$\sigma_i = F_{En}\frac{A_i^{\varepsilon}}{n\ \phi_{int}}, \tag{4.13}$$

where n and ϕ_{int} are the same than in Eq. (4.4), F_{En} is the correction for the non-thermal flux given by Eq. (4.10), and A_i^{ε} is the efficiency-corrected peak area, calculated for a given sample geometry and γ-ray energy as

$$A_i^{\varepsilon}(E_{\gamma,i}) = \frac{A_i}{\varepsilon(E_{\gamma,i})F_{abs}(E_{\gamma,i})F_{geom}}, \tag{4.14}$$

where $\varepsilon(E_{\gamma,i})$ is the energy-dependent detection efficiency shown in Figure 3.11, and $F_{abs}(E_{\gamma,i})$ and F_{geom} are the correction factors of the detection efficiency discussed in Section 4.1.4. For the case of the PGAA set-up, these corrections were also calculated by means of MC simulations using the Geant4 toolkit, taking into account the 30°-tilted orientation of the target with respect to the detector axis.

Following the same procedure than in the activation analysis, a relative measurement is desirable to remove any dependence on the integrated neutron flux over the irradiated surface ϕ_{int} in Eq. 4.13. From Eq. (4.13), the partial cross section for the i^{th} transition of the ^{242}Pu(n,γ) spectrum σ_i relative to a comparator peak yields

$$\sigma_i = \sigma_c\frac{F_{En}^{Pu}}{F_{En}^{c}}\frac{A_i^{\varepsilon}}{A_c^{\varepsilon}}\frac{n_c}{n_{Pu}}, \tag{4.15}$$

where σ_c is the partial production cross section for a well-known prompt transition from our comparator sample; n_{Pu} and n_c are the number of atoms per unit surface in the Pu and comparator samples.

The best option for the relative calculation of σ_i is an internal comparator (i.e. an element that is part of the sample), being the best option an homogeneous chemical compound with precisely known stochiometry [139]. However, this method is not applicable in our measurements due to the high purity of the ^{242}Pu deposits. Instead, a reference target irradiated together with the ^{242}Pu sample serves as a neutron flux monitor.

Table 4.9: *Sample thickness calculation for the two foils used as comparators for the calculation of the 287 keV γ-ray partial production cross section.*

Comparator	**Area (cm^2)**	**Mass (g)**	**Thickness (μm)**
Si	45.41(8)	3.9707(10)	375.4(7)
Al	12.136(4)	0.1259(10)	38.441(13)

The main requisits for a comparator are:

1. High accuracy in the sample thickness n(at/b).
2. Same dimensions than the sample of interest unless the latter is larger than the beam.
3. Prompt or saturated decay line for which σ_i is very well known (within 1-2%).

Our comparator was initially planned to be the Al target backings. However, this idea was discarded due to the uncertainty in the backing thickness. Another source of uncertainty in the calculation of σ_{287} is related to the mass and homogeinity of the ^{242}Pu deposits. Aiming at reducing these uncertainties three additional short measurements (indicated as *Mass Al backings* and *PGAA normalization* in Table 3.4) were carried out:

1. Al foil + Si wafer
2. ^{242}Pu sample #1 + Si wafer
3. ^{242}Pu sample #2 + Si wafer

The thickness of the two comparator samples (Al and Si) was determined with high accuracy from precise measurements of their mass and areas (see Section 3.9). The properties of these samples are summarized in Table 4.9. From these ancilliary measurements we obtained the following results:

- The thickness of the Al backings in the ^{242}Pu samples is accurately determined from the analysis of the Al/Si peak area ratio in measurements (2)-(3) with respect to measurement (1). The resulting value for both ^{242}Pu samples is compatible with a total thickness of the two Al foils of 23.10(10) μm, instead of the expected 20 μm [127].
- A set of different values for σ_{287} are obtained from the PGAA analysis of the two ^{242}Pu irradiated samples relative to different lines in the Al and Si prompt spectra.

The prompt γ-ray spectrum obtained in the irradiation of ^{242}Pu Sample #1 with the Si foil is shown in Figure 4.9. In this figure, the lines of interest have been labeled with the corresponding isotope. The energies of the analyzed lines for each sample and the corresponding correction factors F_{En}, F_{geom} and F_{abs} in Eqs. (4.14) and (4.15) are presented

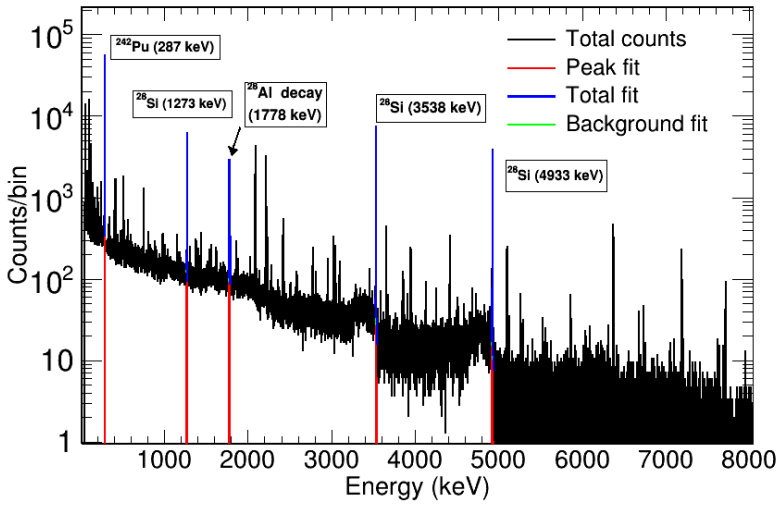

Figure 4.9: *Prompt γ-ray spectrum measured during the irradiation of ^{242}Pu sample #1 + Si comparator. The analyzed prompt γ-ray transitions originated in captures on ^{242}Pu, Al (target backings) and the Si comparator foil are labeled on the plot.*

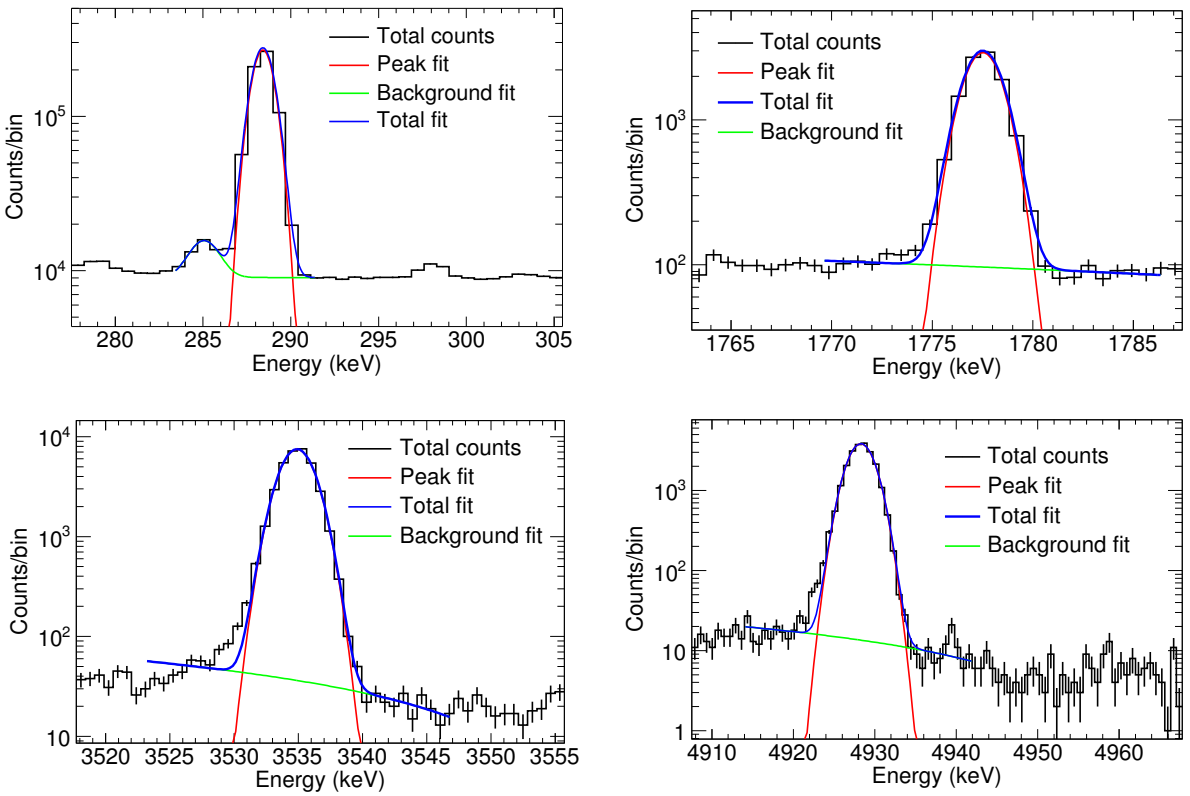

Figure 4.10: *Zooms on Figure 4.9 showing the fits of the main peaks in the PGAA spectrum acquired during the irradition of ^{242}Pu Sample #1 with the Si foil: ^{242}Pu (287 keV) (top left), Al (top right) and Si (bottom).*

in Table 4.10. All the studied lines belong to (n,γ) cascades with the exception of the saturated (i.e. number of decays is balanced with the produced nuclei) 1778 keV decay line of ^{28}Al . The saturation is reached after about 6 x $T_{1/2}$ of irradiation, i.e. 15 minutes for ^{28}Al. Figure 4.10 shows a closer view of the analyzed peaks to illustrate the quality of the fits.

The values of the partial production cross section σ_{287} calculated by means of Eq. (4.15) are presented in Table 4.11. This table includes the result obtained relative to three different peaks of the Si comparator from three different measurements of the ^{242}Pu samples. The uncertainties of the individual values in Table 4.11 combine statistical and systematic ones and are discussed in detail in Section 4.2.5.

A partial cross section of the main prompt γ-ray of $\sigma_{287} = 7.1(4)$ b compatible with all the individual values obtained in Table 4.11, is our final result. This value has been calculated as the weighted average of the individual values. This result will be used in the following to calculate the thermal capture cross section (see Section 4.2.3) assumming as valid the value for the absolute intensity of this line in the literature and to normalize the total cross section by means of the unfolding method (see Section 4.2.4).

Table 4.10: *Correction factors for each of the γ-ray lines analyzed in the PGAA spectra of ^{242}Pu, Al and Si. The uncertainties are due to counting statistics in the Geant4 simulations.*

E_γ (keV)	F_{abs}	F_{geom}	F_{En} **(JEFF-3.3)**
287 (^{242}Pu)	0.9990(7)	1.0130(3)	0.532
1778 (decay ^{28}Al)	0.9998(10)	1.0000(3)	0.525
1273 (^{28}Si)	0.9960(9)	0.9922(3)	0.525
3538 (^{28}Si)	0.9973(11)	0.9922(3)	”
4333 (^{28}Si)	0.9986(11)	0.9922(3)	”

Table 4.11: *Partial capture cross section for the 287 keV prompt γ-ray σ_{287} calculated relative to the partial cross sections σ_c of the most intense γ-rays from the (n,γ) reactions on a Si comparator. The results of three independent measurements of two different ^{242}Pu target are compared and the average partial cross section for each of them is shown in the last row.*

		σ_{287} **(b)**		
E_γ (keV)	σ^c **(b)**	^{242}**Pu (#1)**^{a}	^{242}**Pu (#2)**	^{242}**Pu (#1)**^{b}
1273	0.029	7.5(6)	6.9(5)	7.7(6)
3538	0.119	7.1(5)	6.5(5)	7.3(5)
4333	0.112	7.2(5)	6.8(5)	7.4(6)
	Partial average	**7.27(21)**	**6.74(20)**	**7.36(21)**
	Overall average		7.1(4)	

a) Short measurement for PGAA normalization relative to a Si comparator.
b) Long measurement without Si comparator. Indirect normalization to Si using the ratio of Pu/Al in b) over the value in a).

4.2.3 Capture cross section from the 287 keV line

In general, the partial γ-ray production cross section σ_i is a combination of atomic and nuclear constants and is given by Eq. 3.2. From this expression, the thermal capture cross section of σ_γ yields

$$\sigma_\gamma = C_{isot}\ P_\gamma\ \sigma_i, \tag{4.16}$$

where σ_i is the partial production cross section for a single line determined experimentally as described in Section 4.2.2 and C_{isot} becomes nearly one in highly enriched samples, such as our ^{242}Pu samples.

The main constrain to extract the thermal cross section using Eq. (4.16) is the limited accuracy of the values for the absolute emission probability per capture $P_{\gamma,i}$, that have to be measured in other experiments, for example relative to the β-decay if the product of the (n,γ) reaction is unstable.

For the case of the 287 keV line in the ^{242}Pu(n,γ) cascade, the latest value in ENSDF [19] for the emission probability is $P_{\gamma,287} = 0.41(7)$ [140]. This value was measured in 1976 by Carsten et al. in the Brookhaven National Laboratory (BNL) using 2.66 eV neutrons from the high flux beam reactor and 288 mg of ^{242}Pu. A value of $P_{\gamma,287}$ =0.496(67) was

obtained relative to the intensity of the 382 keV line from the decay of the produced ^{243}Pu nuclei [38]. The original value has been renormalized by 0.83(9) by the evaluators such that the absolute line intensity per ^{243}Pu decay of the 382 keV transition is 0.58(6)% [19].

A value of 17(3) b for the thermal capture cross section of ^{242}Pu is obtained using Eq. (4.16) and the production cross section $\sigma_{287} = 7.1(4)$ b obtained in this work (see Section 4.2.2). The sizable uncertainty is dominated by the 17% in the absolute intensity of the 287 keV line.

4.2.4 Unfolding method and weighted sum rule

The capture cross section of an isotope can be calculated from the full measured prompt γ-ray spectrum. independently of the value of the absolute emission probabilities of the single lines. Different methods have been discussed in the literature in the last years [141, 142, 143], based in the following approaches

1. Sum of all the transitions from the capture state (C) in the compound nucleus (primary transitions) to a final state f. This method applies only for nuclei with relatively simple decay schemes. The cross section is calculated as:

$$\sigma_{th} = \sum_{f=1}^{n-1} \sigma_{C\to f}(1+\alpha_f)(1+PCC_f) \tag{4.17}$$

2. Sum of all the transitions populating the ground state (g.s) (ground state transitions) from any initial state i . As in the previous method, this method can be used only for nuclei with simple decay schemes.

$$\sigma_{th} = \sum_{i=2}^{n} \sigma_{i\to g.s.}(1+\alpha_i)(1+PCC_i) \tag{4.18}$$

3. Weighted sum of all transitions (inverse Q-value formula). This method is more general and applies to any nuclei with resolved γ-ray transitons.

$$\sigma_{th} = \sum_{i} \frac{E_{\gamma,i}\sigma_i(1+\alpha_i)(1+PCC_i)}{S_n} \tag{4.19}$$

In the previous expressions, α_i and $(1+PCC_i)$ are, respectively, the internal conversion coefficient and pair conversion coefficients for the γ-ray energy $E_{\gamma,i}$ of the i^{th} transition. While the pair conversion coefficients are usually rather small and thus neglected, the internal conversion coefficients are a major correction in Method 2 and less relevant but still important for Method 3. Last, S_n represents the neutron separation energy of the compound nucleus.

From the available methods, the third option was chosen in this work due to the complex scheme of the decay from the capture state of ^{243}Pu (see Figures A.3 and A.5 in

Appendix A). In order to carry out the weighted sum given by Eq. (4.19), the compton-unsupressed and background-subtracted spectrum (see Figure 4.7) was transformed to 1 keV/bin and normalized to have an integral equal to unity. The resulting spectrum still contains the full detector response and thus it can not be corrected for the peak efficiency, hence in order to reduce the spectrum to full energy deposition events only, the unfolding method is applied.

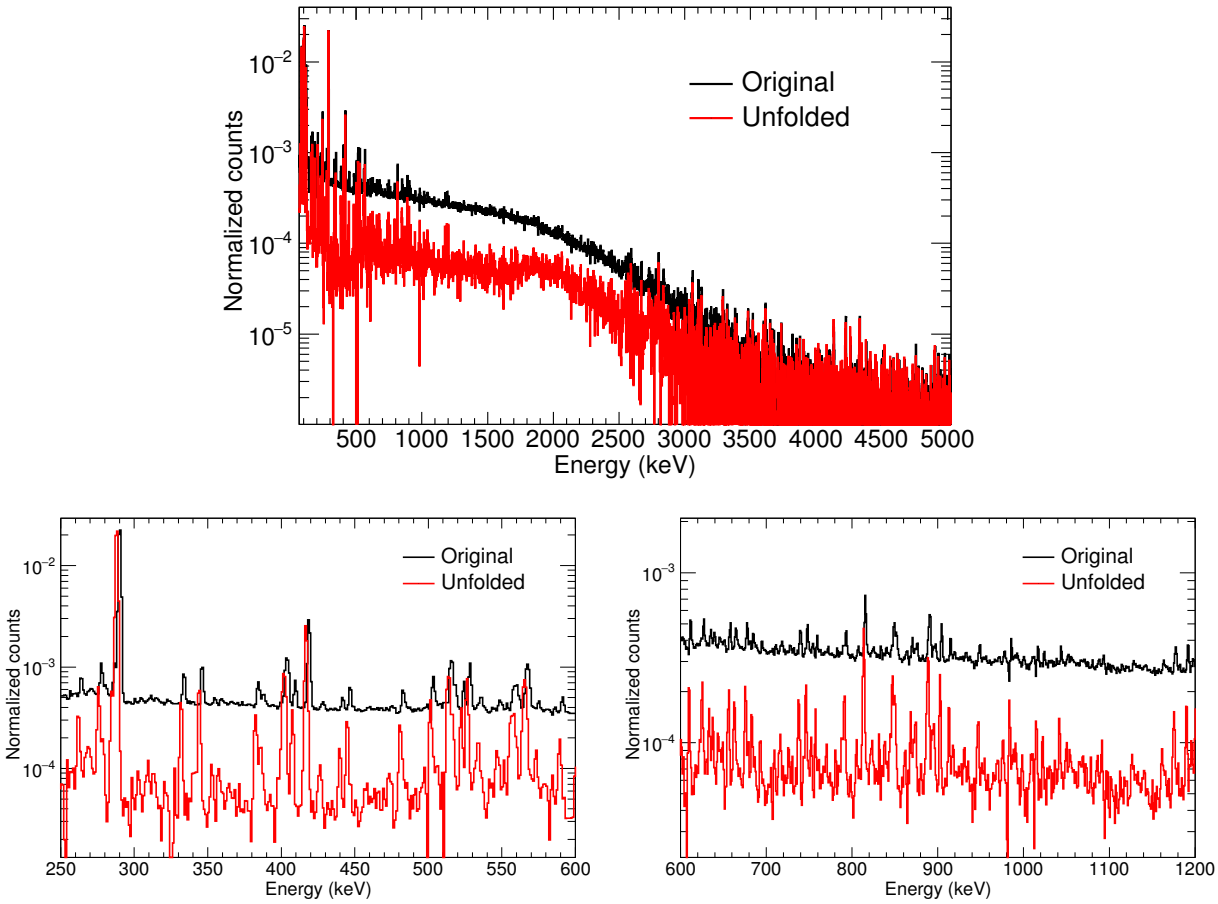

Figure 4.11: *Experimental background-subtracted $^{242}Pu(n,\gamma)$ spectrum (black) compared to the unfolded spectrum (red), where only the full energy deposition remains. The top panel shows the full energy range up to the neutron binding energy while the bottom panels zoom into different energy ranges. The integral of the measured spectrum was normalized to 1.*

The unfolding method (also known as stripping) is based on subtracting for each energy bin the full response function of the detector, with the exception of the full deposition peaks. The detector response to be subtracted is obtained by means of MC simulations of the detection set-up to monoenergetic γ-rays from 50 keV to 250 keV in steps of 50 keV and from 250 keV 12 MeV in steps progressively increasing from 250 keV to 1 MeV. The response functions extracted from the simulations, called node spectra, include the photopeak, the compton continuum, the single and double scape peaks and the annihilation peaks. The node spectra are normalized to unity and the full deposition peak is removed.

The unfolding procedure is an iterative process that starts assumming that the highest energy bin below the neutron separation energy corresponds to a full energy deposition. The unfolding is repeated for each energy bin until the lowest channel is reached, for which simulated responses are available. The energies in-between the simulated nodes are interpolated using the Oslo method [144]. For more details on the unfolding method and the simulations of the PGAA detection set-up the reader is referred to Ref. [145].

The impact of the unfolding on the spectrum is illustrated in the different panels of Figure 4.11, where it is illustrated how the unfolding succesfully removes the continous response between the full energy deposition peaks. The fact that some peaks in the unfolded spectrum present negative value is related to the different width of the single escape peaks, being treated by the unfolding as full energy peaks, though. Last, the remaining continuous structure between discrete transitions can be associated with the expected full energy deposition of transitions in the quasi-continuum.

In order to calculate the thermal cross section with Eq. (4.19), the unfolded spectrum has to be corrected for the efficiency and normalized to cross section units using the experimentally determined partial γ-ray production cross section σ_{287} (see Section 4.2.2). From the counts in the i^{th} bin of the unfolded spectrum C_i^{unf}, corresponding to a γ-ray energy $E_{\gamma,i}$, the partial γ-ray production cross section σ_i is calculated as

$$\sigma_i \;=\; F_\sigma \;\frac{C_i^{unf}}{\varepsilon_i \; F_{abs}(E_{\gamma,i}) \; F_{geom}}, \tag{4.20}$$

where ε_i is the absolute peak efficiency and $F_{abs}(E_{\gamma,i})$ and F_{geom} are the efficiency correction factors introduced in Section 4.1.4. Last, F_σ is the normalization factor to cross section units

$$F_\sigma \;=\; \frac{\sigma_{287}}{A_\varepsilon^{287}}, \tag{4.21}$$

obtained from the experimental value for the partial prodution cross section of the 287 keV γ-ray $\sigma_{287} = 7.1(4)$ b (see Section 4.2.2). In Eq. (4.21), A_ε^{287} represents the efficiency-corrected 287 keV peak area given by Eq. (4.14).

Once the unfolded spectrum is transformed to a histogram containing in each bin the partial production cross section σ_i for the corresponding γ-ray energy, addittional corrections are required before proceeding to calculate the cross section. This corrections affect mainly the low γ-ray energy range:

- Remove (mainly below 200 keV) the characteristic X-rays of Pu, emmitted as a consequence of the internal conversion, and the 60 keV line from the small ^{241}Am traces.
- Correct for the missed γ-rays associated to the internal conversion (IC) process, as described in the following.

The internal conversion coefficients α_i in Eq. (4.19), are strongly dependent on the γ-ray energy and the multipolarity of the transition [146] as it is shown in Figure A.6 in Appendix A. In this figure one appreciates that for a heavy element, such as Pu, the

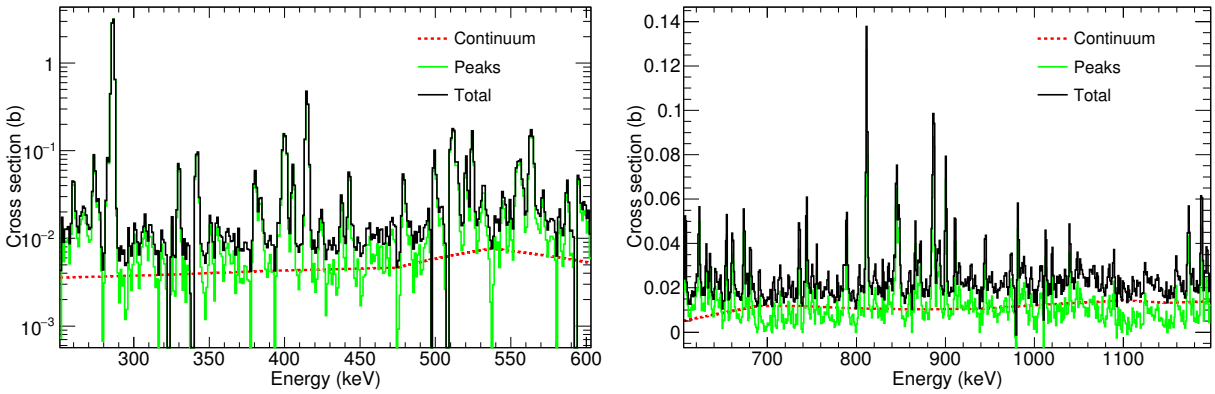

Figure 4.12: *Partial cross section as a function of the γ-ray energy showing the contribution of the continuum (fitted with splines to the valleys between peaks) and the discrete transitions in the energy ranges from 250 to 600 keV (left panel) and from 600 to 1200 keV (right panel).*

correction for internal conversion is very significant ($\alpha_i > 10\%$) for energies as high as 700 keV.

However, the multipolarity is unknown for the vast majority of the secondary γ-rays of ^{243}Pu [19]. Therefore, an statistical approach was followed to calculate the IC correction. First, the discrete transitions below 1500 keV (i.e. peaks) were separated from the continuum as it is shown in Figure 4.12. In this figure one appreciates that the continuum accounts for a significant part o the total cross section. The contribution of the continuum increases for higher γ-ray energies. Indeed, peaks are difficult to identify above 1500 keV and thus the full spectrum has been considered continuum beyond this energy.

The IC correction was calculated under the following assumptions:

- An E1 multipolarity was assigned to the continuum (GEDR) [147] and the peaks above 1500 keV.
- For the transitions with unknown multipolarity: a mixing M1 (50%) and E2 (50%) multipolarities below 1500 keV since no information on the multipole mixing ratios is available. This assumption is based on the fact that the contribution to the electromagnetic transitions (γ-rays + conversion electrons) in the low energy level scheme is mostly between positive parity states for medium heavy and heavy nuclei.
- For the transitions with known multipolarity. The final IC correction for the discrete transitions combined the statistically determined coefficients with the ones in the literature for the transitions with known multipolarity.

Figure 4.13 shows in two different panels, the IC-corrected partial cross section spectrum up to 400 keV. In this figure, the result obtained for the IC correction assumming the purely statistical method (red) is compared to the result with the final IC correction that uses the value for α in ENSDF for the transitions with known coefficients (black). The blue boxes in the plots highlight the peaks with known α coefficients and their height corresponds to the value of α. This comparison shows that the IC correction is under- or

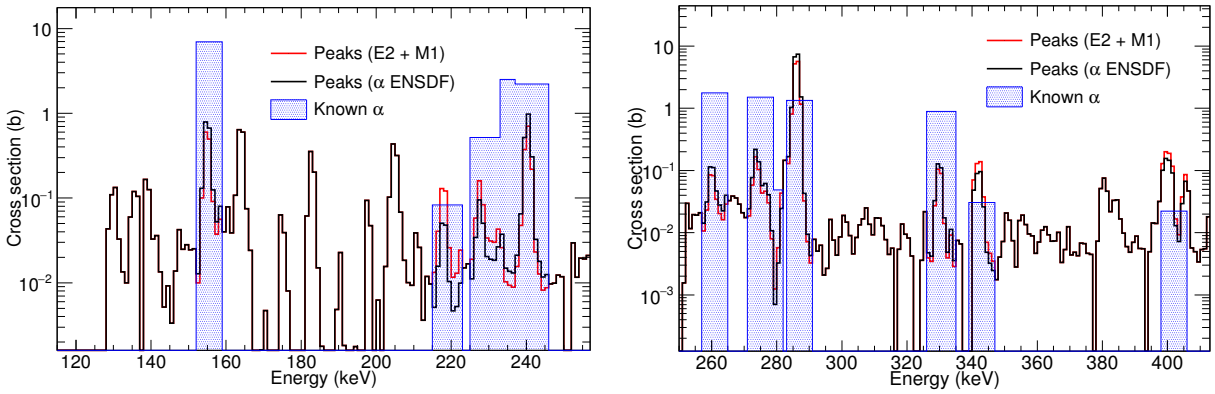

Figure 4.13: *Partial γ-ray production cross section corrected for the internal conversion (IC) in the energy ranges from 100 to 250 keV (left) and from 250 to 410 keV (right). For the transitions with known multipolarity (blue shadowed areas), the correction for IC assuming a statistical mixing (50% M1+ 50% E2) (red) is compared to the one obtained with the real value of α (black).*

overestimated by the statistical method depending on the transition. Overall, the difference in the final cross section obtained with the purely statistical and the combined IC correction methods provides the order of magnitude of the systematic uncertainty associated to the IC correction.

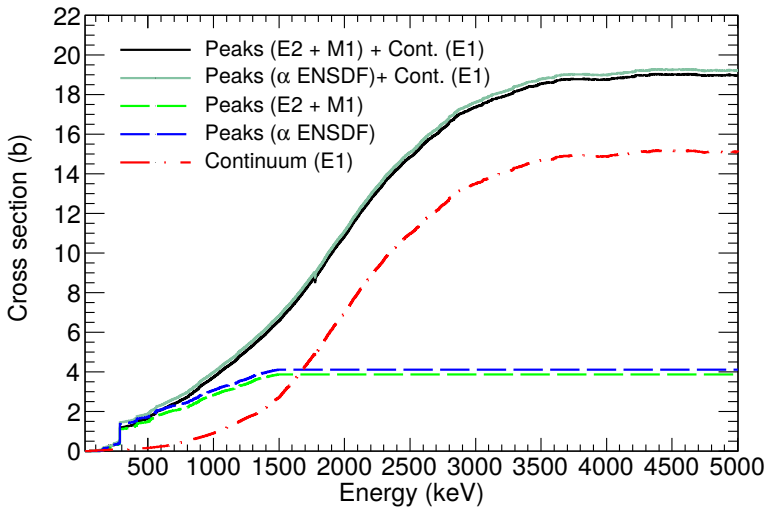

Figure 4.14: *Cumulative capture cross section calculated with the weighted running sum of the spectrum of partial γ-ray production cross section. The contribution of the continuum and peaks are shown separately. For the latter, two approaches for the internal conversion correction are compared (see text for details).*

The cumulative capture cross section as a function of the γ-ray energy is shown in the bottom panel of Figure 4.14. In the calculation shown in this figure, the weighted running sum (Eq. (4.19)) was carried out from 50 keV up to the neutron separation energy. The contribution of the continuum and the peaks to the total capture cross section are shown

Table 4.12: *Thermal capture cross section obtained by means of the energy-weighted sum rule of the unfolded prompt γ-ray spectrum. The contributions of the continuum and the discrete transitions have been computed separately due to the different internal conversion (IC) correction. The final result is obtained from the sum of the contribution of the continuum and the peak contribution corrected with the combined approach (i.e. real α if known and statistical mixing for the rest).*

Contribution	**IC correction**	**Cross section (b)**
Continuum	Stat. (E1)	15.1
Peaks (<1500 keV)	Stat. (E2 + M1)	3.9
Peaks (<1500 keV)	α known + stat.	4.1
TOTAL		**19.2(13)**

separately in this plot. In order to estimate the uncertainty associated to the statistical assignment of multipolarities, the result of the purely statistical M1 and E2 mixing has been compared to the combined method, in which the statistical assignment of multipolarities is replaced by the real conversion coefficients for the transitions with known multipolarity.

The final results of the cross section obtained by means of the unfolding procedure are summarized in Table 4.12. The final value for the capture cross section is 19.2(13) b, from which the continuum accounts for 15.13 b and the discrete transitions (just below 1500 keV) for the remaining 4.11 b. The overall uncertainty in the thermal capture cross section obtained by this method is dominated by that of the normalization factors (i.e the production cross section for the 287 keV γ-ray obtained in Section 4.2.3). Section 4.2.5 deals with the discussion on the uncertanties of both the partial cross section and the unfolding and weighted sum methods.

4.2.5 Uncertainties in the PGAA analysis

Two different methods have been used to calculate the cross section from the PGAA data, both using the partial production cross section of the 287 keV prompt γ-ray σ_{287}. Thus, we first need to evaluate the uncertainties in the calculation of this quantity. These can be splitted in two different groups, using a similar criterion than in the activation analysis:

- Sources of uncertainty which are indepent of the choice of comparator (i.e. related only to the single-line analysis of the ^{242}Pu(n,γ) sprectrum).
- Comparator/energy-dependent sources of uncertainty.

The uncertainties included in the first group are summarized in Table 4.13. The largest sources of uncertainty in this table, such as ^{242}Pu sample mass and homogeinity, are common to the ones in the activation analysis (see Section 4.1.5). The remaining common uncertainties, including the statistical uncertainty of the 287 keV peak area or the efficiency corrections, are below 1%.

On the other side, the uncertainties depending on the sample and γ-ray transition used as a comparator in the calculation of σ_{287} are presented in Table 4.14. This table includes

Table 4.13: *Individual uncertainties in the calculation of the partial γ-ray production cross section the 287 keV line of ^{242}Pu. The uncertainties in this table are independent of the comparator used in the calculation.*

Source of uncertainty	**Uncertainty (%)**
Peak integral Pu	0.2-0.7*
Efficiency Pu peak	1.3
Efficiency correction Pu	0.1
Inhomog. Pu target	4.0
Mass Pu	3.0
Total common uncertainty	**5.1**

**) A statistical uncertainty of 0.2% is achieved in the long measurements while for the short measurements it increases up to 0.7%.*

Table 4.14: *Comparator-dependent uncertainties for the different lines used to monitor the neutron flux in the calculation of the partial γ-ray production cross section the 287 keV line of ^{242}Pu. The last column presents the total relative uncertainty (including the common uncertainties in Table 4.13) and corresponds to the uncertainties in Table 4.11.*

	Relative uncertainties (%)					
E_γ (keV)	**Thickness**	**Stat.**	σ_c	**Efficiency**	**Corrections**	**TOTAL**
1778 (Al)	0.05	0.27	1.3	1.28	0.09	7.4
1273 (Si)	0.2	0.72	1.9	1.27	0.09	7.5
3538 (Si)	0.2	0.54	1.7	1.39	0.11	7.5
4333 (Si)	0.2	0.67	2.0	1.39	0.12	7.6

the statistical uncertainties and several systematic uncertainties associated to the thickness of the comparators (Table 4.9), the correction factors F_{En}, F_{abs} and F_{geom} (Table 4.10), the partial cross section of the comparator lines σ_c and the detection efficiency.

The uncertainty in the final value $\sigma_{287} = 7.1(4)$ b (5.2%) was estimated as the standard deviation of the individual values in Table 4.11 and is smaller than the total uncertainties in Table 4.14 (7.4 - 7.6%). This result is an indication of the compatibility of the different independent values of σ_{287} determined from different ^{242}Pu(n,γ) measurements relative to different compators.

Using the experimentally determined value of σ_{287}, two different methods were used to extract the thermal capture cross section of ^{242}Pu. First, taking the value for the absolute emmission probability $P_{\gamma,287}$ for the 287 keV γ-ray [140], Eq. 4.16 leads to a result of σ_{th} =17(3) b (see Section 4.2.3). The finaly uncertainty of this approach (18%) accounts for the the uncertainties in σ_{287} and in $P_{\gamma,287}$, being clearly dominated by 17% uncertainty in the latter.

The second method (see Section 4.2.4) combines the unfolding technique with the inverse Q-value rule (Eq. (4.19)) to calculate the cross section. The different sources of uncertainty associated to this method are listed in Table 4.15. First, the uncertainty associated to the

multipolarity assignment in the IC correction is around 0.24 b, according to the difference between the purely statistical method (19.0 b) and the final result (19.24 b) with the combined approach. This uncertainty (1.3%), combined with the statistical uncertainty in the background-subtracted spectrum propagated to the weighted sum (3.7%) and the uncertainty in the normalization factor F_σ (5.2%), leads to the total uncertainty of 6.5% displayed in Table 4.12.

Table 4.15: *Individual sources contributing to the final uncertainty of the thermal cross section measured by means of the unfolding method combined with the weighted sum rule.*

Source of uncertainty	**Uncertainty (%)**
σ_{287}	5.2
Correction IC	1.3
Statistical unc.	3.7
TOTAL UNCERTAINTY	**6.5**

4.3 Thermal capture cross section of ^{242}Pu at BRR

4.3.1 Combination of the results from the three methods

The succesful measurements and the analysis described throughout this chapter have lead to three independent values for the thermal capture cross section of ^{242}Pu:

- Activation: Capture cross section from the decay of the produced ^{243}Pu (using the value of Leconte [136] for the intensity of the 84 keV decay) relative to the capture cross section of ^{197}Au. **[18.7(9) b]**
- PGAA single-line: Total capture cross section from the partial cross section of the most intense ^{242}Pu(n,γ) secondary γ-ray of 287 keV and its absolute emmission probability. **[17(3) b]**
- PGAA unfolding method: Total capture cross section using the energy-weighted sum rule with internal calibration applied to the unfolded ^{242}Pu(n,γ) spectrum (i.e. only full energy deposition). **[19.2(13) b]**

The deviation between the unfolded and the othe two methods suggests that the absolute intensity of the 287 keV line may be overestimated. Indeed, the ratio of the partial cross section for this transition relative to the total cross section provides an experimental value for the intensity $P^{exp}_{\gamma,287} = 0.370(14)$, 10% below the most recent value in the literature, 0.41(7) [140], but compatible within the uncertainty.

The nice agreement between the three experimental values for the thermal capture cross section of ^{242}Pu, shown in Figure 4.15, yields an average cross section value of σ^{avg}_{th}=18.8(7) b.

4.3.2 Comparison to previous data and evaluations

In Figure 4.15 we summarize all data available in EXFOR [18] in chronological order, the values present in the current evaluated libraries (which differ from each other by up to 15%) and the results from this work.

From the results in Figure 4.15, one concludes that the weighted average of the values for the thermal capture cross section in this work presents an excellent agreement with the previous measurements from Butler et al. [32], Durham et al. [33] and Bendt & Journey [34]. On the other hand, the large value of Marie et al. [35] (using the same technique than Durham and Butler) can be regarded as an outlier with respect to to all other measurements.

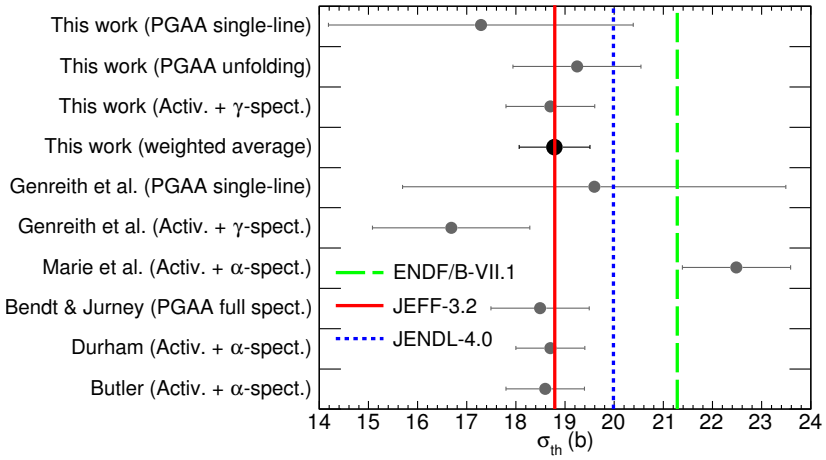

Figure 4.15: *Thermal capture cross section values obtained in this work by means of PGAA and activation followed by γ-ray spectrometry compared to the previous experimental values and the recommended values in JEFF-3.2 (red solid), ENDF/B-VII.1 (green dashed) and JENDL-4.0 (blue dotted).*

The value obtained by means of activation by Genreith et al. [36, 37] was discarded by the authors in their publication due to its small value (see Figure 4.15) and the large absorption corrections that could explain the significant deviation with previous results. In this work, the use of thin fission-like targets has reduced the absorption corrections to a negligible value. With this improvement we have shown that, if one uses the latest value for the intensity of the 84 keV decay line (0.192 vs. 0.23 used by Genreith et al.), the cross section value resulting from the activation analysis of Genreith would be 20.0(14) b compatible with our result (18.7(9) b) and all the previous experiments with the exception of the result by Marie et al.

The partial cross section obtained for the 287 keV prompt line $\sigma_{287} = 7.1(4)$ is 7% (1.5σ) below the 7.67(3) b reported by Genreith et al. in a very similar experiment in the same facility. From this value for the production cross section of this line, we obtained a total cross section $\sigma_{th}^{P,sl} = 17(3)$ b, 12% smaller than the 19.6(39) b of Genreith et al [36]. This deviation is related to the different result of σ_{287} combined with the 5% increase in the recommended value for the absolute emission probability of this γ-ray with respect to the

value used in their work $P_{\gamma,287} = 0.39(8)$ [39].

Regarding the evaluated values, the results in this work support the evaluated cross section in JEFF-3.2 (18.79 b) [20], while the ENDF-VII.1 evaluation (21.28 b) [21], that gives significantly more weight to the result by Marie et al. [35], seems significantly (13%) overestimated. The cross section in the JENDL-4.0 evaluation (19.98 b) [22] seems to be slightly (6%) overestimated as well.

The weighted average of all the available data sets in Figure 4.15, after renormalizing the activation result of Genreith with the new intensity, yields 18.8(4) b if we excludethe outlier of Marie et al. This value is in perfect agreement with the result in this work.

Part III

Experiment at n_TOF (1 eV to 500 keV) and data reduction

Chapter 5

Experimental set-up at n_TOF-EAR1

5.1 The n_TOF facility at CERN

5.1.1 Introduction to n_TOF

The n_TOF facility at CERN is a pulsed neutron source designed for high resolution neutron cross section measurements over a wide energy range. It was first proposed by C. Rubbia as high fluence spallation neutron source at the CERN Proton Synchroton (PS) accelerator [148] to measure neutron cross sections in the energy range from 1 eV to 250 MeV [149]. The location of the n_TOF facility within in the CERN accelerator complex [150] is shown in Figure 5.1, where one can see that along the CERN accelerator chain protons are injected also in other *low-energy* experiments such as ISOLDE, the Antiproton Decelerator (AD), the CLOUD experiment (East Area) and the AWAKE experiment.

The basic principles of the n_TOF facility were inspired in the knowledge acquired from the TARC experiment [151], devoted to transmutation studies for Accelerator Driven Systems (ADS). The first n_TOF facility consisted on a massive target of pure lead combined with a measuring station at 185 m and began its operation in 2000, finishing the first commissioning campaign in 2001 [152], and running physics experiments between 2001 and 2004 (n TOF-Phase1).

Since then, he n_TOF facility has been upgraded several times profitin of the CERN shutdownss in 2004/08 (LS1) and 2012/13 (LS2). During LS1 a new spallation target with improved cooling and a separated moderation circuit was installed. The change from water to borated water moderator reduced the thermal neutron flux and also the 2.2 MeV γ-rays from thermal capture on water, the main component of the γ-ray background that limited may of the measurements in Phase-1. During LS2, a new experimental area was built, located at 20 m vertically from the spallation target. At this shorter flight path, the flux increased by a factor of 40, allowing the measurement of low mass samples and highly radioactive targets [154, 94].

The aim of the n_TOF collaboration is to provide high-quality nuclear data, in partic-

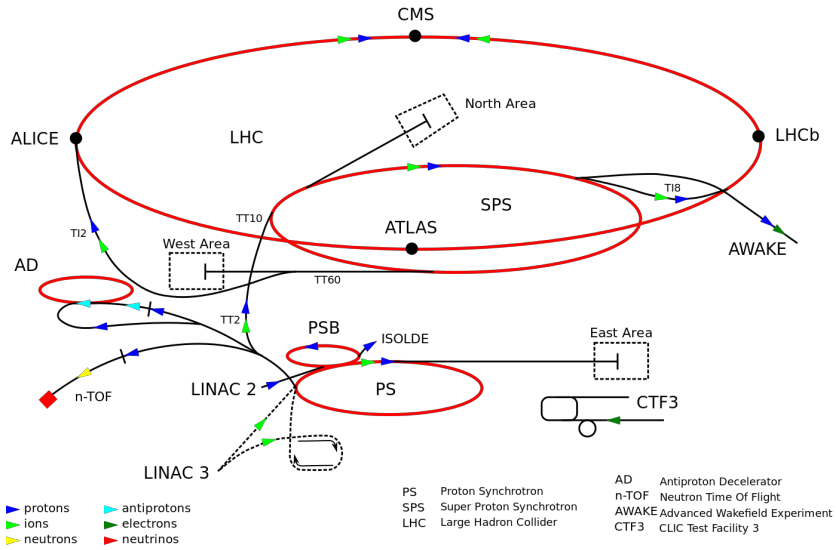

Figure 5.1: *Sketch of the CERN accelerator complex where protons are progressively accelerated in a succesion of machines before reaching n_TOF: Linac 2 (50 MeV), PS-Booster (1.4 GeV) and PS (25 GeV). The latter feeds the n_TOF experiment with proton bunches of 7ns (rms) at a maximum repetition rate of 0.4 Hz. From the PS, protons are injected in the Super Proton Syncrotron (SPS) (450 GeV) and finally transferred to the Large Hadron Collider (LHC) (6.4 TeV).*

ular neutron cross sections, for the design of Innovative Nuclear Systems, such as Gen-IV reactors [8, 76], new fuel cycles [155], incineration of nuclear waste with ADS [77, 11], nucleosynthesis studies related to the slow neutron capture process (s-process) or the Big Bang Nucleosynthesis [78, 79, 156] and medical applications [157], such as the Boron Neutron Capture Therapy [158, 159].

Along its 18 years of existence, the n_TOF experiment at CERN has grown as an international collaboration involving 124 members of 47 institutes of Europe, Asia and Australia (as of 2018). In these years, more than 100 measurements have been carried out, most of them have been published, and new measurements are ongoing. For an updated review of the nuclear data measurements at the n_TOF facility, the reader is referred to Refs. [160, 161].

5.1.2 Neutron production: the spallation target

Neutrons at the n_TOF facility are generated through spallation of 20 GeV/c protons extracted from the CERN PS (see Figure 5.1), impinging on a thick lead target. These proton bunches feature a nominal intensity of $7\text{x}10^{12}$ protons, a time spread of 7 ns (rms) and hit the target with a maximum repetition rate of 0.4 Hz, hence 10^{17} protons per day in average. The spallation neutrons produced in the lead block are partially moderated and travel along two beamlines towards the experimental areas (EARs): EAR1 at 185 m (horizontal) [93] and EAR2 at 18.5 m (vertical) [94].

The general view of the current spallation target (n_TOF Phase2) is shown in Figure 5.2.

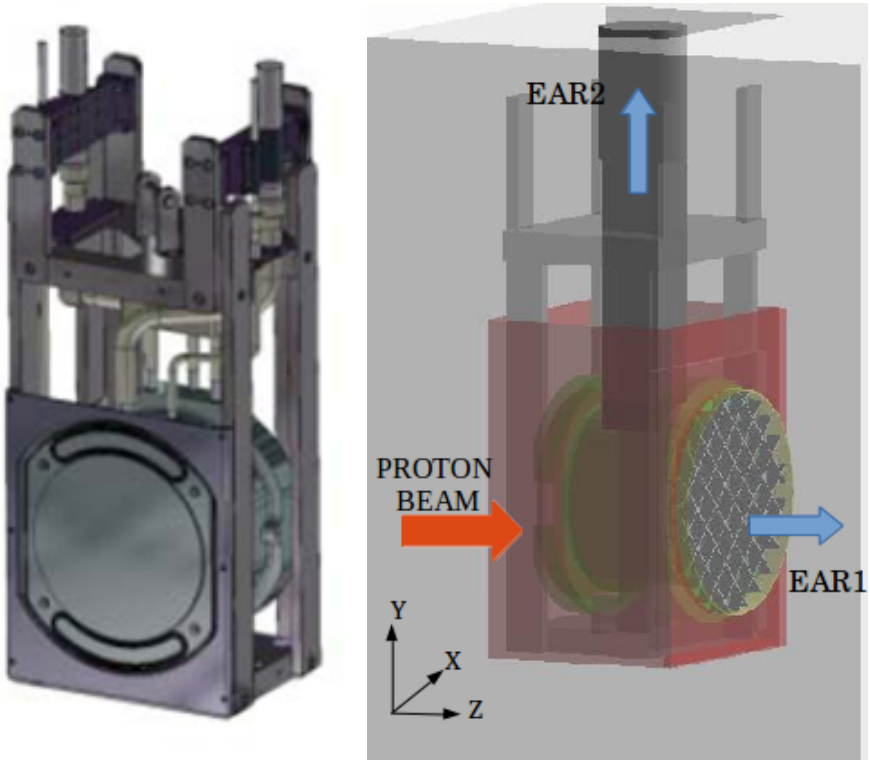

Figure 5.2: *General view of the spallation target geometry shown in a CAD drawing (left) and in a Geant4 geometry model (right), where we indicate direction of incidence of the proton bunche and the exit towards both EARs.*

In this figure we show a CAD drawing and the geometry as implemented in the Geant4 [137, 138] simulations of the n_TOF spallation target [162, 98], consisting on the target vessel, the surrounding structures, the concrete pit in which it is mounted and the beamline exits towards both experimental areas.

The inner structure of the spallation target is better illustrated in the exploded view displayed in Figure 5.3. The core of the spallation target is a cylinder 30 cm in radius and 40 cm in length made out of a lead alloy with a purity of 99.974%. The cooling circuit of the spallation target consists of a circulating layer of demineralized water 1.4 cm thick that surrounds the spallation volume. The water cooling also moderates the neutrons escaping in any direction. The target and water cooling are contained in a cylindrical vessel, made of the aluminum alloy AW5083.

The 20 GeV/c protons imping the spallation target with 10° with respect to the EAR1 beamline axis to reduce the background in the experimental area related to the forward-focused particles escaping the target. The spallation process is defined as the series of nuclear process that occur when a high energy (>150 MeV) light projectile collides with a nucleus and on average leads to the emission of a large number of particles, mostly neutrons, but also protons, pions, other light charged particles and any nuclei lighter than the target nucleus. The spallation process occuring at n_TOF can be described as a two-stage process [163]:

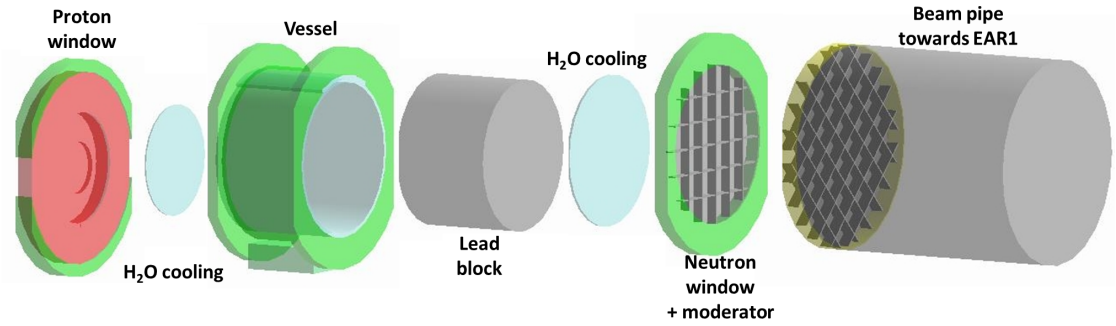

Figure 5.3: *Exploded-view of the various elements of the n TOF-spallation target implemented in the simulations.*

1. Intra-nuclear cascade: The protons react with nucleons inside the nucleus. The reactions that follow create an intra-nuclear cascade of high-energy (larger than 20 MeV) protons, neutrons, and pions within the nucleus. The high energetic hadrons can either escape as secondary particles and induce secondary spallation reactions or give their kinetic energy to the nucleus, leaving it in an excited state.

2. Nuclear de-excitation or evaporation: The excited nuclei de-excite emitting (evaporating) low-energy (less than 20 MeV) neutrons, protons, alpha particles, etc., with the majority of the particles being neutrons.

Each high energy proton generates about 300-400 neutrons with energies in the energy range from MeV to GeV. Figure 5.4 shows the energy distribution of the neutrons produced inside the lead block, showing the contribution of different particles to the neutron production. This results have been extracted from the Geant4 simulations of the n_TOF spallation target [162, 98]. The Intra-Nuclear cascades produce neutrons above 20 MeV while the evaporation is the origin of the dominant peak around 1 MeV. In Figure 5.4 one appreciates that proton induced production of neutrons dominantes only for high energy neutrons. The neutrons produced with energies below 500 MeV are originated mainly in neutron induced reactions. Pions, produced in the intra-Nuclear cascades, have also a relevant role in the balance between neutron and γ-ray production in spallation targets, as it is disccussed in Ref. [164].

In order to expand the energy spectrum in Figure 5.4 down to thermal energies (25.3 meV) to produce a white neutron beam, the neutrons escaping the target in the direction of EAR1 or EAR2 are partially moderated. Those exiting the target towards EAR1 travel through a 4 cm thick layer of borated water, contains 4.2 weight% of H_3BO_3, with a ^{10}B enrichment of 95%. For the case of EAR2, the neutrons emitted vertically are moderated in a layer of demineralized water with a thickness that varis from 1.5 to 3 cm. The details on the resulting neutron energy distribution in each EAR are described in Section 5.1.4.

The future target (Target #3), currently in its design phase, aims at solving some of the limitations of the present target, and has been chosen among different options according to the following conditions:

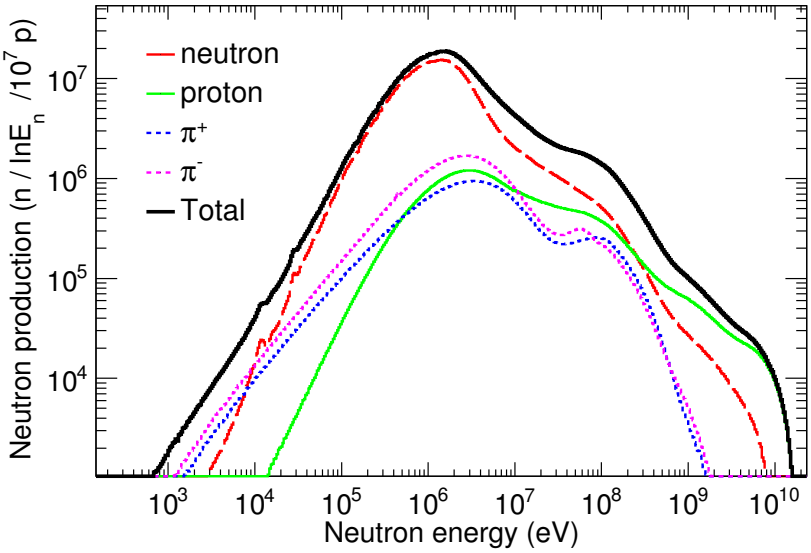

Figure 5.4: *Energy distribution of neutrons produced inside the lead spallation target as a function of the neutron-producing particle.*

- Maintain lead as the main component to preserve the good physics performances in terms of flux, spread of moderation times, γ-ray background (already highlighted in the design of the first spallation target [149]).
- Increase the maximum repetition rate and proton intensity per pulse to accomodate to the new capabilities of the CERN-PS.
- Eliminate the direct contact of lead and water to avoid erosion and corrosion and reduce the radiological issues during the dismantling of the target.
- Optimize the target towards EAR2: Include borated water in the moderator circuit, homogenous water and moderator thickness combined with a flat exit face to improve the Resolution Function (see Section 5.2.2) and increase the flux.
- Do not change the performance of EAR1 in terms of resolution or flux in a significant way.

This new target shall be installed during the CERN LS3 (2019/20).

5.1.3 Time-of-flight technique

Neutron pulses escape from the spallation target and travel trough the beamlines towards EAR1 and EAR2 every time a proton bunch impinges on the lead block. The neutron energies in each pulse expand over a wide range of energies from thermal to several GeV (EAR1) or hundreds of MeV (EAR2). As we introduced in Section 2.4.2, white neutron beams facilities (n_TOF [93, 94], GELINA [91], DANCE [95], ORELA [92], ANRI [96]) carry out either total cross section measurements by measuring the neutrons transmitted

across a sample, or reaction cross sections, where the products of the reactions are detected (this is the case for n_TOF). In these facilities the neutron kinetic energy is determined with high resolution for resolving the resonant structures and abrupt reaction thresholds typical of the neutron cross sections. The best solution to determine the kinetic energy of the neutron that produced a given reaction product (γ-ray, charged particle, fission fragment, etc...) is the time-of-flight technique,sketched in Figure 5.5.

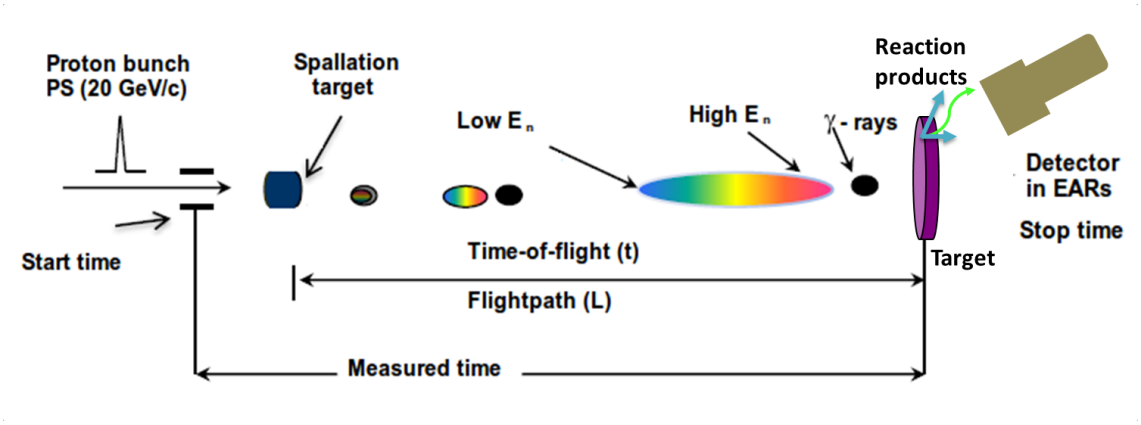

Figure 5.5: *Scheme of the basic principles of the time-of-flight technique.*

In the time-of-flight technique the kinetic energy of the neutrons is determined from their time of arrival at the measuring station. The kinetic energy E_n for neutron travelling with velocity v along the flight path L in a time t is

$$E_n = E - mc^2 = \sqrt{(pc)^2 + (mc^2)^2} = mc(\gamma - 1), \tag{5.1}$$

where $\gamma = (1-(v/c)^2)^{-1/2}$ is the Lorentz Factor. For neutrons below ~100 MeV, the first term of the Taylor expansion of Eq. 5.1 leads to the classical expression:

$$E_n = \frac{1}{2}mv^2 = K^2 \frac{L^2}{t^2}. \tag{5.2}$$

If t is expressed in μs, L in m and E_n in eV, the multiplication factor yields $K = 72.298 \frac{eV^{1/2}\mu s}{m}$. The time-of-flight t of a neutron arriving to one of the measuring stations is calculated from the time of the signal induced in the detectors by a reaction product t_m

$$t = t_m - (t_\gamma - L/c), \tag{5.3}$$

where t_γ is the measured time of arrival of the prompt γ-rays emitted in the spallation reactions, known as γ-flash (see Section 5.2.3), and L/c is the time-of-flight of these γ-rays. The sketch shown in Figure 5.5 illustrates the principles of this technique, showing that the prompt γ-rays arrive always before the neutrons and the neutron pulse expands in time and space as it travels along the beamline as a consecuence of the correspondingly different neutron velocities. For the particular case of n_TOF, Table 5.1 presents the time-of-flight correponding to different neutron energies for the short (EAR2, 19 m) and long (EAR1, 184 m) flight paths.

Table 5.1: *Correspondence between neutron Time-of-flight (TOF) and kinetic energy in EAR1 (184 m) and EAR2 (19 m).*

Neutron energy (eV)	TOF EAR1 (μs)	TOF EAR2 (μs)
10^{-2}	1.330x10^{5}	1.374x10^{4}
10^{0}	1.330x10^{4}	1.374x10^{3}
10^{3}	4.207x10^{2}	4.344x10^{1}
10^{6}	1.331x10^{1}	1.374
3x10^{8}	9.409x10^{-1}	9.716x10^{-2}
2x10^{9}	6.477x10^{-1}	-
TOF γ-rays	6.138x10^{-1}	6.338x10^{-2}

From Eq. (5.2) the relative energy resolution $\Delta E_n/E_n$ of the facility is given by

$$\Delta E_n/E_n \;=\; 2\,\sqrt{\left(\frac{\Delta t}{t}\right)^2 \;+\; \left(\frac{\Delta L}{L}\right)^2} \tag{5.4}$$

and thus the resolution improves as the flight path increases (L and t large) and the neutrons are produced within a short time window Δt and in a small source ΔL.

From Eq. (5.4), it is clear that EAR1, with a nine times longer flight path than EAR2, features a better energy resolution (see Section 5.1.4). On the other hand, the choice of a longer flight path compromises the neutron flux, which decreases approximately proportional to L^{-2}. Last, the time and spatial spread of the neutron production depends on the time width of the charged particle beam, the size of the spallation target and the moderator and the time scale of the moderation processes that lead to the final spectrum. These factors are reflected in a key magnitude in time-of-flight facilities, known as Resolution Function. This concept is discussed in detail in Section 5.2.2.

5.1.4 Beamlines and experimental areas

Two different beamlines connect the EARs with the spallation target: a 184 m horizontal one leading to the first experimental area (EAR1), a 19 m ome leading to the second experimental area (EAR2). Figure 5.6 shows and general view of the neutron beamlines at the n_TOF facility and indicates the main elements placed along them. The positions of the different elements shown in Figure 5.6 are summarized in Table 5.2.

Along both beamlines, a first collimartor removes the beam halo, then a magnet (electromagnetic in EAR1 and permanent in EAR2) deflects the charged particles in the beam, and a last collimator gives the desired shape to the neutron beams (see Refs. [93, 94] for more details).

Inside the experimental areas and along the beamlines, several detection set-ups can be installed in series. In particular, neutron beam monitors are always in place and the detection set-ups change depending on the experiment. The actual view of the experimental

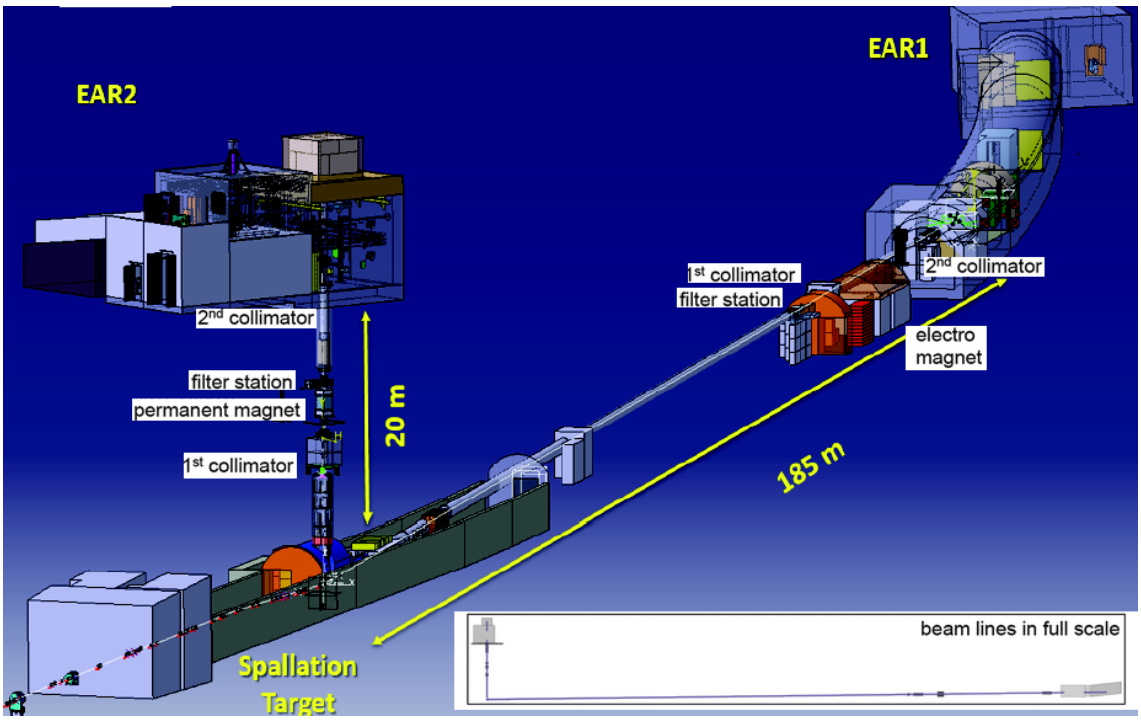

Figure 5.6: *Sketch of the n_TOF spallation target and the two flight paths that connect the neutron source with EAR1, the first underground experimental hall placed at 185 m, and EAR2 the new facility placed on the surface 20 m above the target.*

Table 5.2: *Beamline elements at the n_TOF facility and distance (m) of each component to the center of the spallation target.*

Beamline elements	**EAR1**	**EAR2**
1^{st} collimator	136.7 - 138.7	7.4 - 8.4
Filter box	134.9	11.4
Magnet center	145.4	10.4
2^{nd} collimator	178.0-180.5	15.04-18.04
Experimental area	182.3-190.2	18.16-23.66
Beam dump	200	24.73

areas is shown in Figure 5.7. Both experimental areas are currently certified as Work Sector Type A, with a series of safety and monitoring systems, in order to allow measurements of high-activity samples without certified sealing. This key upgrade was essential to enhance the capabilities of the facility.

The main features of the neutron beam in each experimental area are summarized in Table 5.3, and Figure 5.8 shows the energy distribution of the neutron flux in EAR1 with different moderators is compared to the flux in EAR2. In this figure, one appreciates that the upper energy limit of the neutron spectrum is different in both areas due to the kinematics of the spallation reactions. The total number of neutrons per pulse arriving to EAR2 is about 10^7 n/pulse, about 20 times larger larger than in EAR1 (see Table 5.3). The

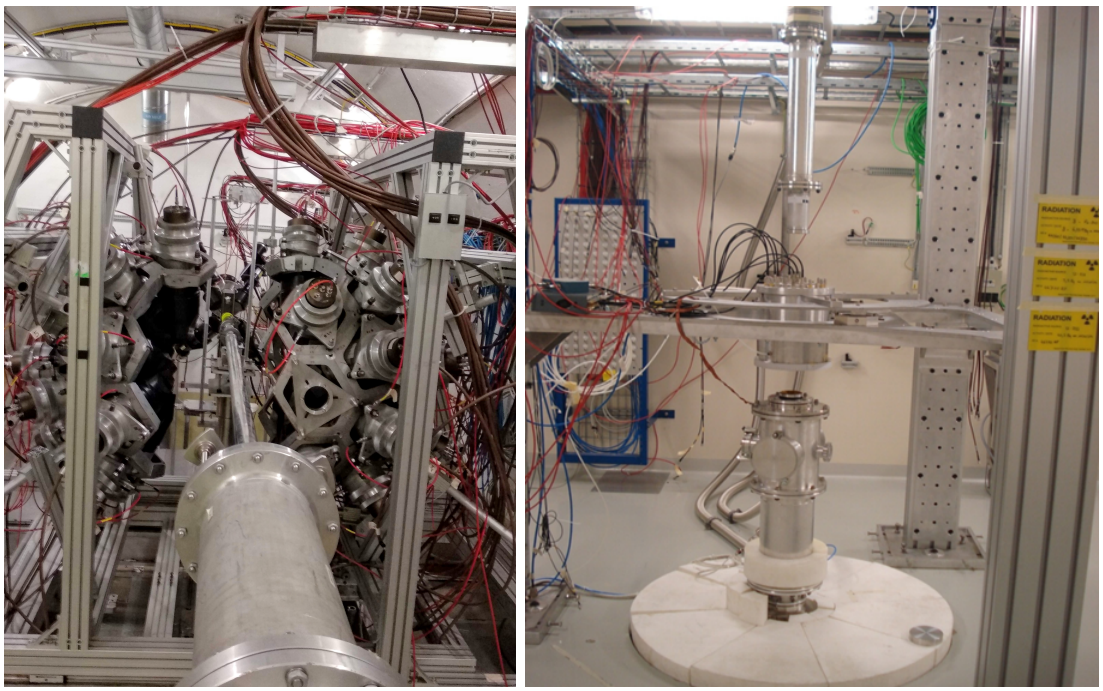

Figure 5.7: *Left: View of the horizontal beamline of EAR1 with the opened Total Absorption Calorimeter in the foreground and the C_6D_6 detectors in the background. Right: Vertical beamline in EAR2 with a set-up for a fission measurement based on a Micro-MGAS detector.*

ratio in neutron flux between both areas increases up to a factor ∼40 if we compare only the region between 10 eV and 100 MeV. Below 10 eV, where the borated water reduces significantly the thermal flux in EAR1, the flux in EAR2 becomes about 500 times higher. The sizable difference in flight path has also and effect in the energy resolution, which, as summarized in Table 5.3, is worse in EAR2; resulting in a limitation for resolving energies above a few tens of keV.

Table 5.3: *Main features of the neutron beams in the experimental areas of the n_TOF facility: nergy range, neutron flux, and energy resolution at different neutron energies.*

	EAR1	**EAR2**
Energy range	thermal to 10 GeV	thermal to 300 MeV
Neutron flux (full range)	5.5x10^5 n/pulse	1.1x10^7 n/pulse
Neutron flux (10 eV - 100-MeV)	n/pulse	^{7} n/pulse
$\Delta E_n/E_n$ (1 eV)	3.2x10^{-4}	4.8x10^{-3}
$\Delta E_n/E_n$ (1 keV)	5.4x10^{-4}	1.4x10^{-2}
$\Delta E_n/E_n$ (100 keV)	2.9x10^{-3}	4.6x10^{-2}

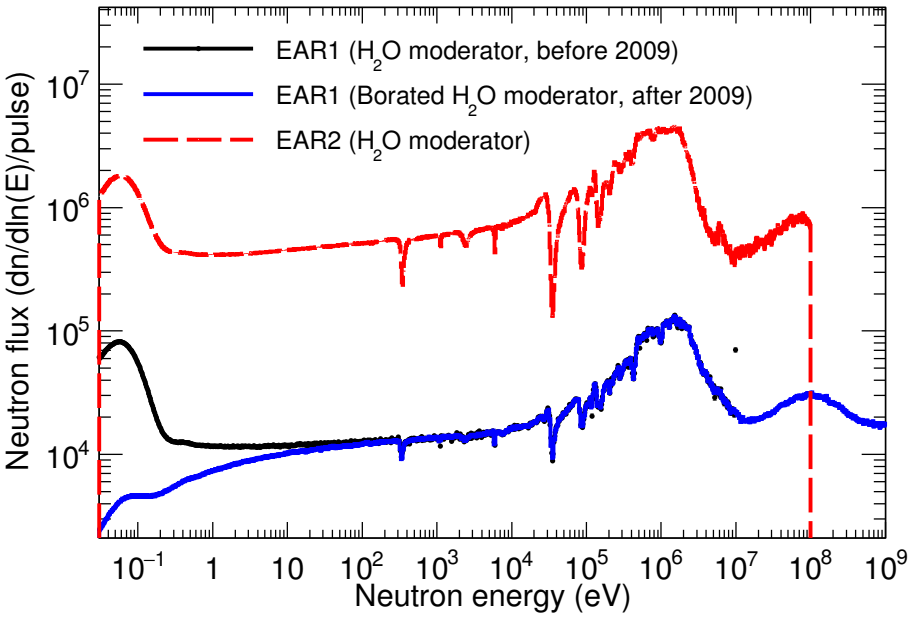

Figure 5.8: *Comparison of the measured energy distribution of the neutron flux in EAR1 and EAR2 with the current spallation target (since 2008). For EAR1 we compare the neutron flux before 2009 (pure water in the moderator) with the current flux (borated water instead). The abrupt cut at 100 MeV for EAR2's flux is related to the analysis and does not reflect the actual distribution.*

5.1.5 Neutron cross section measurements at n_TOF

Along the 17 years of experimental campaigns at n_TOF many different experimental set-ups have been used for experiments, which can be grouped according to the studied neutron induced reaction channels. Figure 5.9 summarizes the measurements carried out to date at n_TOF, illustrating with different colors the reaction channel and separating in blocks the measurements carried out with different detectors.

Capture (n,γ) measurements have been performed using either the Total Absorption Calorimeter (TAC) [111] or a set of C_6D_6 Total Energy detectors [165]. The TAC has also been used in combination with a MicroMegas detector in the first attempt to measure the capture measurements in fissile isotopes ^{235}U and ^{233}U reaction using a veto on the (n,f) reaction [166, 167]. Recently, some tests have been carried out to study the capabilities of the i-TED [168] technique for capture measurements. This method combines the Total Energy Detection technique with the imaging properties of the Compton cameras. More information about the techniques for (n,γ) measurements at n_TOF is given in Section 5.3. The main motivations for capture measurements have been nuclear technologies and nuclear astrophysics, in particular the study of the MACS of unstable s-process branching points [79, 101].

Fission (n,f) measurements use normally a stack of deposits, including some of ^{235}U or ^{238}U (standards) used as reference. Then, the fission yield ratio of the isotope of interest

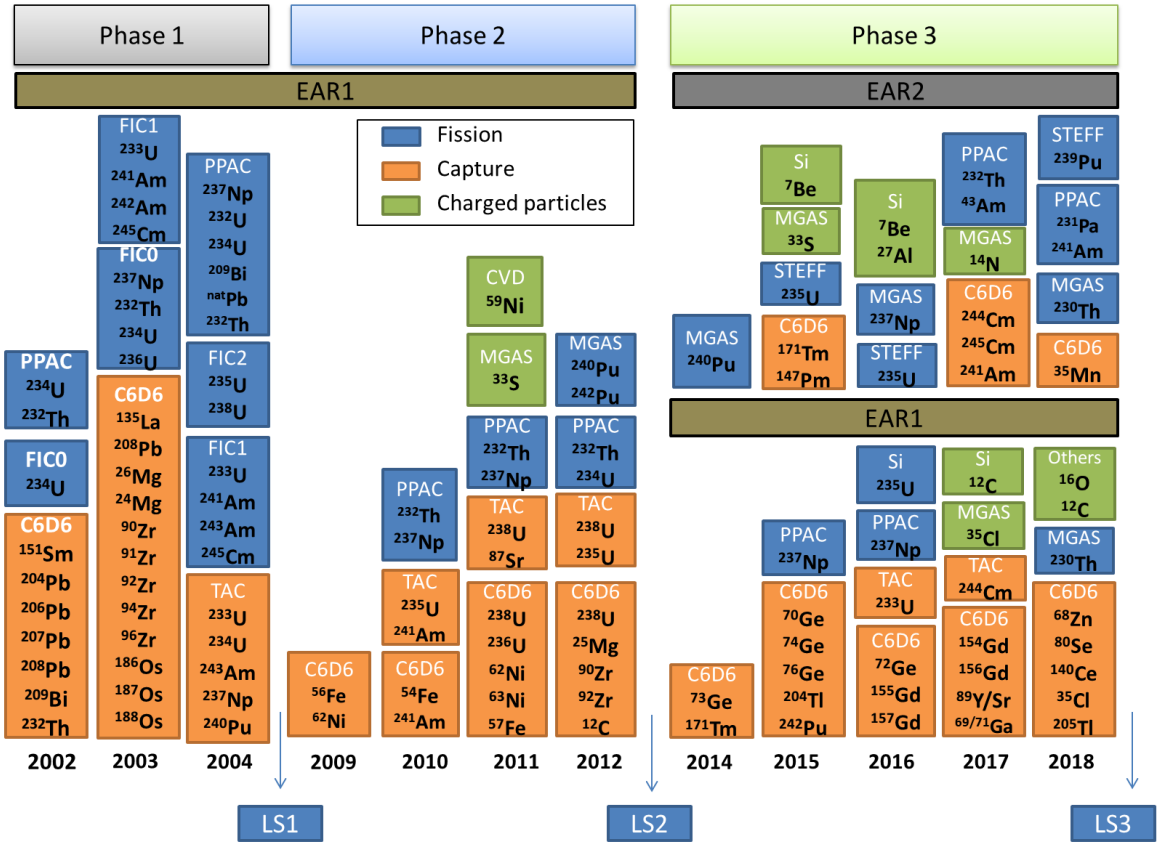

Figure 5.9: *Summary of the measurements carried out at the n_TOF facility along its 17 years of existence. Each of the blocks corresponds to the measurements performed with the one kind of detector and the different colours represent the different neutron induced reaction channels that are studied.*

relative to one of the standards is obtained rather than a fission yield. Different fission ionisation chambers (FIC) [169] were used in Phase1. Another long standing experimental set-up is based on Paralell Plate Avalanche Chambers (PPACs) [170], which allow to identify fission by the simultaneous detection of both fission fragments (FF) and can reach neutron energies as high as 1 GeV (in EAR1). At the end of Phase2 and during Phase3 the MicroMegas (MGAS) detector [171] has been used for fission as well. Last, the multi-detector system STEFF [172] has been used for the first measurement of FF spectroscopy combined with the detection of the corresponding prompt gammas. All the cross section measurements of the neutron induced fission are motivated for the improved accuracy in the neutron induced cross section of actinides required for the design and operation of innovative nuclear systems.

Last, charged particles (cp), mainly (n,p) and (n,α) measurements started only at the end of Phase2 and have become more common during the Phase3. The first (n,cp) measurements were carried out with MGAS detector for medical applications [173, 174], and a CVD diamond detector was used to measure the ^{59}Ni(n,α) cross sections [175] for as-

trophysics. Last, one of the most recient and challenging measurements at n_TOF has been the determination of the (n,p) and (n,α) cross sections on the highly radioactive ^{7}Be using a detection set-up based in a double Si detector sandwich [176, 177]. These measurements could have never been done without the uniquely high instantaneous neutron flux of n_TOF-EAR2 [98].

5.2 Neutron beam properties of n_TOF at EAR1

5.2.1 Neutron flux and beam profile

An accurate determination of the absolute number of neutrons impinging the sample during a measurement and their energy distribution is key for a high accuracy cross section determination. This is especially relevant in the case of capture measurements, such as the ^{242}Pu(n, γ) measurement in this work, in which the absolute reaction yield is extracted, and not the ratio to a reference cross section. Although the flux is usually defined as the number of neutrons per unit time and unit surface, in the following we will call *flux* to the total number of neutrons in a neutron bunch arriving to EAR1, the common definition in n_TOF [178, 179]. The reason to choose this definition is the non-uniform spatial distribution of neutrons and the low repetition rate (<0.8 Hz) at which the proton bunches are delivered by the PS.

Dedicated experimental campaigns have taken place at EAR1 to determine the neutron flux during the facility commissioning after each long shutdown or after any significant change in the spallation target, moderators or collimation system.

The determination of the neutron flux at n_TOF is based on the use of the cross sections standards [180, 181] (i.e. cross sections which are known with a very high accuracy in a given energy range), summarized in Table 5.4. A combination of detectors loaded with highly-enriched samples of the isotopes listed in Table 5.4 are used to extract the neutron flux $\phi(E_n)$. For a given neutron-converting reaction, the flux is calculated according to the following relation

$$\phi(E_n) \;=\; \frac{C(E_n) - B(E_n)}{\varepsilon(E_n)\;(1 - e^{-n\sigma_t(E_n)})\frac{\sigma_r(E_n)}{\sigma_t(E_n)}}, \tag{5.5}$$

where C and B are, respectively, the total and background counts per bunch, n is the areal density(atoms/barn) of the deposit,σ_r and σ_t are, respectively, the reaction and total cross sections. For the calculation of the flux, these cross sections were taken from the ENDF/B-VII.1 evaluation, which is based on the IAEA standards for these reactions. Last, ε represents the detection efficiency for the products of the neutron-converting reaction. All the variables in Eq. (5.5), with the exception of the areal density, depend on the neutron energy E_n.

To reduce systematic uncertainties in the determination of the fluxon different detection systems using different neutron induced reactions were installed along the beamline in EAR1:

Table 5.4: *Neutron induced reactions used to determine the neutron flux in n_TOF-EAR1 and energy range in which they are considered cross section standards.*

Reaction	Energy range
^{6}Li(n,α)	25.3 meV to 1 MeV
^{10}B(n,α)	25.3 meV to 1 MeV
^{235}U(n,f)	25.3 meV and 0.15 MeV to 200 MeV

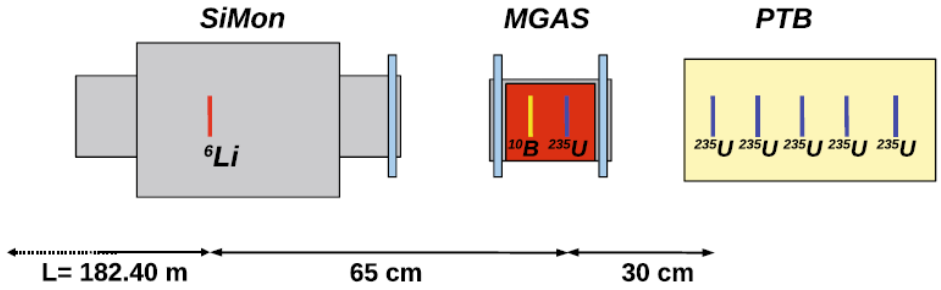

Figure 5.10: *Schematic view of the detection set-up used to characterize the neutron flux. The distance between the neutron source and the SiMon detector in EAR1 is indicated, together with the relative distances along the experimental area between the different detectors (from Ref. [178]).*

- SiMon: a solid state detection system (the Silicon Monitor Device, or SiMon [182]) is equipped with ^{6}Li converter and detects both the α and the triton from the ^{6}Li(n,α)^{3}He reaction.
- MGAS: a set of two Micromegas gas detector (MGAS) [183, 184], each of them loaded with ^{10}B or ^{235}U deposits. The two MGAS detectors are installed inside an aluminum chamber filled with Ar. The α from the ^{10}B(n,α) reaction leave all its energy in the detector, which is not the case for the fission fragments from ^{235}U, but in both cases the signals are clearly separated from the nois and background.
- PTB: a calibrated fission chamber from *Physikalisch Technische Bundesanstalt* (PTB) [185]. This detector is a ionization chamber with five platinum electrodes, covered on both sides with ^{235}U deposits. The good characterisation of this detector makes it a reference in the field of neutron metrology.
- PPAC: set of Parallel Plate Avalanche Counters (PPAC) [186, 187] equipped with a ^{235}U converter. The PPAC used have a central anode flanked by two cathodes. A low-pressure gas fills the 3 mm gaps between the aluminized Mylar electrodes (1.5 μm thick). The low sensitivity of this detector to the γ-flash and its fast signals allows one to extend the measurement of the neutron flux up to 1 GeV neutron energy.

The three first detectors were installed in paralell along the beam line using a small collimator of 1.8 cm in diameter (usually referred as *capture collimator*). The sketch of this experimental set-up for the flux determination in EAR1 is displayed in Figure 5.10. This scheme includes three of the detectors used to determine the flux using the neutron induced reaction in Table 5.4. The PPAC measurement was carried out with a collimator of

8 cm aperture which is used for fission measurements. All the details on the experimental campaing and analysis of the flux measurement at n_TOF-EAR1 can be found in Ref. [178].

From the independent measurements described above, a combined result, called *evaluated flux*, is extracted after a detailed statistical analysis of the deviations between the results of the different detectors. This analysis lead to the energy-dependent systematic uncertainties in the evaluated flux summarized in Table 5.5. The values in this table have been propagated to the uncertainty in the extracted capture yield of ^{242}Pu (see Section 6.10).

Table 5.5: *Overall estimated systematic uncertainty in the evaluated flux of EAR1 (From Ref. [178]).*

Energy range	**Uncertainty (%)**
25 meV - 100 eV	1
100 eV - 10 keV	2
10 keV - 100 keV	4-5
100 keV - 10 MeV	∼2
10 MeV - 1 GeV	∼4

The *evaluated* fluxes measured in 2011 and 2014 are compared in Figure 5.11 with the results of the Geant4 simulations in Ref. [162]. In this work it was shown that after the implementation of the high precision neutron transport package *Neutron_HP*, the simulated neutron flux reproduces the shape of the *evaluated* flux below 20 MeV, thus validating the use of Geant4 for neutron transport simulation. On the other hand, the simulations overestimate by 15-70%, depending on the choice of Physics List (PL), the magnitude of the neutron flux in both experimental areas. Figure 5.11 shows the result obtained with the PL that provided the best agreement with the evaluated flux in terms of the absolute value of the flux (*QGSP-INCL++-HP* [188, 189]).

The main features of the neutron energy distribution in Figure 5.11 are the abscence of a thermal peak in the tens of meV region due to the presence of ^{10}B in the moderator, the isolethargic epithermal region between a few eV and tens of keV, which then overlaps with the evaporation peak in the MeV region and part of the spallation neutrons in the tens of MeV region (see Section 5.1.1). In addition, the aluminium alloy layers around the spallation target and along the beamline are responsible for a series of transmission dips in the flux, dominated by the ^{55}Mn and ^{27}Al resonances between 200 eV and 500 keV.

Another characteristic of the neutron beam is its spatial profile in the experimental area. This information is required for measurements with samples smaller than the beam. In this case, it is important to accurately determine the fraction of the neutron beam impinging on the sample, known as *beam interception factor* (BIF), and its dependence on neutron energy. The Geant4-simulated beam profile in EAR1 is shown in Figure 5.12 for the whole range of neutron energies. The results are consistent with measurements performed in various campaigns summarized in Ref. [93].

The simulations of the beam profile are relevant to calculate the energy dependent BIF [162]. According to the simulations, the full beam is intercepted for all the neutron

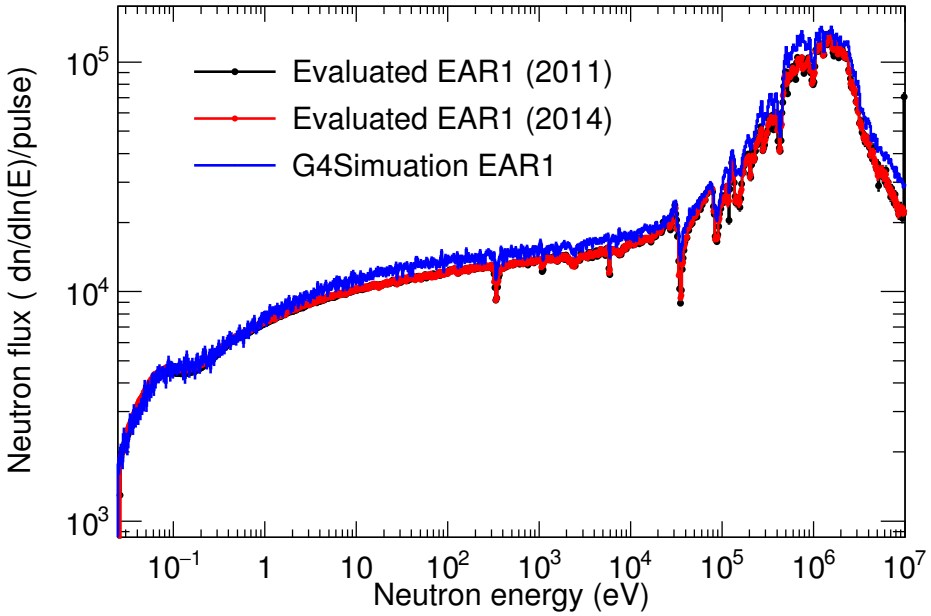

Figure 5.11: *Evaluated flux measured in 2011 and 2014 from Ref. [178] compared to the result obtained from a MC simulation carried out with the Geant4 toolkit [162]. The neutron flux is shown only up to 10 MeV since this is the highest energy in the measurement of 2014.*

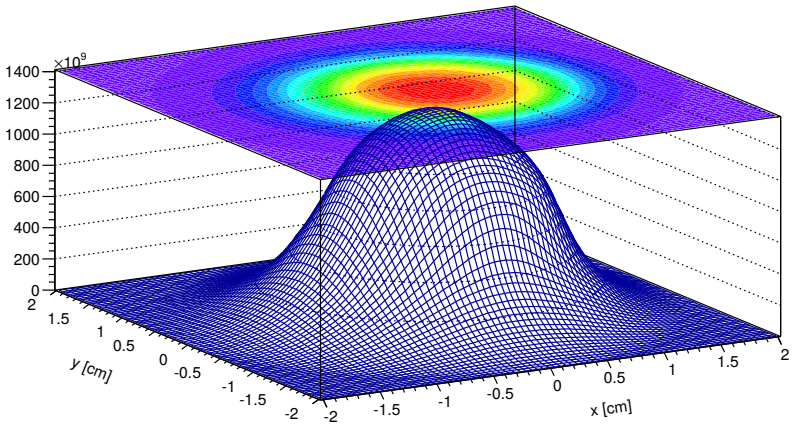

Figure 5.12: *Simulated neutron beam profile in EAR1 (at a distance of 185.2 m from the spallation target). The profile is obtained by propagating through the collimation system neutrons emerging from the target in Geant4 simulations. The RMS of the spatial distribution is about 0.61 cm, in agreement with the measured standard deviation.*

energies using a sample of radius larger than 18 mm. This is the case in this work, where the ^{242}Pu deposits are 45 mm in diameter (see section 3.3.1).

5.2.2 Resolution Function

As we introduced when we discussed the time-of-flight technique in Section 5.1.3, an important feature of neutron time-of-flight facilities is the fact that all the neutrons of a given energy do not exit the target-moderator assembly at the same time, thus making the time-to-energy relation non-univocal. The relation between these two quantities is known as the Resolution Function (RF) of the facility and it can only be determined by means of simulations, which can then be validated with experimental data. The resolution function of EAR1 has been simulated within the n_TOF collaboration using the FLUKA [190], MCNP [191] and Geant4 [137, 138] Monte Carlo codes and the results are included in Refs. [93, 162].

The neutron production time, defined as the time it takes, after the proton beam impinges the target, for a neutron to be generated, moderated and transported outside the spallation target assembly, is not constant for all the neutrons of a given energy. The spread of production times for a given neutron energy is related to different effects:

- The time spread of the original charged particle beam.
- The neutron production mechanism.
- The neutron moderation process.

The latter two effects are related to the composition and size of the spallation target and the moderation system. The spread in the production time for a given neutron energy introduces a broadening in the structures or resonances observed in time-of-flight experiments. This spread is, in general, significantly asymmetric, leading not only to a broadening of the resonances but also to a shift in their position (see Figure 5.14).

Mathematically, the Resolution Function $R_E(E_n)$ for a given neutron energy can be either expressed as a distribution in energy (E_n), time-of-flight (t) or distance (L).

$$R_E(E_n)dEn = R_t(t)dt = R_L(L)dL, \tag{5.6}$$

where E_n, L and t are related to each other via Eq. (5.2). R_t corresponds to the distribution of production times of the neutrons arriving to EAR1 around a time-of-flight t and R_L is the distribution of equivalent flight paths. The equivalent flight path for a neutron is the sum of the fixed flight path distance and the neutron path inside the target-moderator assembly moderation, and it can be calculated from the output of MC simulations as

$$L_{mod} \;=\; v\; t_{mod}, \tag{5.7}$$

where v is the velocity of the neutron at the target exit and t_{mod} its moderation time. The distribution of L_{mod} as a function of the neutron energy is the most common way to illustrate the Resolution Function, and it is shown in Figure 5.13.

The effects of the RF are usually treated in a different way in the analysis of experimental time-of-flight data:

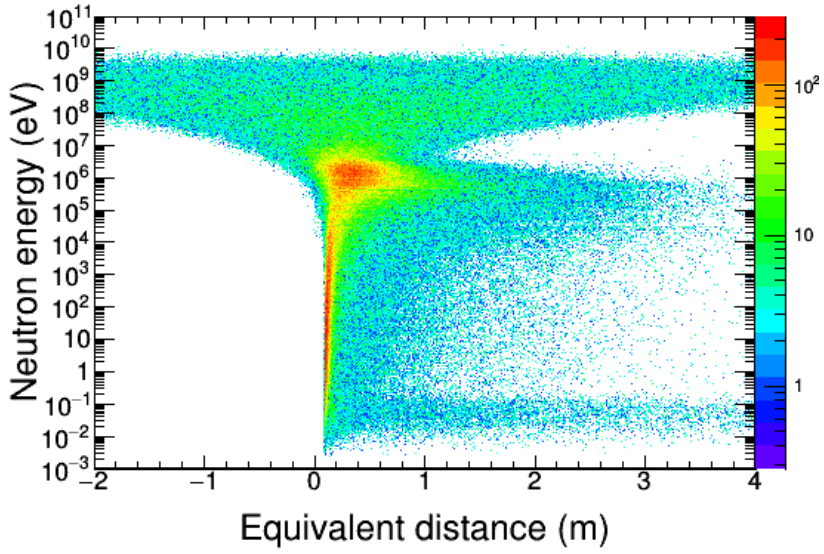

Figure 5.13: *Probability distribution of the equivalent moderation distance, as a function of neutron energy, obtained from GEANT4 simulations of the n TOF spallation target. The simulated moderation time was convoluted with the Gaussian distribution of the proton pulse (7 ns RMS). The latter dominates the broadening above 10 MeV.*

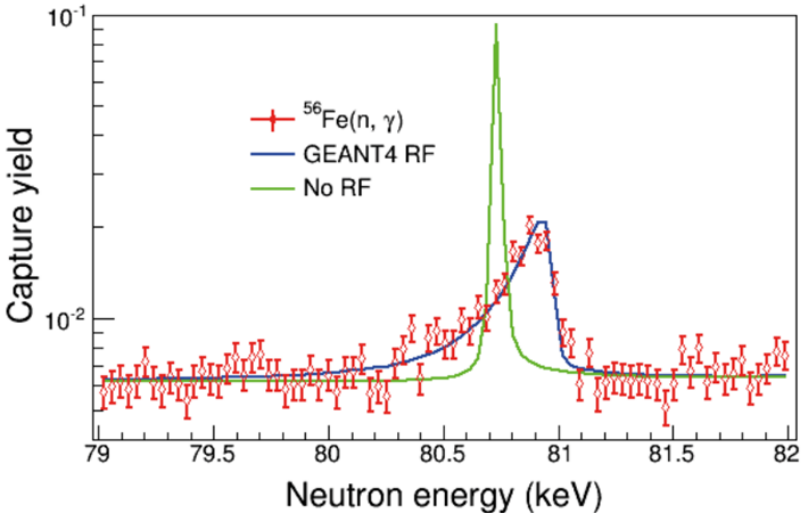

Figure 5.14: *Comparison between the theoretical (green) and the experimental resonance of* ^{5}6*Fe at 81 keV measured at n_TOF-EAR1, showing the broadening and energy shift associated to the RF. The blue curve is the theoretical cross section calculated with the SAMMY R-Matrix code after including the numerical RF from the Geant4 simulations [162].*

- The broadening of the resonances is taken into account by including the numerical RF in the R-Matrix analysis code (SAMMY [62], REFIT [64]) (see Figure 5.14).
- The energy shift in the conversion from time-of-flight to neutron energy is corrected by replacing the fixed L in Eq. (5.2) by a fixed geometrical flight path length plus an energy-dependent effective moderation length. An similar result is achieved by

includding a time offset in Eq.(5.2) [192].

The details on the implementation of the RF in time-to-energy calibration and in the R-Matrix analysis are given in Sections 6.4 and 7.1.1, respectively.

5.2.3 γ-flash and in-beam γ-ray background

Photons are produced along with neutrons as spallation reaction products as well as in capture reactions occurring within the target/moderator assembly. These in-beam photons cannot be removed from the beam, as it is done for charged particles by means of a suitable magnet, and thus represent an important source of background in all neutron capture experiments. Figure 5.15 shows the γ-ray flux, obtained from the Geant4 simulations the n_TOF spallation target and transported to EAR1 [162] using different PL, as a function of their arrival time. Two different components can be distinguished in this figure: he large sharp peak at the beginning constitutes what is called *prompt* component hereafter and is followed by a long *delayed* component.

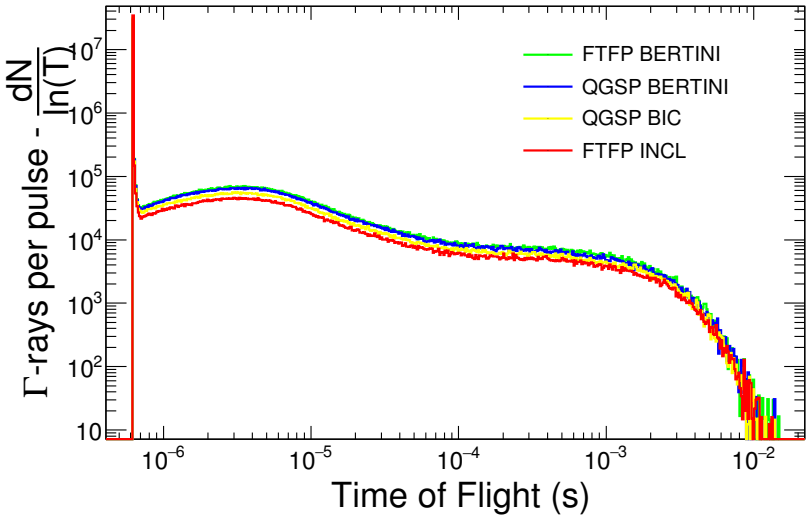

Figure 5.15: *Simulated total number of γ-rays per proton pulse produced in the spallation target and transported to EAR1 as a function of their arrival time in EAR1. Two components can be clearly distinguished: prompt γ-rays (at 615 ns) and delayed γ-rays beyond 1 μs.*

The first γ-ray component is emitted prompt with the arrival of the proton beam in high-energy interactions during the spallation process and arrives at EAR1 in less than $\sim$1 μs, but no less than the 615 ns needed to travel the 184 m flight path at the speed of light. The energy distribution of the prompt γ-ray component, shown in Figure 5.16, is characterized by a hard spectrum with a maximum at a few MeV and reaching up to tens of GeV. Together with relativistic charged particles, the prompt γ-ray component constitutes the so called γ-flash, producing in most detectors a sharp signal at a time t_γ, which is used as the time reference in Eq. 5.3 to determine the neutron time-of-flight.

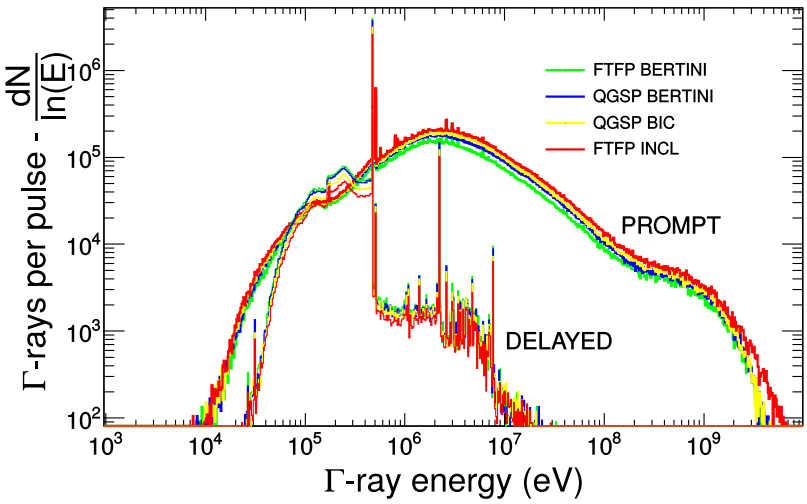

Figure 5.16: *Energy distribution of the two γ-ray components produced in the spallation target assembly obtained from the Geant4 simulations of Ref. [162]. The prompt component includes the γ-rays reaching EAR1 within 1μs and the delayed one those arriving at larger times. The different curves correspond to the results of different Physics Lists.*

The second component, usually called *delayed*, is generated in capture reactions occurring within the target/moderator assembly. It presents a much softer spectrum than the prompt one characterized by well defined γ-rays belonging to cascades from (n,γ) reactions, mainly the 478 keV and 7.4 MeV lines from capture in ^{10}B (borated water moderator) and aluminium (see Figure 5.16). The 2.2 MeV peak from the thermal neutron capture in hydrogen is still present but strongly suppressed compared to EAR2 (see for instance Ref. [98]) because the moderator in EAR2 consists only of water, and not borated water like in EAR1.

5.3 Detection techniques for capture measurements at n_TOF

In Section 2.5.2 we already introduced different techniques used to measure neutron capture cross section by detecting the prompt γ-rays emmitted in the de-excitation of highly-excited compound nucleus. Capture measurements at n_TOF have been carried out to date using two of these techniques, featuring very different philosophies: the Total Absorption technique, implemented with the n_TOF Total Absorption Calorimeter [111] and the Total Energy Detection Technique by using a set of C_6D_6 detectors [165]. The main advantages and drawbacks of both detection techniques are summarized in Table 5.6. Since 2016, several tests have been carried out as a proof of concept of a new technique with γ-ray imaging capabilities called i-TED [168].

Table 5.6: *Comparison between the main advantages and drawbacks of the detection systems for capture measurements to date at n_TOF.*

	TAC	**C_6D_6**
Advantages	Good background rejection	Low neutron sensitivity
	High efficiency	Simple set-up
	High resolution	Fast detectors
Drawbacks	Neutron sensitive	Poor background rejection
	Slow detectors: pile-up problems	Low efficiency
	Complex detector (42 crystals)	Software manipulation (PHWT) needed

5.3.1 Total Absorption Calorimeter (TAC)

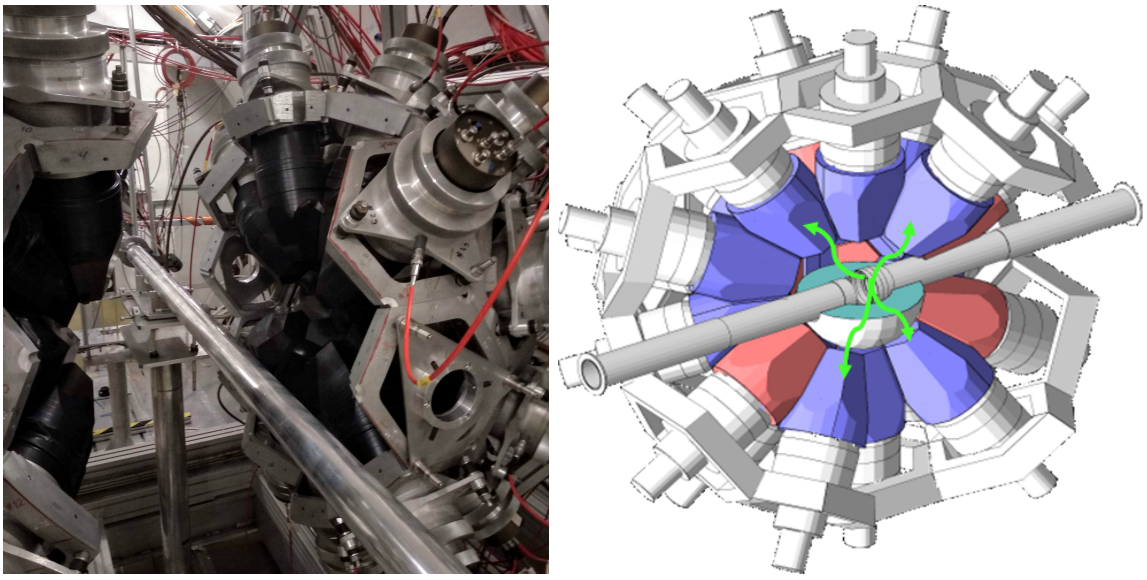

Figure 5.17: *Left: Inner view of the separated TAC hemispheres with the neutron beamline of EAR1 between them. Right: Geant4 model for the developed for the efficiency assesment (from Ref. [193]).*

The n_TOF Total Absorption Calorimeter (TAC) is a segmented 4π detector array made of 40 BaF_2 crystals, 12 pentagonal and 28 hexagonal, which cover 95% of the 4π solid angle. Each individual module is mounted on an aluminum honey-comb structure that is holding the complete detector. The detector assembly is divided into two hemispheres, one of which can be moved to access the interior of the detector (see Figure 5.17), and in particular the centre of the TAC where the sample is placed. To lower the neutron sensitivity of the system, the sample is surrounded by a spherical neutron moderator/absorber made lithium compound loaded with ^{10}B.

Figure 5.17 shows the actual view of the detector from the inside. This calorimeter was designed to meet the main requirements of the Total Absorption Technique.

- Large solid angle coverage

- High total γ-ray efficiency
- High segmentation

Under these conditions, this detector is able of sorting events by the total energy deposited in all the crystals (E_{sum}) and the number of cristal that were fired, the so-called *multiplicity* (m_{cr}) (see Figure 5.18). Setting clever conditions on these two quantities allows to improve significantly the capture to background ratio since most background events do not fire more than one crystal and they are mainly events with total energy depostions below the sum energy of a capture event (i.e. neutron separation energy of the compound nucleus). However, an accurate assesment of the detection efficiency, reduced by 20-30% after the cuts are applied, needs from detailed MC simulations of the detector including the implementation of realistic capture cascades [193]. The geometry model implemented in Geant4 for this purpose is shown in the right side of Figure 5.17.

The main drawback of this detection system is the relatively high neutron sensitivity and slow detector response that combined limit the maximum measurable neutron energy. Previous measurements at n_TOF have shown that these limitations restrict the upper energy limit of the extracted cross sections to at most 80 keV (see for instance Ref. [195]).

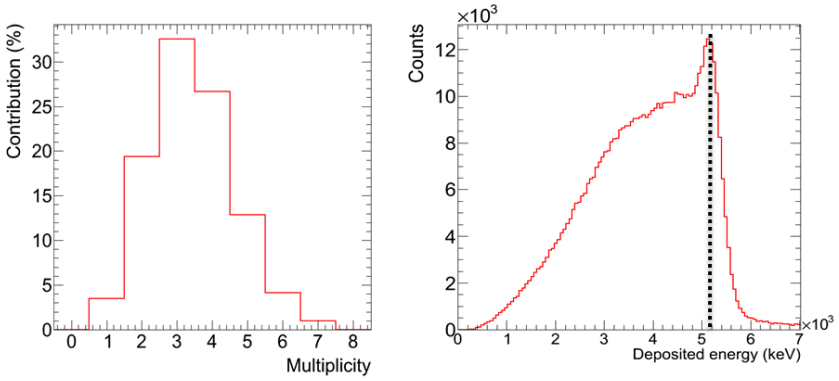

Figure 5.18: *Left: Typical multiplity distribution of the events in the ^{237}Np(n,γ) measurement with the TAC [194]. Right: Total γ-ray energy deposited in the TAC crystals E_{sum} peaked at the neutron separation energy indicated with a dashed line.*

5.3.2 C_6D_6 Total Energy Detectors (TED)

The second technique used at n_TOF to measure neutron capture cross sections is the Total Energy Detection (TED) technique. This method is based on having a detection system that registers a capture event with an efficiency that is directly proportional to the total energy of the cascade (i.e. the neutron separation energy plus the neutron energy). This condition is a priori not easy to achieve since the de-excitation of the compound nucleus can follow many different cascade patterns, i.e. different γ-ray energies and multiplicities (see left panel of Figure 5.19).

A Total Energy Detector should fulfill the following conditions:

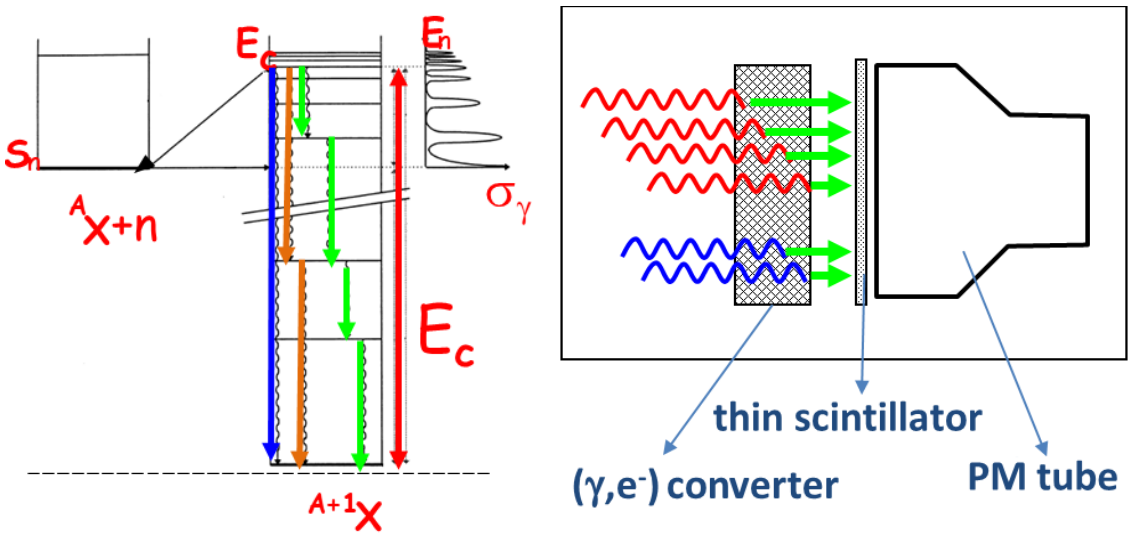

Figure 5.19: *Left: Scheme showing in different colours the variable cascade pattern emitted after a neutron capture. Right: Sketch of a Moxon-Rae detector indicating its main components.*

1. The efficiency of the detectors must be low enough so that at most one γ-ray per cascade is detected. If this is the case, the total efficiency for detecting a cascade ε_c becomes
$$\varepsilon_c = 1 - \prod_i (1 - \varepsilon_i) \approx \sum_i \varepsilon_i, \tag{5.8}$$
ε_i being the efficiency to detect a γ-ray of the cascade. The sum goes over all emitted gammas i in the cascade.
2. The efficiency to detect each γ-ray is proportional to its energy E_i
$$\varepsilon_i = k \cdot E_i. \tag{5.9}$$

Under these two conditions the efficiency for detecting a cascade is proportional to the known energy of the cascade (E_c) and independent of the actual decay path.

$$\varepsilon_c = k \sum_i E_i = k \cdot E_c = k \cdot (S_n + E_n). \tag{5.10}$$

The first idea to develop such a detection system was the Moxon-Rae detector [109, 196]. This detector, shown in the right panel of Figure 5.19, consists of a converter, typically of carbon or bismuth, where electrons are produced by the impinging capture γ-rays by Compton scattering, pair production, or photoelectric effect. These electrons are either absorbed in the converter or detected in a thin plastic scintillator, which is mounted between the converter and a photomultiplier (see Figure 5.19). The efficiency of such a detector increases almost linearly with the γ-ray energy and the probability of detecting more than one γ-ray out of a cascade is negligible, thus fulfilling the conditions given by Eqs. (5.8)-(5.9). However, this detectors were replaced by others due to their excesively small efficiency

and the fact that the proportionality could never be met by real Moxon-Rae detectors [197], resulting in sizable systematic uncertainties.

The next idea to implement the TED method was to eliminate the converter and use larger scintillators [198]. Organic hydrogen-free scintillators have been extensively used since more than 40 years, when Mackin and Gibbons started using the Total Energy Detection method on C_6F_6 [110] scintillation detectors. This material was later replaced by C_6D_6 (deuterized benzenene), which have been used at n_TOF since the beginning and also for the capture measurement on ^{242}Pu in this work.

C_6D_6 detectors present several conditions that make them very well to neutron capture measurements:

- High efficiency compared to the Moxon-Rae detectors,
- low neutron sensitivity,
- excellent time resolution (∼ns) and
- low costs and simple construction.

However, C_6D_6 detectors do not longer satisfy the required proportionality between ε_i and E_i. Therefore, a mathematical manipulation of the detector response is needed to achieve this proportionality: the counts recorded are weighted by a factor dependent on its energy (pulse height), given by the so-called weighting function (WF). This is known as the *Pulse Height Weighting Technique (PHWT)* [199, 200]. The basic principles of this method are described in Appendix B.1 and its implementation in the ^{242}Pu(n,γ) measurement is discussed in Section 6.8.

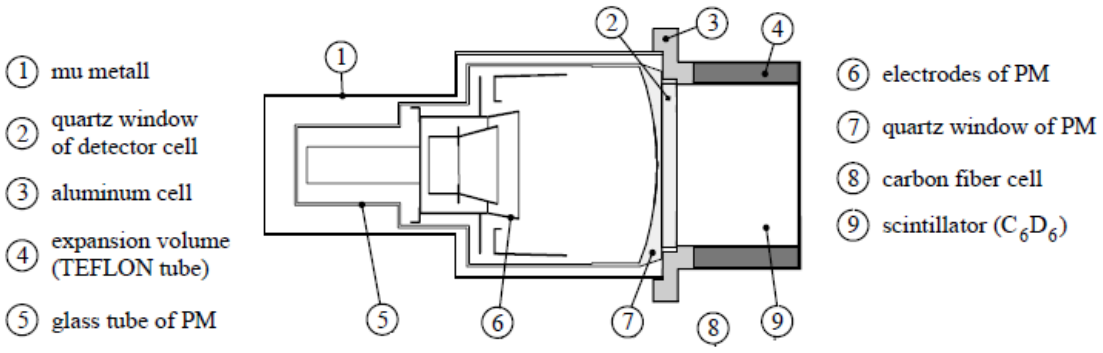

Figure 5.20: *Sketch of the commercial BICRON C_6D_6 detector extracted from Ref. [165].*

Different models of C_6D_6 detectors have been used to carry out capture measurements at n_TOF:

- BICRON detector: This is a commercial detector, consisting of a thin aluminum cell (0.4 mm-thick walls and 1 mm-thick entrance window) based on the design of Nuclear Enterprise and manufactured by BICRON. The original model by BICRON was optimized in terms of low neutron sensitivity by replacing the original borosilicate

window of the Photomultiplier Tube (PMT) for the quartz window [165] of the current XP1208 PMT. The C_6D_6 active volume of this model is 0.612 l. Figure 5.20 illustrates the main components of this detector model.

- FZK detector: This model, developed and used in the Forschungszentrum Karlsruhe [201], presented originally a thin aluminum cell and a quartz PMT window to minimize the neutron absorption. The neutron sensitivity was further reduced by choosing carbon fiber for the cell (0.4 mm-thick) and by removing all parts which are not essential, e.g. the window of the cell and the photomultiplier housing. Capture measurements at n_TOF were carried out with this detector during Phase2 and its use was abandoned in Phase3 due to the new safety requirements in the Type A experimental areas. The C_6D_6 active volume of this model was 1 l.
- Legnaro detector: These new detectors manufactured at the Legnaro National Laboratory (LNL) in Italy are entirely made of carbon fiber to keep the low neutron sensitivity of the FZK detector. However, the need of long durability and safety of detector to avoid the safety issues of the FZK detector implies the use of thicker carbon fiber walls (2 mm for the side walls and 1.1 mm for the window), which has been compensated by a reduction of material in the PMT. The size of this PMT (2 inch) is significantly smaller than the 5 inch ones used in both commercial BICRON and the FZK detectors. The carbon fiber cell has a conical reduction to fit the PMT, which works both as a light guide and active scintillation volume. The total C_6D_6 active volume of this model is 1 l. For more details on the design of these detectors, the reader is referred to Ref. [202].

A comparison of the first two models in terms of neutron sensitivity studied with Geant4 simulations can be found in Ref. [203]. Some preliminary studies on the simulated neutron sensitivity including the three detector models are presented in Ref. [204].

5.3.3 i-TED

This innovative method is based on appliying the TED technique to a detection set-up with imaging capabilities [205]. This combination enhances the background rejection capabilities compared to the normal TED by enabling the distinction between γ-rays arising from the target (true capture events) and γ-rays produced elsewhere (background events). This method reduces both the sensitivity to scattered neutrons directly coming from the sample and to stray neutrons that are captured (normally after thermalization) around the experimental hall. The latter represents the major source of background of typical TED detectors [203].

Among the different techniques to implement γ-ray imagining, the i-TED employs a system based on Compton imaging [206] (i.e. electronic collimation), with which the direction of origin of a detected photon can be determined from the energies and positions registered in a detector made of two position sensitive scintillators: the first one records the position where a Compton scattering takes place and the corresponding energy loss, and the second

records a second position and absorbs the photon. A simple calculation using the Compton scattering formula provides a direction cone within which the photon was emitted.

In order to apply the Compton scattering law, a good energy and position resolution have to be achieved. These features can be acomplished by using high resolution fast scintillation detectors, such as $LaBr_3$, $LaCl_3$ or $CeBr_3$, coupled to thin photosensors such as position senstive photomultipliers (PSPM) [207] or silicon photomultipliers (SiPMs) [208]. A proposed i-TED design is shown in the right panel of Figure 5.21.

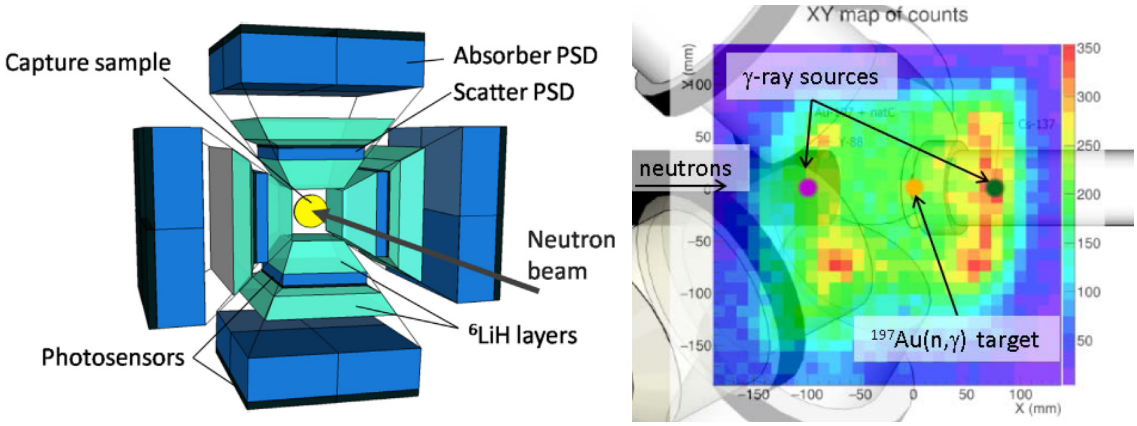

Figure 5.21: *Left: Sketch of the i-TED design showing a cylindrical capture target of 2 cm diameter surrounded by four assemblies of thin scatter + thick absorber detectors making an i-TED detection set-up (from Ref. [205]). Right: Reconstructed origin of the photons during a* $^{197}Au(n,\gamma)$ *experiments with γ-ray sources around the gold target (2D colour histogram) on top of a drawing of the set-up mounted in n_TOF EAR-1 (from Ref. [101]).*

The first tests on the application of the γ-ray imaging in hard background enviroments, such as the n_TOF experimental areas, were succesfully carried out in 2016 and showed promissing results [168]. The right panel of Figure 5.21 illustrates the imaging capabilities of a monolithic $CeBr_3$ scintillating crystal coupled to a PSPM. Last, the first prototype of the i-TED detector based on $LaCl_3$ scintillation crystals has been already designed and tested with succesful results at n_TOF, and the first measurements using this detection set-up will be carried out in 2018.

5.4 ^{242}Pu(n,γ) experimental campaign at n_TOF-EAR1

5.4.1 ^{242}Pu sample: stack of fission-like targets

A suitable sample design is a key factor for a succesful capture measurement. The most critical features in the design of radioactive capture target have been discussed in Section 3.3.1.

A high-quality ^{242}Pu sample for the capture measurement at n_TOF was prepared within the EC FP7 CHANDA project [123] by the JGU University of Mainz and the HZDR

research center in Germany [127]. A set of seven thin fission-like targets 45 mm in diameter, were assembled to create the 8 mm thick sample stack, sketched in Figure 5.22 containing a total mass of 95(4) mg of ^{242}Pu and a total Al backing thickness of only 70 μm. The individual target thickness homogenity, studied by means of alpha radiography, was found to be 75%, leading to an overall thickness inhomogeneity of the seven targets combined below 0.1%. The details on the sample production and quality assurance were already described in Section 3.3.1.

The innovative sample geometry consisting of a stack of targets required the production of a new capture holder with a much thicker slit than for normal capture targets. The latter are usually mounted on few mm thick PCV ring that gives support to a thin mylar foil where the sample is sticked. The right panel of Figure 5.22 shows the ^{242}Pu sample assembly mounted on the sample holder before the latter was installed in the neutron beamline.

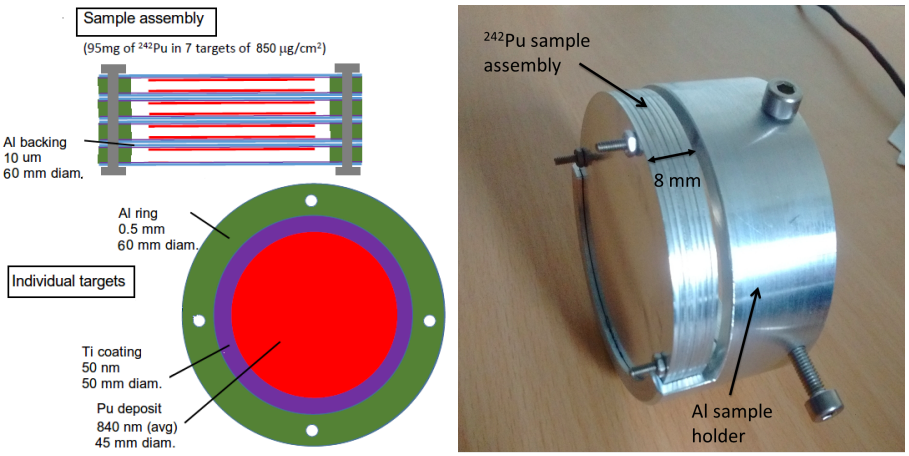

Figure 5.22: *Left: Sketch of each of the seven thin Al backings containing 95(4) mg of electrodeposited ^{242}Pu. Right: Actual view of the sample assembly mounted on the new sample holder designed for this target geometry.*

One particular aspect of this measurement is the use of thin fission-like targets instead of the typical thick targets used in previous capture measurements in time-of-flight facilities. The ^{242}Pu targets designed for this measurement, featuring an average density of 0.85 mg/cm^2 with 45 mm diameter on thin Al backings, reminds of fission-like targets but present several advantages for capture measurements with respect to the typical thick target for (n,γ) measurements [217]:

- First, it features a uniquely high actinide mass to capture in backing ratio in the keV region compared to previous capture samples. This ratio is calculated as

$$R_{b2t} = \frac{n_{Pu242}}{\sum_i n_i \cdot \sigma_i^{MACS}}, \tag{5.11}$$

  n_{Pu242} and n_i being the surface density of ^{242}Pu and the i-component of the backing, respectively. σ_i^{MACS} is the MACS of the i-component of the backing at 30 keV (see

Eq. 2.53), used to cuantify the capture rate on the target backings. The backing-related neutron scattering background was the main limitation to extend the analyzable neutron energy range in previous measurements at n_TOF (see for instance Refs. [194, 219, 218]), but it is not in this case.

- The large dimension of the ^{242}Pu deposits in our target ensures that the full neutron beam is intercepted and thus no correction for a possible missalignment is required.
- The use of thin fission-like targets also presents advantages in the implementation of the Pulse Height Weighting Technique [213] (see Section 6.8), where smaller corrections need to be applied and a higher accuracy is achieved.
- The use of thin targets with thin backings reduces the self-absorption and multiple scattering of neutrons in the target down to a negligible level. This improves significantly the situation, especially for the analysis of the URR, compared to previous capture measurements (see Section 8.1).

5.4.2 Samples for ancilliary measurements

Besides the ^{242}Pu sample described in the previous section, other samples where produced to be measured in the same experimental campaign. The measurement of this targets aims at determining the different background components, obtaining an absolute normalization of the extracted capture yield or validating the measurement. The ancilliary samples are:

- *Dummy*: exact replica of the ^{242}Pu 7-target assembly without ^{242}Pu electrodeposited on the target backings.
- ^{197}Au: gold sample, 100 μm thick and 45 mm in diameter (like the ^{242}Pu targets) mounted on a 10 μm-thick mylar foil sticked to a PVC ring 60 mm in diameter.
- ^{nat}Pb: Natural lead sample, 1 mm thick and 45 mm in diameter (like the ^{242}Pu targets) mounted on a 10 μm-thick mylar foil sticked to a PVC ring 60 mm in diameter.
- *Empty*: PVC ring with a 10 μm-thick mylar foil sticked on it.

Sample	Diameter (mm)	Mass (g)	Atomic density (at/b)
^{242}Pu	45 mm^a	0.095	1.49x10^{-5}
Dummy (Al)	60 mm	0.534	4.22x10^{-4}
^{197}Au	45 mm	3.073	2.41x10^{-4}
^{nat}Pb	45 mm	18.03	3.30x10^{-3}

Table 5.7: *Properties of the ancilliary samples measured during the ^{242}Pu(nγ) campaign at n_TOF-EAR1. a: Dimension of the ^{242} deposit. The diameter of the Al backing is 60 mm.*

The properties of these samples are summarized in Table 5.7. Figure 5.23 shows the ancilliary samples in the measuring position in-front of the capture setup. The specific

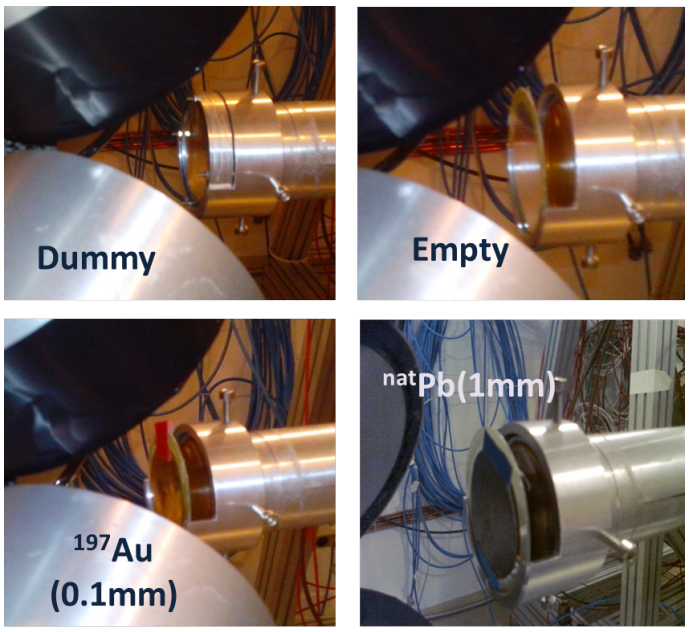

Figure 5.23: *Pictures of the ancilliary samples during the measurements for background assesment, normalization and validation purposes.*

goal of each ancilliary target and the measurement planning of the ^{242}Pu(nγ) campaign are discussed in Section 5.4.5.

5.4.3 Capture set-up and neutron beam monitors

The properties of C_6D_6 detectors, and in particular the low neutron sensitivity and fast response were key to choose a set-up based in these detectors for the measurement of the capture cross section of ^{242}Pu. This set-up was better suited to this measurement than the TAC mainly because they suffer significantly less from the so-called γ-flash (i.e. prompt γ-rays produced in the spallation reactions) than the latter, due to their fast response and light components, thus allowing us to measure up to a higher energy. Moreover, the reduced neutron sensitivity is a clear advantage in the URR, where scattering dominates over capture.

At the time of the design of the experimental set-up, the new Legnaro detectors were still in commissioning phase and did not offer the desired stability, resolution or linearity. Therefore, the long-standing BICRON detectors were the final choice. The set-up of four BICRON detectors mounted on an aluminum holder structure is shown on the left side of Figure 5.24.

An accurate knowledge of the sample-to-detector distance is required to implement the geometry in the MC simulations. The right panel of Figure 5.24 shows a sketch of the measured distances from the sample center to the entrance window of each of the four BICRON detectors in this measurement. Fortunately, any deviation between the real set-

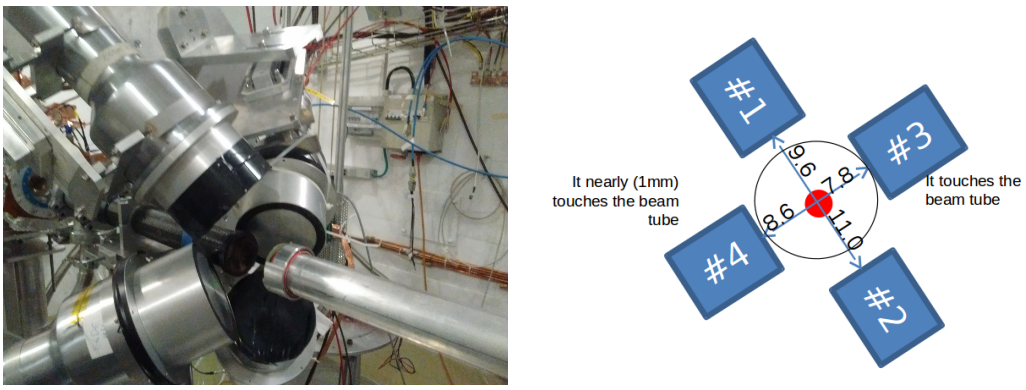

Figure 5.24: *Left: Array of four BICRON C_6D_6 detectors used to detect the γ-ray cascades emmited following the neutron capture on the ^{242}Pu sample. Right: Sketch of the four BICRON detectors indicating the distances from the detectors to the target center.*

up and the simulated geometry model associated to the positioning or to possible differences between the different detectors (assummed to be exact copies in the simulations) is later corrected through the individual normalization of the ^{242}Pu capture yield extracted from each detector to the ^{197}Au yield with the SRM method (see Section 6.9.1).

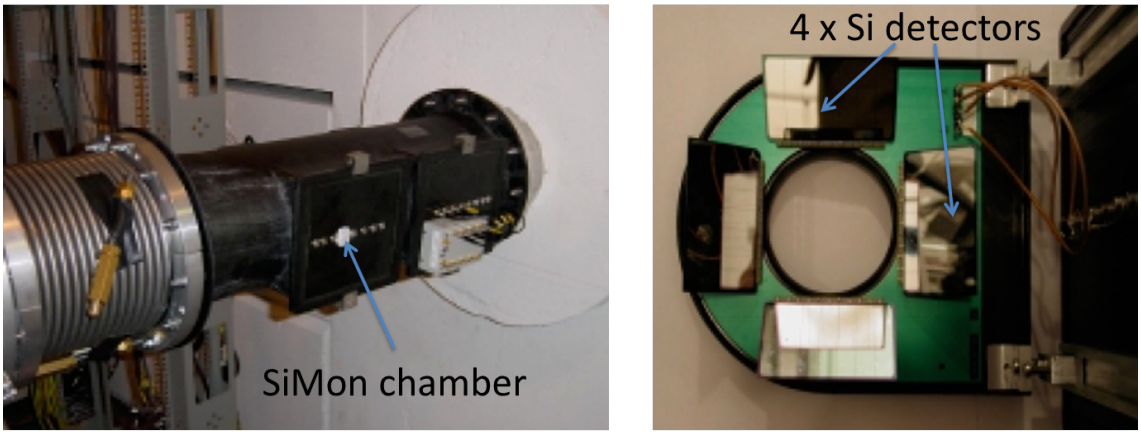

Figure 5.25: *General view of the SiMon chamber in the beamline entrance to EAR1 (left) and detailed view of the opened SiMon detector showing the four Si detectors (right).*

Together with the capture detectors, different systems are used at n_TOF for monitoring the proton and neutron beams:

- **BCT:** The proton intensity sent onto the target is measured pulse by pulse with a Beam Current Transformer located about 6 meters upstream with respect to the spallation target in the proton beamline. This system provides the absolute number of protons, which is saved in the same file for the offline analysis of the data.
- **PKUP:** A resistive Wall Current Monitor, usually referred as Pick-up, measures the intensity of the proton beam in each pulse just after the BCT and provides a signal with an area proportional to the instantaneous proton beam intensity which is sent

to the n_TOF Data Acquisition System.

- **SiMon:** The neutron beam is monitored with the SiMon system [182] placed upstream from the capture set-up in the entrance of the experimental area as it shown in Figure 5.25. It consists on an array of four silicon detectors placed outside the beam and looking at a thin enriched lithium fluoride foil for detecting the products of the ^{6}Li(n,α) reaction, whose cross section is considered a standard from thermal up to 1 MeV. This detector is the same used to characterize the neutron flux (see Section 5.2.1).

The CERN Proton Syncroton provided during this measurement full intensity (*dedicated*) pulses of $\sim$8x10^{12} protons combined with low intensity (*parasitic*) ones of $\sim$2x10^{12} protons. The correlation between the three different beam monitors and the associated uncertainties are discussed in Section 6.3.1.

5.4.4 Data Acquisition System and storage

The Data Acquisition System (DAQ) of a time-of-flight facility such as n_TOF must be versatile, flexible and scalable to adapt itself to the large variety of cross-section measurements and detectors. According to these requirements, the n_TOF DAQ was designed on the basis of high performance 12-bit flash-ADCs capable of recording up to 100ms-long movies at a sampling rate of 1 GHz with a negligible dead time. The main features of the n_TOF DAQ are the following:

- All the detectors raw signals are digitized for the offline analysis.
- The sampling rate is fast enough to digitilize with sufficient accuracy the signals of fast detectors, such as C_6D_6 scintillators, with a $\sim$10 ns signal width.
- Most of the electronic chain (e.g. preamplifiers, time and energy amplifiers, ADCs . . .) is not required.
- A fast zero suppression algorithm selects only those data with an amplitude above an user-defined threshold for each flash-ADC channel, reducing in this way the amount of data to be stored.
- After the zero suppression is applied, the raw data are sent to a temporary disk pool close to the measurement station and, once closed, to the CERN Advanced STORage manager (CASTOR) [222].

In the ^{242}Pu(nγ) campaign each of the BICRON detectors in the capture setup and the beam monitoring systems (PKUP and SiMon) were connected to a channel of the n_TOF Data Acquistion System. The recored lenght of 100 ms following the arrival of the proton pulse to the spallation target allows recording signals corresponding to a neutron energy as low as 18 meV.

5.4.5 Measurements and beam time distribution

During the experiment, with a total number of 3.17x10^{18} protons impinging on the spallation target (i.e. approximately one month long), most (64%) of the beam time was allocated to measure the Pu target. The remaining beam time was splitted between the different ancilliary samples described in Section 5.4.2. A summary of the beam time distribution and measured samples along the experimental campaign is presented in Table 5.8.

Sample	Nr. protons	Nr. bunches	Objective
^{242}Pu	2.02x10^{18}	3.77x10^{5}	^{242}Pu(n,γ)
Dummy	7.73x10^{17}	1.44x10^{5}	Backing-related background
Empty	1.52x10^{17}	2.52x10^{4}	Beam related background for Au and Pb
^{197}Au	1.17x10^{17}	2.25x10^{4}	Normalization (SRM) and validation of URR
^{nat}Pb	1.07x10^{17}	2.11x10^{4}	γ-ray and neutron background
TOTAL	3.17x10^{18}	5.89x10^{5}	

Table 5.8: *Summary of statistics and samples measured during the ^{242}Pu(nγ) campaign at n_TOF-EAR1 (1 day $\sim 10^{17}$ protons).*

Together with ^{242}Pu(n,γ), it was necessary to perform some auxiliary measurements on the samples described in Section 5.4.2 to accurately characterize the background, normalize the capture yield and validate the analysis procedure:

- The background induced by the sample assembly was determined with the *dummy* target.
- The background caused by the γ-rays in the beam was assessed by using the lead target, that scatters photons without absorbing significantly neutrons in the beam (see Section 6.6.2).
- The same lead measurement allowed extracting the shape of the neutron scattered background, since its neutron cross section is completely dominated by the elastic channel (see Section 6.6.2).
- The measurement the gold target having the same diameter than the ^{242}Pu one was used for normalization via the Saturated Resonance Method (SRM) [210] (see Section 6.9.1) and for validation of the analysis in the URR (see Section 8.2).
- The beam-related background for the measurements of the gold and lead samples was assesed by measuring the *empty* sample.
- Last, measurements without beam were carried out without and with the ^{242}Pu targets in place for determining the environmental and ^{242}Pu activity backgrounds.

Chapter 6

Capture yield at n_TOF-EAR1

This chapter is devoted to the data reduction process from the digitized signals of the C_6D_6 to the final capture yield. The description of the pulse shape analysis and histogram building routines in Section 6.1, is followed by the calibration of the C_6D_6 detectors and the analysis of the neutron beam monitors in Sections 6.2 and 6.3, respectively. The calculation of the capture yield as a function of the neutron energy requires a reconstruction from the measured time-of-flight (Section 6.4), the correction for the detector dead time (Section 6.5) and the subtraction of the backgound in our measurement (Section 6.6). Last, the details on the efficiency assesment with help of the Pulse Height Weighting Technique, the absolute normalization of the yield via the Saturated Resonance Method, high neutron energy limit of the extracted yield, and the systematic uncertainties in this analysis are given in Sections 6.7-6.10. The high energy resolution of the facility, large accumulated statistics and careful analysis methods have allowed to extract a capture yield from 1 eV to 500 keV. The resolved resonance region (RRR) of the capture yield extends up to 4 keV, with a systematic uncertainty of just 3% dominated by the normalization and efficiency assesment. The fast region or unresolved resonance region (URR), where the background subtraction is the critical issue, has been determined with an accuracy ranging from 7 to 16%.

6.1 Data processing and event building

6.1.1 Pulse Shape Analysis (PSA) routine

The digitized signals recorded for each detector by the n_TOF DAQ (see Section 5.4.4) are first stored in the CERN Advanced STORage manager (CASTOR). The data reduction process starts with the offline analysis of the digitized movies carried out with a flexible (i.e. can be easily adapted to different detectors) Pulse Shape Analysis routine. The details on this PSA routine, especially designed for the analysis of n_TOF data and written in C programming language, are described in Refs. [223, 224].

The PSA routine has the following goals:

- Identify all the real signals and reject the spur artifacts, such as electronic noise, etc...
- Correct for the experimental issues related to baseline distorsion after the γ-flash, pile-up, etc...
- Reduce the amound of data for each identified pulse from the original digitalized signal (14 bits, 1 GHz sampling rate) to the relevant parameters of each pulse: time, amplitude, area.
- The common information of all the signals recored during a neutron bunch must be stored for every signal and for all the detectors: date, time, type of bunch, area of the PKUP, BCT value.
- Generate small and easily accesible output files, being a ROOT [225, 226] file with an internal *Tree* structure the best suited for this purpose.

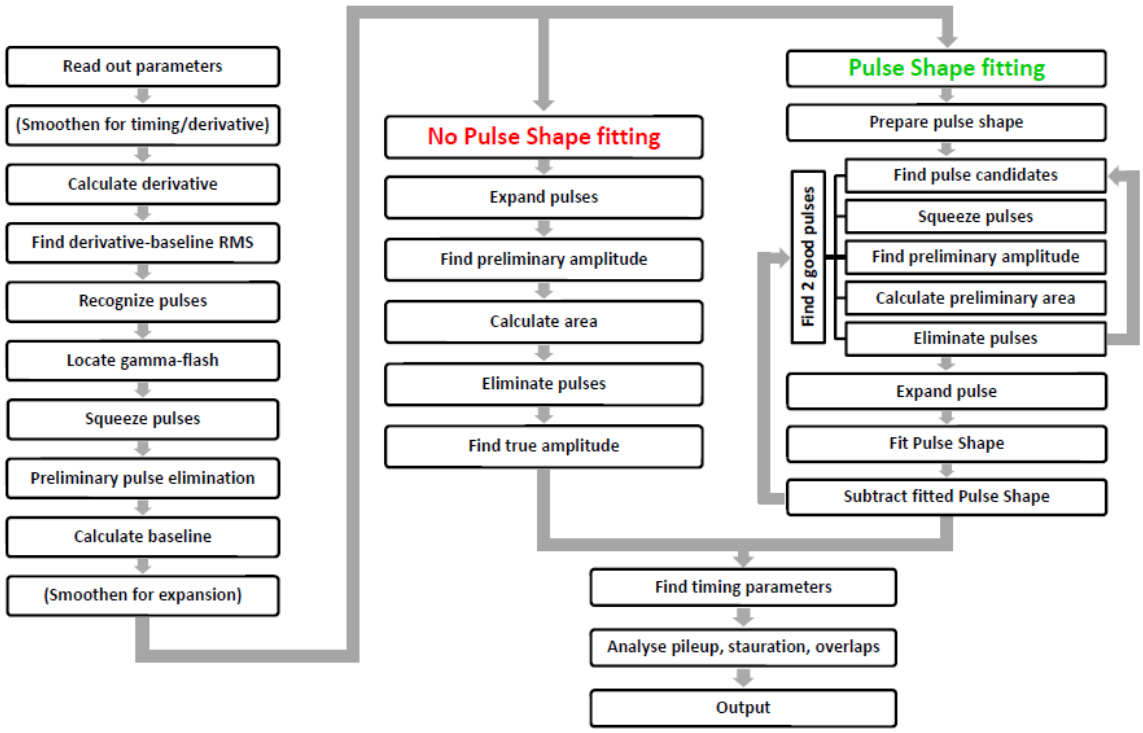

Figure 6.1: *Flowchart of the Pulse Shape Analysis Routine showing the steps followed to extract the relevant parameters of each signal identified in the digitized movies.*

The basic working procedure of this program is summarized in the flowchart in Figure 6.1. The main steps in the working process of the PSA routine are (in the order they are performed) [224]:

- User input readout: The main parameters of the routine (detector name, number, step sizes, γ-flash identification options, Pulse Shape Fitting or direct integration, etc...) are given in a separate user input file.

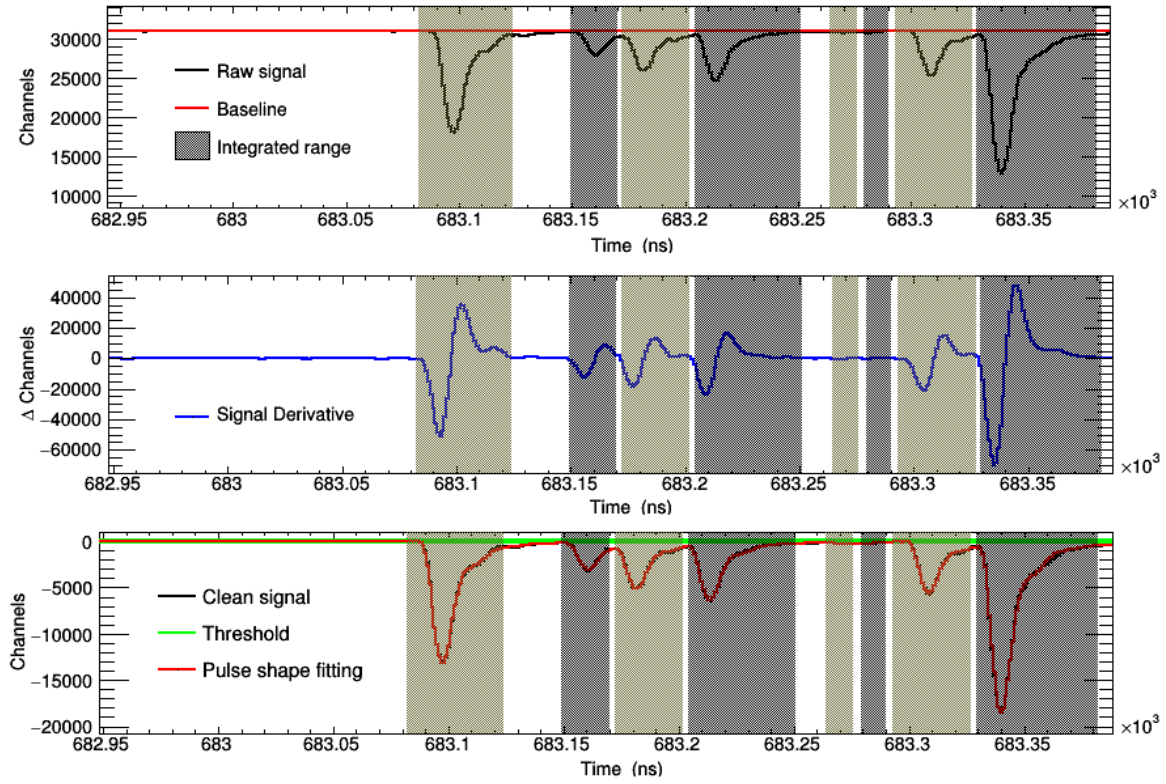

Figure 6.2: *Peak fitting procedure followed by the Pulse Shape Analysis routine: fragment of the raw digitized movie and baseline determination (top), signal derivate used for pulse identification (middle), Pulse Shape Fitting of the baseline-subtracted (clean) signal (bottom).*

- Derivative calculation and pulse recognition: Pulses are recognized in the raw signal (top pad of Figure 6.2) when its derivative (middle pad of Figure 6.2) crosses in a given sequence two thresholds determined from the Root Mean Square (RMS) of the baseline.
- γ-flash identification: It is identified as the first pulse either crossing a given threshold (much larger than normal signals) or reaching saturation (always the case for the response of C_6D_6 detectors to the γ-flash). The γ-flash is later eliminated during the Pulse Shape Fitting.
- Preliminary pulse rejection: Possibility to reject pulses using an amplitude, width or area/amplitude ratio threshold. The latter is very useful because the signals and the noise usually very different values.
- Baseline calculation: Different approaches can be implemented in two or three separated time intervals. Usually, the baseline is calculated as a smooth adapting function (*moving maximum*) in the time range where the baseline is still restoring from the γ-flash, and is set to a constant value at longer time-of-flight values.
- Direct pulse area and amplitude extraction: If no Pulse Shape Fitting is used, the amplitude is extracted either from the pulse maximum or from a parabolic fitting

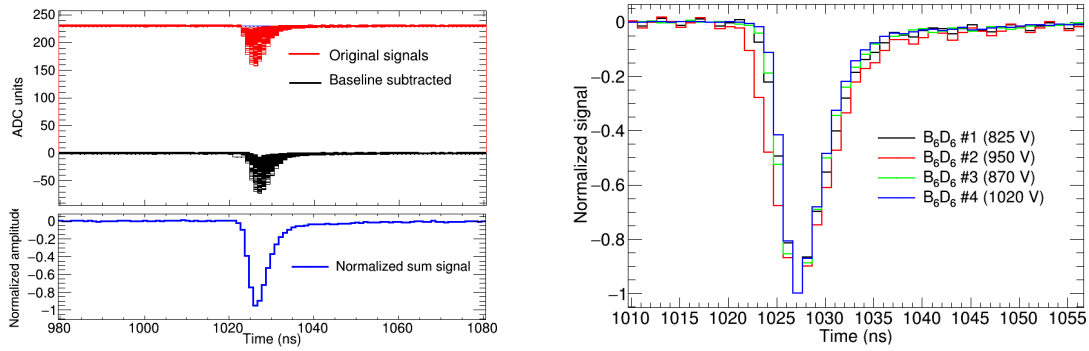

Figure 6.3: *Left: Output of the average pulse calculation code showing hundreds of aligned pulses and the result of their normalized sum. Right: Average pulse shape of the four BICRON detectors used for the Pulse Shape Fitting of the digitized signals.*

around the maximum. Then, the area under the pulse is calculated by the simple pulse integration.

- Pulse Shape Fitting: This was the option used in this work. The signals are analyzed by comparing each of them with reference pulse shapes characteristic of each detector (see Ref. [227] for details). The reference pulse shapge (right panel in Figure 6.3) for each detector is calculated as the average of many signals (see left panel of Figure 6.3). The performance of the Pulse Shape Fitting on a real signal is shown in the bottom panel of Figure 6.2. This method improves the accuracy of the extracted pulse area, even in situations of low amplitued with significant pile-up. In this case, the tails of the fitted pulse shapes serve as the baseline for the following (see Figure 6.4).
- Timing properties: The measured arrival time of a signal t_m, related to the neutron time-of-flight by means of Eq. (5.3), is calculated using a constant fraction discrimination approach.

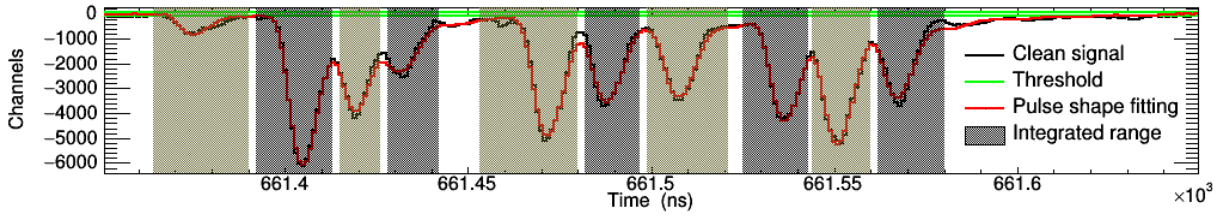

Figure 6.4: *Fragment of a C_6D_6 detector digitized movie with a significant pulse pile-up illustrating the good performance of the Pulse Shape Fitting procedure implemented in the PSA routine.*

6.1.2 TTOFSort data reduction routine

The relevant parameters of each signal (detector number, time, area, amplitude, etc...) together with the information of the corresponding neutron bunch (proton intensity (BCT value), PKUP signal integral, time of the γ-flash, type of bunc, etc...) are extracted with

the PSA routine and stored in a ROOT file with one *TTree* structure per detector type and one *TBranch* for each parameter. Each ROOT file contains the data for one *run* of the DAQ, which contains usually thousands of neutron bunches, corresponding to a few hours of beam time.

The second step in the data reduction process is carried out with a routine developed within the n_TOF Collaboration, called TTOFSort [228]. This library contains commands to create neutron time-of-flight histograms from n_TOF event data stored in a series of the mentioned ROOT files. The main features of this library are the following:

- It aims at setting a well stablished procedure for the time-of-flight data analyses, avoiding common mistakes and allowing the physicists in the n_TOF collaboration to concentrate on data analysis instead of on coding.
- It allows to follow the data analysis steps in a clear way and thus facilitates the intercomparison between the analysis carried out by different physicists.
- Requires only a simple ROOT script which contains only the commands reflecting the decisions taken by the physicist on cuts, coincidences, binning, calibrations, weighting functions, etc...
- The functions are implemented in a separate file from the analysis script.
- The main analysis routines required for the data reduction of a large variety of detectors, including the C_6D_6 detectors, are implemented in this library.
- It outputs the distribution of counts for each detector as a function of the signal amplitude, area and time as histograms in a series of ROOT files.

For the case of the analysis of the C_6D_6 detectors, the data reduction was carried out following these steps. The data TTOFsort routine takes the ROOT data with the information from the invidual signas and produces a series of histograms of interest for the analysis after calibrating the detector signal in energy and appliying the selected tthressholds in time (i.e. neutron energy), deposited energy and pulse intensity. It also applies the multiplication by the weighthing function, hence generating both weighted and unweighted histograms. The histograms of interest, summed for all the runs corresponding to the same measured sample (Pu, Au, dummy, empty, beam-off), are weighted and unweighted counts as a function of γ-ray energy deposition and of time-of-flight.

The histograms for the C_6D_6 can later be normalized to the number of bunches, to the proton beam intensiy (using either the BCT value or the PKUP signal area) or to the neutron beam intensityy, given by the counts in the triton peak of the SiMon (see Section 5.4.3).

6.2 Detector calibration

6.2.1 Calibration in energy and resolution

As we introduced in Section 5.3.2, C_6D_6 detectors do not behave as Total Energy Detectors (TED). To satisfy the principles of the TED, they require mathematical manipulation of the detector response, the Pulse Height Weighting Technique (PHWT) (see Appendix B.1 for the details), which consists on multiplying each signal by a deposited-energy-dependent weight, and for this, it is crucia to have a very accurate amplitude to energy calibration. the application of the PHWT.

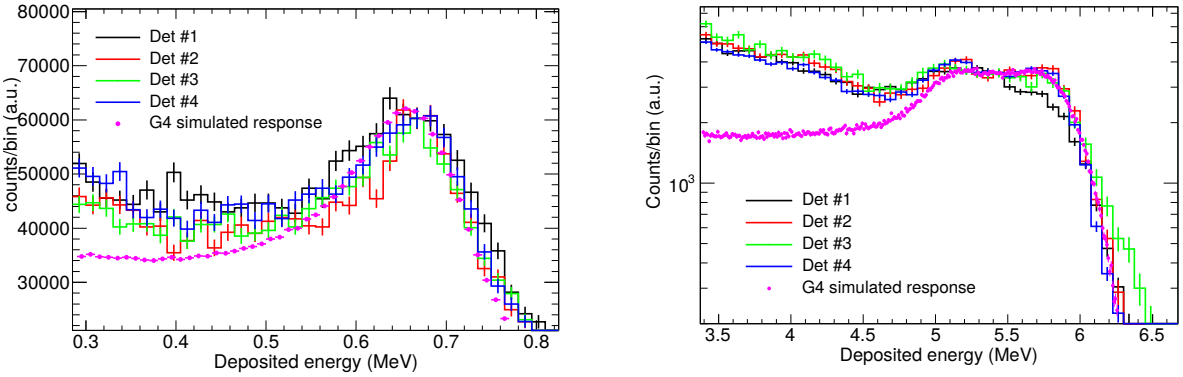

Figure 6.5: *Comparison between the simulated (broadened) response and the experimental energy-calibrated response of the individual C_6D_6 detectors to the γ-rays emmited from ^{88}Y (left) and ^{244}Cm-^{13}C (right).*

The C_6D_6 detectors were periodically calibrated using the following sources: ^{137}Cs, ^{88}Y, ^{241}Am-^{9}Be and ^{244}Cm-^{13}C. Since the response of C_6D_6 detectors presents no photopeaks due to its low Z and density, the position of the compton edges in the amplitude histograms was used to carry out the calibrations based on a comparison of the measured and simulated deposited energy distributions. Figure 6.5 shows the good agreement between the experimental and simulated responses. An example of the energy and resolution calibrations is given in Figure 6.6. In reality, the right panel in Figure 6.6 shows the dependence of the resolution broadening $\sigma_E(E_\gamma)$ with the γ-ray energy, fitted to a function of the form

$$\sigma(E_\gamma) = p_0 \cdot E_\gamma^{1/2} \; + \; p_1 \cdot E_\gamma \; + \; p_0 \cdot E_\gamma^2, \tag{6.1}$$

from which the energy resolution is calculated as

$$R(E_\gamma) = \frac{2.35 \; \sigma(E_\gamma)}{E_\gamma}, \tag{6.2}$$

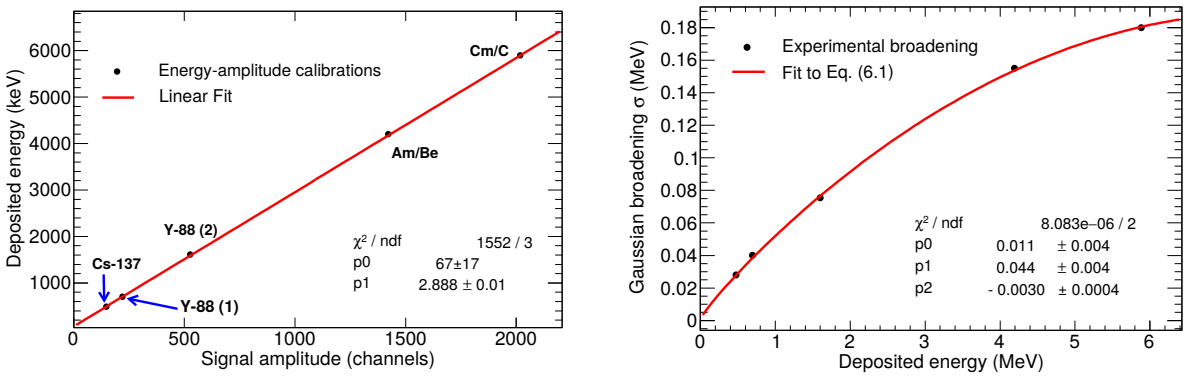

Figure 6.6: *Calibration of C_6D_6 detector #1 in energy (left) and resolution broadening (right). The energy to amplitude correlation and the energy dependence of the detector resolution were obtained from the measurement of the γ-ray sources indicated on the left panel.*

6.2.2 Gain stability

The stability of the gain along the measurement also affects the weighting factor in a significant way. Previous works [200] have shown that the weight for signals of a given energy deposition varies linearly with the variation in gain (i.e. a 5% increase in the gain will mean 5% more counts in the weighted histograms). Gain variations, which have been a serious issue in experiments with highly radioactive samples using C_6D_6 detectors [229, 230, 231], were monitored with the evolution of the calibration spectra along the measurement. In particular, short measurements with an ^{88}Y source taken periodically along the experimental campaign served to appreciate a slow gain shift, shown in the left panel of Figure 6.7. The impact of the gain shift is better observed for higher γ-ray energies (see right panel of Figure 6.7). Small time-dependent corrections to the original calibrations were required to recover a stable position of the calibration *peaks* along the measurement. After the correction, the energy-calibrated spectra registered with calibration sources on different dates fall on top of each other, as it is illustrated in the right panel of Figure 6.7.

The time dependent energy calibration required to split the full set of runs into five different time intervals, and apply a different (time-dependent) calibration to each of them. Table 6.1 summarizes the distribution of runs and calibrations along the measurement. After the application of the PHWT, the original amplitude-to-energy calibration was inducing sytematic deviations of 3% in the ^{242}Pu weighted counting rate along the measurement. After the inclusion of the time-dependent calibrations, the ^{242}Pu weighted counting rates in the differents subsets were in agreement within 0.5%, which has been assumed as the associated uncertainty.

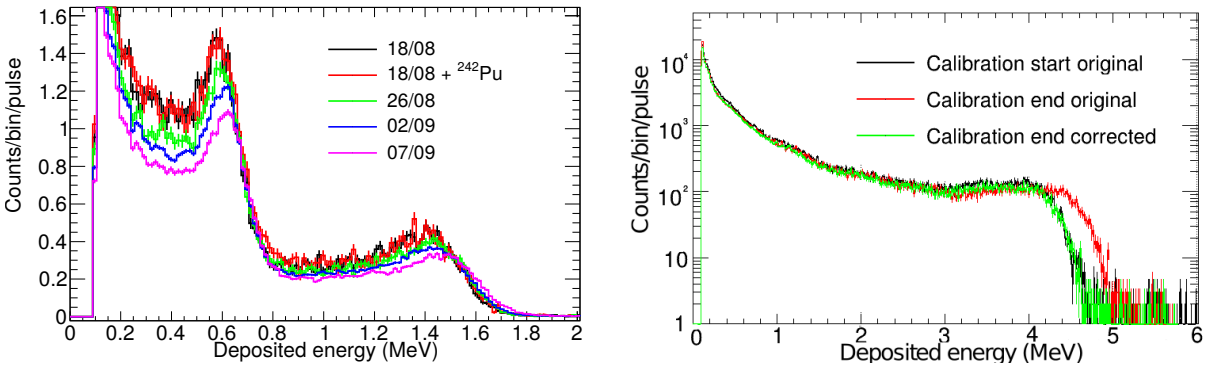

Figure 6.7: *Left: Time evolution of BICRON #1's response to an ^{88}Y calibration source along the experimental campaign using a fixed amplitude to energy calibration. Right Energy-calibrated response of BICRON #1 to a ^{241}Am-^{9}Be source at the beginning (black line) and the end (red line) of the measurement using a fixed calibration. A time-dependent calibration is required to correct for the shifting gain (green line).*

Table 6.1: *Time-dependent calibration: Range of runs, dates and measurements included in each data subset of the $^{242}Pu(n,\gamma)$ measurement.*

Calib.#	Run range	Dates	Measurements
1	2410 - 2437	17/08 - 21/08	^{242}Pu, dummy, beam-off
2	2438 - 2470	22/08 - 28/08	^{242}Pu,^{197}Au,dummy, empty
3	2472 - 2534	29/08 - 07/09	^{242}Pu, dummy, Pb, beam-off
4	2535 - 2575	08/09 - 14/09	^{242}Pu, beam-off
5	2579 - 2592	14/09 - 16/09	dummy

6.3 Beam monitors and detector counting rates

6.3.1 Analysis of the beam monitors and correlations

The counting rates resgistered by the C_6D_6 detectors for each of the measurements described in Section 5.4.5 must be normalized to the integrated neutron flux or, equivalenty, to the number of protons before we can proceed to substract the backgrounds. Typically, measurements at n_TOF are normalized to the nominal proton intensity per pulse (7x10^{12} p) and expressed as *coumts/pulse*. For the case of the measurements with no beam (*beam-off*), the normalization is carried out relative to the number of bunches (i.e. DAQ trigers, equivalent to adquisition time).

Three different monitors (BCT, PKUP, and SiMon) are available at n_TOF (see Section 5.4.3) to ensure an accurate determination of the beam intensity. In order to study the consistency of the value extracted from the three systems, a detailed analysis of the bunch-per-bunch correlation has been carried out. This analysis allowed us to reject bunches were the ratio between the monitors deviated significantly from the average.

In the top panel of Figure 6.8 we show the ratio of the PKUP signal area to the BCT value

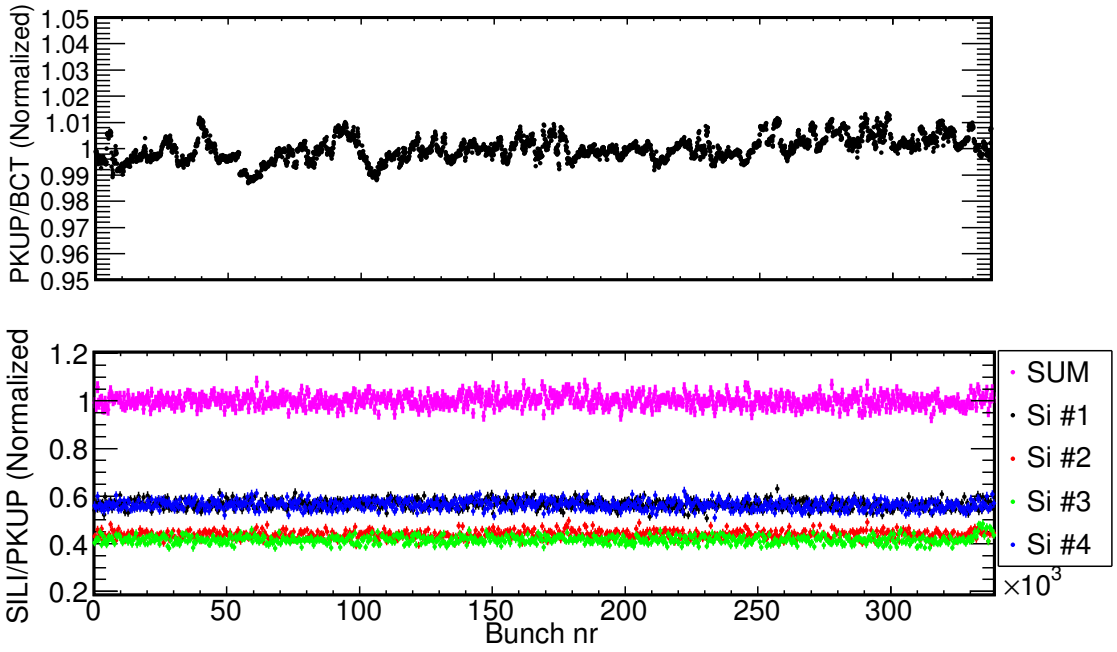

Figure 6.8: *Top: Ratio of the PKUP area to the BCT value as a function of the bunch number. Bottom: Ratio of the SiMon counting rates (i.e. integral of the triton peak, for neutron energies from thermal to 1 keV) to the area of the PKUP signal (see text for details).*

after the wrong bunches had been excluded. Aiming at reducing the statistical fluctuations of the bunch-per-bunch values, each point correspond to one hundred bunches. The ratio PKUP/BCT (normalized to the average value of the whole measurement) fluctuates within 1% around unity. The bottom panel of Figure 6.8 shows the nice stable behaviour of the ratio of the counts in the SiMon to the BCT value (again normalized to the average ratio). A small deviation of the normalized counting rate of Si detectors #1 and #3 was observed at the end of the measurement(from bunch nr. 330x10^3). For this reason, only Si #2 and #4 were used as a reference to monitor the neutron beam.

The study shown in Figure 6.8 was carried out individually for each measured sample to identify possible systematic deviations in the beam monitors between the different data subsets. These possible deviations would affect the relative normalization to proton/neutron intensity, thus affecting the background subtraction and the normalization. The distributions of buch-per-bunch normalized ratios (PKUP/BCT, SiMon/BCT and SiMon/PKUP) for the ^{242}Pu(n,γ) measurement are shown in Figure 6.9 and summarized, for each measurement and only dedicated bunches in Table 6.2.

From the values in Table 6.2 we conclude that the most accurate variable for monitoring the beam in the BCT, for which the normalization to beam intensity is in agreement within less than 0.5% for all the measurement. This value is assumed as the uncertainty related to the normalization to protons in the background subtraction (see Section 6.6) and in the absoute normalization of the ^{242}Pu capture yield to the measured ^{197}Au yield (see

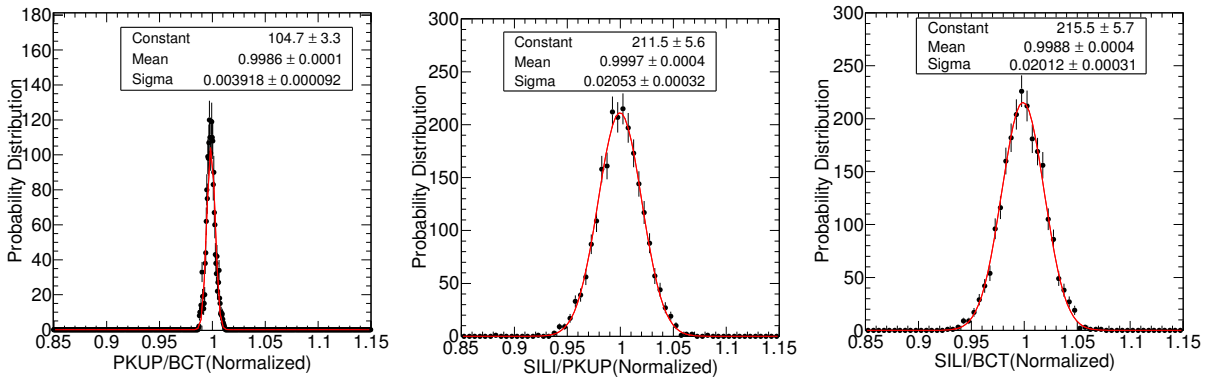

Figure 6.9: *Distribution of the ratios between beam monitors for the runs corresponding to the $^{242}Pu(n,\gamma)$ measurement normalized to the average value of the whole campaign: PKUP/BCT (left), SiMon/PKUP (center) and SiMon/BCT (right).*

Table 6.2: *Ratios of the integrated beam intensity (PKUP/BCT, SiMon/BCT and PKUP/SiMon) for the different sub-measurements in the experimental campaign.*

	Ratio normalized to average		
Measurement	**PKUP/BCT**	**SiMon/BCT**	**PKUP/SiMon**
^{242}Pu	0.999	0.998	1.002
Dummy	1.001	1.004	1.003
Empty	0.995	1.002	0.998
^{197}Au	1.004	0.999	1.004
^{nat}Pb	1.002	1.006	1.004

Section 6.9).

6.3.2 Stability of the C_6D_6 detectors' counting rates

Figure 6.10, shows the ratio between the counting rates per pulse (using the BCT as reference) registered in the four C_6D_6 detectors as a function of the bunch numbeer. In order to reduce the statistical fluctuations each point in this plot corresponds to 100 bunches. This kind of plot allowed us to identify bunches with problems associated to beam stops, wrong detector performance, etc... Figure 6.10 shows the nice correlation between the counting rates in the C_6D_6 detectors and the neutron beam itensity after the anomalous bunches, representing a negligible fraction of the statistics (<5%), had been discarded.

6.4 Time-to-energy calibration

The classic relation in Eq. (5.2) allows us to calculate the kinetic energy of the neutron from its time-of-flight. This expression considers that the flightpath and time-of-flight for a

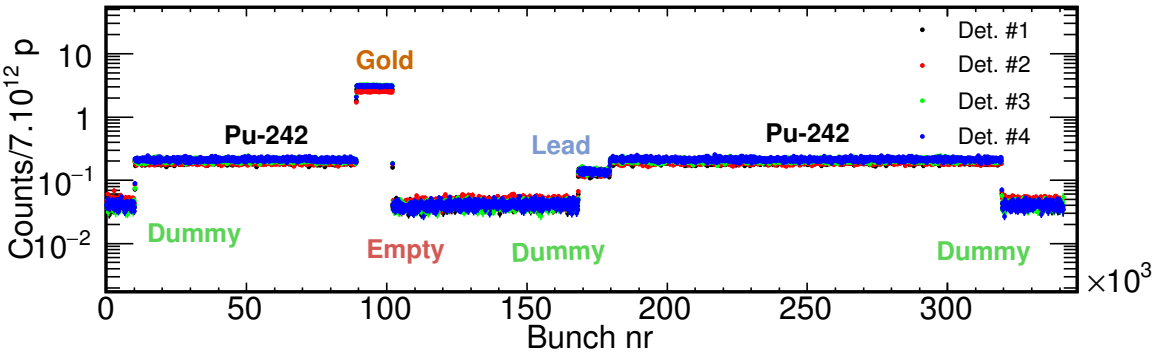

Figure 6.10: *Counting rates of the individual C_6D_6 detectors normalized to the BCT value showing a stable value with time for the different measurements in the experimental campaign.*

neutron of energy E_n are fixed values. However, different experimental effects characteristic of the time-of-flight facilities turn these fixed value into distributions (see Section 5.2.2 for the details). The convolution of these distributions is known as the Resolution Function (RF) $R_E(E_n)$. As we introduced in Section 5.2.2, one of the consequences of the RF is the shift between the real neutron energy and the one calculated from the measured time-of-flight.

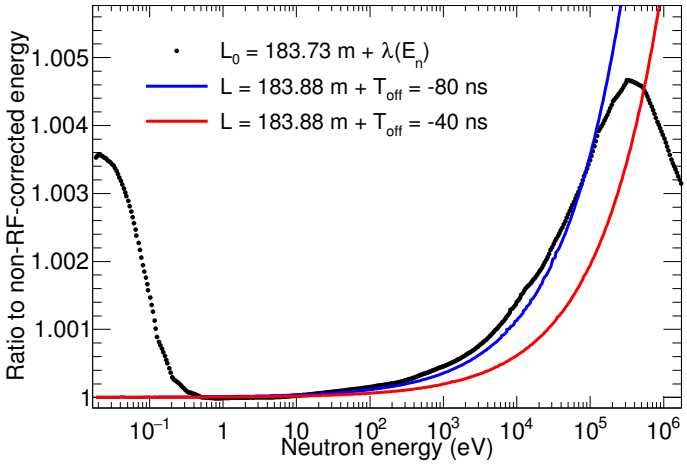

Figure 6.11: *Ratio between reconstructed neutron energy using methods (2) and (3) and the non-RF-corrected energy of method (1). Two different time values of T_{off} for method (3) are compared to illustrate that none of them is able of reproducing the real shift extracted from the MC simulations.*

Different approaches to include the effect of the RF in the time-to-energy conversion can be followed:

1. Assume that there is no shift (i.e. assume fixed L and t) and include the full numerical RF in the R-Matrix analysis so that the position of the resonances is shifted in the fitted cross section (see Figure 5.14). With this method, the correct resonance energies

are extracted from the R-Matrix parameterization, although the position in energy of the resonances in the experimental yield is wrong.

2. Replace the fixed L in Eq. (5.2) by an energy-dependent effective flightpath

$$L_{eff}(E_n) \;=\; L_0 \;+\; \lambda(E_n), \tag{6.3}$$

where L_0 is a fixed length between the target exit to the sample position in the experimental area. The value of L_0 is fitted using a resonance of energy E_0, so that it satisfies

$$E_0 \;=\; 72.29^2 \;\frac{L_{eff}(E_0)^2}{t^2}. \tag{6.4}$$

$\lambda(E_n)$ in Eq. (6.3) is the average moderation path for neutrons of a given energy, calculated from MC simulations as the mean value of the L_{mod} distribution in Figure 5.13.

3. Use a fixed L_0 and add a suitably chosen time offset T_{off} to the time-of-flight t in Eq. (5.2). For each neutron energy, T_{off} corresponds to a given equivalent moderation lenght λ. This method, explained in Ref. [192], leads to an equivalent shift in energies in the energy range from 1 eV to 100 keV to that of method 2.

Figure 6.11 shows the ratio of the corrected neutron energy, using methods (2) and (3), to the uncorrected neutron energy obtained with a fixed L and the measured time-of-fligh t. Different values for T_{off} are compared in solid lines to illustrate that method (2) does not provide a perfect reproduction of the shape of the $\lambda(E_n)$ distribution (black dots) at thermal and at high energy.

6.4.1 Resolved Resonance Region

The goal of the data reduction process described in this chapter is to extract the capture yield as a function of the neutron energy. Aiming at correcting for the energy shift of the resonances in the experimental yield we chose method (2) for our time-energy calibration.

After the fixed flight path L in Eq. (5.2) is replaced by the energy-dependent effective flightpath in Eq. (6.3), the time-to-energy calibration becomes

$$E_n \;=\; 72.29^2 \left(\frac{L_0 + \lambda(E_n)}{t_m - t_0}\right)^2, \tag{6.5}$$

where t_m is the signal time extracted by the PSA routine (see Section 6.1.1) and t_0 is the start time calculated via Eq. (5.3) using as time reference the arrival time of the γ-flash. In order to extract the value of L_0, we first fitted $L_{eff}(E_n)$ to adjust the energy of the well known 4.9 eV resonance in the ^{197}Au(n,γ) yield. From the fitted value $L_{eff}(4.9\ eV) = 183.88(5)$ m, Eq. (6.3) leads to a value of the geometrical flightpath $L_0 = 183.73(5)$ m.

The distribution of total counts in the ^{242}Pu(n,γ) measurement as a function of the time-of-flight is shown in the left panel of Figure 6.12. The right panel of the same figure

shows the corresponding distribution as a function of the neutron energy calculated by means of Eq. (6.5).

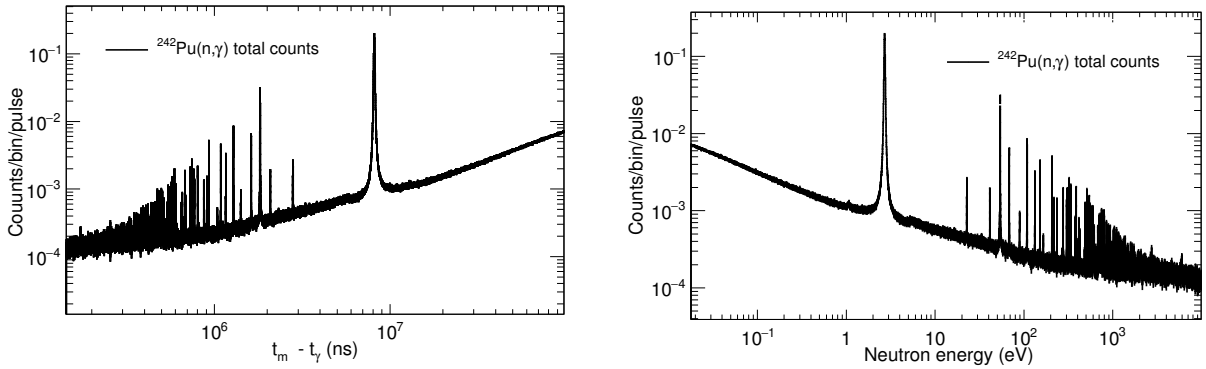

Figure 6.12: *Left: Total counting rate registered in the ^{242}Pun,γ) measurement as a function of the measured time (T_γ subtracted). Right: Same distribution as a function of the reconstructed neutron energy calculated with Eq. (6.5).*

6.4.2 Unresolved resonance Region

The time-to-energy calibration in the URR (1-500 keV), should perfectly match the dips in the counting rate with the ones in the evaluated flux [178] (absorption in Al and Mn in the spallation target). However, the approach for the time-to-energy calibration used in this work (see Section 6.4.1) and the method used for the neutron flux evaluation [178] are not the same, and as a result a significant missmatch in the dip positions was found.

To solve the deviation in the dip position, an effective time-enegy calibration was implemented for the URR. The goal of the conversion from time-of-flight to neutron energy was to match the energy position of the most prominent dips in the evaluated flux $\phi(E_n)$ [178], in the energy region between 30 and 500 keV (see Figure 5.11), to their corresponding position in the time-of-flight distribution of the capture counting rates. In order to achieve this goal we used method 3, hence adding a time offset T_{off} to the measured time-of-flight to introduce the appropiate energy shift in the energy range of interest for the URR.

With the addition of this time offset, the general expression for the time-energy calibrations in Eq. (5.2) becomes

$$E_n \;=\; 72.29^2 \left(\frac{L}{t_m - t_0 - T_{off}}\right)^2, \tag{6.6}$$

where the fixed flight $L \;=\; L_{eff}(4.9\ eV)$ is the effective flightpath that provides a good energy calibration at low neutron energies (4.9 eV ^{197}Au resonance). The time offset $T_{off} = -100(30)\ ns$ was fitted to match the neutron energy of the dips in the evaluated flux with the corresponding dips in the time-of-flight distribution of the ^{197}Au(n,γ) data, as it is shown in the left panel of Figure 6.13.

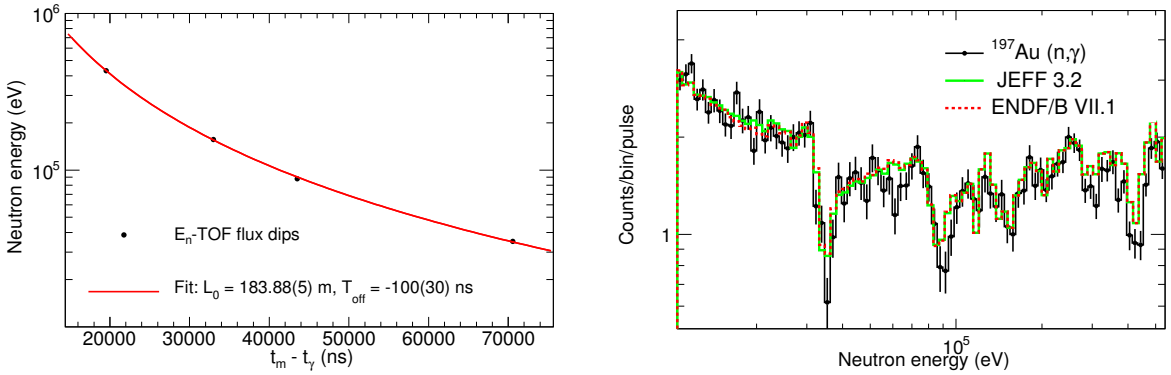

Figure 6.13: *Effective time to energy conversion in the keV region. Left: Time-of-flight (t_m-t_γ) position of the dips in the ^{197}Au counting rate vs. the corresponding neutron energy in the evaluated neutron flux. The red line is a fit of the time offset t_{off} assuming a fixed flightpath L_{eff} = 183.88 m, that matches the low energy resonances. Right: $^{197}Au(n,\gamma)$ counting rate as a function of the reconstructed neutron energy using Eq. (6.6) compared to the ENDF and JEFF cross sections convoluted with the n_TOF evaluated flux [178].*

The good reproduction of the dip energies in the flux using this effective time-to-energy calibration is shown in the right panel of Figure 6.13, where we compare the neutron-energy-calibrated ^{197}Au(n,γ) with the expected counting rate ($\sigma_\gamma(E_n)$ x $\phi(E_n)$) according to the ENDF/B-VII.1 and JEFF-3.2 evaluations.

6.5 Dead time/Pile-up correction

One of the corrections to be applied to the counting rates (see Figure 6.12) is related to the dead time or the signal pile-up. The pile-up is usually defined as the situation when two detector signals occur within a given time interval, τ, in which they can not be distinguished as two independent signals by the PSA routine and are thus considered as a single signal. In Section 6.1.1, we showed that the Pulse Shape Fitting of the C_6D_6 detectors allows us dealing with situations with significant pile-up (see Figure 6.4). However, for increasing counting rates, the routine starts to loose pulses. The time τ corresponds to the time after one signal in which the PSA routine is not able of recognize a new one, and can be treated as a dead time.

Depending on the type of the dead time, different methods are described in the literature to correct for the count loss. First, the dead time of a detection can be classified as:

- Paralyzable: The second pulse overlaps with the previous one, expanding the dead time to $\tau + \Delta\tau$.
- Non-paralyzable: The detector is completely blind to the arrival of a second pulse during the time interval τ.

In the case of our detection system, were are affected by a paralyzable dead time. In

this case, the corrected counting rate R has to be calculated numerically from

$$C_d = R\,T\,e^{-R\tau}, \tag{6.7}$$

where C_d are the counts measured in a time interval T and $R = C/T$ is the true (dead time corrected) counting rate. This calculation of R is rather complex. However, it can be proofed that if the pile-up correction is small, the correction for paralyzable and non-paralyzable dead time is approximately the same [232]. For a non-paralyzable system, the true number of counts C in a time interval T is

$$C = C_d + \frac{C}{T}C_d\tau, \tag{6.8}$$

and from this expression the true C and measured C_d number of counts are related by

$$C = \frac{C_d}{1-\tau\frac{C_d}{T}} = F_\tau C_d, \tag{6.9}$$

where F_τ is defined as the dead time correction. From the analysis of the time lapse

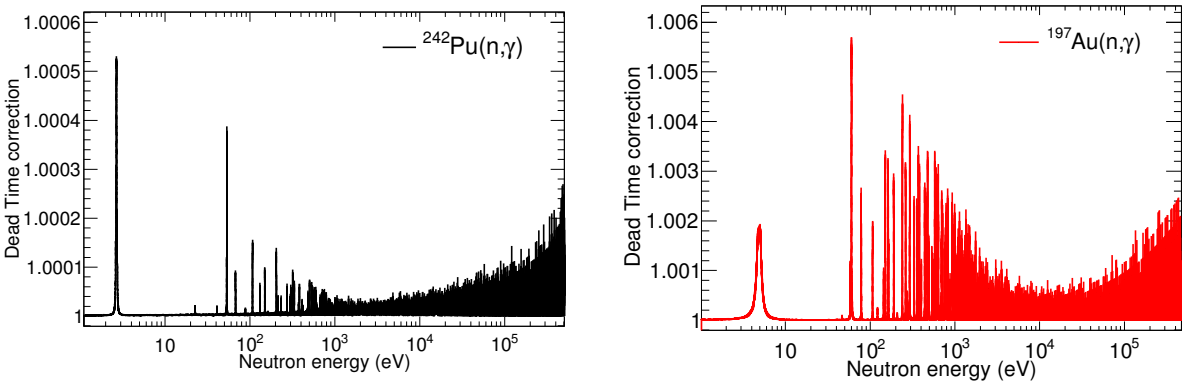

Figure 6.14: *Dead time correction for C_6D_6 detector #4 during the $^{242}Pu(n,\gamma)$ (left) and $^{197}Au(n,\gamma)$ (right) measurements calculated under the non-paralyzable approximation given by Eq. (6.9).*

between consecutive signals in different measurements along the campaing, we observed that this distributions presents a smooth drop below 20 ns. This value, which corresponds approximately to twice the FWTM of the BICRON detectors' signals (see Figure 6.3), has been assumed as the dead time τ of the detection system. The corresponding dead-time correction, displayed in Figure 6.14, is lower than 1% even in the case of ^{197}Au. The small value of the dead time correction supports the validity of the paralyzable model.

6.6 Background subtraction

Assessing the background in our measurement is a critical point for the analysis, in particular in the URR where both background and capture show a smooth shape without

resonant structures. A series of ancilliary measurements were carried out to assess the different sources of background. The total background as a function of the neutron energy $B_T = B_T(E_n)$ is given by

$$B_T = B_{dummy} + B_{off}^{Pu} + B_n^{Pu} + B_\gamma^{Pu}, \tag{6.10}$$

where the individual background contributions are either directly asessed or indirectly estimated from the measurement the ancilliary samples described in Section 5.4.2. The background sources which can be directly determined are discussed in Section 6.6.1. On the other hand, the indirect estimation of the contribution of in-beam γ-rays and neutrons scattered in the sample is described in Section 6.6.2.

Table 6.3 summarizes the integral contribution of each term in Eq (6.10) in the URR, showing that the capture accounts only for at maximum 15% of the total counting rate. In the RRR, the background subtraction is not so critical since we can always observe resonant structures on top of a residual background. Moreover, even if the background has not been completely removed, it can be fitted and subtracted during the R-Matrix analysis (see Section 7.1.2).

6.6.1 Direct assesment with ancilliary measurements

Among the different background contributions in Eq. (6.10), some are directly assesed from several ancilliary measurements (see Section 5.4.5). Figure 6.15 shows the total counts per pulse (with energy deposited in the detectors E_{dep} larger than the threshold of 150 keV) registered in each detector as a function of the reconstructed neutron energy. In the following, the data reduction process will be shown for all the detectors combined, unless otherwise specified.

The major background contributions in Eq. (6.10), displayed in Figure 6.15, are:

- B_{dummy}: The measurement of the *dummy* target includes all the beam-related background in Eq. (6.10) accounting for neutrons and γ-rays scattered in the beamline, vacuum windows and target backings. Thanks to the use of thin backings, the increase in background is just 5% in the URR with respect to the situation with no

Table 6.3: *Relative contribution of capture and the different background components in two energy regions in the URR. The result for the low and high energy threshold used for the final cross section are compared.*

	Contribution (1-10 keV)(%)		**Contribution (10-100 keV)(%)**	
	E_{thr}=250 keV	**E_{thr}=1 MeV**	**E_{thr}=250 keV**	**E_{thr}=1 MeV**
B_{dummy}	75.8	80.7	80.1	84.3
B_{off}^{Pu}	7.5	4.4	4.1	2.4
B_γ^{Pu}	0.9	0.2	1.3	0.3
B_n^{Pu}	1.1	0.8	1.2	1.1
^{242}Pu(n,γ)	14.7	13.9	13.2	11.9

sample in the beam (*empty* background in the following). This implies that a deviation of 10% in the *dummy* backings mass with respect to the ones in the ^{242}Pu target would affect the overall background by just 0.5%, which is crucial in the URR, where the *dummy* background accounts for 75-80% of the total counts (see Table 6.3).

- B_{off}^{Pu}: The *beam-off* contributions B_{off}^{Pu} with and without the ^{242}Pu target in place where estimated with *beam-off* measurements. In addition, the *beam-off* counting rate was fitted to a constant value as a function of time and then substracted to each measurement (^{242}Pu, ^{197}Au, Pb, *dummy*, *empty*) individually. This contribution dominates the background only at time-of-flight corresponding to neutron energies below 10 eV.

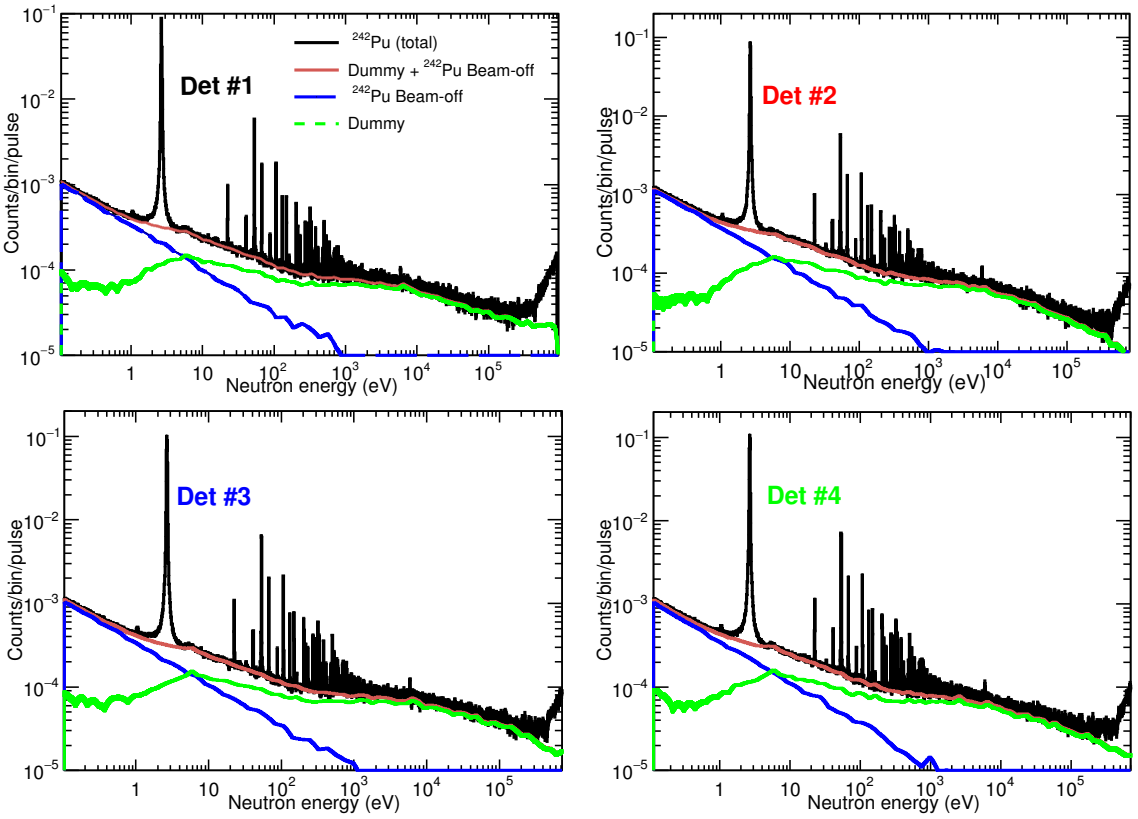

Figure 6.15: *Total Counting rates per pulse for the ^{242}Pu and major background contributions as a function of the neutron energy registered by the four C_6D_6 detectors.*

The two panels of Figure 6.16 show the measured counting rates as a function of the deposited γ-ray energy showing the same background contributions than in Figure 6.15. While the left pannel contains data for the whole neutron energy range under study (1 eV to 500 keV), the right panel corresponds just to neutron energies inside the first capture resonance (2.1 - 3.3 eV). The latter hence shows an enhaced capture to background ratio compared to the detector response integrated over the full neutron energy range. The spectra of deposited energy indicate that the the *beam-off*, i.e. the room and ^{242}Pu sample activity background are mainly low energy γ-rays while the high energy γ-ray background is related to the beam (*dummy*).

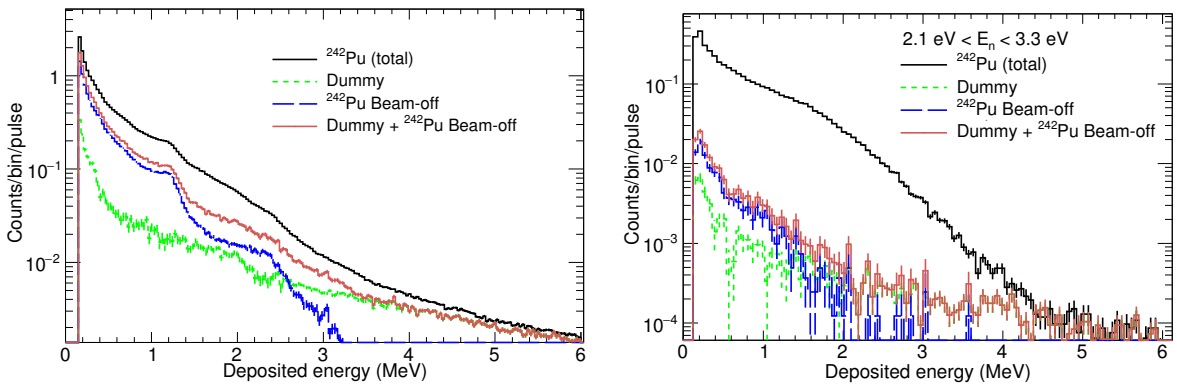

Figure 6.16: *Energy deposition in the C_6D_6 detectors corresponding to the full neutron energy range (left) and with neutron energy cuts to select just the largest resonance (2.67 eV) (right).*

6.6.2 Estimation of the neutron and γ-ray scattering backgrounds

Besides the directly measured backgrounds discussed in the previous section, two minor contributions in Eq. (6.10) are shown in the left panel of Figure 6.17:

- B_n^{Pu}**:** related to the neutrons scattered in the ^{242}Pu targets and captured in the detector materials or elsewhere around the experimental hall.
- B_γ^{Pu}: related to the scattering of the *delayed* in-beam γ-rays present in the ^{242}Pu targets. The origin and energy distribution of these γ-rays was described in Section 5.2.3.

These two background components are especially relevant in the URR, where, any additional small contribution to the background is critical since the *dummy* and the *beam-off* are aready around 82-85% of the total counts (see Table 6.3).

The neutron and γ-ray scattering in the ^{242}Pu sample can not be measured directly and have thus been inferred from the measurement of a ^{nat}Pb sample. This sample features, similarly to the ^{242}Pu sample, a high γ-ray interaction probability due to its large atomic number Z and high density but presents a negligible capture to elastic neutron cross section ratio. First, the contribution of neutrons and γ-rays was disantangled from the measured Pb counting rate (after B_{off} had been substracted). Then, the separated contributions of neutrons and γ-rays were scaled from Pb to the ^{242}Pu as it is explained in the following.

The total counting rated measured with the lead sample as a function of the time-of-flight was separated in two contributions $C^{Pb}(t) = C_\gamma^{Pb}(t) + C_n^{Pb}(t)$ as follows:

1. To remove the fluctuations and capture resonances, the total counting rate $C^{Pb}(t)$ was fitted to the following phenomenological expression:

$$C^{Pb}(t) = k_0 + \sum_i^3 a_i \cdot (1 - e^{-b_i t}) \cdot e^{-c_i t}, \tag{6.11}$$

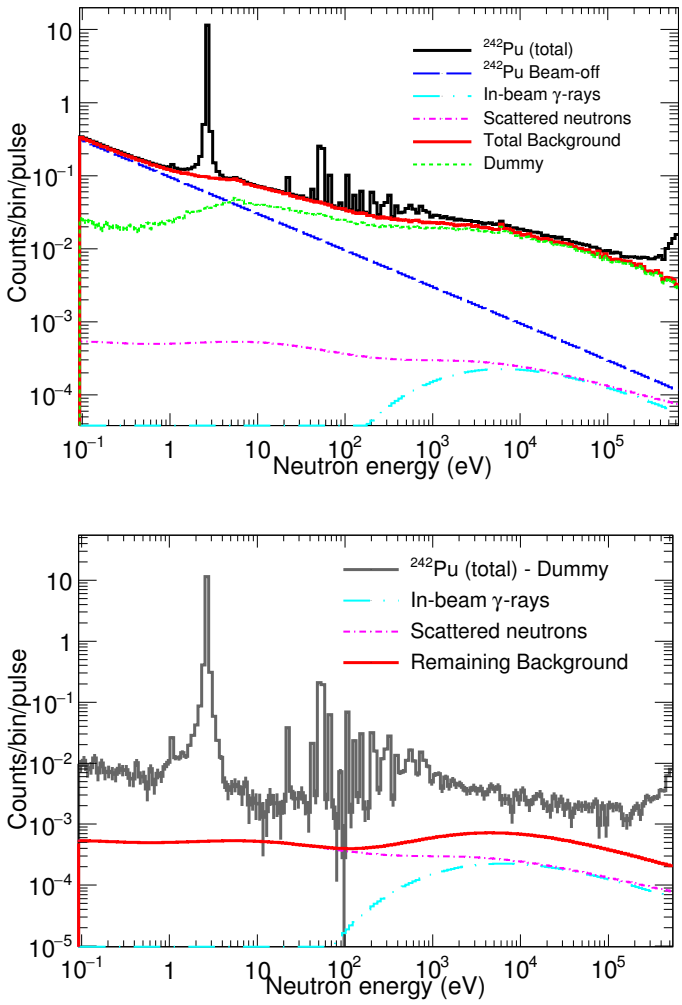

Figure 6.17: *Left: Total counting rate per pulse of ^{242}Pu and contribution of the different background components using a detection threshold (E_{thr}) of 250 keV. The counting rate in the URR (E_n > 1 keV) is dominated by the beam related background (dummy) (see text for details). Right: Counting rate after the dummy and beam-off are subtracted compared to the remaining background (i.e. scattered in-beam neutrons and gammas).*

2. Since the contribution of γ-rays is known from simulations [93, 162] to arrive to EAR1 at $t \lesssim$1.5 ms (see Figure 5.15), at larger times all the fitted Pb counting rate is considered as due to scattered neutrons, as in the case of the *empty* background.

3. The neutron scattering also contributes during the arrival of the in-beam γ-rays. This contribution is obtained by scaling the *empty* to $C^{Pb}(t)$ at t=2 ms under the assumption that the time-of-flight distribution of the background induced by scattered neutrons is approximately the same in the *empty* measurement and with the the Pb sample in place, while in the *empty* measurement the γ-ray scattering is negligible.

Following this approach, the total fit of the Pb counting rate is shown in black in the left panel of Figure 6.18. In the same plot, the extracted contributions of scattered neutronn

B_n^{Pu} and γ-rays B_γ^{Pu} are shown as red and blue lines, respectively. The *empty* background scaled to the total counting rate of Pb at t>2 ms is shown as black dots.

The lower panel of Figure 6.18 shows that the relative contribution of scattered neutrons and γ-rays changes with the detection threshold (E_{thr}) applied during the analysis, being the γ-rays less relevant as the threshold increases. This confirms that the fitted Pb counting rates are a sum of two different contributions.

The background contributions in our measurement related to the scattering of neutrons $B_n^{Pu}(E_n)$ and γ-rays $B_\gamma^{Pu}(E_n)$ in the ^{242}Pu targets are calculated as

$$\begin{aligned} B_n^{Pu}(E_n) &= F_n \cdot C_n^{Pb}(E_n), \\ B_\gamma^{Pu}(E_n) &= F_\gamma \cdot C_\gamma^{Pb}(E_n), \end{aligned} \tag{6.12}$$

where F_n and F_γ are the factors needed to scale the scattering of γ-rays and neutrons in the 1-mm-thick Pb target to the ^{242}Pu sample.

The calculation of the neutron background scaling factor F_n has been carried out with two methods:

1. F_n can be extracted from the ratio of neutron elastic cross sections (i.e. energy dependent) and expressed as

$$F_n(E_n) = \frac{\sigma_n^{Pu}(E_n) \cdot n_{Pu}}{\sigma_n^{Pb}(E_n) \cdot n_{Pb}}, \tag{6.13}$$

   where σ_n^X is the elastic cross section and n_X the areal density of the samples.

2. Simulations of the neutron background showed that the main contribution of the neutron scattering background is not the direct scattering from the sample but the

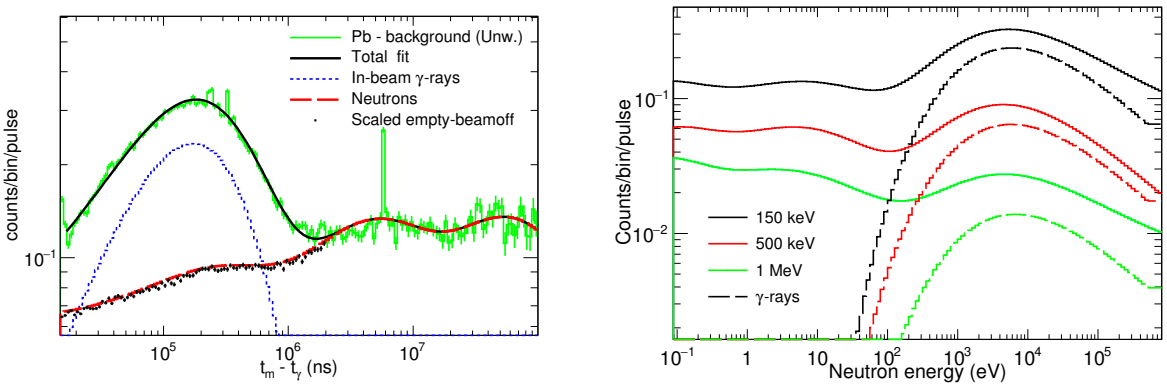

Figure 6.18: *Left: Pb counting rate as a function of the time-of-flight fitted to the expression in Eq.6.11 (black curve). The contribution of the in-beam γ-rays (blue) and the remaining scattered neutron component (red) have been fitted separately. The shape of the scattered neutron background below the γ-ray hub is extracted from a similar fit of the measured counting rate with an empty sample holder. Right: Fitted Pb(n,γ) (solid lines) and in-beam γ-ray counting rate as a function of the reconstructed neutron energy for different detection tresholds.*

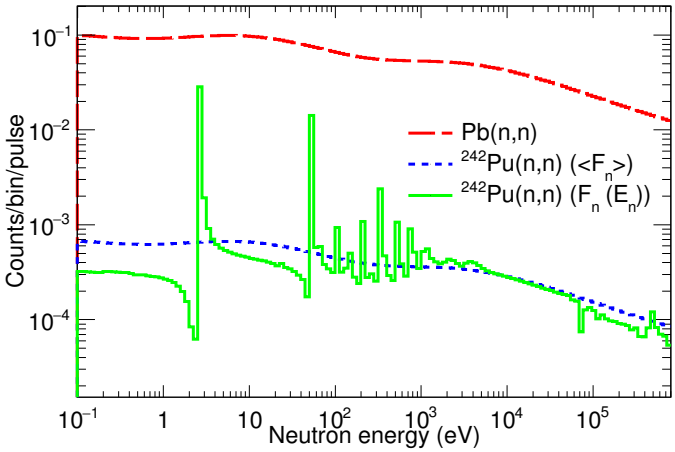

Figure 6.19: *Neutron scattering background fitted from the Pb measurement (red dashed curve) scaled to the ^{242}Pu using the energy dependent scaling factor $F_n(E_n)$ (green solid line) or the average factor $\langle F_n \rangle$ (blue dotted line).*

capture of scattered neutrons after moderation around the experimental hall. As a consequence, the time-of-flight distribution of the final background is smooth and does not directly follow the neutron energy distribution of scattered neutrons (i.e. the elastic cross section) [203]. Hence an average constant scaling factor given by

$$\langle F_n \rangle = \langle \frac{\sigma_n^{Pu}}{\sigma_n^{Pb}} \rangle \frac{n_{Pu}}{n_{Pb}}, \tag{6.14}$$

being $\langle \sigma_n^{Pu} / \sigma_n^{Pb} \rangle$ the average ratio of cross section in the URR (1-500 keV), may be more realistic.

Both methods for the scaling of the neutron scattering background are compared in Figure 6.19. The difference in the resulting ^{242}Pu capture yield using each method serves to estimate the associated uncertainty, which is 1.5% below 10 keV, 1% between 10 and 50 keV and 2.5% above 50 keV.

For the case of the γ-ray background, the scaling factor F_γ does not depend on the neutron energy, but it does on the detection threshold. In previous works at n_TOF-EAR1 F_γ was fitted with the help of black resonance filters (see for instance Refs. [211, 212]). However, during the ^{242}Pu campaing no measurements were taken with filters and F_γ was, instead, calculated as

$$F_\gamma = F_\gamma^{abs} \cdot F_\gamma^{thr}, \tag{6.15}$$

where F_γ^{thr} depends on the the experimental detection threshold and was calculated using Monte Carlo simulations of the in-beam γ-rays scattered in Pb, Au and Pu targets of different thicknesses using the Geant4 toolkit. On the other hand, F_γ^{abs} was determined as the absolute scaling factor that leads to a consistent result for the background-substracted ^{242}Pu(n,γ) counting rate result in the URR regardless of:

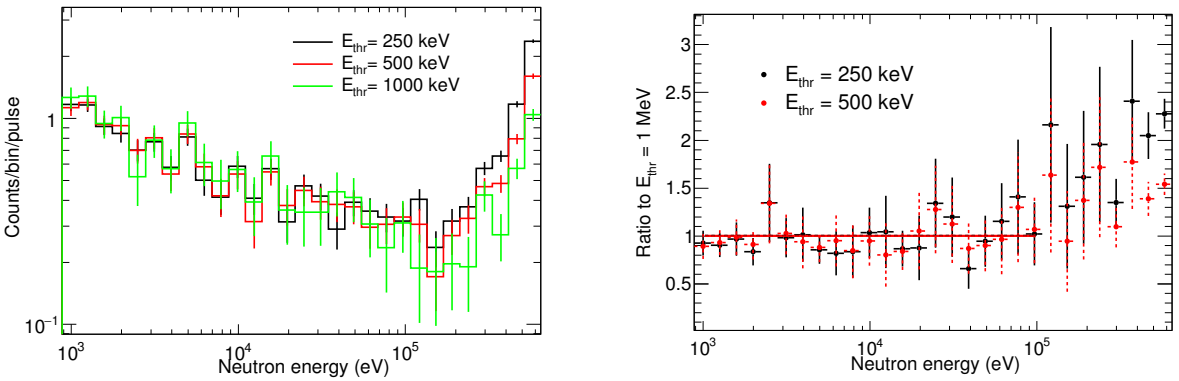

Figure 6.20: *Left:* $^{242}Pu(n,\gamma)$ *counting rate per pulse in the URR as a function of the neutron energy obtained with different thresholds* (E_{thr}). *Right: Ratio of counting rates with respect to the results with* E_{thr} = 1 *MeV (The values of the average ratios (solid lines) are displayed in Table 6.4).*

1. The minimum threshold in γ-ray energy deposition set for the analysis: the γ-ray background contains mainly 478 keV γ-rays and for this reason is strongly suppressed with increasing thresholds as it is concluded from the results in Table 6.3.

2. The use of unweighted or weighted (PHWT) data sets in the background substraction: The in-beam γ-ray background to capture ratio is significantly reduced after the PHWT is applied due to the much softer γ-ray energy distribution of the in-beam γ-rays compared to that of a capture event. This result is quantified in Table 6.3.

Since these two conditions are very sensitive to the very different γ-ray energy distributions of the in-beam γ-ray background compared to that of the capture cascade, they serve to find the absolute level of the in-beam γ-ray background. The resulting values for F_γ are listed in Table 6.5. With these values a nice agreement of the background-substracted counting rate is obtained up to E_n = 100 keV for different thresholds, as shown in Figure 6.20 and quantified in Table 6.4. The standard deviation of 3% in the ratios in this table has been assumed as the uncertainty in the cross section associated to the in-beam γ-ray background. For energies above E_n = 100 keV, new background contributions related to the fission and inelastic channels arise and limit the upper energy limit of the capture yield in this work, but this is discussed in the next section.

The final results for the contribution of the scaled scattered neutron and in-beam γ-ray backgrounds in the URR, presented for two different thresholds in Table 6.3, indicate that they account for a 14-19% of the remaining counts after the *dummy* and the *beam-off* background are substracted (see right panel of Figure 6.17).

Table 6.4: *Average ratios of $^{242}Pu(n,\gamma)$ counting rate in the URR (1-100 keV) with the adjusted in-beam γ-ray background scaling factor. Second column: ratio between different thresholds E_{thr} with respect to the E_{thr}= 1000 keV. Third column: Ratio between weighted and unweighted scaled counts as a function of the detection threshold.*

	Average ratio (1-100 keV))	
E_{thr} (keV)	**E_{thr}/1 MeV**	**Unweighted/Weighted**
250	1.01(5)	0.99(6)
500	0.99(5)	1.00(6)
1000	1	1.05(7)

Table 6.5: *Scaling factors for scattered in-beam γ-rays (F_γ) and neutron (F_n) backgrounds fitted from the Pb ancilliary measurement. F_n is assumed to be independent of the γ-ray energy detection threshold used in the analysis since the nuclei where the scattered neutrons are captured do not depend on the sample.*

E_{thr} (keV)	F_γ $(x10^3)$	F_n $(x10^3)$
250	1.67(7)	
500	1.89(8)	6.8(3)
1000	1.98(10)	

6.7 High neutron energy limit

Capture measurements at n_TOF-EAR1 using the fast C_6D_6 detectors with low-neutron sensitivity allow extracting pointwise data up to a neutron energy of at least 1 MeV (see for instance Ref. [233]), which corresponds to a time of 1.3 μs after the arrival of the γ-flash to the first experimental area. The upper energy limit is reduced to few hundreds of keV in EAR2 due to the 10-times smaller time scale. The high energy limit is also smaller if the TAC is used as detection system due to its higher neutron sensitivity and dead time issues [234] and longer baseline restoring time after the γ-flash compared to a C_6D_6 detector. Thus, aiming at extracting the ^{242}Pu(n,γ) cross section up to hundreds of keV, this measurement was carried out with C_6D_6 detector.

Athough theoretically, every capture measurement carried out at n_TOF-EAR1 with C_6D_6 detector could be extracted up to 1 MeV, several experimental factors could restrict the high energy limit: reduced capture to background ratio, γ-flash and increasing counting rate and new reaction channels.

6.7.1 γ-flash and high counting rates

As one approaches a neutron energy of 1 MeV, two possible experimental effects can affect the detector behaviour:

- The effect of the γ-flash, which distorts the detector baseline and can affect the area of the pulses identified on top of the restoring baseline.

- The increasing dead time losses due to the higher counting rate associated to the shorter time-of-flight intervals as the neutron energy increases.

In order to validate the performance of the detector at high neutron energies we take advantage of the different beam intensities along the experimental campaign. In particular, *parasitic* bunches, featuring one third of the nominal proton intensity, were excluded in the final analysis but they are really valuable for validating the detector behaviour in extreme conditions since both the γ-flash intensity and the counting rate for a given bunch scale with the number of neutrons in the bunch. Therefore, the good agreement between the counting rate per pulse for the two kind of pronton pulses, shown in Figure 6.21, indicates that we are not affected by the γ-flash or the high counting rate up to 900 keV. The use of thin backings combined to the fast response of the detectors are key to achieving this result.

6.7.2 Inelastic and fission channels

Another limitation for the highest neutron energy that can be reached is related to the production of γ-rays by reactions other than capture, for instance inelastic scattering (n, n') and fission (n, f). The first (n, n') channels on ^{242}Pu open at 45, 147 and 307 keV respectively, and the total contribution of this channel increases with the neutron energy [21]. However, this low-energy γ-ray background is removed by increasing the detection threshold in γ-ray energy beyond the maximum neutron energy under study.

Fission is a more delicate issue since C_6D_6 detectors do not allow us to distinguish capture and fission events. In order to estimate the fraction of the background-subtracted counting rate coming from (n, f) reactions, we have calculated the detection efficiency for

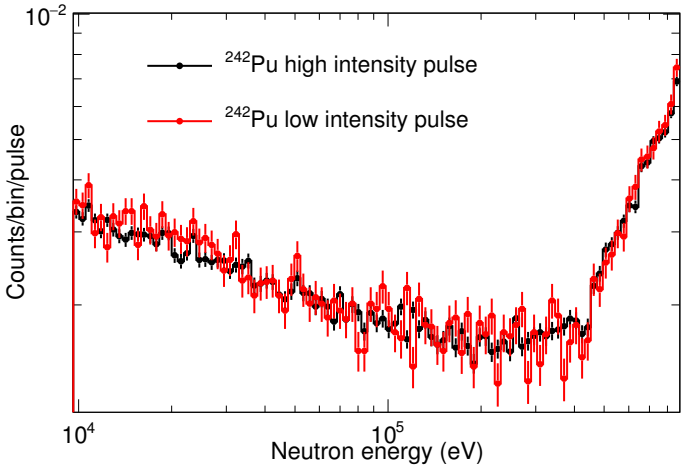

Figure 6.21: *Total counting rate as a function to the neutron energy showing the very good agreement of the dedicated (full intensity) and the parasitic (low intensity) bunches. This result confirms that the counting rate at shot time-of-flight (i.e high neutron energy) is not affected by the γ-flash and dead time due to the low mass of the backings together with the fast response of the detectors.*

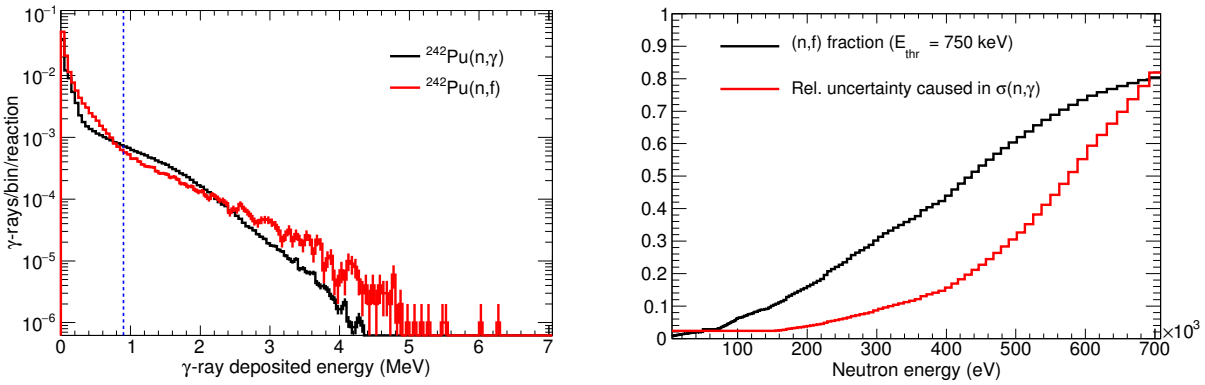

Figure 6.22: *Left: Simulated response of Detector #1 to capture cascades and a fission events. The dashed line indicates the detection threshold that optimizes the capture/fission efficiency ratio. Right: The black line represents the relative contribution of the fission channel to the background-subtracted counting rate calculated with a threshold of 750 keV using the ENDF/B-VII.1 library. The red curve corresponds to the systematic uncertainty in the cross section associated to the uncertainty in the (n,f) cross section.*

Table 6.6: *Total detection efficiency of the capture set-up for fission and capture events and capture to fission efficiency ratio $\varepsilon_c/\varepsilon_f$ as a function of the detection threshold. The uncertainties are statistical (simulations).*

E_{thr} **(keV)**	$\varepsilon_c(\%)$	$\varepsilon_f(\%)$	$\varepsilon_c/\varepsilon_f$
150	14.411(19)	19.00(5)	0.758(4)
750	5.250(11)	4.34(5)	1.210(13)
900	4.304(10)	3.49(4)	1.234(15)
1250	2.547(8)	2.24(3)	1.132(17)

capture and fission events. The γ-ray spectra emitted in these two reactions was simulated as follows:

- Capture: the same capture cascades generated for the correction of the count loss below the detection threshold (see Ref. [246] for the details) were used for this purpose.
- Fission: the energy spectrum of fission γ-rays was obtained using the *GEF* code [238].

The simulated γ-ray distributions for fission and capture events were coupled to the Geant4 application developed to simulate the detector response for the PHWT. The resulting simulated response of the C_6D_6 detector for both fission and capture is shown in the Left panel of Figure 6.22.

The absolute total efficiencies (i.e. four detectors combined) for fission ε_f and capture ε_c events and their ratio ($\varepsilon_c/\varepsilon_f$) was studied as a function of the detection threshold (see Table 6.6), and the results indicate that the efficiency for fission is higher than for (n,γ) for detection thresholds below 500 keV, and the opposite for an increasing threshold up to a γ-ray energy of 900 keV (see Figure 6.22), for which the maximum $\varepsilon_c/\varepsilon_f = 1.23$ is reached.

Using the simulated efficiency for capture and fission events, the fraction of the background subtracted counts that actually come from fission events $F_{n,f}$ was calculated as

$$F_{n,f}(E_n) \;=\; \frac{\varepsilon_f \sigma_f(E_n)}{\varepsilon_c \sigma_\gamma(E_n) \;+\; \varepsilon_f \sigma_f(E_n)}, \tag{6.16}$$

where σ_f and σ_γ are the evaluated (ENDF/B-VII.1) fission and capture cross section, respectively. The right panel of Figure 6.22 shows the energy dependence of the relative contribution of fission $F_{n,f}$ calculated, indicating that the contribution of fission is negligible below 50 keV and becomes larger than capture beyond 450 keV. In the same plot we also present the systematic uncertainty in the cross section associated to the (n,f) subtraction as a function of the neutron energy. This uncertainty has been obtained from the current 19% uncertainty in the ^{242}Pu(n,f) cross section in the energy region from 183 keV to 1.35 MeV [29, 239] and becomes the dominant source of systematic uncertainty in our data for neutron energies higher than 250 keV (see Section 8.3.2).

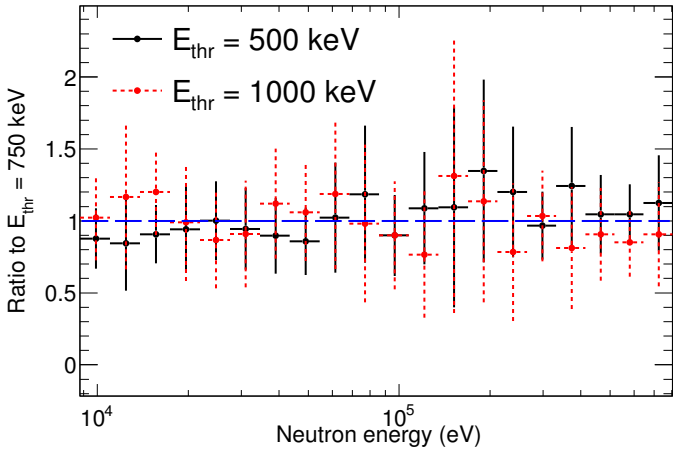

Figure 6.23: *Ratio of the high energy region of the extracted cross section with three different thresholds (500 keV, 750 keV and 1 MeV), showing a fair agreement within the uncertainties after the fission background is removed.*

The fission background was the cause behind the large discrepancies between the results obtained for different thresholds above 100 keV as shown in Figure 6.20. After the counting rates are corrected for this contribution, the results obtained with thresholds larger than 500 keV show a good agreement within the statistical uncertainties (see Figure 6.23). However, a systematic deviation of about 8% is found in the ratios of Figure 6.23) in the energy region above 200 keV that may be related to the uncertainty in the fission correction. Indeed, the observed deviation is at the level of the systematic uncertainty associated to the fission cross section in that neutron energy range.

According to the disscussion carried out throught this section, the neutron energy range above 100 keV can be analyzed when a sufficiently high (750 keV) threshold is applied. The negligible impact of the γ-flash in the fast C_6D_6 detectors combined with the rejection

of the (n, n') background and the correction for the estimated (n, f) contribution allow us to report the capture data up to a neutron energy of 500 keV. The high energy limit of the capture data in this work has been set at the energy beyond which the large fission contribution leads to a total systematic uncertainty in the cross section that overcomes the current 35% (see Section 6.10).

6.8 The PHWT in this analysis

6.8.1 Calculation of the weighting functions

When we introduced the Total Energy Detectors in Section 5.3.2, we mentioned that C_6D_6 detectors do not fulfill the condition of featuring a detection efficiency for γ-rays proportional to their energy (see Eq. (5.9)). Following the theoretical principles of the PHWT (see Appendix B.1) we calculated the Weighting Function that transforms the detector response to achieve the desired proportionality. The main ingredient to calculate the Weighting Functions are the individual response functions of the detector R_{ij}, defined as the fraction of γ-rays of a given energy E_i that make an energy deposition of E_j.

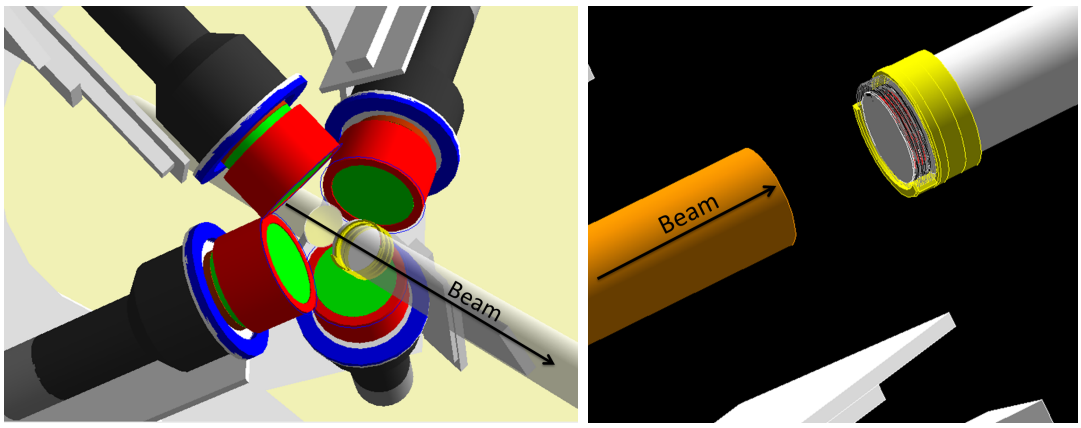

Figure 6.24: *Left: General view of the geometry implemented in Geant4 to simulate the response of the detection setup. Right: Detailed implementation of the 7-target stack in the Geant4 geometry model.*

In this work, the response functions R_{ij} have been extracted with help of simulations carried out using the Geant4 toolkit. A flexible Geant4 application has been developed for this purpose (described in Appendix B.2). The simulation of the detector response takes into account all the relevant experimental details, including a very detailed geometry illustrated in Figure 6.24.

From the accurate Geant4 simulations we extract the response functions for each individual detector to a large number of γ-ray energies from 50 to 14 MeV. The obtained response functions are then appropiately broaden to consider the detectors' energy resolution, resulting in the distributions displayed in Figure 6.25.

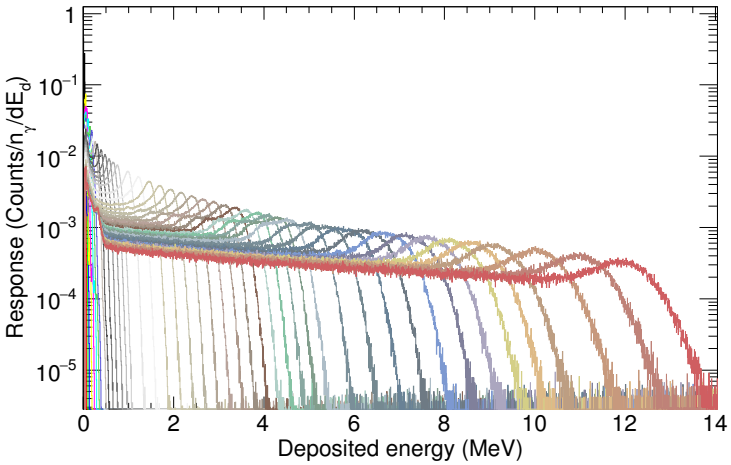

Figure 6.25: *Simulated response of detector #1 to monoenergetic γ-rays of 45 different energies ranging from 50 keV to 14 MeV. The experimental resolution broadening has been included.*

The easiest implementation of the WF (W_j in Eqs. (B.4) and (B.5)) is to assume an analytical function of the deposited energy E_j of the form

$$W_j = \sum_k a_k E_j^k, \tag{6.17}$$

with the parameters a_k obtained by minimizing the χ^2 of a least square fit for a number of γ-ray energies

$$\chi^2 \;=\; \sum_i \left(E_i \;-\; \sum_{j=E_L}^{j=E_H} W_j \; R_j \right)^2 \tag{6.18}$$

In this work, the minimization was performed using the *Minuit* function minimization code included in the ROOT analysis toolkit [225, 226]. The sum over the deposited energy $\sum_j$ runs from a lower limit E_L up to E_H=10 MeV. While the simulations provide the detector response for any deposited energy, a lower detection threshold E_{thr} = 150-250 keV is applied in the real experiment to the C_6D_6 detectors aiming at preventing the detection of noise or very low energy background. The loss of counts corresponding to deposited energies smaller than E_{thr} has to be corrected. In this sense, two different approaches can be followed to calculate the WF depending on the choice of E_L:

1. $E_L = 0$: The WF is calculated assumming no lower threshold in the minimization of Eq. (6.18). This method satisfies with high accuracy the proportionality between the weighted efficiency and the γ-ray energy (see Figure 6.26), leading to a small systematic uncertainty associated to the PHWT. On the other hand, the resulting weighted counting rates have to be corrected for the missed fraction of the detector response for all the γ-ray energies (i.e. for all the events with $E_d < E_{thr}$) [200, 213]. This correction is carried out with help of accurate simulations of the detector response to capture cascades as it is explained in detail in Section 6.8.2.

2. $E_L = E_{thr}$: The second approach is based on setting the detection threshold as lower limit for the WF calculation. This induces significant deviations from the desired proportionality between weighted efficiency and γ-ray energy, in particular as one gets closer to the threshold (see Figure 6.26). The main advantage of this method is that the WF already corrects for the fraction of the response falling below the threshold for the detected γ-rays (i.e $E_\gamma > E_{thr}$). Therefore, the addittional correction should take into account only for the γ-rays with an energy smaller than E_{thr}. This correction can be negligible for light nuclei with low level densities (see for instance Ref. [209]). This method also avoids further corrections for self-normalized measurements using the Saturated Resonance Method (SRM) [210], such as in previous measurements at n_TOF using C_6D_6 detectors described in Refs. [211, 212].

In this work we chose method 1 due to its higher accuracy.

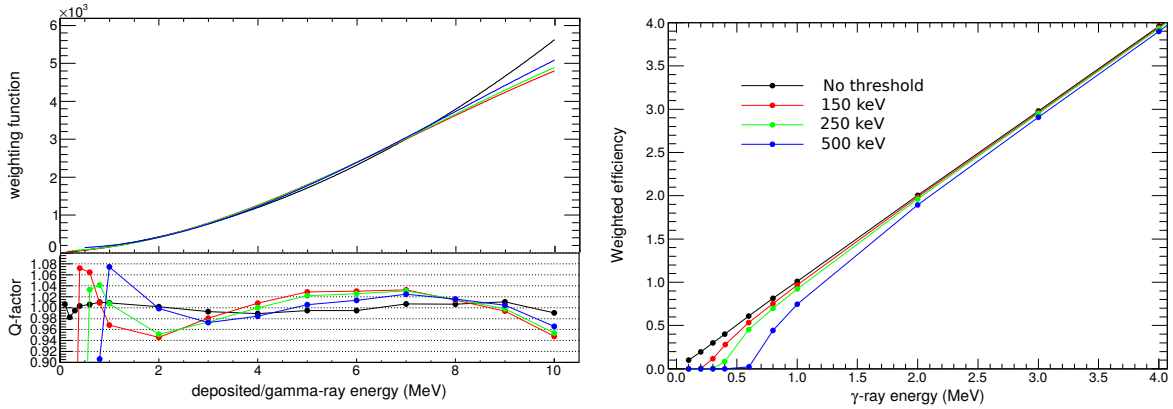

Figure 6.26: *Left: Analytical weighting function for detector #1 calculated with different values of E_L and the associated Q-factor as a function of the γ-ray energy (residual). Right: Weighted efficiency as a function of the γ-ray energy showing the deviation from proportionality as the lower energy limit E_L threshold increases.*

Since the WF is sample and detector dependent, the WF was calculated separately for each of the four BICRON detectors and the two different samples for which the yield has been extracted: ^{242}Pu target stack (see Section 5.4.1) and Au (100 μm) (see Section 5.4.2). The impact of the neutron self-shielding for large resonances or thick samples also affects the distribution of neutron captures along the sample. For each of the samples two WFs were calculated:

- Assumming an homogenous distribution of the γ-ray emmission in the sample along the beam axis. This applies for all the weak resonances (i.e. $n\sigma << 1$).
- Considering the self-shielding effect for strong resonances (for instance, for the 4.9 eV resonance of Au all the neutrons are stopped in the first 30 μm).

The WF's for detector #1 for the ^{242}Pu and Au samples are shown in the left and right panels of Figure 6.27, respectively. One appreciates that for the Au target, there is a sizable difference between the two WFs, hence the effectof the neutron self-shielding

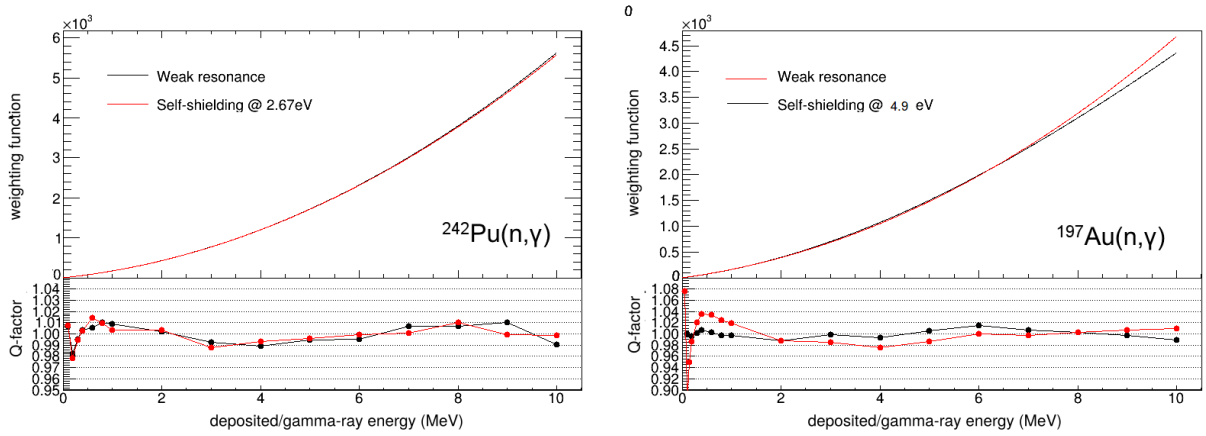

Figure 6.27: *Weighting functions as a function of the deposited energy (top panels) obtained for detector #1 for the ^{242}Pu (left) and Au (right) samples. The red and black lines correspond to a γ-ray emmission typical of a weak resonance and strong resonance (see text for details). The residuals in the bottom pads show the Q-factor given by Eq. (6.19) as a function of the γ-ray energy.*

is sizable, which is not the case for ^{242}Pu. The residuals in Figure 6.27 show the quality Q-factor of the WF, defined as

$$Q = \frac{\sum_j W_j \cdot R_{ij}}{E_i}. \tag{6.19}$$

According to Figure 6.27, the Q factor fluctuates around unity within 1%. This means that the application of these WFs to the simulated response of the detectors allows satisfying the proportionality condition $\varepsilon_i = k \cdot E_i$ within 1% for all the simulated γ-ray energies between 0.1 and 10 MeV. The experimental corrections and systematic uncertainties associated to the PHWT are discussed in detail in the next section.

The use of simple analytical WFs of the form given by 6.17 does not provide a succesful Q factor in the case of thick samples, even when calculated with zero threshold. In this cases, the large self-absorption of γ-rays generates a sharp reduction of the efficiency for low γ-ray energies. In order to satisfy the proportionality in this situation a numerically calculated WF is the best solution [213].

6.8.2 Accuracy of the PHWT and corrections

6.8.2.1 Intrinsic accuracy of the PHWT

The application of the PHWT (described in the detail in Appendix B.1) results in a detection efficiency numerically equal to the energy of the capture cascade E_c, given by Eq. (5.10) with k = 1 MeV^{-1}. However two factors have to be studied to validate this technique and determine its accuracy:

- The systematic uncertainty in the weighted counting rates associated to the deviation from the desired proportionality ($Q = 1$ in Eq. (6.19)) of the Weighting Functions.
- The experimental corrections to the PHWT and their corresponding uncertainties.

The uncertainty associated to the PHWT can be evaluated from the deviation from unity of ratio of the experimental weighted efficiency for detecting a cascade $\varepsilon^w_{c,exp}$ to the theoretically expected $\varepsilon^w_{c,th} = (1\ MeV^{-1})\ E_c$,

$$\frac{\varepsilon^w_{c,exp}}{\varepsilon^w_{c,th}} = \frac{\sum_j W_j R^c_j}{E_c}, \tag{6.20}$$

where W_j and R^c_j are, respectively, the weighting factor and the fraction of the detector response to a capture cascade corresponding to an energy deposition E_j. In Eq. (6.20) the response of the detector R^c_j to capture cascades can not be completely determined from the experimental data since a fraction of the detector response is lost below the lower detection threshold. The only solution to reproduce the full detector response to capture cascades is to carry out Monte Carlo simulations of the detection system response to realistic cascades and validate the simulations using the experimental responses.

The cascade generator CAPTUGENS [235] was used to generate the realistic cascades emitted by the compound nuclei ^{243}Pu and ^{198}Au at an excitation energy S_n. For both nuclei, the input for the cascacade generation code consisted of

1. The known level scheme, γ-ray transition probabilities and internal conversion factors (all from ENSDF [19]) below a certain excitation energy E_{cut} (400 keV for ^{243}Pu and 1600 keV for ^{198}Au)
2. A statistical model (based on Level Density Parameters and Photon Strength Functions) to generate transitions starting above E_{cut}. The statistical parameters were taken from Refs. [236] and [147] for ^{198}Au and ^{243}Pu, respectively.

The generated cascades were coupled to the Geant4 application developed to simulate the detector response. The good agreeement between the experimental and simulated responses for both ^{242}Pu(n,γ) and ^{197}Au(n,γ), shown in Figure 6.28, validates the energy and multiplicity of the simulated cascades. All the details on the cascade generation, optimization of statistical model parameters to match the experimental responses, and MC simulations of the detector response are described in Appendix C.

In order to determine the experimental/theoretical ratio in Eq. (6.20) we generated large number N_c (thousands) of realistic ^{242}Pu(n,γ) and ^{197}Au(n,γ) capture cascades with CAPTUGENS and coupled them to the Geant4 geometry model (see Figure 6.24) to extract the cummulative response of the individual C_6D_6 detectors to the N_c cascades. Last, the corresponding Weighting Function was applied to the simulated response. After the weighted response to N_c cascades has been calculated from the results of the simulation, the ratio in Eq. (6.20) becomes

$$\frac{\varepsilon^w_{c,exp}}{\varepsilon^w_{c,th}} = \frac{\sum_i^{N_c} \sum_j W_j R^c_j}{N_c E_c}, \tag{6.21}$$

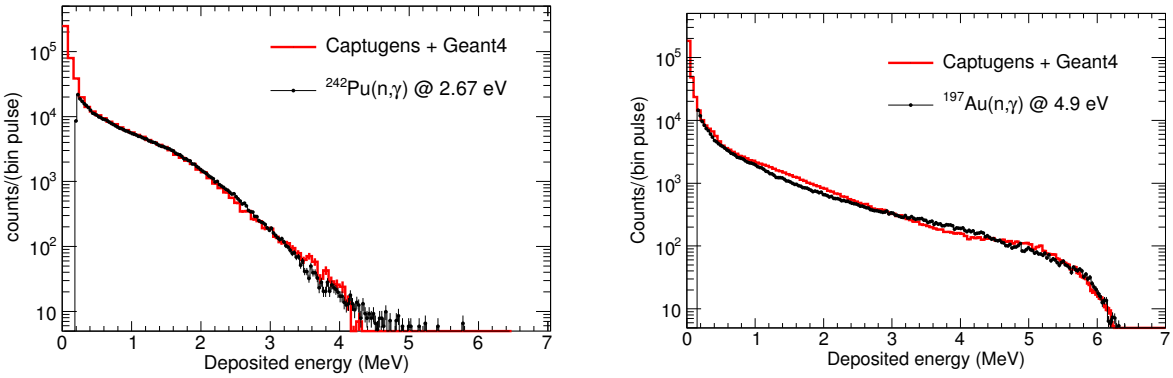

Figure 6.28: *Left: Energy deposited spectrum in the C_6D_6 in the 2.67eV $^{242}Pu(n,\gamma)$ resonance compared to the simulated response. Bottom: Experimental response compared to the simulated one for the 4.9 eV resonance of $^{197}Au(n,\gamma)$ cross section. The low energy fraction missing in the experimental spectra f_{thr} is corrected according to the simulations.*

Table 6.7: *Ratio $\varepsilon^w_{c,exp}/\varepsilon^w_{c,th}$) between the theoretical weighted efficiency and the one resulting from the application of the WF to the simulated detector response to realistic capture cascades.*

	^{197}**Au**		^{242}**Pu**	
	Self-shielding (4.9 eV)	Homogenous	Self-shielding (2.7 eV)	Homogenous
$\varepsilon^w_{c,exp}/\varepsilon^w_{c,th}$	1.0002(19)	0.998(3)	1.0051(11)	1.0058(13)

where $\sum_i^{N_c}$ is the sum over the individual detector responses to the N_c cascades. The deviation from unity of this ratio, serves as an estimation of the systematic uncertainty associated to the PHWT. Table 6.7, shows the value of this ratio for the individual detectors and the studied WF's, indicating that the deviation from unity is well below 1%.

6.8.2.2 PHWT correction factors

Besides the intrinsic systematic uncertainty, different experimental corrections generate deviations between the PHWT theory and its experimental application:

1. the counts lost below the detection threshold, f_{thr}, and
2. the possible detection of more than one γ-ray (multiple counting) from a cascade in our detection setup, f_{mc},
3. the probability of internal conversion leading to the emission of non-detectable electrons instead of γ-rays, f_{ce}.

The associated corrections f_{mc}, f_{thr} and f_{ce} are calculated with the help of the same Monte Carlo simulations of the detection system response to capture cascades described above (see Appendix C for the details). The calculation is carried out in an analogous way than for the systematic uncertainty:

Table 6.8: *Yield correction factors related to the deviations from the PHWT theory, being just f_{thr} sizable with the actual experimental conditions. The uncertainties in the table are derived from the statistics in the simulations.*

	f_{thr}			f_{ce}	f_{mc}
E_{thr}	150 keV	200 keV	250 keV	150 keV	
^{242}Pu	1.150(4)	1.121(4)	1.090(3)	1.004(3)	0.995(3)
^{197}Au	1.078(3)	1.066(3)	1.052(3)	1.001(3)	0.998(3)
^{242}Pu/^{197}Au	1.067(4)	1.052(4)	1.035(4)		

1. Each of the effects is considered separately in the cascade simulations: presence of a detection thresholds, partial substitution of γ-rays by conversion electrons or simultaneous emission of γ-rays belonging to the same capture event.
2. For each case the deviation of the ratio in Eq. 6.21 from unity is studied.

From this analysis we concluded that (see Table 6.8):

- The f_{mc} correction is always below 0.5% for both ^{242}Pu and ^{197}Au. Indeed, this correction is already applied the multiple detection of γ-rays is already rejected during the analysis with the TTOFSort routine by considering only one of the simultaneously detected γ-rays (i.e. belonging to the same capture cascade) (see Section 6.1.2).
- f_{ce} has been calculated for several detection thresholds, showing a value which is at most 0.4% for the chosen threshold of 150 keV applied in the subsequent analysis and becomes completely neglible for increasing thresholds.
- f_{thr} is sizable and quite different for each isotope, ranging up to 15% and 8% for ^{242}Pu(n,γ) and ^{197}Au(n,γ), respectively, for energy thresholds smaller than 250 keV. In order to keep this correction small, a threshold of 150 keV was used for to extract the final absolute normalization.

It is important to remark that the value of f_{thr} is significantly different for ^{242}Pu and ^{197}Au, meaning that this correction does not cancel out even if the ^{242}Pu(n,γ) yield is normalized to the measurement of ^{197}Au (see Section 6.9).

The validation of these corrections is assessed by comparing the threshold-corrected counting rates in the largest resonance for different energy thresholds. Figure 6.29 shows the threshold-corrected counting rates for the resonances at 2.67 eV (^{242}Pu(n,γ)) and 4.9 eV (^{197}Au(n,γ)). The quantitative analisis of this results, indicates that for thresholds between 150 and 250 keV, the threshold-corrected resonance integrals agree within 0.2% and 1% for ^{197}Au(n,γ) and ^{242}Pu(n,γ), respectively. Therefore, a systematic uncertainty of 1.5% has been assumed for the corrections described in this section.

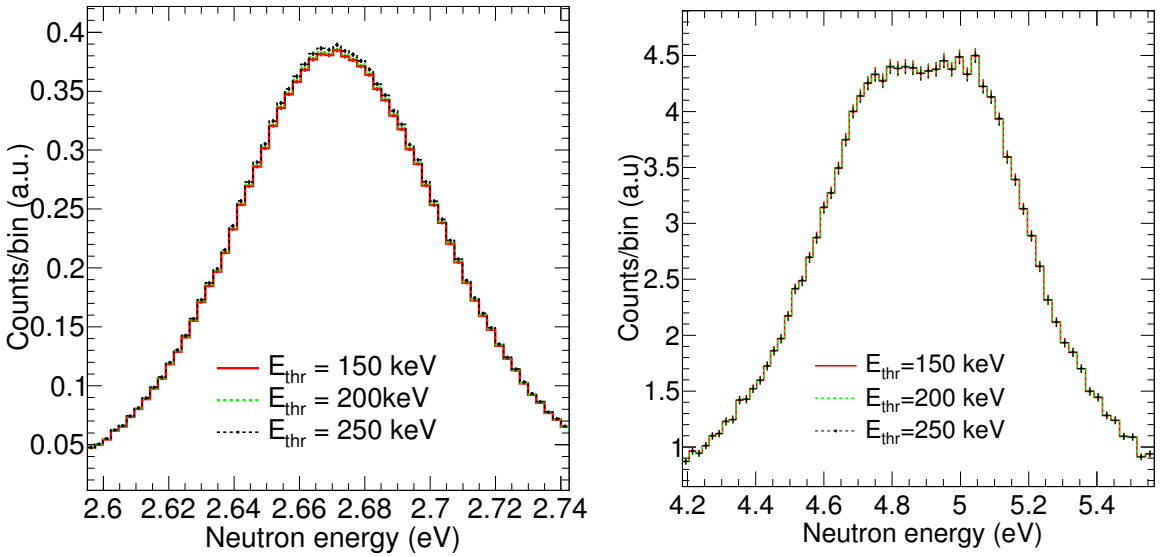

Figure 6.29: *Background substracted counting rates obtained with three different detection thresholds corrected with f_{thr}: $^{242}Pu(n,\gamma)$ resonance at 2.67 eV (left) and 4.9 eV resonance of $^{197}Au(n,\gamma)$ (right).*

6.8.3 Impact of the PHWT in the ^{242}Pu(n,γ) analysis

The use of the Pulse Height Weighting Technique in the analysis of capture measurements with C_6D_6 has typically the following consecuences in the data analyis:

1. This method modifies the detection efficiency in such a way that C_6D_6 detectors behave as Total Energy Detectors, featuring an efficiency which is proportional to the total cascade energy, and independent of the capture cascade pattern (see Section 5.3.2 for the details).

2. For compound nuclei with significantly different cascade paths, the efficiency may vary significantly from resonance to resonance. As a result of the PHWT, the relative strenght of the resonances is modified.

3. For most nuclei, the major background components present a softer γ-ray spectra (i.e lower average γ-ray energies) than the capture cascade. Since the WFs are increasing functions with energy, the application of the PHWT, leads to a reduction of the background components relative to capture for such nuclei.

4. The main disadvantage of the PHWT is the onset of artificial statistical fluctuations in neutron energy bins with limited statistics as an intrinsic consecuence of the weighting procedure.

However, the relative impact of points (1)-(4) varies depending on the isotope, the average energy distribution of both capture and background, and the specific goals of the measurement. In particular, for the analysis of the ^{242}Pu(n,γ) capture yield we have

Table 6.9: *Relative contribution of capture and the different background components in two energy regions in the URR. The results of the unweighted and weighted spectra using a detection threshold of 250 keV are compared.*

	Contribution (1-10 keV)(%)		**Contribution (10-100 keV)(%)**	
	Unweighted	**Weighted**	**Unweighted**	**Weighted**
B_{dummy}	75.8	83.2	80.1	85.6
B_{off}^{Pu}	7.5	4.1	4.1	2.3
B_{γ}^{Pu}	0.9	0.4	1.3	0.6
B_{n}^{Pu}	1.1	0.9	1.2	1.0
^{242}Pu(n,γ)	14.7	11.4	13.2	10.5

concluded that:

- The efficiency for the ^{242}Pu and ^{197}Au capture cascades has to be assesed using the PHWT before normalizing the ^{242}Pu capture yield to the ^{197}Au saturated resonance (see Section 6.9). This is mandatory since the energy distribution of the capture cascade is different for these isotopes and, as a consecuence, the efficiency to detect the a capture event varies from one isotope to the other.
- For the case of ^{242}Pu(n,γ), the weighting procedure does not modify within the statistical uncertainties the relative intensities of resonances (point 2 of the previous list). This result, which may be true for heavy 0^+ nuclei in general, reflects that the cascade spectrum is the same independently of the resonance energy (see Section 6.9.2 for the details).
- The enhancement of the capture to background ratio associated to the PHWT (point 3) is not true in our case since the ^{242}Pu(n,γ) features a low end point (5.035 MeV) compared to the majority of nuclei and a soft energy distribution (see discussion in Section 4.2.1). On the other hand, the *dummy* has, in average, a harder spectrum, as it is clearly seen in Figure 6.16. This result is specially relevant in the URR, where the unweighted *dummy* background is responsible for 76-80% of the counting rate. After the PHWT is applied, thd relative contribution of this background increases to 83-86%. The impact of the PHWT in the relative contribution of capture and backgrounds in the URR is summarized in Table 6.9.
- The background substracted ^{242}Pu(n,γ) counting rates obtained following the prescription of the PHWT show enhanced statistical fluctuations, especially in the resonances with few counts or in the URR, where the statistics are scarce, with respect to those related to counting statistics. The enhanced fluctuations in the extracted capture yield limit the maximum energy of analyzable resonances and the accuracy of the data in the URR (see Section 6.9.3).

In order to avoid an increase in the background to capture ratio and of the statistical fluctuations, we have propose, for the first time, to apply an average weighting factor to the original (unweighted) background-subtracted histograms. This method is valid in the RRR, as it is shown in Section 6.9.2, but could fail in the URR if the weighting affects

differently to p- and d-wave contribution to the yield, which is neglible in the RRR.

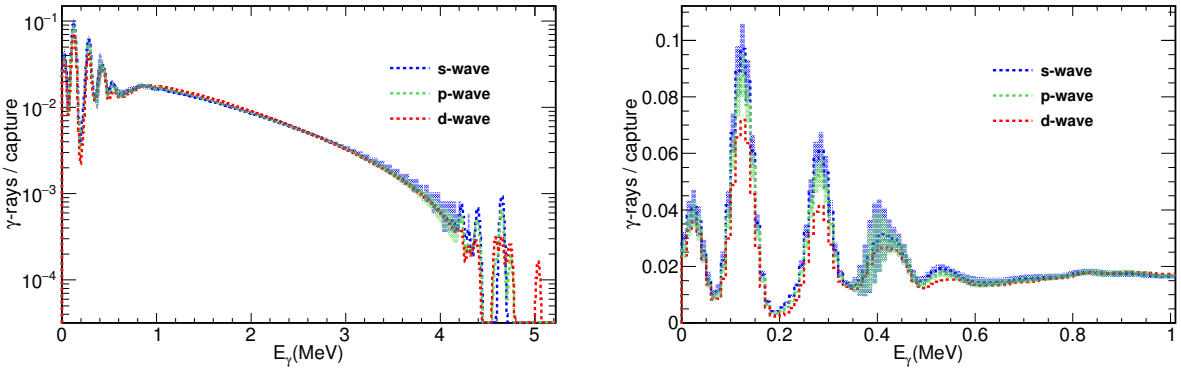

Figure 6.30: *Energy distribution of the statistically generated ^{242}Pu(n,γ) capture cascades for s-, p- and d-waves. The bottom panel zooms into the low energy regio to show the perfect agreement within standard deviation (shadowed region) for s- and p-waves and the small deviation for d-wave. The spectra are convoluted with a experimental resolution of FWHM = 50 keV.*

Aiming at studing the valididity of the average weighting factor approximation in the URR, we have simulated s-, p- and d-wave cascades using the Photon Strenght Functions and Level Density Parameters of Ref. [26]. Using a fixed parameterization, a different statistical nuclei characterized by a level scheme and its transition probabilities is generated in each run of the code, known as *realization*. Figure 6.30 shows the γ-ray energy distribution for s-, p- and d-wave cascades for 1000 *realizations*. The solid lines in this figure correspond to the average result of all the *realizations* and the shadowed areas indicate their standard deviation. The left panel shows the overall general agreement for the three partial waves in the whole energy range and the bottom panel zooms into the first MeV to illustrate the good agreement of the s- and p-wave. The d-wave, although slightly different, is only dominant at neutron energies beyond the range studied in this work. As a consequence, the deviation related to the use of a constant weight instead of the common PHWT implementation is expected to be small also in the URR.

From all of the above and in order to expand the energy range in the subsequent resonance analysis and minimize the statistical uncertainties in the URR, the approach in this analysis has been:

1. The PHWT is applied to the count distributions as a function of the neutron energy.
2. The weighted and unweighted ^{242}Pu(n,γ) histograms are used to calculate the average weighting factor (i.e. the average ratio of weighted to unweighted resonance areas).
3. The background subtraction (see Section 6.6) is carried out using the unweighted count distributions.
4. The average weighting factor serves to scale the yield (see Section 6.9) and allows using the detection efficiency given by Eq. (5.10).

6.9 Capture yield calculation

The neutron capture yield is defined as the probability for an incident neutron to undergo a capture reaction and is defined, from the general expression of the reaction yield in Eq. 2.48, as:

$$Y = F_{ms} \cdot (1 - e^{-n\sigma_{tot}}) \frac{\sigma_\gamma}{\sigma_{tot}}, \tag{6.22}$$

where F_{ms} is the the multiple scattering correction, explained in Section 7.1.1 and n represents the sample's areal density. All the terms in Eq. (6.22), with the exception of n, are neutron energy dependent.

Experimentally, the ^{242}Pu capture yield in this work is calculated using Eq. 2.47, which in the case of n_TOF leads to:

$$Y(E_n) = F^{thr}_{norm} \cdot \frac{C(E_n) - B(E_n)}{\Phi(E_n) \cdot \varepsilon_c}, \tag{6.23}$$

C and B being the unweighted distributions of total and background counts per pulse displayed in Figure 6.17, $\Phi(E_n)$ the *evaluated* neutron flux [178], shown in Figure 5.11, and ε_c the weighted detection efficiency, numerically equal to the cascade energy according to Eq. (5.10).

Last, F^{thr}_{norm} is the threshold-dependent factor that accounts for the normalization and the efficiency corrections. This factor is calculated as:

$$F^{thr}_{norm} = \frac{\langle W^{thr} \rangle}{f^{thr}_{SRM}} \frac{F^{thr}_{c,Pu}}{F^{thr}_{c,Au}}, \tag{6.24}$$

where the different factors correspond to:

- $F^{thr}_{c,Pu}$ and $F^{thr}_{c,Au}$: are the product of f_{mc}, f_{thr} and f_{ce} corrections factors for ^{242}Pu and ^{197}Au, respectively. These corrections, associated to the PHWT, have been described in Section 6.8.2 and summarized in Table 6.8.
- f^{thr}_{SRM}: is the absolute normalization factor obtained via the *Saturated Resonance Method* (SRM) [210]. The calculation of this factor and the uncertainties associated to the absolute normalization of the ^{242}Pu capture yield are discussed in Section 6.9.1.
- $\langle W^{thr} \rangle$: is the average weighting factor calculated in Section 6.9.2 required to use the unweighted counts together with the weighted efficiency.

The capture yield extracted in this work using the unweighted counting rates and a constant weighting factor is compared to the one obtained with the usual prescription for the PHWT in Section 6.9.3, to prove their compatibility and the reduced statistical uncertainties of the former. Last, a detailed summary of the energy-dependent systematic uncertainties in capture yield in the RRR and the URR is given in Section 6.10.

6.9.1 ^{197}Au(n,γ) yield and the Saturated Resonance Method

Different factors in the calculation of the capture yield can introduce systematic deviations which must be corrected with an absolute normalization method. Among other effects, the most relevant are:

- Total number of neutrons: The absolute value of the neutron flux, the relation between the number of neutrons and the proton beam intensity or the sample alignment could introduce a sytematic deviation in the extracted capture yield.
- Absolute efficency assesment: The overall efficiency of the detection set-up in this work is extracted from MC simulations that assume that the detector geometry, for instance their active volume, is exactly the same for the four detectors. In addittion, the orientation of the detectors with respect to the sample is assumed to be symetrical and the sample-to-detector distance are measured with a limited accuracy. This factors may introduce systematic deviations between the capture yields extracted with the individual detectors.

Aiming at providing an absolute normalization to remove all this possible deviations, the capture yields are always normalized to a well known absolute value, using either

- Self-normalization: The capture yield is normalized to a well known resonance in the same (n,γ) measurement (see for instance Refs. [233, 212]).
- Normalization from an ancilliary measurement: The capture yield is normalized to a well known yield value in a (n,γ) measurement of a different sample.

For the case of the ^{242}Pu(n,γ) yield in this work, the absolute normalization factor f_{SRM} in Eq. (6.24) was obtained individually for each detector via the *Saturated Resonance Method* (SRM) [210] using the first (4.9 eV) resonance of ^{197}Au.

The SRM is based on the following principles:

1. The use of a sample which satisfies $n\sigma_{tot} >> 1$ for a given resonance.
2. A resonance width dominated by the capture channel $\Gamma_\gamma >> \Gamma_n$

Under these two conditions, a given resonance saturates, i.e. all neutrons of that energy undergo at least one interaction. The saturation level has a well known value which is independent of the cross section value and on the sample thickness (provided that is high enough to reach saturation).

The 4.9 eV capture resonance of ^{197}Au was used to apply the SRM since it reaches saturation for a thickness of only 30 μm and has $\Gamma_\gamma = 124$ meV and $\Gamma_n = 15.2$ meV [20]. The following steps were followed to extract the normalization factor:

- The neutron capture on a 100-μm-thick Au target having the same diameter than the ^{242}Pu targets (see Table 5.7) was measured using the same detection set-up consisting of four C_6D_6 detectors.

- The different backgrounds components in the ^{197}Au(n,γ) measurement, shown together with the total counting rate in Figure 6.31, were assesed following the description in Section 6.6. The beam related background *empty* and the ambient background *beam-off* were determined from direct measurements and the background due to scattered neutrons and in-beam γ-rays were estimated from the measurement of a lead target.

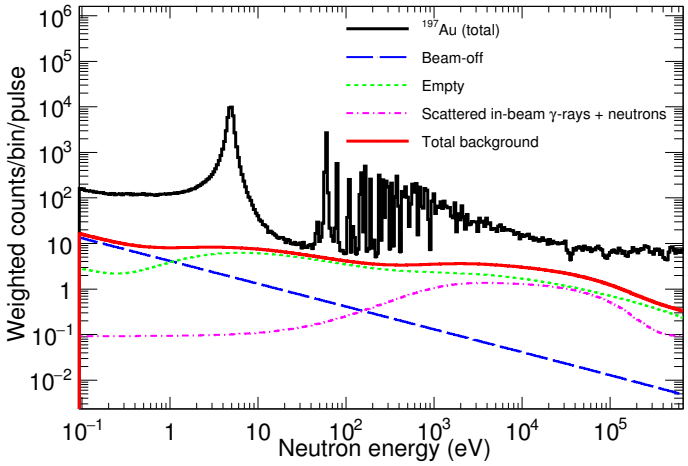

Figure 6.31: *Total weighted counting rates per pulse of ^{197}Au and contribution of the different background components using a detection threshold (E_{thr}) of 250 keV.*

- From the experimental background subtracted ^{197}Au(n,γ) counting rate, the capture yield obtained applying a certain detection threshold is given by

$$Y^{thr}(E_n) = \frac{C_w(E_n) - B_w(E_n)}{\Phi(E_n) \cdot \varepsilon_c}, \tag{6.25}$$

where ε_c is given by Eq. (5.10), taking into account the binding energy of ^{198}Au $S_n = 6.512$ MeV [19]. In Eq. (6.25), $C_w(E_n)$ and $B_w(E_n)$ represent, respectively, the total and background weighted counts per pulse in the ^{197}Au(n,γ) measurement. The reasons to use the weighted histograms in the case of ^{197}Au(n,γ), following the standard application of PHWT, are:

1. The ground state of ^{197}Au has $I^P = 3/2^+$ and as a consequence s-wave resonances with two different spins ($J = 1,\ 2$) are present in the ^{197}Au(n,γ) cross section [237]. Therefore, the weighting factor is expected to change from resonance to resonance due to the spin-dependence of the cascade pattern.

2. The weighting process does not limit the extraction of an accurate yield since the statistics and the capture to background ratio are much better for the ^{197}Au(n,γ) measurement than for ^{242}Pu(n,γ).

- Using the ^{197}Au(n,γ) capture yield individually extracted for each detector, the ab-

solute normalization factor f_{SRM}^{thr} in Eq. 6.24 is calculated as

$$f_{SRM}^{thr} = \frac{Y^{thr}(4.9eV)}{Y_{calc}(4.9eV)}, \tag{6.26}$$

being $Y^{thr}(4.9eV)$ the measured saturated yield value, and $Y_{calc}((4.9eV)$ the calculated one. This is calculated with the SAMMY code [62] by fitting the normalization of the calculated yield to the experimental one. The normalization factor extracted from the fit of the 4.9 eV resonance is kept in SAMMY for the resonance analysis of the ^{242}Pu(n,γ) yield (see Section 7.1). The left panel of Figure 6.32 shows the 4.9 eV resonance in the average experimental yield of the four detectors together with the fitted theoretical yield.

The individual values of f_{SRM}^{thr} for the four C_6D_6 detectors and different detection thresholds are presented in Table 6.10. The normalization factors in this table are, in average, significantly below 1 since the calculation of the experimental Au yield in Eq. 6.25, does not include the $F_{c,Au}^{thr}$ correction for the missed counts below the threshold. These factors were included afterwards in the calculation of the global normalization factor for the ^{242}Pu(n,γ) yield in Eq. (6.24).

Table 6.10: *Normalization factors f_{SRM}^{thr} obtained for each detector from the fit of the ^{197}Au(n,γ) 4.9 eV saturated resonance using the SAMMY code. The right column presents the ratios of the individual normalized ^{242}Pu 2.67 eV resonance kernels, Y_{norm}, with respect to the average value of the four detectors, $\langle Y_{norm}\rangle$. The uncertainties in the table are due the uncertainty in the fit of the saturated resonance and the counting statistics.*

	f_{SRM}^{thr}			$Y_{norm}/$
	E_{thr}=150 keV	E_{thr}=200 keV	E_{thr}=250 keV	$\langle Y_{norm}\rangle$
C_6D_6-1	0.853(3)	0.842(3)	0.832(3)	1.012(4)
C_6D_6-2	0.994(3)	0.980(3)	0.970(3)	1.003(4)
C_6D_6-3	0.891(3)	0.842(3)	0.870(3)	0.990(4)
C_6D_6-4	0.914(3)	0.903(3)	0.893(3)	0.995(4)
All C_6D_6	0.914(2)	0.902(2)	0.892(3)	

A verification of the correctness of the individual f_{SRM}^{thr} values comes from the fact that the 2.67 eV resonances in the normalized ^{242}Pu yields from individual detectors are perfectly compatible to each other, as it is shown in the right panel of Figure 6.32. A quantitative analysis of the area of this resonance in the normalized ^{242}Pu yield shows that the individual detectors agree with the average within about 1%, as presented in Table 6.10. This has been assumed as a good estimation of uncertainty associated to the absolute normalization of the ^{242}Pu capture yield.

An additional source of uncertainty associated to the absolute normalization to ^{197}Au is related to the use of a thick sample holder suited to the 7-target stack geometry (see Section 5.4.1). With this sample holder, the uncertainty in the relative positioning along the beam line of the ^{197}Au and ^{242}Pu samples is assumed to be $\pm$1 mm. According to the MC simulations of the detector response, this uncertainty leads to an additional 1.5% uncertainty in the absolute normalization.

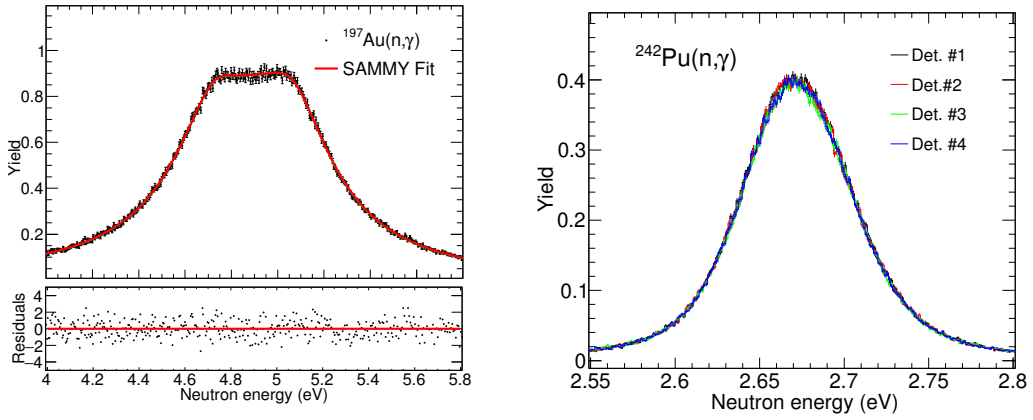

Figure 6.32: *Saturated resonance at 4.9 eV in the experimental capture yield of ^{197}Au fitted with the SAMMY code. The average of the four detectors is shown.*

6.9.2 Individual weighting factors and average value

The common application of the PHWT, following the principles described in Appendix B, can result in a different weight for each resonance if they present a significantly different cascade pattern. In order to quantify this effect in the ^{242}Pu(n,γ) data, the *resonance weighting factor* WF_{res} for the largest resonances below 1.3 keV has been calculated. This parameter can be defined as

$$WF_{res} = \frac{A_{res,w}}{A_{res}}, \tag{6.27}$$

where A_{res} and $A_{res,w}$ are, respectively, the resonance areas (or integrals) of a given resonance in the unweighted and weighted counting rate distribution as a function of the neutron energy.

The individual values of WF_{res} as a function of the resonance energy are presented in the left panel of Figure 6.33. The values in this figure have been obtained with a detection threshold of 150 keV. In this plot one can appreciate the good compatibility of the most of the individual values with their weighted average within the statistical uncertainties (1σ error bars). In order to illustrate the statistical compatibility of the individual values WF_{res} with their average we show in the right panel of Figure 6.33 the deviation of the individual values relative to their weighted average. From this plot one concludes that for most resonances WF_{res} is compatible with the average value within 1σ and none of them deviates more than 1.5 σ.

The weighted average of the *resonance weighting factors* in Figure 6.33 has been used as the average weighting factor $\langle W^{thr} \rangle$ in Eq. (6.24). The values obtained for this factor are presented in Table 6.11 for different detection thresholds E_{thr}. The average weighting factor increases for higher detection thresholds, as it is expected from the energy dependence of the Weighting Functions (see Figure 6.27).

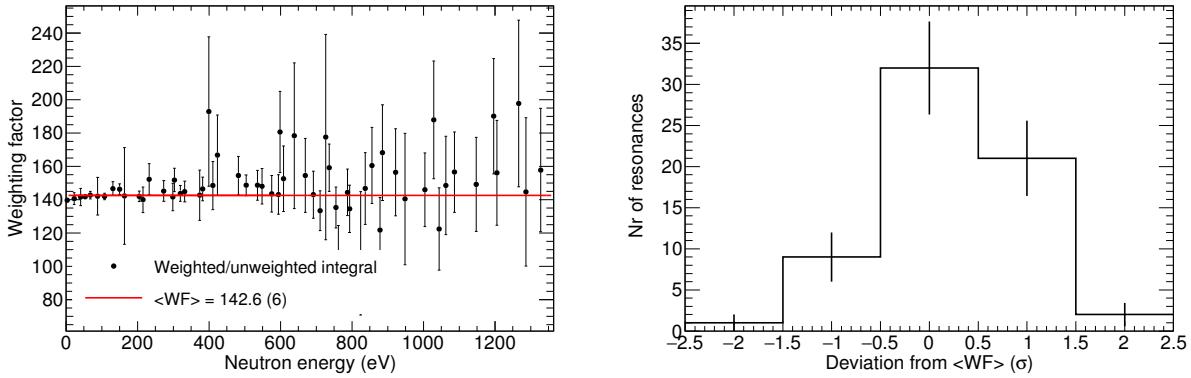

Figure 6.33: *Individual values of the resonance weighting factors for the main resonances below 1.3 keV weighted average (red line) (right) and statistical distribution of the individual values around the weighted average value, showing their compatibility within 1.5 σ.*

Table 6.11: *Average weighting factors $\langle W^{thr} \rangle$ obtained with different detection thresholds E_{thr} for each detector.*

	$\langle W^{thr} \rangle$		
	E_{thr} = 150 *keV*	E_{thr} = 200 *keV*	E_{thr} = 250 *keV*
C_6D_6-1	148.7(8)	166.8(9)	180.0(10)
C_6D_6-2	172.2(9)	196.6(10)	212.9(11)
C_6D_6-3	130.6(8)	147.6(8)	159.5(9)
C_6D_6-4	125.9(8)	142.2(8)	153.2(9)
All C_6D_6	142.6(6)	161.4(6)	174.3(7)

6.9.3 Unweighted vs weighted yield: compatibility and statistical fluctuations

The extracted capture yield calculated in this work by means of Eq. (6.23) does not follow the standard prescription of the PHWT. Instead of applying a neutron energy-dependent weight on the capture and background counting rates (see Eq. (B.5)), a constant weighting factor has been used to scale the unweighted background-substracted capture counting rates.

This section aims at proving the validity of the alternative method followed in this analysis and showing its advantages:

1. The method followed in this work leads to a capture yield perfectly compatible within the uncertainties with the weighted yield extracted following the usual PHWT method. The comparison between the yield derived with the two methods is shown for different energy regions in the RRR in Figure 6.34. A quantitative support to this conclusion was given in Section 6.9.2, when we demonstrated the statistical compatibility of the individual weighting factors for many resonances.

2. The statistical fluctuations are significantly reduced with our approach and, as a

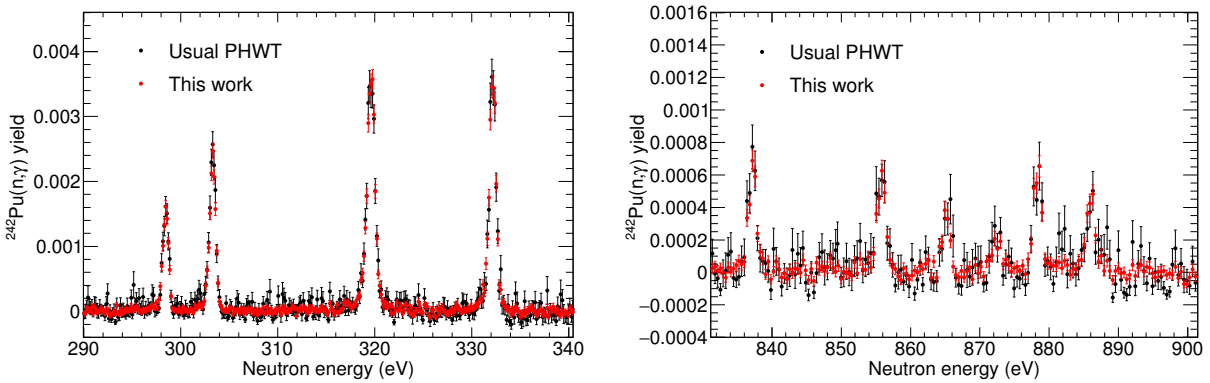

Figure 6.34: *Capture yield of ^{242}Pu calculated with the usual PHWT method (black) compared to the approached followed in this work (blue). The comparison is shown in two different energy regions in the RRR below 1 keV to illustrate their compatibility within the statistical uncertainties and the significantly reduced statistical uncertainties in this work, which allow to a much better indentification of resonances up to higher energies.*

consequence, the R-Matrix analysis can be extended to much higher neutron energies (see Figure 6.34). Moreover, the enhancement of the statistical fluctuations is also observed in the background subtracted counting rate in the URR (see Figure 6.35.

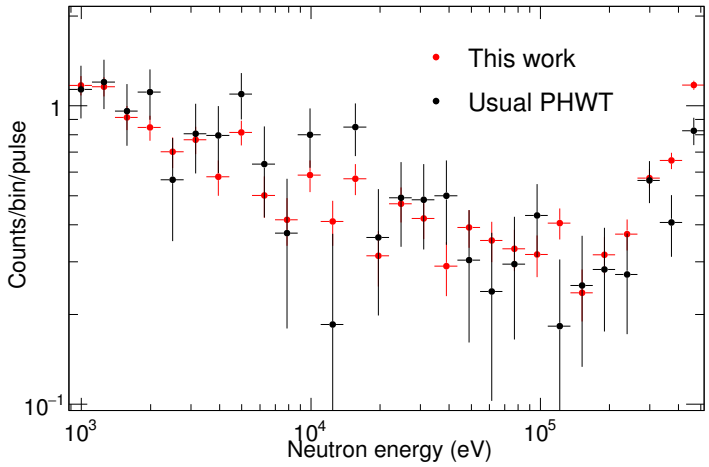

Figure 6.35: *Background-subtracted ^{242}Pu(n,γ) in the URR calculated with the usual PHWT method (black) compared to the approached followed in this work (blue). The compatibility of both methods and the reduction of the statistical fluctuations in this work are clearly appreciated.*

6.10 Summary of systematic uncertainties

The different systematic uncertainties affecting to the final ^{242}Pu(n,γ) yield in this work have been discussed along this chapter. In order to make a clear summary, we will treat

them separately in the RRR (1 eV - 4 keV) and the URR (1 - 500 keV).

This choice is motivated by the different sources of uncertainty affecting the capture yield in each case:

- **RRR (1 eV - 4 keV)**: the main sources of uncertainty are the normalization and the efficiency assesment (accuracy of the PHWT and associated corrections). On the other hand, the background substraction plays a secondary role for the analysis of individual resonances. The systematic uncertainty in this region is the almost constant, with the exception of a minor energy-dependence associated to the uncertainty in the flux shape.
- **URR (1 - 500 keV)**: The uncertainties associated to the normalization and efficiency assesment are exactly the same than for the RRR. In addittion, the uncertainties associated to the different background components and the flux shape vary significantly with the neutron energy in this range. Therefore an energy-dependent study is required in this energy region.

6.10.1 Resonance region (1 eV - 4 keV)

The systematic uncertainties from different sources contributing to the resulting yield in the RRR are summarized in Table 6.12. A detailed description of the origin of the individual contributions in this Table has been given throughout Chapters 5 and 6:

- Efficiency (PHWT): The uncertainty associated to the accuracy of method and the associated correction factors are discussed in 6.8.2 . An addittional 0.5% uncertainty is included due to the effect of the gain shift (see Section 6.2.2).
- Normalization: The uncertainties related to the absolute normalization to the ^{197}Au yield via the SRM method are discussed in Section 6.9.1 and the uncertainty in the relative normalization to the beam intensity of the ^{242}Pu and ^{197}Au measurements is described in Section 6.3.1.
- Neutron flux shape: The determination of the energy distribution of the neutron flux was presented in Section 5.2.1 and the systematic uncertainties in the shape of the neutron flux are given in Table 5.5.

It is to be noted that the uncertainty in the background subtraction is considered negligible because it does not affect the analysis of individual resonances. Moreover, all the individual systematic uncertainties in Table 6.12 have a constant value in the full energy range under consideration with the exception of the neutron flux, which features and uncertainty of 1% below 100 eV and 2% at higher energies (see Table 5.5). The resulting quadratic sum of partial systematic uncertainties in the ^{242}Pu yield is 3.2% or smaller.

From the experimental capture yield in the RRR, the parameterized capture cross section is extracted by means of an R-Matrix analysis (see Chapter 7). Although the capture yield itself does not depend on the sample mass, the uncertainty of 4% related to the determination of the sample mass (see Section 3.3.1) has to be considered for the estimation

Table 6.12: *Summary of the individual systematic uncertainties contributing to the final uncertainty in the ^{242}Pu capture yield in the RRR grouped according to their origin. The uncertainty in the sample mass contributes additionally in the extraction of the cross section from the capture yield.*

General group	Partial origin	Syst. unc.(%)
Neutron flux	Flux shape (E_n <100 eV)	1
	Flux shape (100 eV< E_n <4 keV)	2
Efficiency (PHWT)	Efficiency correction factors	1.5
	Deviation PHWT theory	0.5
	Gain shift	0.5
Normalization	Deviation yields individual detectors	1
	Relative position Au/Pu	1.5
	Beam monitors	0.5
	Sample mass	4
	Total (capture yield)	**<3.2**
	Total (cross section)	**<5.1**

of the final systematic uncertainty in the capture cross section. The latter has also been included in Table 6.12.

The resulting systematic uncertainty in the cross section is 5.1% or smaller, clearly below the 8% required by the NEA for the design and operation of advanced nuclear devices (see Section 1.5.2). The statistical uncertainties in the resonance areas and resonance parameters are discussed in Section 7.2.

6.10.2 Unresolved resonance region (1 - 500 keV)

The systematic uncertainties in the capture yield in the URR (summarized in Table 6.13) can be splitted into two groups:

- Those which do not depend on the neutron energy: normalization (2%) and efficiency (2%). These are common to the analysis of the resonance region (see previous section) since they correspond to global scaling factors.
- The neutron-energy-dependent uncertainties, related to the background substraction and the flux shape, are the major contribution to the total systematic uncertainty in the cross section in the URR and have been evaluated in four different energy intervals (see Table 6.13).

The systematic uncertainty in the dummy background, estimated to be 1% and dominates the overall uncertainty in the cross section in the energy range below 250 keV, as it accounts for more than 75% of the counts in the URR. The uncertainty in this background is obtained by combining a 0.5% associated to the proton/neutron beam monitoring (see Section 6.3.1) with an additional 0.5% related to a deviation up to 10% in the thickness of

Table 6.13: *Summary of individual systematic uncertainties and contribution to the systematic uncertainty in the capture capture yield in the URR. The energy range under study has been divided into three energy intervals to evaluate the energy-dependency of these uncertainties.*

		Syst. Unc. capture yield(%)			
Sources uncertainty	**Unc. (%)**	**1-10 keV**	**10-50 keV**	**50-250 keV**	**250-500 keV**
E_n-independent					
Normalization yield	2	2	2	2	2
PHWT (Efficiency)	2	2	2	2	2
E_n-dependent					
Dummy	1	5.2	6.3	6.9	4.0
Beam-off	1	0.8	0.5	0.3	0.1
In-beam γ-rays	[a]	3	3	3	3
Scattered neutrons	[a]	1.5	1	2.5	1.5
Fission	19	0	0.3	2.2	15.4
Shape of the Flux	2-5	2	4.5	2-5 [b]	2
Tota (capture yield)		**7.0**	**8.6**	**9.4**	**16.5**

a) The systematic uncertainty in the cross-section was estimated and not calculated from the uncertainty in this background (see text for details).
b) Uncertainty in the shape of the flux: 4-5% (50-100 keV),∼2% (100-250 keV).

the backing layer, as it was discussed in Section 6.6.1. An additional relevant contribution to the uncertainty is the shape of the neutron flux, that is known with an accuracy ranging from 2% up to 4-5% in the energy region of the dips (10-100 keV) (see Table 5.5). Last, the uncertainty associated to the correction for the (n,f) background, shown in Figure 6.22, is the dominant one above 250 keV. Its average value in the four energy intervals is presented in Table 6.13, where one can appreciate that it is negligible below 50 keV and increases with energy up to an average uncertainty of 15% between 250 keV and 500 keV.

The systematic uncertainties in the capture cross section in the URR calculated from the capture yield, discussed in Section 8.3.2, show that we have achieved the target accuracies of 8-12% at least up to 50 keV and we have reported data for the first time up to 500 keV with a total uncertainty below the current 35%.

Chapter 7

Capture cross section of ^{242}Pu in the RRR from 1 eV to 4 keV

The ^{242}Pu capture yield extracted from the measurement carried out at n_TOF-EAR1 has been analyzed in its resolved residual resonance region (RRR) in order to extract a parameterized cross section. The fit of the experimental yield was carried out with the SAMMY code [62], based on the Reich-Moore approximation to the R-Matrix theory [57], introduced in Section 2.2.2.

The good neutron energy resolution of the facility and the large accumulated statistics have allowed to observe individual resonances and determine their parameters up to 4 keV, clearly overcoming the current high energy limit of 1.3 keV for the RRR in the evaluations. The individual resonance parameters of 251 resonance have been extracted, 180 of which had never been reported before in any neutron radiative capture measurement of this isotope.

7.1 Resonance analysis

7.1.1 The SAMMY code

The SAMMY code [62], developed by the Oak Rigde National Laboratory (ORNL), is a multilevel multichannel R-Matrix code for the analysis of neutron-induced time-of-flight data. It is based on the phenomenological description of the neutron-induced cross sections of the R-Matrix theory, already introduced in Section 2.2.1. In particular, this code allows to fit the experimental data using different approximations of the R-Matrix theory: Reich-Moore approximation, Single-level Breit-Wigner (SLBW) and Multi-level Breit-Wigner (MLBW) (as in the ENDF-102 report [240]).

By default, the Reich-Moore approximation is the formalism chosen for SAMMY analyses since it is the preferred framework for the modern nuclear data evaluations. The other

approximations were used in older nuclear data files owing to the less demanding computational effort. However, they are found to be more often inadequate and thus discouraged for new data analysis.

Aiming at comparing the experimental data with those generated via R-Matrix theory, SAMMY allows including several experimental effects:

- **Doppler broadening**: Impact of the non-zero temperature of the nuclei in the sample. Different models are available in SAMMY to include this condition:

  1. Free-gas model (FGM) [241]: The most extensively used model and set by default in SAMMY. The Doppler-broadened cross section σ_D is calculated from the original cross section σ as

  $$\sigma_D(E) = \frac{1}{\Delta_D\sqrt{\pi}} \int \left(e^{-4(E-\sqrt{EE'})^2/\Delta_D^2} - e^{-4(E+\sqrt{EE'})^2/\Delta_D^2} \right) \sigma(E') \sqrt{E'/E} dE, \tag{7.1}$$

  where Δ_D is the Doppler width defined as

  $$\Delta_D = \sqrt{\frac{4\ m_n\ E\ k\ T}{M_A}}. \tag{7.2}$$

  In this expression m_n and M_A correspond, respectively, to the neutron mass and the mass of the target nuclei; k is the Boltzmann constant and T is the target temperature. This model has been used for all the resonances in this work except for the largest one of ^{242}Pu at 2.67 eV.

  2. Crystal-lattice model(CLM) [242]: This is a more realistic approximation and is used for resonances where the FGM does not provide a satisfactory result, as it was the case for the 2.67 eV resonance in this work (see Section 7.1.2).

- **Resolution broadening**: Effect of the so-called Resolution Fuction (RF) of the time-of-flight facility (see Section 5.2.2), which englobes the finite time-resolution and the spread in neutron production times and neutron flight paths. The RF can be included in the SAMMY calculation by means of a parameterized function [93] or using the full numerical representation of the RF extracted from MC simulations [162]. The latter was used in this work, including in SAMMY the numerical RF of n_TOF-EAR1 shown in Figure 5.13.

- **Single-/multiple scattering effects**: The finite size of the target generates addittional interactions beyond those described by the interaction cross section of a neutron with a single nuclei. The self-shielding correction accounts for the neutron flux reduction along the sample due to the first collision of incident neutrons with the sample nuclei and is given by the $(1 - e^{-n\sigma_{tot}})$ factor in the general expression for the capture yield given by Eq. (6.22). This factor makes the capture yield decrease and increases with the sample thickness n. The Multiple scattering (MS) correction corresponds to neutrons that are captured in the sample after undergoing one or more scatterings, which slow them down. The calculation of the MS correction is

more complex than the self-shielding, and tends to make the capture yield larger, and becomes as well more relevant as the sample thickness n thickness.

The capture yield calculated by SAMMY is given by a sum of different terms including these effects:

$$Y = Y_0 + Y_1 + Y_2 + Y_{ms}, \tag{7.3}$$

where Y_0 is the self-shielded capture yield (given in Eq. 6.22 with $F_{ms} = 1.$), Y_1 and Y_2 represent the contribution of the single- and double-scattering, and Y_{ms} accounts for the neutrons that suffer more than two scatters within the sample. The impact of these effects in the calculation of the cross section in the URR will be discussed in Section 8.1.

- **Residual background**: The SAMMY code allows to fit any residual background in the reaction yield using an neutron-energy-dependent analytical function of the form

$$B(E) = a + b/\sqrt{E} + c \cdot \sqrt{E} + d \cdot e^{-f \cdot \sqrt{E}}. \tag{7.4}$$

Several minimum input files and theoretical information are required to run a SAMMY calculation. First, the *.inp* file includes the different adjustable choices in the SAMMY calculation, type of output files and parameters that should remain fixed during the SAMMY fit. The second main file is the *.par* file that includes all the parameters that are elegible to be fitted along with their initial values. A relevant parameter during the calculation is the so-called *Fudge Factor* that limits the maximum variation and maximum uncertainty in the fitted resonance parameters.

7.1.2 Initial parameters and fitting procedure

The resonance analysis has consisted in the following steps: //were followed in this work to carry out resonance analysis in this work.

1. Fit the residual background: SAMMY was used to fit the constant background in the resonance valleys at different neutron energies intevals and the dependence of this value with energy was fitted to Eq. (7.4). Figure 7.1 shows the neutron energy dependence of the residual background, the fitted distribution and the reduced residual background after the fit (see bottom panel). It is important to note that the residual background is at the level of 10^{-6} in yield units, very small compared to the values of 10^{-3} to 10^{-4} (see Figures 7.2-7.10).

2. Identify and discard from the analysis the resonances where fission contributes significantly to the measured yield. The criterion two discard these resonances was that $\Gamma_f > 0.1\Gamma_\gamma$. As a result, only a few resonance clusters (see Table D.1 were discarded, being the resonance at 762 eV the only one where fission clearly dominates over capture (see Figure 7.2).

3. The spin of all resonances have been set to J = 1/2 (assumed to be s-waves) since ^{242}Pu is an even-even target. A statistical study was carried out to indentify p-wave candidates among the observed resonances (see Section 7.4).

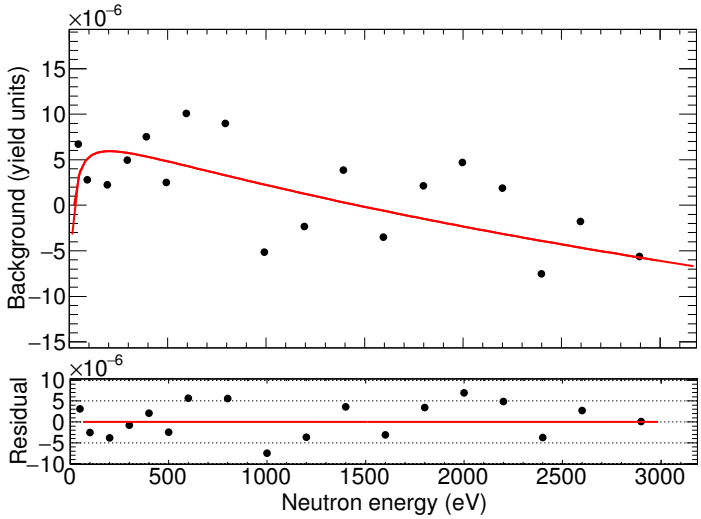

Figure 7.1: *Residual background in the capture yield as a function of the neutron energy fitted with sammy. The red line corresponds to the parameterization using Eq. (7.4). The bottom panel shows the reduced background oscillating around zero after the fit is subtracted.*

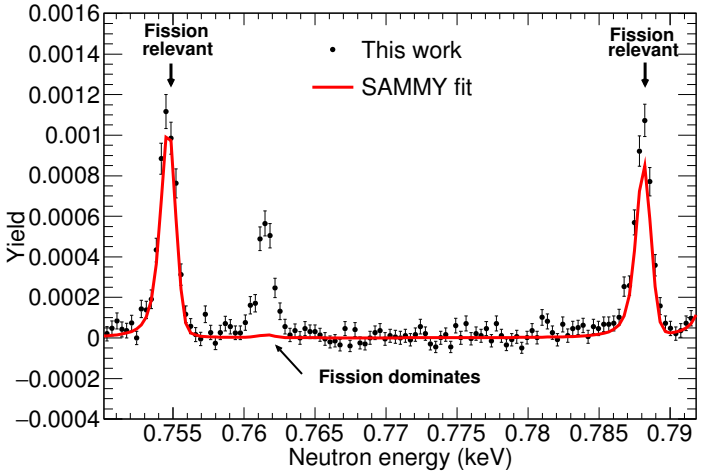

Figure 7.2: *Experimental capture yield as a function of the neutron energy showing the resonances with the largest fission contribution (left out of the analysis). The red curve corresponds to the capture yield calculated by SAMMY, which clearly underestimates the experimental data for these resonances, especially for the one at 762 eV.*

4. For the resonances with small fission contribution, the values of Γ_f were fixed to the values measured by Auchampaugh et al. [244] or Weigmann et al. [245], ofr the resonances reported by them and 0.01 meV for all the others, as recommended in JEFF-3.2 (see Table D.1).

5. The radiative capture width Γ_γ is expected to be a constant (within ∼3% according to statistical model simulations [243]). In order to determine the value of $\langle\Gamma_\gamma\rangle$, a systematic study of the χ^2 of the SAMMY calculations was carried out among the

largest resonances below 1.5 keV, using those showing a well bound Γ_γ around the minimum χ^2 to compute the average Γ_γ. The details are given in Section 7.1.3.

6. The radiative width of the remaining resonances is fixed to $\langle\Gamma_\gamma\rangle$ and only the neutron width is fitted in the SAMMY calculation.

7. In the resonance analysis above 1.3 keV, where no resonance parameters are available in the evaluations, the energies and neutron widths in Refs. [244, 245] were used as initial parameters for the fit and to help identifiying small resonances.

7.1.3 Γ_n vs $\Gamma_\gamma\chi^2$-study to extract $\langle\Gamma_\gamma\rangle$

As the radiative width should present a constant value, the average value has been calculated from the individual Γ_γ values of a set of resonances. The criteria to choose the more significant resonances to extract the radiative width have been:

1. High statistics: therefore just large resonances below 1.5 keV have been selected.

2. High sensitivity to Γ_γ: the SAMMY fit is actually sensitive to the resonance area. As we introduced in Section 2.2.3, the resonance area (or Radiative Kernel) is dominated by the Γ_γ value for resonances with $\Gamma_n \gg \Gamma_\gamma$. Thus, only resonances with $\Gamma_n \gtrsim \Gamma_\gamma$ were selected to extract their radiative widths.

In order to analyze the degree of correlation between Γ_γ and Γ_n and identify resonances with well bound Γ_γ values, we performed a systematic study of the χ^2 of the SAMMY fits as a function of the values of the Γ_γ and Γ_n (see Figure 7.3). The reduced χ^2 of the fit was calculated from the deviation of the experimental cature yield vs. parameterized yield as a function of Γ_γ and Γ_n, using the following expression:

$$\chi^2 \;=\; \left(\frac{1}{N}\sum_{i}^{N}\frac{(x_i - T_i)^2}{\sigma_i^2}\right)^{1/2}, \tag{7.5}$$

where x_i, σ_i and T_i are the experimental value of the yield, its uncertainty and the value from the SAMMY calculation, respectively. The sum in Eq. (7.5) runs over all the points within a given resonance.

Studing the 2D distributions of the reduced χ^2 we found that:

- Many resonances, such as the two largest ones at 2.67 and 53 eV shown in Figure 7.3, showed a well bound minimum which leads to a well defined pair of Γ_γ and Γ_n values. If these pairs are chosen as initial parameters, we confirmed that the fitted parameters remained compatible with the initial ones within uncertainties.

- Some of the studied resonances presented strongly correlated values between Γ_γ and Γ_n and the fit converged after many iterations towards too large Γ_n values, inconsistent with the evaluated resonance value extracted from a multi-channel analysis

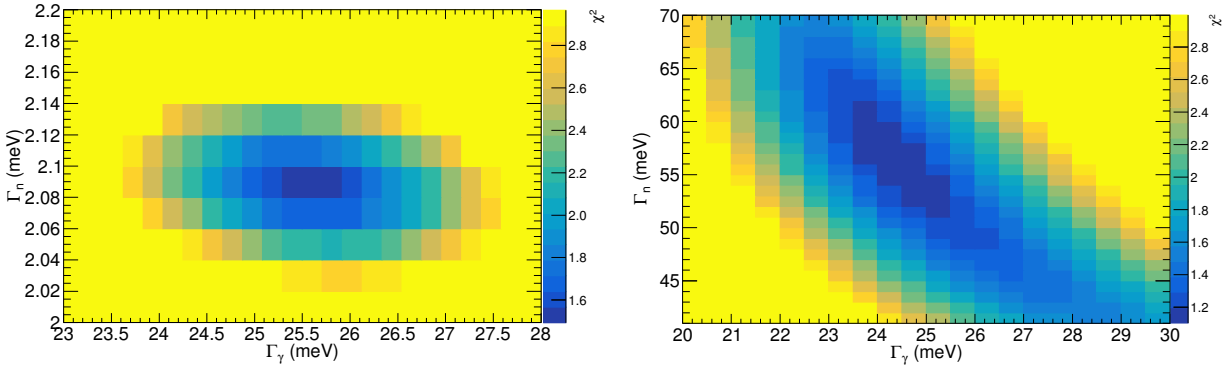

Figure 7.3: *2D plots showing the evolution of the reduced χ^2 of the fit (color scale) as a function of the Γ_n-Γ_γ values for the 2.67 eV (top) and 53.5 eV (bottom) resonances.*

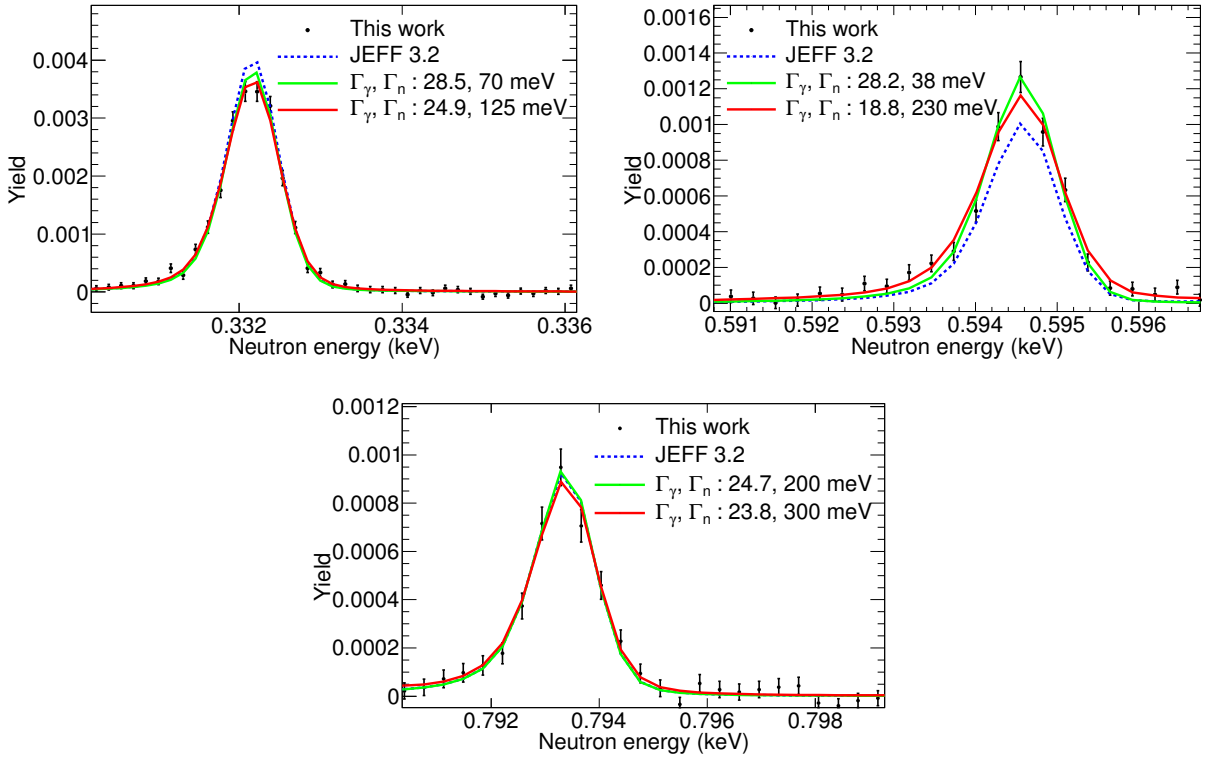

Figure 7.4: *Example of the sensitivity of resulting SAMMY fits to different combination of Γ_n and Γ_γ showing the compatibility of the fit with overestimated Γ_n (red) compared to the fit with a Γ_n value consistent with evaluations (green). JEFF-3.2 is also shown as a reference (dotted blue line).*

of all available cross section measurements (capture, scattering, total [40] and fission [244, 245]). For those cases, the Γ_n was bound to a value consistent with the evaluations and then Γ_γ was fitted.

Figure 7.4 shows the most extreme cases where one can see that a large reduction in Γ_n does not compromise the quality of the fit. This result serves as a validation of the method followed for the resonances with no clear minima in the 2D Γ_γ-Γ_n distributions. The difficulties to constrain the value of Γ_n during the analysis of capture data would be solved with help of transmission data measured with the same sample, which could the be fitted in paralell with SAMMY (see for instance Ref. [194]).

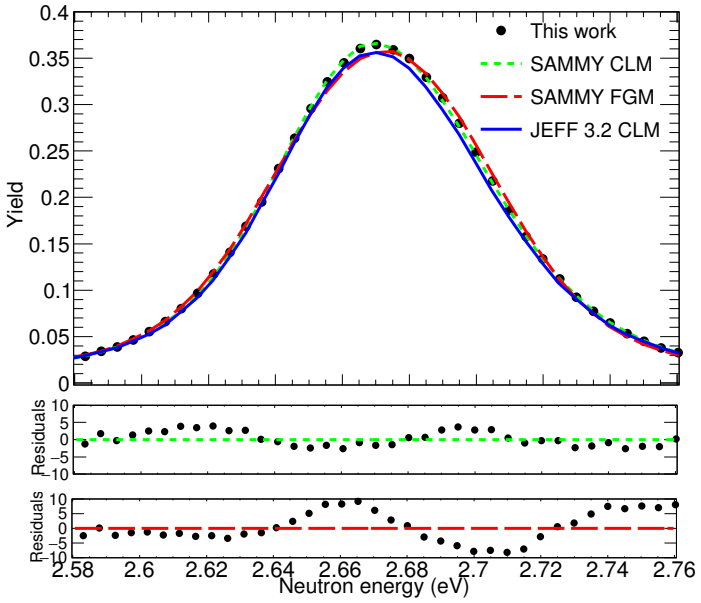

Figure 7.5: *SAMMY fits and residuals for the largest ^{242}Pu capture resonance using Free Gas (FGM) and a Crystal Lattice (CLM) models to describe the Doppler broadening (top). The fit obtained using the resonance parameters in JEFF-3.2 or ENDF/B-VII.1 (CLM) is shown as a reference.*

The χ^2 method also served to identify resonances for which the fit did not converge to a succesful reproduction of the resonance shape. In particular, the analysis of the lowest energy resonance with the commonly employed Free Gas Model (FGM) for the Doppler broadening is not satisfactory, giving for instance a reduced χ^2 of 4.7 at best. The use of the more realistic Crystal Lattice Model (CLM), was tested with different example files in SAMMY (see Table 7.1). The best reduced $\chi^2 = 1.91$ was obtained in this case with a Uranium Oxide phonon description (SAMMY example file 124d). The comparison between the calculation with the GM and the best CLM fit is shown in Figure 7.5, where the reduction of the residuals, defined as the deviation (in σ) between the fit and the experimental points, illustrates the success of the latters Regarding the second largest resonance, at 53.5 eV, the fits are excellent with both models and the extracted radiative kernels agree within 0.1%; therefore the resonances at higher energies were all analyzed using the FGM, since the difference with respect to the results with the CLM are negligible but the computing time needed is significantly reduced. This result shows that the sensitivity to Doppler broadening is higher at low energies.

Table 7.1: *Resonance parameters, quality of the fit and radiative kernel of the main capture resonance as a function of the Doppler model (FGM or CLM). For the latter the result of the different example phonon files distributed with SAMMY are compared.*

		CLM Phonon file		
Resonance parameter	**FGM**	**124a/e/f**	**124d**	**124c**
Energy	2.6762	2.6762	2.6762	2.6760
Γ_γ	25.63	25.22	25.34	25.46
Γ_n	2.09	2.10	2.10	2.06
χ^2	4.74	1.98	1.91	2.65
R_K	1.931	1.935	1.936	1.908

7.2 Individual resonance parameters and radiative kernels

Following the procedure described in Section 7.1.2, a total of 251 resonances have been observed and analyzed between 1 eV and 4 keV. Figure 7.6 shows the experimental capture yield fitted with SAMMY in different energy ranges up to 1 keV. In this figure we compare the same SAMMY calculation in this work with both the *unweighted* (used in this work) and the *weighted* (extracted with the usual prescription of the PHWT) yields. The results in this figure support the conclusions drawn in Section 6.9.3:

1. The same SAMMY calculation (i.e. with the final parameters in this work) perfectly agrees with the two results for the capture yield.
2. The usual PHWT procedure enhances the fluctuations, making difficult to distinguish the small resonances already below 1 keV.

The good neutron energy resolution of n_TOF-EAR1, combined with the high statistics of the new capture data and the use of a new approach for the PHWT, have allowed to extend the resolved resonance region up to 4 keV, significantly beyond the current high energy limit in the evaluations, which are based on the resonance parameters reported in Refs. [40, 244, 245]. The extension of the R-Matrix analysis in different neutron energy intervals from 1.5 keV to up to 4 keV is shown in Figure 7.7.

The resulting list of individual resonance parameters up to 4 keV is presented in Table D.1. In this table several resonances are marked as possible p-waves. The criterion for identifiying possible p-wave resonances is based on the probability of ocurrence of p-wave resonances according to the result of statistical model simulations (see Section 7.4).

In order to assess a realistic uncertainty to the fitted resonance parameters we have proceeded as follows:

- We carried out a systematic study of the uncertainty in the fitted parameters as a function of the *Fudge Factor* FF (described in Section 7.1.1).
- The fit was carried out with FF ranging from 2.5% to 60%.

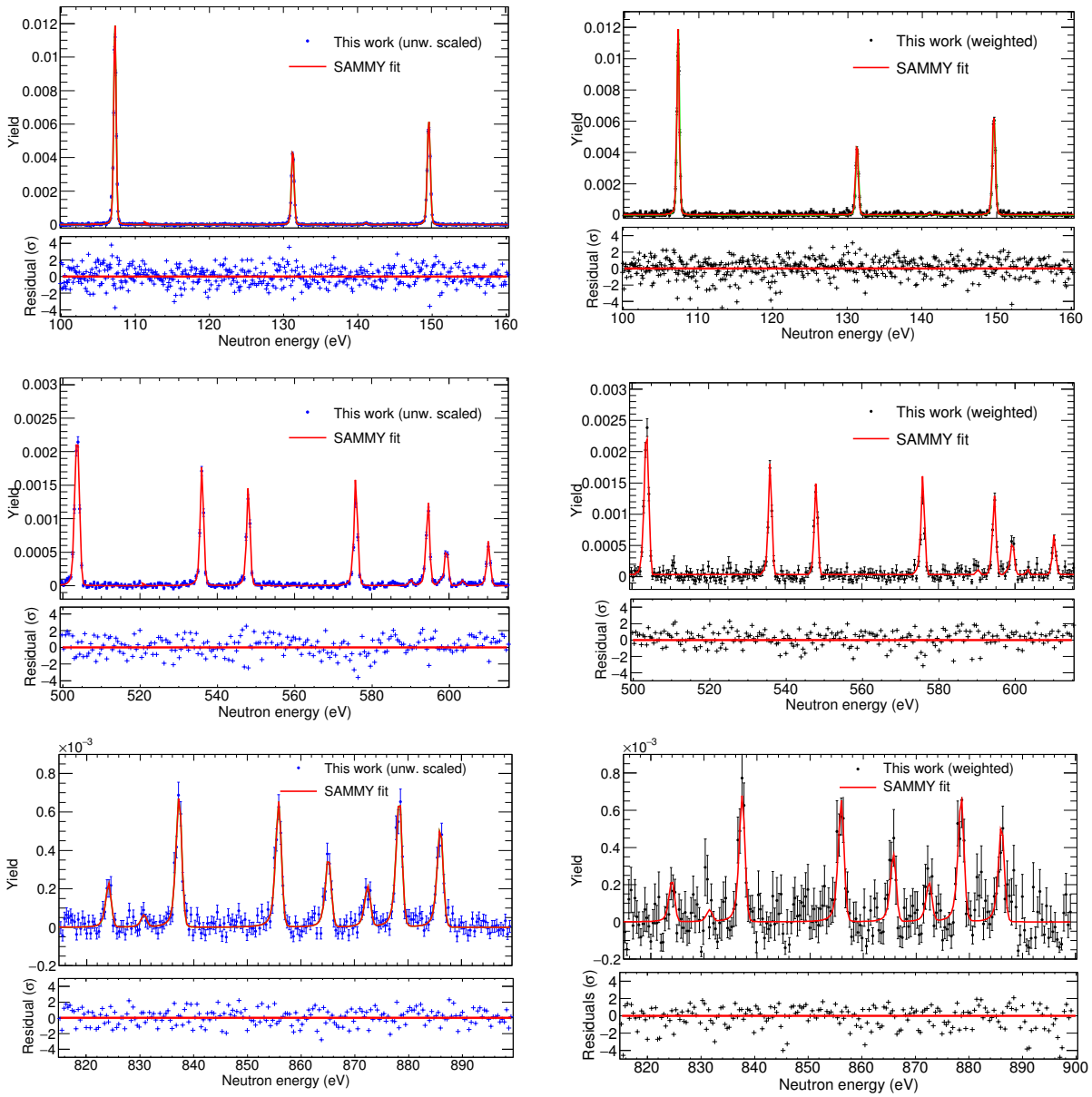

Figure 7.6: *The capture yield in this work fitted using the SAMMY code (left panels) and the same calculation on top of the weighted yield (right panels) in different energy ranges from 100 to 900 eV. The residuals show the deviation of the data in σ to the calculation.*

- The uncertainty of each fitted parameter was taken from the uncertainty given by SAMMY from the calculation with the minimum FF for which the uncertainty remained below 80% of the FF value.

The quantitative comparison between the cross section in this work and that of JEFF-3.2 in Section 7.3 is made in terms the of Radiative Kernel (R_K) of the individual resonances. From the general expression for the Reaction Kernel in Eq. (2.24), the Radiative Kernel is

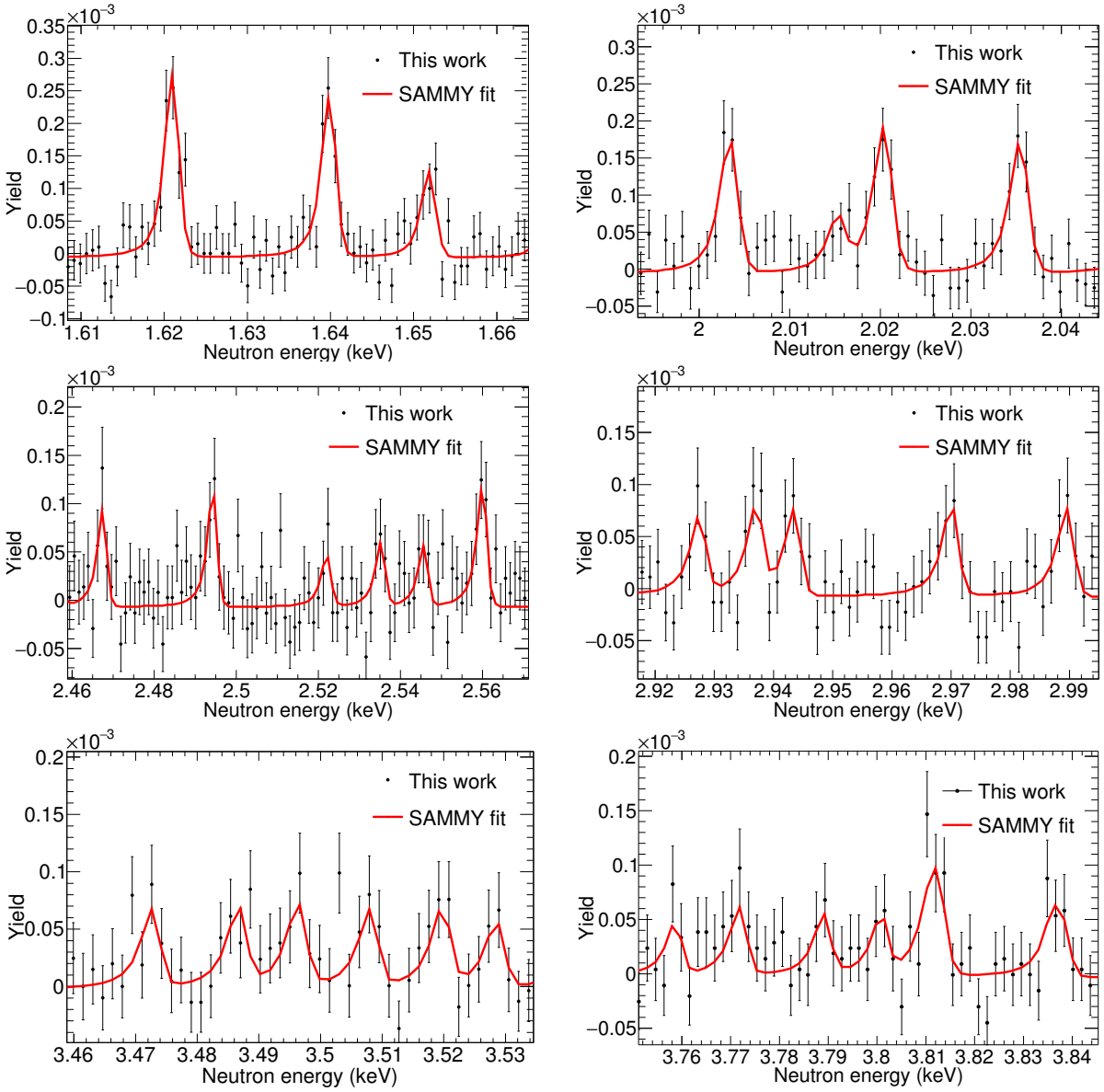

Figure 7.7: *The capture yield in this work fitted using the SAMMY code in different energy ranges from 1 to 4 keV.*

calculated as

$$R_K = g_J \frac{\Gamma_\gamma \Gamma_n}{\Gamma_\gamma + \Gamma_n + \Gamma_f}, \tag{7.6}$$

For the case of ^{242}Pu, the spin factor g_J in this equation takes the following values:

- s-wave resonances ($J^P = 1/2^+$): $g_J = 1/2$.
- p-wave resonances ($J^P = 1/2^-$ or $3/2^-$): $g_J = 1$ or 2.

The R_K of each resonance is listed in Table D.1. Although all the resonances were analyzed as s-waves, the R_K in Table D.1 are also correct for those resonances which are

considered p-wave candidates (see Section 7.4). On the other hand, the extracted neutron widths are spin-dependent. In order to remove this dependency, the fitted Γ_n values in Table D.1 are given as $g_J\Gamma_n$.

7.3 Comparison to previous experimental data and evaluations

7.3.1 Qualitative comparison: energy range and new resonances

The main improvement of this new data set with respect to the previous situation is the significant expansion of the neutron energy range where resonance parameters are reported. The status of the resonance parameters before this measurement was the following:

- Poortmans et al. [40] had reported resonance parameters up to 1300 eV from a combined measurement of the total, elastic and capture cross sections, but Γ_γ values only up to 920 eV.
- The recent experiment by Buckner et al. [41] provided data up to 40 keV but resonance parameters were extracted only up to 500 eV.
- Resonance parameters above 1300 eV were extracted from the fission measurements carried out by Auchampaugh et al. [244] and Weigmann et al. [245].

The current high energy limits of the RRR in the evaluations are shown in Figure 7.8. The bottom panels of this figure show the SAMMY fit of the data in this work just above the current 920 eV and 1.3 keV energy limit for resonance parameters in ENDF/B-VII.1 [21] and JEFF-3.2 [20], respectively. At lower energies, significant differences with the evaluations have been found. In this sense, the different resonances displayed in the top and middle panels Figure 7.8 are illustrative examples of resonances currently present in the evaluations that can be confirmed (75) or rejected (7) according to the new capture data reported herein. The main differences between the identified resonances and the ones present in the current RRR of the evaluations are:

- We confirm the presence of a doublet at 504 eV, as already suggested by Poortmans et al. [40]. The inclusion of this doublet is required to fit this resonance with a Γ_γ value consistent with the average and a Γ_n which is not orders of magnitude higher than the others.
- The resonance at 14 eV listed in the evaluated files is not observed in this work, confirming what Buckner et al. reported [41].
- 19 new resonances have been identified within JEFF-3.2's resonance region (some examples in Figure 7.8).
- The new resonances are usually weak, therefore some of them are most likely p-wave resonances, as it is discussed in Section 7.4.

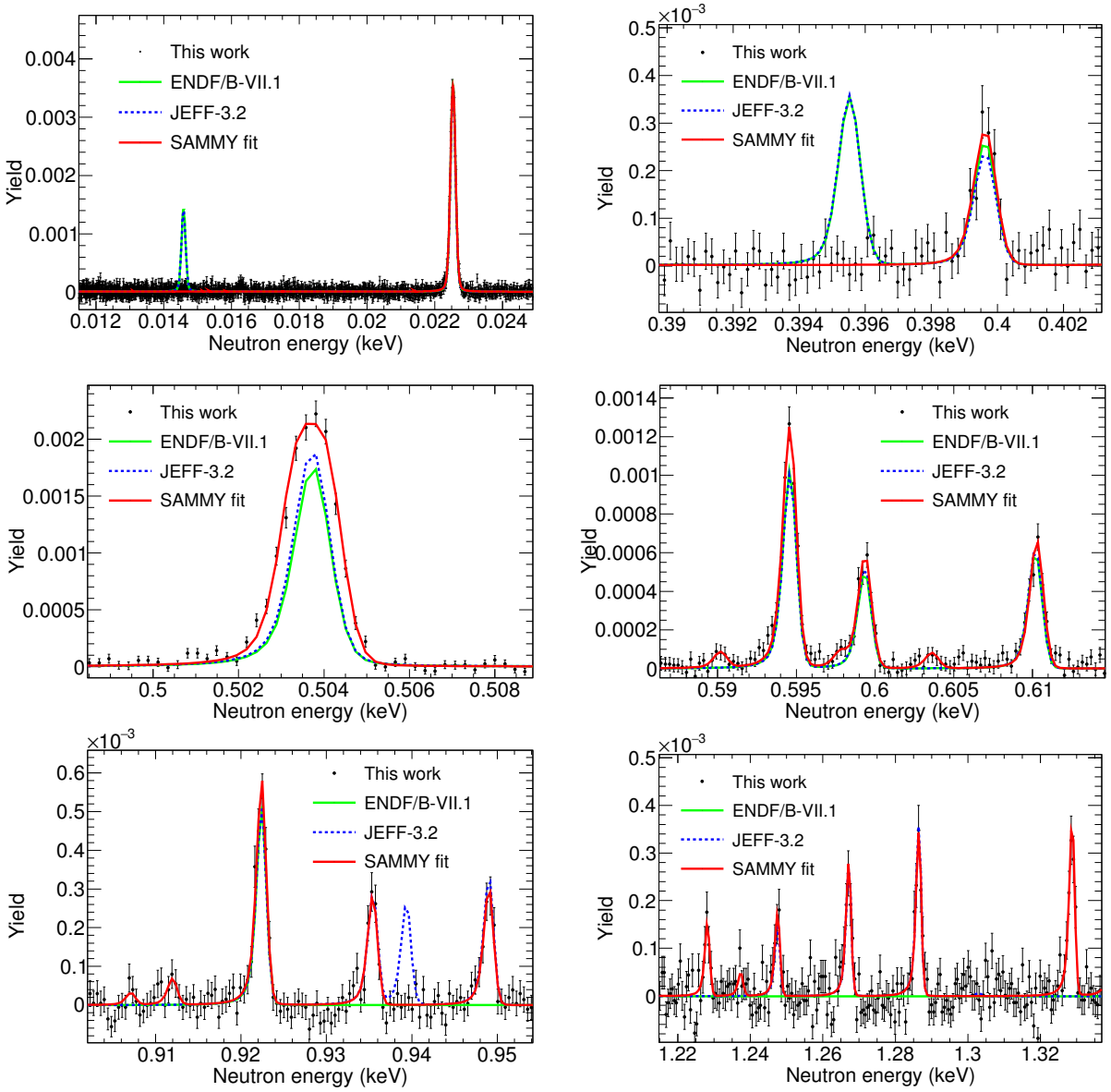

Figure 7.8: *Capture yield from n_TOF together with the SAMMY fit (red/dark grey line) and the predictions from JEFF-3.2 (dashed line) and ENDF/B-VII.1 (green/light gray line) in several neutron energy ranges below 1.3 keV where significant differences are found.*

7.3.2 Quantitative comparison: Radiative kernels

The ratio between the R_K in this work, calculated using Eq. (7.6) for each resonance, with respect to those calculated from the resonance parameters in JEFF-3.2 and in the recent measurement at DANCE [41] have been calculated to compare the cross sections quantitatively. The ENDF/B-VII evaluation has been excluded from the comparison since it presents similar results than JEFF-3.2 for the common resonances while the number of resonances in the former is significantly smaller than in the latter. The R_K ratios, also listed in Table D.1, have been studied as a function of the fission and scattering to capture

width ratios in order to look for trends that could hint at systematic errors or biases, but no correlations have been found (see Figure 7.9).

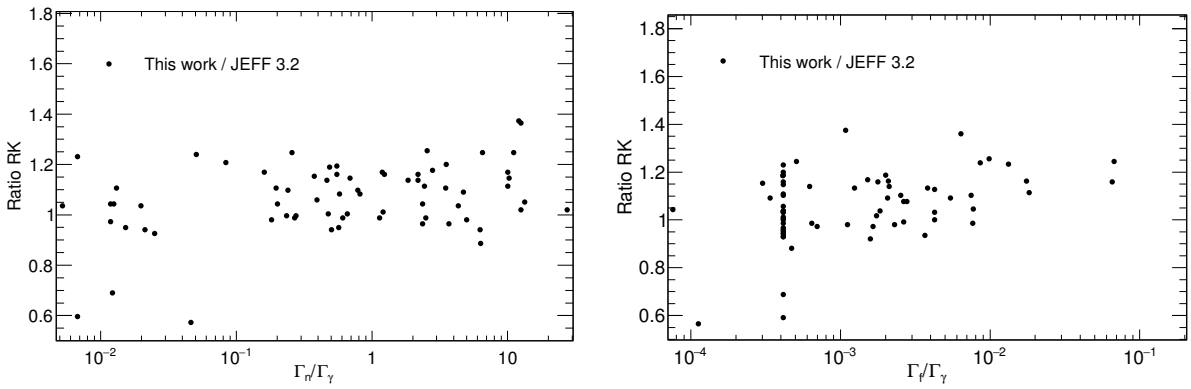

Figure 7.9: *Ratio of individual radiative kernels obtained in this work with respect to JEFF-3.2 as a function of* Γ_n/Γ_γ *(top) and as a function of* Γ_f/Γ_γ.

The top panel of Figure 7.10 shows the individual ratios of n_TOF kernels (this work) with respect to JEFF-3.2 (72 common resonances), indicating in average an underestimation in JEFF-3.2 of 4.0(4)%. For an overall comparison, the invididual kernels have been grouped over 200 eV energy intervals and the ratios of the integrated R_K in each energy interval are presented in Table 7.2 and shown with a red line in the top panel of Figure 7.10, where the shadowed area corresponds to the statistical uncertainty of the sum of R_Ks in each range. According to the results in Table 7.2, a minimum integral ratio n_TOF/JEFF-3.2 of 1.028(5) is found below 200 eV, while average differences larger than 12% are observed in the 400 to 800 eV region, and compatible results within the statistical uncertainty are obtained above 1 keV.

The bottom panel of Figure 7.10 zooms in on the first 500 eV and includes the ratio of individual R_Ks in this work with respect to the recent measurement in DANCE (35 common resonances). Overall, the n_TOF data suggest that the R_Ks are on average 4.0(4)% higher than JEFF-3.2 and 6.2(10)% higher than DANCE, in terms of weighted mean (weighted by the radiative kernel). The comparison of the largest ^{242}Pu resonance, at 2.67 eV, indicates that the new value is 4.2(2)% than in JEFF-3.2 (or ENDF-VII.1), and just 1.8% larger than the value of DANCE [41].

The 4% higher cross section found in this work below 1 keV with respect to the evaluations does not compromise the suggested [46, 47, 48] reduction of 14% in the integral cross section between 1 keV and 1 MeV because the evaluations are based on completely different data sets below and above 1.3 keV. In the resonance region, the resonance widths and energies are taken from Refs. [40, 244, 245], while the unresolved resonance region is based in the 40-year-old measurements of Refs. [43, 44, 45] between 6 and 210 keV. The analysis of the ^{242}Pu(n,γ) cross section in the unresolved resonance region is presented in Chapter 8.

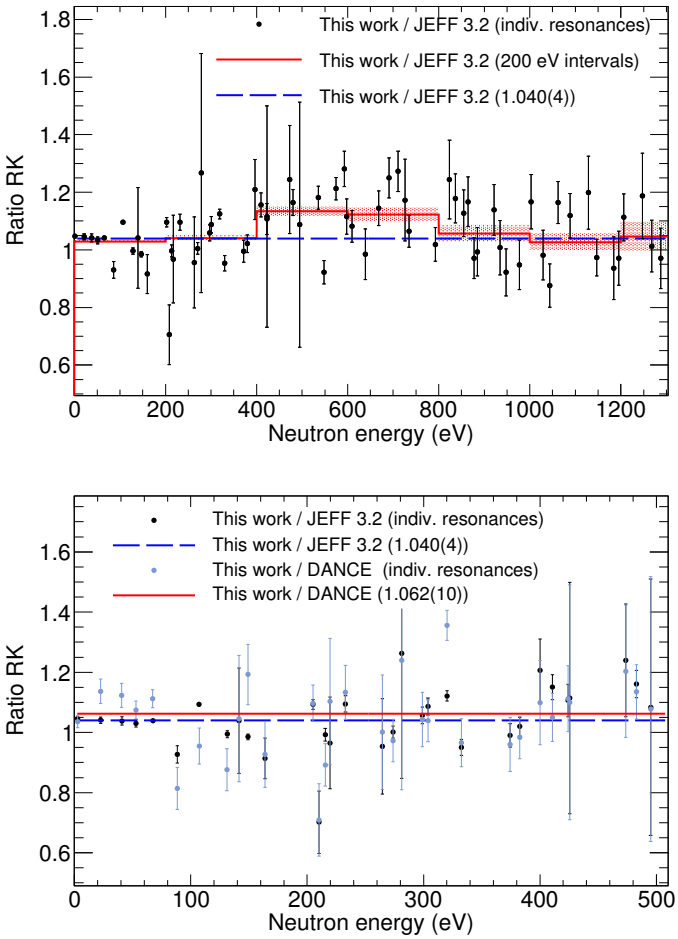

Figure 7.10: *Top: Ratio of individual radiative kernels obtained in this work with respect to JEFF-3.2 (black) as a function of the neutron energy together with the weighted mean (dashed blue line). The solid red line coresponds to the ratio of the integrated R_K over 200 eV intervals and the shadowed area illustrates the statistical uncertainty of the R_K integral in each energy interval (see Table 7.2). Bottom: Ratio of individual R_K in this work to JEFF-3.2 and DANCE below 500eV together with their weighted means (dashed and solid line, respectively). The values in brackets in the legend correspond to the weighted mean of the ratios.*

7.4 Statistical properties of resonance parameters

7.4.1 s-wave level spacing and observed p-wave resonances

The average level spacing D_0 is usually calculated using Eq. (2.28), as the number of observed observed resonances N_0 in an interval of neutron energies ΔE_n. Its statistical uncertainty, given by Eq. (2.31), is indirectly proportional to the square root of the number of resonances in the studied energy range. Experimentally, D_0 is usually estimated from the cumulative distribution of observed resonances as a function of the neutron energy, shown in Figure 7.11. In this plot the distribution of observed resonances in this work is compared to the one from JEFF-3.2, showing that both are in fairly good agreement with this work up to ∼500 eV, while at higher energies new resonances are observed in this work.

The resonance distribution in Figure 7.11 shows a constant slope up to an energy beyond which a fraction of resonances missed due to the reduced statistics and increasing resonance widths with increasing energy. The value of D_0 was extracted as follows:

1. The distribution in Figure 7.11 was linearly fitted up to different maximum energies, and the value of D_0 was extracted as the inverse of the slope.
2. The individual values of D_0 were compared and the final result was taken from the linear fit up to the maximum energy below which the resulting the D_0 value was compatible to the values extracted at lower energies (see Table 7.3).

The final value, obteined from the linear fit to our data below 1.1 keV shown in Figure 7.11, indicates a D_0 value of 12.5(7) eV. However, this estimate can be affected by missing s-wave resonances or p-wave resonances wrongly considered as s-wave.

7.4.1.1 Statistical simulations: p-wave bias of D_0

The possible biasing of the D_0 value obtained in the previous section was studied with help of statistical model simulations. These simulations consisted of several thousands of artificial resonance sequences generated using the values extracted in this work for $\langle\Gamma_\gamma\rangle$

Table 7.2: *Ratio of the integrated R_K over 200 eV interval in this work with respect to the results obtained from the resonance parameters in JEFF-3.2.*

Energy range (eV)	n_TOF/JEFF-3.2
0-200	1.028(5)
200-400	1.041(9)
400-600	1.134(18)
600-800	1.122(24)
800-1000	1.06(3)
1000-1200	1.03(3)
1200-1400	1.05(5)

Together with the observed distribution of $g_J\Gamma_n^0$, Figure 7.12 shows an example of a (randomly selected) set of reduced neutron widths for s- and p-wave resonances from our statistical model simulations.

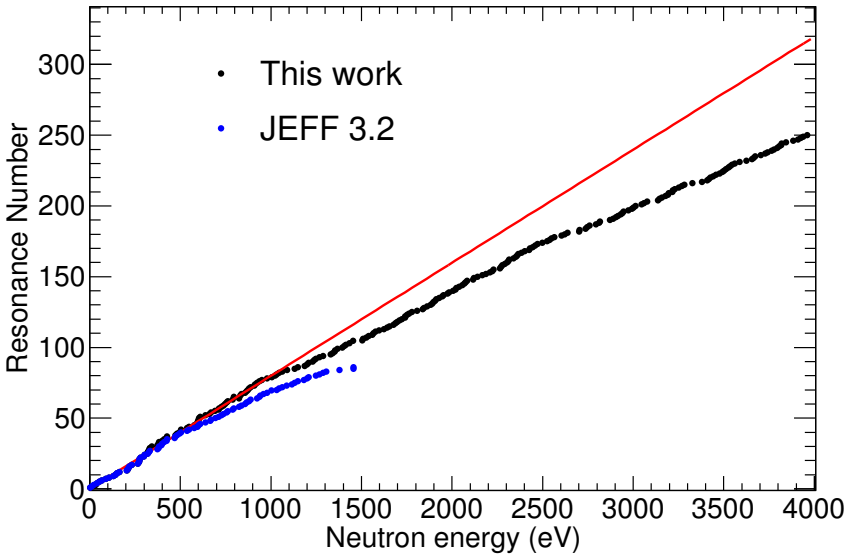

Figure 7.11: *Cumulative number of resonances as a function of the neutron energy showing a compatible D_0 for JEFF-3.2 and this work up to ∼500 eV. The solid red line corresponds to the linear fit of this distribuiton in the energy region below 1.1 keV (see text for the details).*

Max. energy (eV)	D_0 (eV)
500	11.9±1.0
750	12.3±0.8
1000	12.4±0.7
1100	**12.5±0.7**
1250	13.0±0.7

Table 7.3: *Average level spacing as a function of the upper energy limit of the fit. The last compatible value (E_n <1100 eV) with the energy ranges below is chosen as the D_0.*

(see Section 7.4.2) and S_0 (see Section 7.4.3). and the value of p-wave neutron strength function $S_1 = 2.07 \cdot 10^{-4}$ recommended by Rich et al. in Ref. [42]. These sequences were simulated for several different values of D_0. The resonance parameters on the simulated sets of resonances were distributed as follows:

- The spacing between neighboring resonances was assumed to follow the Wigner distribution [68] and no long-range correlations between the resonance energies were assumed. The position of the first resonance was assumed to be random.
- The level density for p-waves was scaled from D_0 assuming a $2J+1$-dependence for the level density.
- The reduced neutron widths $\Gamma_n^0 = \Gamma_n/\sqrt{E_n}$ were assumed to fluctuate around the

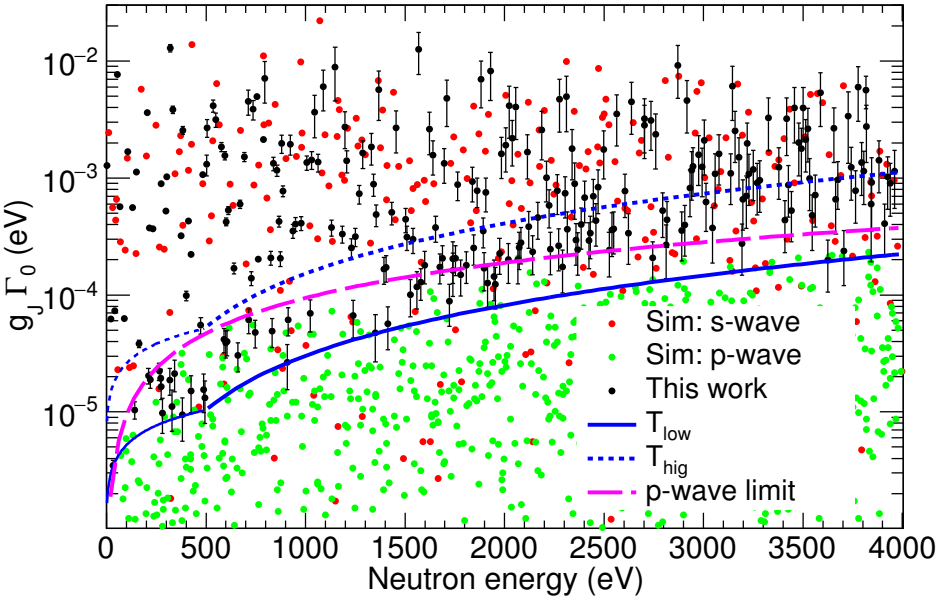

Figure 7.12: *Experimental distributions of reduced neutron widths together with a random simulated set of s- and p-wave resonances ($D_0 = 12.5$ eV) as a function of the neutron energy along with different thresholds for observation of resonances used in the study. The purple line corresponds to the threshold used to indentify p-wave candidates (details in the text).*

expectation values according to a Porter-Thomas distribution [69].

- The radiative widths were assumed to fluctuate according to the expectation value obtained in this work according to the ν^2 distribution with $\nu = 180$ [243].
- A channel radius $R = 1.35 \cdot A^{1/3}\ fm$ was used to compute the p-wave penetrability.

The experimental distribution of $g_J\Gamma_n^0$ is shown in Figure 7.12 together with an example of a (randomly selected) set of reduced neutron widths for s- and p-wave resonances from our statistical model simulations. In order to compare the experimental and simulated distributions, one should note that in the real experiment the weakest resonances are lost. Thus, an experimental observation threshold in reduced neutron width has to be applied to the simulated results. This detection limit T_{low} was empirically estimated from the reduce neutron width of the weakest observed resonances as a function of the neutron energy, as it is shown in Figure 7.12 and corresponds to the following analytical expressions:

$$\begin{aligned} T_{low}(E_n < 500eV) &= 10^{-3}(1 \cdot 10^{-3} + 4.24 \cdot 10^{-4}\sqrt{E_n}) \\ T_{low}(E_n > 500eV) &= 10^{-3}(2.5 \cdot 10^{-4} - 5 \cdot 10^{-4}\sqrt{E_n} + 4 \cdot 10^{-5}E_n + 6 \cdot 10^{-9}E_n^2), \end{aligned} \tag{7.7}$$

where T_{low} is given in eV. In addittion to the experimental threshold, additional higher thresholds were tested: $T_{med} = 3 \times T_{min}$ and $T_{hig} = 5 \times T_{min}$ (see Figure 7.12). As one could expect, the experimental observation threshold T_{low} seems to lie well below the majority of the s-wave resonances only the few strongest p-wave resonances are found above

it.

Using these statistical simulations we have compared the predicted number of visible resonances (s- and p-waves combined) with the experimental results for different D_0 values ranging from 12 to 19 eV. This was performed as a function of

- the maximum neutron energy range: 600 keV, 1 MeV and 4 MeV and
- the value of the threshold: T_{low}, T_{med} and T_{high}.

The results presented in Table 7.4 show the ranges of D_0 values for which the simulations are compatible with the experimental data within one standard deviation for each combination of energy range and observation threshold. The uncertainties in brackets in Table 7.4 correspond to the standard deviation of the results of the individual simulated sequences.

Table 7.4: *Number of predicted and experimentally observed levels for three different maximum neutron energy ranges (600, 1000 and 3700 eV) and three different thresholds (T_{min} is the observation threshold, $T_{mid} = 3 \times T_{low}$ and $T_{hig} = 5 \times T_{low}$). The row labeled as "Range D_0" gives the interval of D_0 compatible within one standard deviation with the number of observed levels.*

	T_{low}			T_{mid}			T_{high}		
D_0 (eV)	600 eV	1000 eV	4000 eV	600 eV	1000 eV	4000 eV	600 eV	1000 eV	4000 eV
12.5	54(5)	89(6)	290(12)	42(4)	69(5)	212(10)	41(4)	65(5)	184(10)
13.5	51(5)	86(6)	277(12)	40(4)	64(5)	200(10)	38(4)	61(5)	174(10)
14.5	49(5)	82(6)	266(11)	37(4)	60(5)	189(10)	35(4)	57(5)	166(9)
15.5	47(5)	79(6)	256(11)	35(4)	57(5)	180(9)	33(4)	54(5)	158(9)
16.5	45(5)	76(6)	247(11)	33(4)	54(5)	171(9)	31(3)	51(5)	150(9)
17.5	44(5)	73(6)	239(11)	32(3)	51(4)	164(9)	30(3)	48(4)	144(9)
18.5	42(5)	71(6)	233(11)	30(3)	49(4)	158(9)	28(3)	46(4)	139(8)
EXP.	48	78	251	32	56	187	31	54	155
RANGE D_0	15.4(26)	16.0(20)	16.4(14)	17.1(21)	15.7(13)	15.0(9)	16.5(20)	15.4(14)	16.2(13)

With help of this statistical study, an average value of $D_0 = 15.8(8)$ eV, consistent with the observed number of levels for all the energy intervals and thresholds within $\sim 1\sigma$, is the proposed average spacing of s-wave resonances from our analysis. This value indicates that the D_0 extracted from the fit of the distribution in Figure 7.11 is actually biased (lower by 21%) by the p-wave contribution.

In order to validate the distribution of level spacing for s-wave resonances, one should compare it to the theoretically expected Wigner's Law, given by Eq. 2.30). However, the mixture of the s- and p-wave component makes this comparison less meaningful. On the other hand, the statistical model simulations provide a powerful tool to validate the experimental results. In this sense, the nice agreement of the experimental cumulative number of observed resonances (s- and p-wave combined) as a function of the neutron energy is compared with the predictions of a few simulated sequences obtained with $D_0 = 15.8$ eV in Figure 7.13.

From the results of our simulations, we can estimate the total and visible number of s- and p-wave resonances, thus the total number of observed levels. The comparison of this

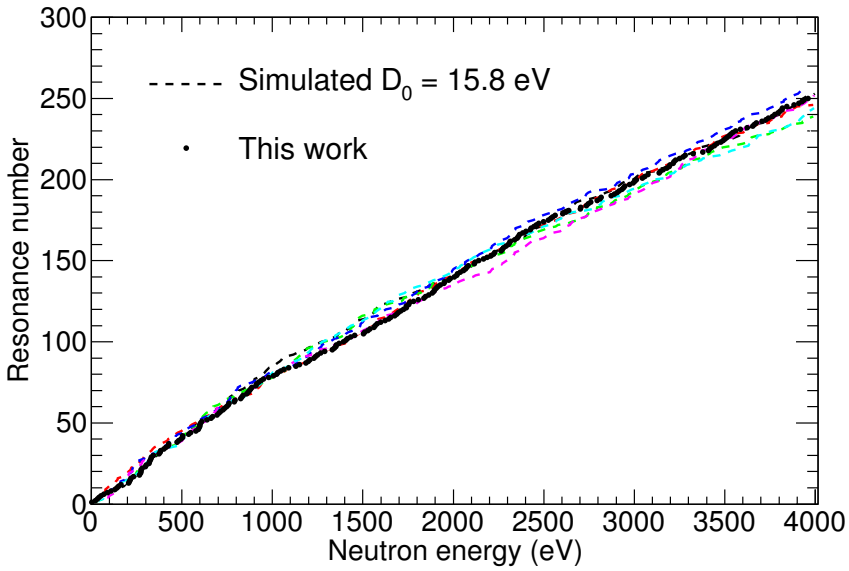

Figure 7.13: *Experimental cumulative energy distribution of observed resonances compared to several individual resonance sequences obtained from statistical model simulations showing the good reproduction of the data. The simulated sequences were generated with* $D_0 = 15.8$ *eV,* $S_0 = 0.91 \cdot 10^{-4}$ *and* $S_1 = 2.07 \cdot 10^{-4}$ *[42] and corrected for the experimental observation threshold* (T_{low}).

Table 7.5: *Number of predicted visible resonances (s- and p- wave combined) compared to the actual experimental observation.*

E_{max} (eV)	Predicted	Experimental
600	47(5)	48
1100	85(6)	85
2000	145(9)	139
4000	253(8)	251

result with the experimental observation observed levels serves as a quantitative validation of the extracted value for D_0. The results are presented in Table 7.5, indicating a very good agreement between the predictions and the experimental observations. This result is illustrated in Figure 7.14, where we show the predictions for the total and visible number of s- and p-wave resonances as a function of the neutron energy. The cummulative number of resonances in this work (black dots) is in perfect agreement with the predicted number of observed (s- + p-wave) within the uncertainties.

7.4.1.2 p-wave resonance candidates

Besides the global understanding of the number of missed s-waves and observed p-waves, this study aimed at identifiying p-wave candidates, which are indicated in Table D.1. The possible p-wave resonances were identified according to statistical model simulations of the

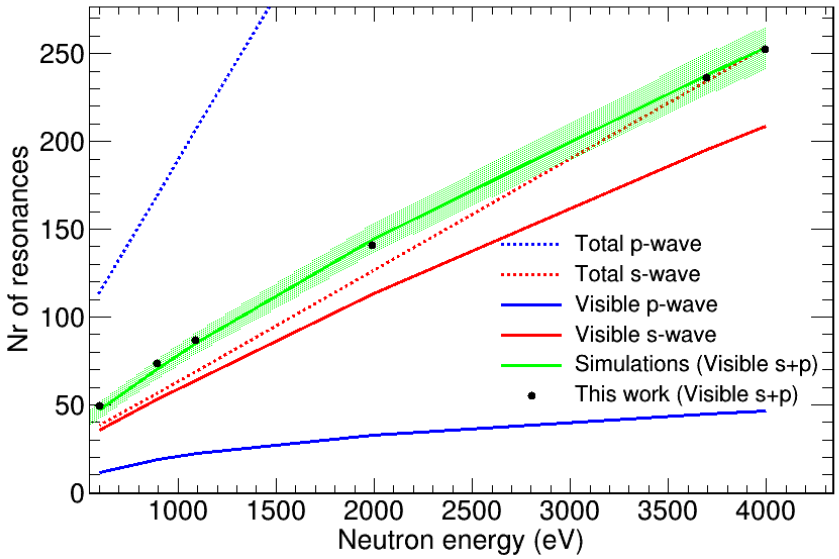

Figure 7.14: *Evolution of the number of predicted s- (red) and p-wave (blue) resonances as a function of the neutron energy. The total number of resonances is represented with doted lines while the visible fraction is shown in solid lines. The black dots represent the total number of observed resonances (s- + p-wave) showing a very good agreement with the prediction of the simulations (green line) within its uncertainty (shadowed corridor).*

distribution of reduced neutron widths for the p-wave component. From these simulations we concluded:

- The energy dependence of the average value of $g_J\Gamma_n^0$ was found to be $\langle g_J\Gamma_n^0\rangle = 1.10 \cdot 10^{-8}E_n$, where E_n is given in eV.
- According to the Porter-Thomas distribution, given by Eq. (2.36), there is only just 1% chance that one p-wave resonance has a $g_J\Gamma_n^0$ value larger than 6.64 times the average and 0.35% chance that it is larger than 8.53 times the average.

The resonance tagged as p-wave candidates in Table D.1 were those having $g_J\Gamma_n^0$ values smaller than 8.53x$\langle g_J\Gamma_n^0\rangle$. This threshold, shown as a pink dashed line in Figure 7.12, is a well suited one since:

1. A negligible number of observable p-wave resonances (0.35% according to the simulations) present larger $g_J\Gamma_n^0$ values.
2. The number of s-wave resonances tagged as p-wave candidates remains small.

According to this analysis, the p-wave contribution is mainly observable below 2 keV, where we found in our data 37 p-wave candidates out of a total of 43 in the full energy range. This result is consistent with the 31(5) and 9(3) candidate resonances with p-wave and s-wave origin, respectively, predicted by the simulations below 2 keV. Among the p-wave candidates we find the 10 observed resonances below 500 eV, which are already considered p-wave in ENDF/B-VII.1 (s-wave in JEFF-3.2) (see Table D.1).

7.4.2 Radiative widths

Total radiative widths are given by the sum of partial radiation widths to all levels below the neutron separation energy S_n. As we introduced in Section 2.2.4, the huge number of available final levels, especially for heavy nuclei, turns the distribution of the total radiation widths into a very narrow distribution and the radiative width can be assumed to be constant for all resonances(see Eq. (2.34)). Actually, statistical model calculations of total radiative widths for ^{242}Pu, carried out using the constant-temperature level density model, indicate that the individual Γ_γ values of s-wave resonances should fluctuate within 3 to 3.5% around $\langle\Gamma_\gamma\rangle$.

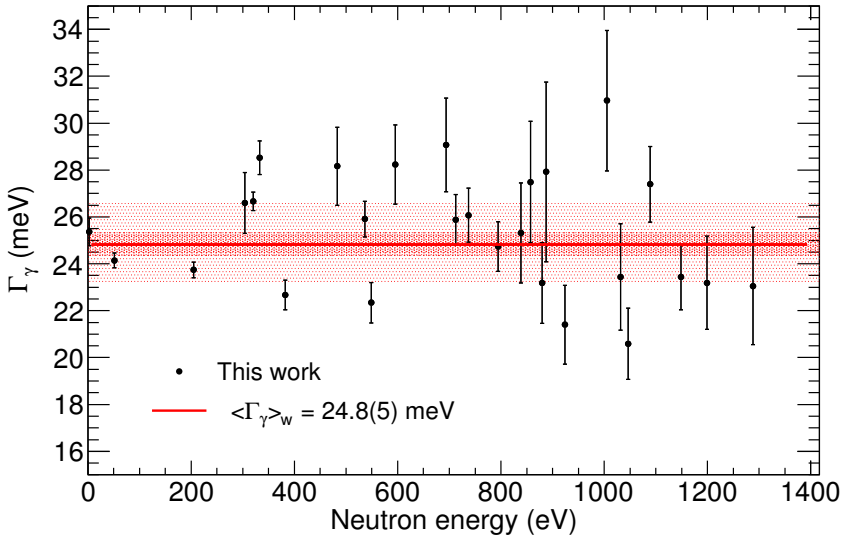

Figure 7.15: *Experimental values of Gamma$_\gamma$ for individual resonances are shown together with the the average total radiative width. The narrow shadowed region indicates the uncertainty in* $\langle\Gamma_\gamma\rangle$ *and the broader one shows the one standard deviation corridor around the obtained average.*

The average total radiative width $\langle\Gamma_\gamma\rangle$ has been obtained from 27 large resonances for which both Γ_γ and Γ_n were fitted following the procedure explained in Section 7.1.3. In Table D.1, these resonances are the ones for which uncertainties in Γ_γ are reported. The set of total radiation widths is shown in Figure 7.15 with its weighted average 24.8(5) meV, taken as the result for $\langle\Gamma_\gamma\rangle$. The dark shadowed region in Figure 7.15 corresponds to the 0.5 meV uncertainty of the average value. The $\langle\Gamma_\gamma\rangle$ is in very good agreement with the accurate individual Γ_γ values for the two largest resonances (2.67 eV and 53.46 eV) in the ^{242}Pu(n,γ) yield (see Table D.1).

The light shadowed region in Figure 7.15 corresponds the standard deviation ($\pm$2.7 meV) of the weighted distribution of Γ_γ. The width of the distribution is likely affected by *experimental* uncertainties and does not represent the physical width of the distribution, expected to be about 3-4% of the expectation value.

7.4.3 Neutron widths and strength function

As it was explained in Section 2.2.4, the statistical properties of the resonance widths for the neutron exit channel are studied in terms of the energy-idependent reduced neutron widths $\Gamma_n^0 = \Gamma_n^0/sqrtE$. The probability of finding a reduced neutron width normalized to the average value $\Gamma_n^0/ < \Gamma_n^0 >$ follows the Porter-Thomas (PT) distribution given by Eq. (2.36).

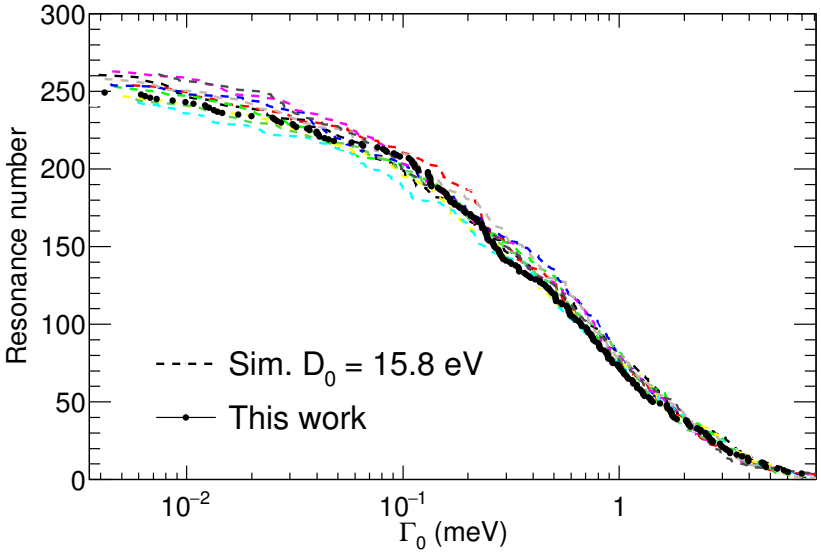

Figure 7.16: *Experimental cumulative distribution of observed levels as a function of the reduced neutron width $g_J\ \Gamma_n^0$ compared to several simulated sequences showing a very good agreement as in the case of the level distribution in Figure 7.13. The simulations were performed with $D_0 = 15.8$ eV, $S_0 = 0.91 \cdot 10^{-4}$ and $S_1 = 2.07 \cdot 10^{-4}$ [42] and the minimum threshold was used.*

As we already discussed for the case of the level spacings, a direct comparison of the experimental set of reduced neutron widths with the expected PT distribution for s-wave resonances is not possible since the resonances in this work combine the s- and p-wave contributions. Instead, we have tested the consistency of the experimental distribution of reduced neutron widths with the result of different resonance sequences from the statistical model simulations (see Figure 7.16). In this figure, the x-axis corresponds to $g_J\ \Gamma_n^0$ to cancel the spin dependency, as explained before in this chapter.

The neutron strength function for s-wave resonances S_0 (Eq. (2.38)), is calculated as the sum of reduced neutron widths in a given neutron energy range. The cumulative distribution of experimental widths is shown in Figure 7.17. This figure shows the compatibility of this work within the statistical uncertainty with the S_0 of previous measurements up to 1300 eV compiled in JEFF-3.2. Individual widths Γ_n^0 were summed in different energy ranges up to 4000 eV to extract the average neutron strengths. The results are presented in Table 7.6, showing consistent values of S_0 within 1σ for all the studied energy intervals. The impact of the observed p-waves in the extracted S_0 is negligible since these resonances feature, in average, much smaller neutron widths than the s-waves, as it is shown in Figure 7.12.

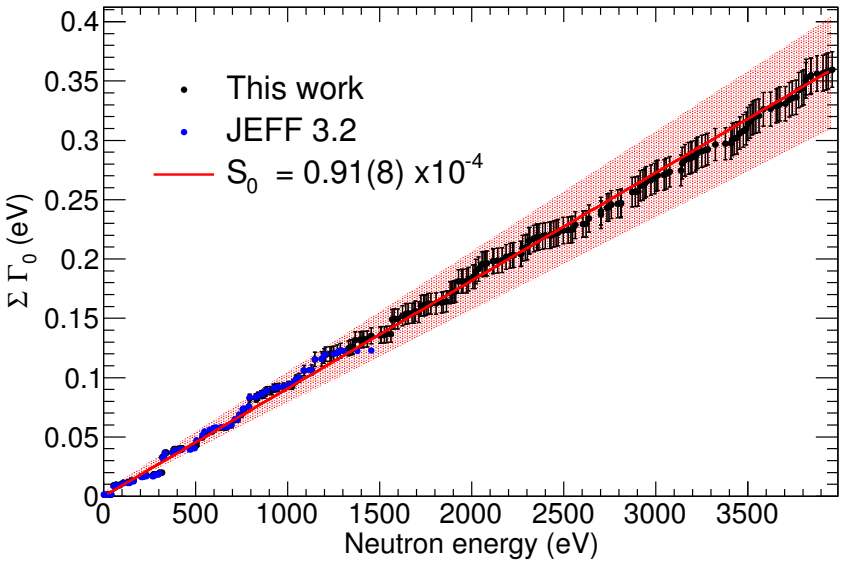

Figure 7.17: *Sum of the reduced neutron widths Γ_n^0 as a function of the neutron energy in this work compared to JEFF-3.2. The red line shows nice consistency of the obtained value for S_0 in the full energy range up to 4 keV. The total uncertainty of S_0 is shown as a shadowed area.*

The uncertainties of S_0 presented in Table 7.6 have two different origins:

1. The uncertainty related to the statistical variation of the sum of neutron widths distributed in accordance with the Porter-Thomas law [69], given by Eq.(2.39), which is shown in brackets in Table 7.6.
2. The contribution of the statistical uncertainty in the invidual values of Γ_n^0 (errors bars in Figure 7.17), which is presented in a separate column in Table 7.6.

Table 7.6: *Neutron strength function S_0 in different energy intervals and the full energy range up to 4000 eV. $\sigma(\Sigma_i g_J \Gamma^0_{n,i})$ is the uncertainty in S_0 from the sum of reduced neutron widths. The right column shows the deviation of the individual strength in each interval with respect to the value extracted in the full range.*

$\mathbf{E}_n$**(eV)**	$\mathbf{10^4}$ **x** $\mathbf{S_0}$	$\sigma(\Sigma_i g_J \Gamma^0_{n,i})$	**Deviation**(σ)
0 - 500	0.84(20)	0.02	-0.78
500 - 1000	1.01(25)	0.06	1.09
1000 - 1500	0.9(3)	0.12	-0.48
1500 - 2000	0.95(24)	0.15	0.51
2000 - 2500	0.82(21)	0.10	-0.95
2500 - 3000	0.9(3)	0.13	-0.38
3000 - 3500	0.84(25)	0.10	-0.73
3500 - 4000	1.0(3)	0.12	0.94
0 - 4000	**0.91(8)**	**0.04**	

Last, we have to note that in the energy range above 3.7 keV, the S_0 was found to be

strongly dependent on two resonances:

- The resonance at around 3840 eV could not be fitted using a value of Γ_n compatible with the overall S_0 value from lower energies unless a doublet was included.
- Following the same consistency criterion, the neutron width of the resonance at 3728 eV, with a very large value reported in Ref. [244], was set to 200(180) meV since the SAMMY calculation did not converge to a unique value due to the scarce statistics.

Removing these resonances (three after inserting a doublet) would affect the extracted value of S_0 less than 1% and even if the full energy range above 3700 eV is discarded the value of S_0 obtained from 0 to 3700 eV would be just 1.7% smaller than the $S_0 = 0.91 \cdot 10^{-4}$ resuting from this analysis.

7.4.4 Comparison to evaluations

The average resonance parameters extracted from the analysis of the resonance region of the radiative capture cross section of ^{242}Pu are compared to previous values in the literature in Figure 7.18 and listed in Table 7.7. The larger energy range and number of resonances analyzed in this work reduces the uncertainty of these parameters with respect to previous measurements and should help to solve the existing discrepancies. The main differences in the s-wave average parameters with respect to the values in the literature are:

- The level spacing $D_0 = 15.8(8) eV$ reported in this work is the second largest value although new resonances are reported. Our result is consistent with the value in JEFF-3.2 [20] (15.3 eV) and the one proposed by Rich et al. [42] (16.8(5) eV). The smaller values of D_0 in the literature, in particular in ENDF/B-VII.1 (13.6 eV) and RIPL (13.50(15), may indicate that p-wave resonances have been wrongly taken into account as s-waves.
- The average radiative width in this work $\langle \Gamma_\gamma \rangle = 24.8(5)$ meV is higher than all the previous results, statistically compatible to the value reported in RIPL [26], and nearly compatible within uncertainties to JEFF-3.2. The low values in the literature are surprising since the $\langle \Gamma_\gamma \rangle$ value in this work is in very good agreement with the two largest resonances of the ^{242}Pu(n,γ) cross section (2.67 and 53.46 eV), for which the radiative width can be accurately determined.
- The neutron strength function $S_0 = 0.91(8) \cdot 10^{-4}$ has a reduced uncertainty compared to previous experimental values (see for instance [40]) due to the much larger number of observed resonances in this work. Our result is compatible with the ones provided by JEFF-3.2 [20] ($1.00 \cdot 10^{-4}$) and ENDF/B-VII.1 [21] ($1.02 \cdot 10^{-4}$) but suggests a reduction of 9 and 11%, respectively. A very good agreement is found with the value proposed by Rich et al. [42], while the uncertainty in our work is significantly smaller.

The consistency between the s-wave average resonance parameters exctracted from the analysis of the RRR and those required to reproduce the shape of the cross section in the

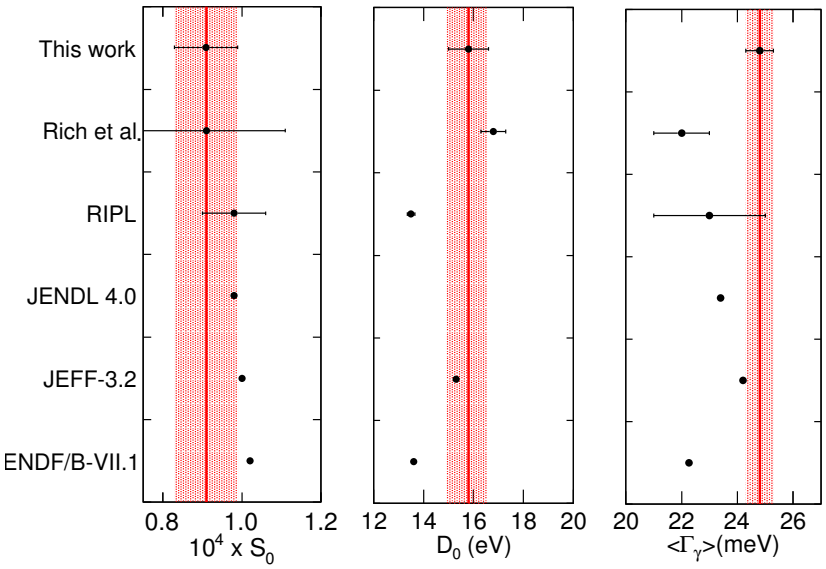

Figure 7.18: *Average resonance parameters obtained in this work (n_TOF) compared to the values in the literature: S_0 (left), D_0 (middle), $\langle\Gamma_\gamma\rangle$ (right). The shadowed area corresponds to the uncertainty from our analysis.*

Table 7.7: *Average resonance parameters of the $^{242}Pu(n,\gamma)$ cross section obtained in this work compared to the values in the literature.*

	S_0 (10^{-4})	D_0 (eV)	$\langle\Gamma_\gamma\rangle$ (meV)
ENDF/B-VII.1 [21]	1.02	13.6	22.27
JEFF-3.2 [20]	1.00	15.3	24.2
JENDL-4.0 [22]	0.98	-	23.4
RIPL [26]	0.98(8)	13.50(15)	23.0(20)
Rich et al. [42]	0.91(20)	16.8(5)	22.0(10)
This work	0.91(8)	15.8(8)	24.8(5)

URR will be studied in Section 8.4.2. In the URR, higher angular momenta (p- and d-waves) will play a significant role and it is hence interesting to study the consistency between the RRR and the URR also for the p-wave component. However, the calculation of the p-wave average parameters in the RRR was discarded owing to the small and uncertain number of p-wave candidates and the large uncertainty in their individual resonances parameter

Chapter 8

Capture cross section of ^{242}Pu in the URR up to 500 keV

The capture yield measured at n_TOF-EAR has been analyzed in its resonance region (1 eV - 4 keV) in terms of individual resonances by means of the R-Matrix formalism. Above 4 keV the resonances start to overlap and the statistics are scarce and the data has been analyzed using the formalism for the Unresolved Resonance Region (URR). In order to study the compatibility of the cross section described in terms of individual resonances with the smooth average cross section, the analysis of the URR has started at 1 keV.

The usual formalism in the URR is better suited for the analysis of the average cross section instead of the reaction yield. The average cross sections in this work been compared to the existing data and the evaluations, showing a good agreement with the measurements carried out in the 70's by Whissak and Kaeepeler and showing a reduction of 10-14% with respect to JEFF-3.2, in the line of the PROFIL experiments. In addition, the average cross section has been parameterized in terms of average resonance parameters with help of the FITACS [75] code as it is implemented in SAMMY, based on Hauser-Fesbach calculations with width fluctuations [70, 71]. The s-wave average parameters extracted from this fit are consistent to those extracted from the statistical analysis of the resonances.

8.1 Calculation of the average cross section in the URR

In the URR, the resonances overlap and therefore a broader binning is used to calculate the average capture yield in each energy interval. From the general expression for the average reaction yield in Eq. 2.49, the average capture yield $\langle Y(E_n)\rangle$, is related to the average capture cross section $\langle\sigma_\gamma\rangle$ by

$$\langle Y(E_n)\rangle = F_{sample}(E_n)\cdot n\cdot\langle\sigma_\gamma(E_n)\rangle, \tag{8.1}$$

where n is the sample thickness in atoms per barn and $F_{sample}(E_n)$ is a sample-related correction for self-shielding and multiple scattering. These experimental effects were explained for the R-Matrix analysis of the RRR in Section 7.1.1.

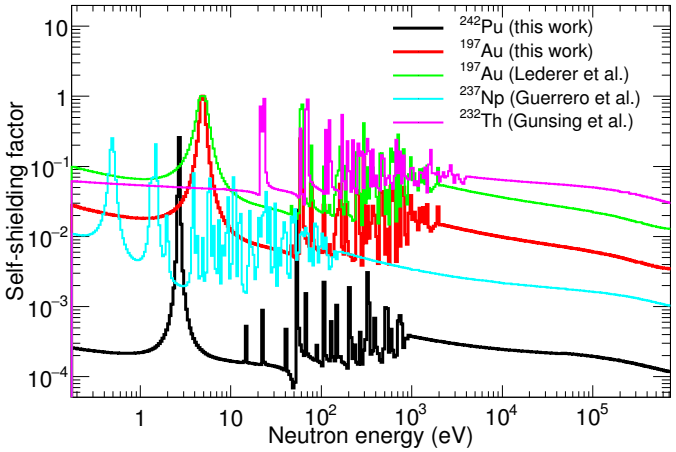

Figure 8.1: *Neutron self-shielding factor as a function of the neutron for the two samples measured in this work ^{197}Au and ^{242}Pu compared to other measurements at n_TOF. The small self-shielding correction in the URR, especially for ^{242}Pu, allows as to neglect the multiple scattering and assume the thin target approximation in the calculation of the average cross-section.*

The $F_{sample}(E_n)$ correction, usually calculated with the SESH [247] code or MCNP [191], is relevant if thick capture targets are used. This is illustrated in Figure 8.1, where the self-shielding correction $(1 - e^{-n\sigma_{tot}})$ for the targets used in this work is compared to those of previous n_TOF measurements using thicker targets [233, 211, 194]. From the measurements in this figure, the $F_{sample}(E_n)$ correction was at most 4% in the URR for the ^{232}Th [233] and ^{197}Au [211], while it remained clearly below 1% for the case of ^{237}Np [194]. The self-shielding factor in this work in the energy region of interest (above 1 keV) of the order of 1% for ^{197}Au and negligible for ^{242}Pu and thus we can expect a negligible multiple scattering correction, as well. Therefore, the average capture cross section of ^{242}Pu has been extracted assumming the thin-target approximation by dividing the capture yield obtained with Eqs. (6.23) and (6.24) by the sample thickness n. It is important to remark that the thin-target approximation is applicable thanks to the use of thin ^{242}Pu fission-like targets in this work [217].

8.2 Validation of the results in the URR: $^{197}Au(n,\gamma)$

The $^{197}Au(n,\gamma)$ ancilliary measurement aims mainly at obtaining the absolute normalization of the capture yield (see Section 6.9.1). Additionally, we took advantage of the fact that the $^{197}Au(n,\gamma)$ cross section is very well known. Indeed, it is a IAEA Neutron Cross Section Standard [181] for neutron energies above 200 keV. Therefore it serves to validate

the measurement and analysis technique of the ^{242}Pu capture cross section in the URR since the full data reduction process followed the same steps for both ^{197}Au and ^{242}Pu.

The ^{197}Au(n,γ) average yield in the URR was obtained with a detection threshold of 250 keV and self-normalized to the 4.9 eV saturated resonance (see Section 6.9.1). Then, the average cross section was calculated by means of Eq. (8.1) assumming the thin target approximation (i.e. $F_{sample}(E_n) \simeq 1$). The resulting average capture cross section of ^{197}Au in the URR is compared to the evaluated cross section in JEFF-3.2 [20] in Figure 8.2. The choice of a different evaluation to make the comparison (ENDF/B-VII.1 [21], JENDL-4.0 [22]) would have lead to the same result. The comparison to to IAEA standard [181] was not possible since the latter is available only above $E_n = 200$ keV.

The top panel of Figure 8.2 shows the capture cross section multiplied by $E_n^{1/2}$ in order to appreciate the entire energy range. The ratio of experimental to evaluated cross section is shown in the bottom panel of Figure 8.2. From the results in this plot we conclude that measured and evaluated cross sections agree on average within 3% and the ratio fluctuates around the average with a standard deviation of 7%. The slightly larger discrepancies observed below 5 keV are related to the still existing resonant structures in the ^{197}Au cross section. At higher energies the differences obtained around 80 keV occur a the exact position of the Al absorption dip of the n_TOF neutron flux, even if the time-to-energy calibration in the URR was optimized to match the flux dips (see Section 6.4). The comparison stops at 600 keV, above which the inelastic channels of gold starts playing a role (See Ref. [211] for details).

8.3 ^{242}Pu radiative capture cross section in the URR

8.3.1 Combination of detection thresholds in the final cross section

In Section 6.7.2 we discussed the importance of the choice of lower threshold in deposited γ-ray energy E_{thr} for an optimized rejection of the inelastic and fission background in the neutron energy region above 100 keV. Following the conclusions drawn in this section, the final cross section has been obtained with the following combination of values for E_{thr}:

1. The capture yield below a neutron energy of 100 keV does not depend on the chosen E_{thr} as it is shown in Figure 6.20. Therefore in this energy region we calculated the cross section from the yield extracted with $E_{thr} = 150$ keV, for which the corrections for fraction of counts loss below the threshold (see Section 6.8.2) are minimized and the statistics are kept as high as possible.

2. For neutron energies beyond 100 keV, the inelastic background contribution becomes more important and hence the detection threshold needs to be increased up to, at least 750 keV to analyze the full neutron energy range shown in Figure 8.3. Regarding the fission channel, its ratio to capture is minimized with detection threshold between

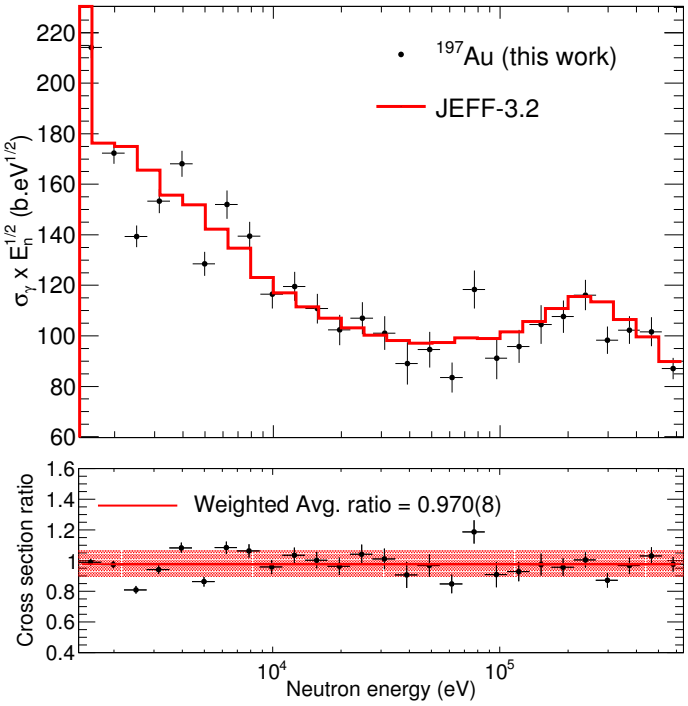

Figure 8.2: *Top: Comparison of the capture cross section of ^{197}Au in the URR obtained in this work compared to JEFF-3.2. The cross section has been multiplied by the square root of the neutron energy to remove the 1/v dependence of the cross section. Bottom: Ratio of this work with respect to JEFF-3.2 showing an average ratio of 0.970(8) and a good agreement up to a neutron energy of 500 keV. The largest deviations from unity are found at the the flux dips energies.*

750 and 1000 keV. The (n,f) contribution has been corrected (see Section 6.7.2) and, as a result, the cross sections extracted using different thresholds agree to eachother within the statistical uncertainties. For all of the above, the cross section for neutron energies higher than 100 keV has been calculated with E_{thr} = 750 keV.

3. The capture cross section is reported up to a neutron energy of 500 keV, to keep the systematic uncertainties below the current 35%. Beyond this energy the systematic uncertainty rapidly increases domintated by that of the (n,f) correction, shown in Figure 6.22.

Figure 8.3 shows the very good agreemeent of the final cross section obtained in the energy range from 1 to 500 keV with two different combinations of values for E_{thr}. The final average capture cross section with 10 bins per decade is presented in Table 8.1, where both the statistical and systematic uncertainties are listed. The origin of the uncertainties is discussed in the next section.

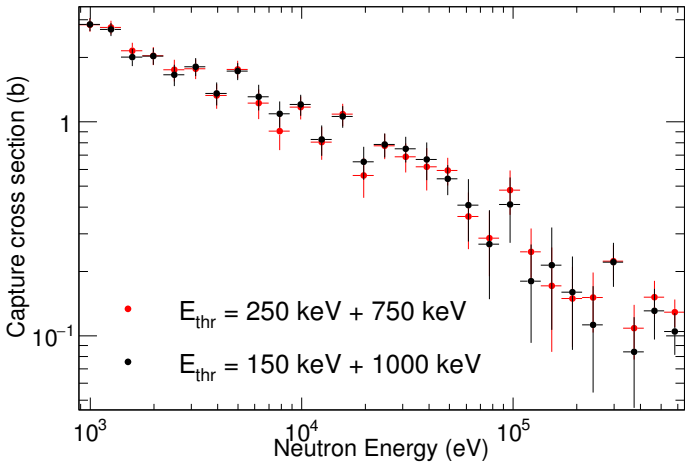

Figure 8.3: *Final ^{242}Pu capture cross section obtained in this work by showing the perfect consistency of the result obtained with different threshold combinations: A threshold of 150 or 250 keV is chosen below a neutron energy of 100 keV, where all the thresholds give consistent results, to reduce the statistical uncertainty. For energies over 100 keV, a consistent result is obtained after we correct for the (n,f) background using a threshold higher than 750 keV, that allows removing the (n,n´) background up to a neutron energy of 500 keV.*

8.3.2 Systematic and statistical uncertainties

The different sources of systematic uncertainty affecting the capture yield in the URR were discussed in detail in Section 6.10.2, were we concluded that the major sources of uncertainty are the subtraction dummy background below 250 keV and the correction for the fission background at high energies. Since the cross section in the URR is obtained in the thin-target approximation, only the uncertainty in the sample thickness has to be added to that of the capture yield. The uncertainty in the ^{242}Pu target thicknesses is dominated by the 4% uncertainty in the sample mass (see Section 3.3.1 since the uncertainty in the overall thickness homogeinity is considered negligible (see Section 5.4.1).

The individual sources of systematic uncertainties leading to the total values in Table 8.1 are summarized in Table 8.2. As we presented in Table 6.13 for the final systematic uncertainties in the capture yield, the systematic uncertainties in the cross section have been evaluated separately in different neutron energy intervals (see Table 8.2). From the average values of this uncertainties in the energy intervals in Table 8.2, we have interpolated the values of the systematic uncertainty in each energy bin in Table 8.1. Only the uncertainty associated to the fission background was evaluated in each energy bin individidually due its strong neutron energy dependence, shown in Figure 6.22.

The final average systematic uncertainty in the URR ranges from 8% to 10% below 250 keV, and increases to 17% above 250 keV, due to the high systematic uncertainty related to the fission background correction. In a point by point analysis, the statistical uncertainties, ranging from 6% at 1 keV up to 35% for some energy bins above 100 keV, dominate over the systematic ones (see Table 8.1). However, if they are integrated over the

Table 8.1: *Average neutron capture cross section ($\langle\sigma_\gamma\rangle$), absolute uncertainties u_{stat} and u_{syst} and relative uncertainties (%) Δ_{stat} and Δ_{syst}. for each neutron energy bin between 1 and 500 keV. See Tables 6.13 and 8.2 for a breakdown of the relative systematic uncertainties.*

E_{low} **(keV)**	E_{high} **(keV)**	$\langle\sigma_\gamma\rangle \pm u_{stat} \pm u_{syst}$**(b)**	Δ_{stat}(%)	Δ_{syst}(%)
0.8830	1.111	2.85± 0.19± 0.23	6.8	8.1
1.111	1.398	2.71± 0.19± 0.22	6.9	8.1
1.398	1.759	2.01± 0.19± 0.16	9.2	8.1
1.759	2.214	2.03± 0.18± 0.17	9.1	8.1
2.214	2.785	1.66± 0.19± 0.14	12	8.1
2.785	3.504	1.81± 0.17± 0.15	9.6	8.2
3.504	4.408	1.36± 0.17± 0.11	12	8.2
4.408	5.544	1.73± 0.16± 0.14	9.1	8.2
5.544	6.973	1.31± 0.18± 0.11	14	8.3
6.973	8.769	1.09± 0.15± 0.09	14	8.3
8.769	11.03	1.21± 0.14± 0.10	11	8.4
11.03	13.86	0.83± 0.13± 0.08	16	9.4
13.86	17.42	1.06± 0.12± 0.10	12	9.5
17.42	21.90	0.65± 0.11± 0.06	18	9.6
21.90	27.51	0.78± 0.10± 0.08	13	9.7
27.51	34.56	0.75± 0.10± 0.07	14	9.7
34.56	43.41	0.67± 0.13± 0.07	20	9.8
43.41	54.50	0.54± 0.09± 0.05	16	9.9
54.50	68.40	0.36± 0.11± 0.04	30	10
68.40	85.82	0.29± 0.10± 0.03	34	10
85.82	107.6	0.41± 0.14± 0.04	34	10
107.6	134.9	0.247± 0.071± 0.024	29	9.6
134.9	169.0	0.171± 0.062± 0.016	36	9.5
169.0	211.7	0.149± 0.048± 0.014	32	9.5
211.7	264.9	0.151± 0.047± 0.015	31	10
264.9	331.3	0.22± 0.04± 0.03	19	12
331.3	414.0	0.109± 0.031± 0.016	29	15
414.0	516.9	0.152± 0.029± 0.039	19	25

energy ranges in Table 6.13, the statistical uncertainty remains below the systematic ones with the exception of the neutron energy interval between 50 and 250 keV. At this point, it is important to remark that the use of the scaled yield instead of the common PHMT in this work (see Figure 6.35) has allowed reducing the statistical uncertainty significantly.

From the combined result of the systematic and integrated statistical uncertainties, we conclude that we have achieved the aimed accuracy of 8-12% in the average cross section required for all the fast reactors listed in Table 1.9 below 50 keV. At higher energies, we are slightly above the required accuracy but still below the current uncertainty of 35%.

Table 8.2: *Summary of the partial contributions and the overall relative systematic uncertainty of the cross section Δ_{syst} in four energy intervals of the URR. The relative statistical uncertainty Δ_{stat} integrated in the same energy ranges is shown for the sake of completness.*

	Partial contributions			
Energy range	**Yield**	**Sample thickness**	**Average Δ_{syst}(%)**	**Integrated Δ_{stat}(%)**
1 - 10 keV	7.1	4	8.2	2.9
10 - 50 keV	8.8	4	9.7	5.8
50 - 250 keV	9.4	4	10.2	13.0
250 - 500 keV	16.5	4	17.0	11.9

8.4 Average parameter description of the cross section

The experimental ^{242}Pu capture cross section between 1 and 500 keV, shown in Figure 8.3, has been parameterized in terms of average resonace parameters using a Hauser-Feshbach (HF) calculation with width fluctuations [71]. The theoretical principles of the HF were described in Section 2.3. This approach is based in the generation of ficticious resonances to describe the average cross section in the URR. The generation of individual resonances according to a set of average parameters is specially relevant because it is also used in the calculation of self-shielding factors or probability tables for applications.

The cross section in the URR has been parameterized in terms of average parameters using the SAMMY-FITACS code (see Section 8.4.1) and the fitted resonance parameters have been compared to those extracted in this work from the statistical analysis of the individual resonance parameters in the RRR in Section 7.4.

8.4.1 The SAMMY-FITACS code

In this work we have used the version of the FITACS code [75] included in SAMMY [62] to fit the average capture cross section measured at n_TOF. The following average resonance parameters are adjusted in the FITACS code for each partial wave (s, p, d):

- Neutron strenght function S_l: This parameter, defined in Eq. 2.38, is fitted independently for each partial included in the calculation.
- Level spacing D_l: The level spacings can be adjusted but are not fitted in the calculation. Its value for s-wave resonances D_0 is given as an input and the D_l values for higher angular momenta are calculated assumming a $2J+1$ dependence for the level density.
- Average radiation width $\langle\Gamma_\gamma\rangle_l$: This parameter is fitted with the restriction of being only parity-dependent (i.e. $\langle\Gamma_\gamma\rangle_0 = \langle\Gamma_\gamma\rangle_2 \neq \langle\Gamma_\gamma\rangle_1$).

- Distant level parameter R_l^∞: This parameter is related to the scattering radius R' by

$$R' = a \cdot (1 - R^\infty), \tag{8.2}$$

where a is the nuclear radius $a = A^{1/3} + 0.8\ fm$. R_l^∞ is fitted for each partial wave individually.

The FITACS code takes into account the energy dependence of these parameters is obtained energy is obtained from the Bethe formula [67] for the level density, and from the giant dipole resonance model [248] for the capture widths.

The HF calculation with FITACS considers not only the capture and elastic scattering as open reaction channels but also the the competitive widths from inelastic scattering. For this purpose, the energy, spin and parity of the ^{242}Pu levels, extracted from ENSDF [19], are given as an input.

8.4.2 Results of the FITACS analysis

The FITACS calculation was carried out aiming at describing the experimental cross section in the URR in terms of average parameters. In order to cover the energy range of interest, the inclusion of the three first partial waves (s, p, d) was required. The initial parameters for the fit were the following:

- s-wave: The initial values of S_0, D_0 and $\langle\Gamma_\gamma\rangle_0$ are those obtained from the RRR (see Table 7.7). The initial value of R_0^∞ was calculated using Eq. (8.2) with the same value for the scattering radius used in the analysis of the RRR, $R' = 9.46$ fm.
- p- and d-wave: The initial parameters for $S_{1,2}$ and $R_{1,2}^\infty$ and $\langle\Gamma_\gamma\rangle_1$ were taken from Ref. [42]. $D_{1,2}$ and $\langle\Gamma_\gamma\rangle_2$ were assigned following the rules described in Section 8.4.1.

A summary of the initial values for the average parameters is presented in Table 8.3.

Table 8.3: *Initial average parameters for the fit of the capture cross-section in this work from 1 to 500 keV using the SAMMY/FITACS code.*

Partial wave	S_l **x** $\mathbf{10^4}$	$\langle\Gamma_\gamma\rangle_l$ **(meV)**	D_l **(eV)**	R_l^∞
s-wave (l=0)	0.91(8)	24.8(5)	15.8(8)	-0.152
p-wave (l=1)	2.07	28	5.35[a]	0.130
d-wave (l=2)	1.22	24.8	3.30[a]	-0.055

a) From D_0 assumming a $2J+1$ dependence for the level density

The average capture cross-section in this work and the corresponding SAMMY/FITACS calculation are shown in the top panel of Figure 8.4 together with the contribution of the three first partial waves. The bottom panel of the same figure shows the relative contribution of each partial wave, indicating that the p-wave dominates in most of the energy range studied. The fitted s-wave parameters, which can be compared to the ones from the RRR, dominate the cross section only up to about 7 keV. On the other side, the

d-wave contribution becomes relevant above 100 keV but does not overcome the p-wave contribution in the energy range of interest.

The calculation in Figure 8.4 has been obtained with fixed average level spacings D_l calculated from the value for s-wave resonances $D_0 = 15.8(8)eV$ (RRR). The average parameters S_l and $\langle\Gamma_\gamma\rangle_l$ were fitted to the capture cross section in this work, obtaining the values presented in Table 8.4. The s-wave average resonance parameters obtained in the analysis of the RRR [246] are included in the same table to show their compatibility with the new values presented herein. This confirms the consistency of the cross sections extracted in the RRR and URR below 10 keV. Beyond this energy, the p-wave contribution clearly dominates the capture cross section (see Figure 8.4) and the fit is not sensitive to the s-wave parameters anymore.

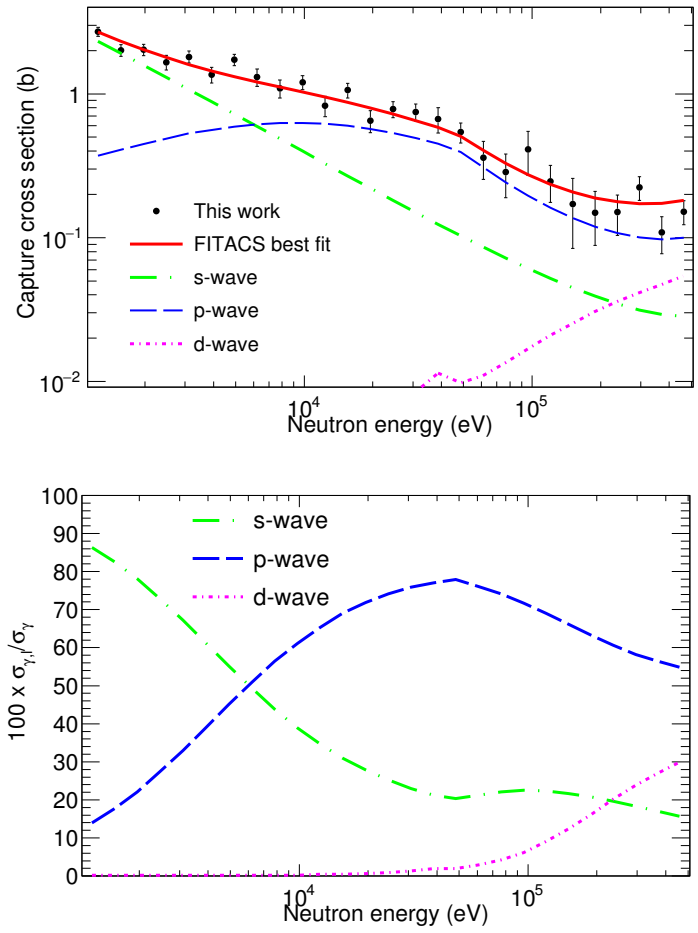

Figure 8.4: *Capture cross section in the URR obtained in this work together with the Hauser-Fesbach calculation that provides the best fit to the data. The contribution of the different angular components is included to show that the s-wave cross section, that can be compared to the parameters obtained from the RRR, dominates just up to 7 keV.*

Table 8.4: *Average parameters (neutron strength function S_l, average radiative width $\langle\Gamma_\gamma\rangle_l$ and level spacing and D_l(eV)) obtained from the fit of the capture cross-section in this work from 1 to 500 keV using the SAMMY/FITACS code (see Figure 8.4). The average resonance parameters obtained in the statistical analysis of the resonance region [246] are also presented for comparison.*

Angular momentum	S_l **x** $\mathbf{10^4}$	$\langle\Gamma_\gamma\rangle_l$ **(meV)**	D_l **(eV)**
s-wave (l=0)	0.90(12)	24.1(20)	15.8
p-wave (l=1)	2.6(3)	28(3)	5.35
d-wave (l=2)	0.6(3)	24.1(20)	3.30
s-wave (RRR [246])	0.91(8)	24.8(5)	15.8(8)

Table 8.5: *Correlation between the extracted values of S_l and $\langle\Gamma_\gamma\rangle_{ll}$ resulting from the FITACS parameterization of the cross section in the URR. The distant level parameters are completely uncorrelated to the other paramters and thus excluded from the table.*

	S_0	$\langle\Gamma_\gamma\rangle_{0,2}$	S_1	$\langle\Gamma_\gamma\rangle_1$	S_2
S_0	100				
$\langle\Gamma_\gamma\rangle_{0,2}$	-52	100			
S_1	-11	-40	100		
$\langle\Gamma_\gamma\rangle_1$	10	-8	-32	100	
S_2	8	-15	16	-39	100

The sizable uncertainties in the fitted parameters listed in Table 8.4 are mainly due to the large correlation between the parameters, up to 50% between parameters of the same partial wave (see Table 8.5). This means that sets with different parameters would lead to a good reproduction of the average cross section. The optimal approach to constrain the parameters and reduce their correlations would be to fit the capture and total cross section simultaneously due to their different sensitivity to each parameter:

- The capture cross section is typically more sensitive to the average radiation widhts $\langle\Gamma_\gamma\rangle_l$.
- The total cross section is more dependent on the distant level parameter R_l^∞.

However, in this work just the capture data was considered in the SAMMY/FITACS calculation since no experimental data on the ^{242}Pu total cross section is available in EXFOR from 6 to 270 keV. Due to the low sensitivity of the capture cross section to the distant level parameters R_l^∞, the initial values are not modified along the FITACS calculation and, therefore, this parameter is not included in Tables 8.4 and 8.5.

8.5 Comparison to existing data and evaluations

8.5.1 Comparison to previous measurements

In Section 1.5.1 we reviewed the currents status of the experimental data for the ^{242}Pu capture cross section available in the literature. For the case of the cross section in the URR, the previous measurements presented the following limitations:

- The first measurement by Hockenbury et al. [43] presents large dispersion and no uncertainties are presented in EXFOR [18].
- The most accurate measurements, carried out in the 70's by Wisshak and Kaeppeler [44, 45], start only at 10 keV and show significant discrepancies with the latest measurement by Buckner et al. [41], which covers the RRR and the URR up to 40 keV.
- No measurement covers at the same time the RRR and URR up to the neutron energy required for the design of the different innovative systems [29]. This is required to evaluate the URR in terms of average parameters extracted from the analysis of the RRR and study the consistency with the cross section in the URR [30].

The capture cross section reported in this work becomes the first data set to cover in a single measurement the complete energy range from 1 to 250 keV and to provide data in the energy range between 250 and 500 keV. The upper panel of Figure 8.5 compares the result in this work with the recient measurement from 1 to 40 keV at LANSCE by Buckner et al. [41] and with the three time-of-flight measurements from the 70's by Hockenbury at RPI (6-87 keV) [43] and Whissak and Kaeppeler at FZK (10-90 and 50-250 keV) [44, 45]. The cross sections by Wisshak and Kaeppeler in Figure 8.5 have been calculated via multiplication of the experimental $^{242}Pu(n,\gamma)/^{197}Au(n,\gamma)$ data given in Refs. [44, 45] by the $^{197}Au(n,\gamma)$ cross section in JEFF-3.2.

A quantitative comparison in terms of cross section ratios, displayed in the bottom panel of Figure 8.5), allows us to draw the following conclusions:

1. The cross section in this work is in good agreement with the two data sets of Wissak and Kaeppeler within the statistical uncertainties.
2. Our result is significantly above the new measurement at LANSCE (as much as a factor 2.5 above 10 keV), but seems to agree at 1 keV as it was observed in the comparison of the resonance region (see Section 7.3).
3. The ratio to the measurement by Hockenbury et al. has been excluded since the data points are widely spread and their uncertainties. are not reported.

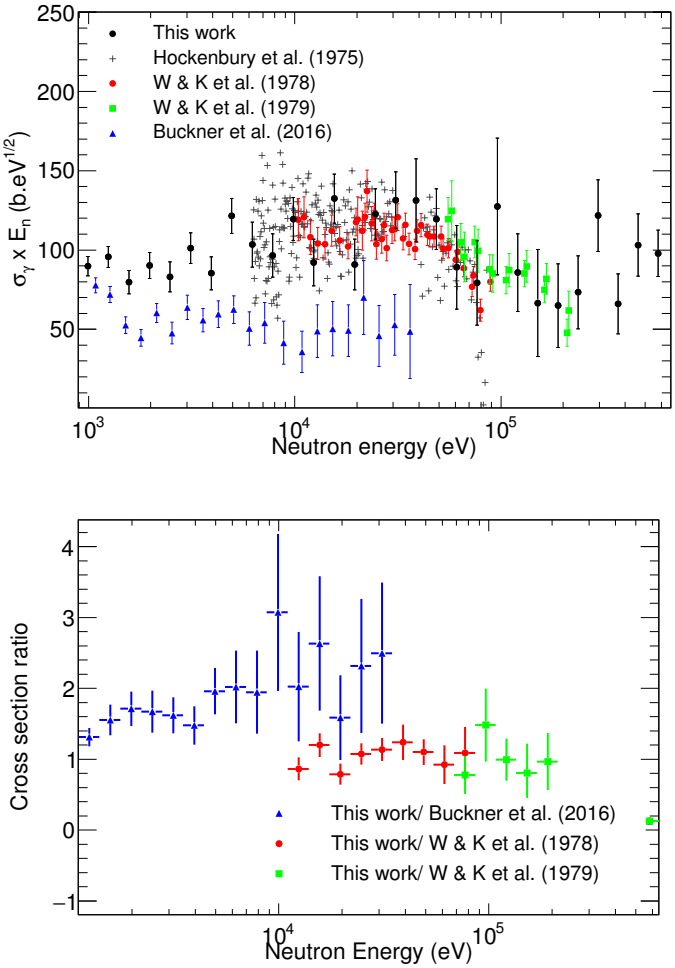

Figure 8.5: *Top: Capture cross section of ^{242}Pu in the URR obtained in this work compared to the previous measurements available in EXFOR. The cross section has been multiplied by the square root of the neutron energy to remove the 1/v dependence of the cross section. Bottom: Ratio of this work with respect to the previous ones. The ratio to the data by Hockenbury et al. was not included in the bottom pad due to its large dispersion and the absence of error bars.*

8.5.2 Comparison to evaluations and calculations

One of the main motivations for this work was to clarify the overestimation of around 14% in the calculated over experimental ratios (C/E) when interpreting the PROFIL and PROFIL2 experiments with JEFF-3.1 [46, 47, 48]. Indeed, the justification to include ^{242}Pu(n,γ) in the HPRL [30] claims that even if the data by Hockenbury et al. and Wisshak and Kaeppeler follow the trend of the PROFIL, JEFF overestimates the measurements.

The top panel of Figure 8.6 shows the capture cross section in this work compared to the ENDF/B-VII.1 [21] and JEFF-3.2 [20] evaluated files. The cross section calculated by Rich et al., aiming at describing the neutron induced reactions on ^{242}Pu with a set of consistent average resonance parameters [42], is also included in Figure 8.6 as a reference

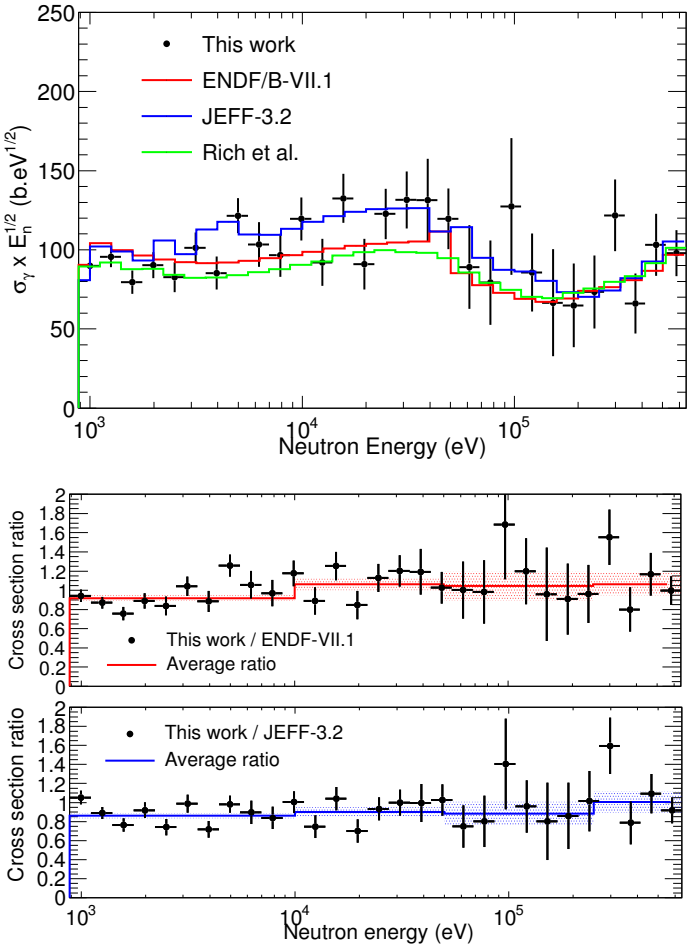

Figure 8.6: *Top: Comparion of the capture cross section in this work with the main evaluated files, JEFF-3.2 (blue) and ENDF/B-VII.1 (red). The cross-section calculated by Rich et al. is shown in green. Bottom: Ratio between the cross section in this work and the evaluations. The solid lines correspond to the average ratios in three energy ranges and the shadowed corridors to their uncertainties (results in Table 8.6).*

and provides indeed the best agreement with our data below 10 keV. The ratio of this work with respect to the evaluations is shown in the bottom panel of the same figure. In this plot, the average ratios in the energy ranges from 1 to 10 keV, 10 to 50 keV, 50 to 250 keV and 250 to 500 keV are indicated with a solid line, being the shadowed corridor the statistical uncertainty of the ratio. The results of the average ratios, presented in Table 8.6, illustrate the overall good agreement of our result with the evaluated cross sections within the systematic uncertainty. However, it is important to note that some trends are observed. First, we see that our result is, on average, 10-14% below JEFF-3.2 in the energy range from 1 to 250 keV (thus compatible with the results from PROFIL) and in agreement within the uncertainties at higher energies. Below 10 keV our cross section is 8% below ENDF/B-VII.1 but we are slightly above the latter, although still compatible, above this energy.

Table 8.6: *Average ratio of the cross section in this work with respect to JEFF-3.2 and ENDF/B-VII.1 in different energy ranges shown in the bottom path of Figure 8.6. The uncertainties in brackets are statistical and the systematic ones are given in the last row.*

	1-10 keV	**10-50 keV**	**50-250 keV**	**250-500 keV**
ENDF/B-VII.1	0.92(3)	1.06(6)	1.04(13)	1.06(11)
JEFF-3.2	0.86(3)	0.90(6)	0.88(11)	1.00(10)
Systematic uncertainty (%)	8	10	10	17

8.5.3 Expected cross section range from average parameters

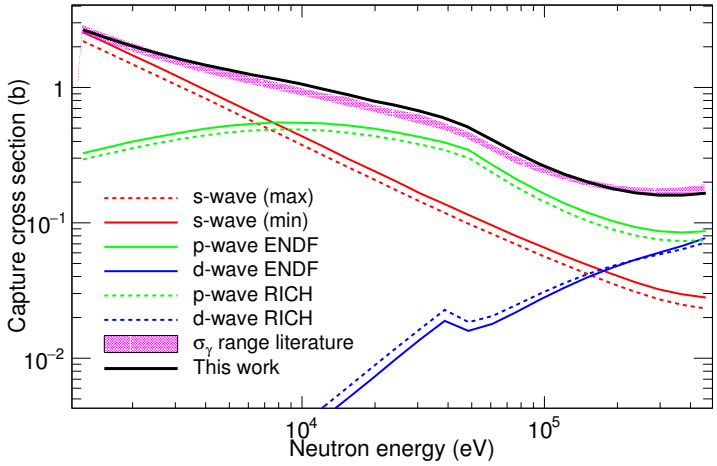

Figure 8.7: *The best fit to the cross section in this work obtained with SAMMY/FITACS (black line) is compared to the expected cross section range (shadowed area) compatible with the average resonance parameters extracted from the RRR for L=0 and the parameters in the literature (ENDF and Rich et a.l) for higher angular momenta. The upper and lower limits for the partial cross section (s-,p- and d-waves) are shown with solid and dashed lines, respectively.*

The parameterized average capture cross section in Figure 8.4 has been compared with the expected cross section range. The latter has been calculated with FITACS the following parameters for each of the partial waves:

- s-wave: average resonace parameters obtained in the RRR [246], assuming for each of the a maximum and minumum value given by the 1σ uncertainty in Table 8.4.
- p- and d-wave: parameters reported in ENDF/B-VII.1 [21] and Rich et al. [42].

The resulting expected range is shown as a shadowed area in Figure 8.7, where it is compared to the parameterized cross section fitted to the experimental cross section in this work. From the results in Figure 8.7 we conclude:

- Our result is in agreement within the expected range below 7 keV. This is consistent with the good agreement between the s-wave average parameters obtained from the HF calculation and the average parameters of the RRR.

- The fitted cross section is slightly above the expected range in the energy range from 7 keV to 80 keV, where the p-wave is clearly dominant. The underestimation of the p-wave contribution in the literature is reflected in Table 8.4, where we appreciate the difference between the fitted p-wave parameters S_1= 2.6(3) x 10^{-4} and $\langle\Gamma_\gamma\rangle_1 = 28(3)$ meV and the values in ENDF/B-VII.1 ($S_1 = 2.3$ and $\langle\Gamma_\gamma\rangle_1 = 20.7$ meV) or those reported by Rich et al. [42] ($S_1 = 2.1$ and $\langle\Gamma_\gamma\rangle_1 = 22$ meV).
- The difference observed in Figure 8.7 between the p-wave partial cross-sections by Rich et al. and ENDF/B-VII.1 is mainly related to the 20% larger average level spacing reported by Rich et al, $D_0 = 16.8$ eV, compared to the value given in ENDF/B-VII.1, $D_0 = 13.6$ eV.

Part IV

Summary and Conclusions

Chapter 9

Summary and conclusions

9.1 Motivation for measuring ^{242}Pu(n,γ)

The long-term sustainability of nuclear energy as a relevant technology in a low-carbon energy outlook points to innovative nuclear systems and nuclear fuel cycles aiming at reducing the nuclear waste and the demand for uranium. The viability and operation of such systems, like the Generation-IV reactors and Accelerator-Driven Systems, featuring fast neutron spectra, and the use of new fuel compositions, such as MOX, require an improved knowledge of neutron cross sections.

Among the neutron cross sections that need to be improved in terms of accuracy, the NEA recommends in one of its reports that the capture cross section of ^{242}Pu should be measured with an accuracy of 8-10% in the energy range between 2 keV and 500 keV. Moreover, the 14% deviation found between the calculated (JEFF) and experimental results of the post-irradiation experiments PROFIL and PROFIL2 for the ^{242}Pu(n,γ) cross section, require a consistent evaluation of the fast region in terms of resonance parameters from the RRR. For this reason, the NEA-HPRL requested high-resolution measurements of the capture cross section of this isotope in its resonance region up to 2 keV. Last, the discrepancies in this cross section also affect its thermal value, for which the spread of experimental results leads to a deviation of 15% between the different evaluated libraries.

9.2 Complementary measurements of the radiative capture on ^{242}Pu

This thesis deals with description of a new measurement of the capture cross section of ^{242}Pu from thermal to 500 keV. The results presented in this manuscript were obtained from two different experiments carried out at the Budapest Research Reactor (BRR) and the n_TOF-EAR1 facility at CERN.

9.2.1 Measurement at the cold neutron beam of the BRR

The experimental campaign in the PGAA facility at the Budapest Research (BRR) aimed at obtaining an accurate value for the thermal cross section of ^{242}Pu. An experimental campaign was carried out in the cold neutron beam of the BRR. Two 30 mg ^{242}Pu samples were irradiated and two different measurements were carried out:

- Activation of the ^{242}Pu samples using a ^{197}Au sample as reference and subsequent measurement of the γ-rays from the ^{243}Pu and ^{198}Au β^- decays in a low-background chamber using a high-resolution HPGe detection system.
- Measurement of the prompt ^{242}Pu(n,γ) spectrum using a high-resolution HPGe detector to resolve the characteristic γ-ray lines. Two different methods to extract the cross section have been applied: single-line analysis and weighted sum of the unfolded spectrum.

The use of high quality thin ^{242}Pu targets featuring negligible neutron self-shielding and γ-ray absorption have been crucial to reduce the corrections and final uncertainties. In addition, the combined analysis of the prompt and decay spectrum has validated our results and improved the accuracy of the final result.

9.2.2 Time-of-flight measurement at n_TOF-EAR1

The neutron capture cross section of ^{242}Pu has been measured by means of the time-of-flight technique at the high-resolution CERN n_TOF-EAR1 facility employing an array of four C_6D_6 total energy detectors to register the capture γ-rays.

A high quality sample was produced consisting of a set of seven fission-like targets of ^{242}Pu enriched to 99.959%, each of 45 mm in diameter, with a total mass of 95(4) mg electrodeposited on thin aluminum backings. The use of fission-like targets with a uniquely high actinide to backing mass ratio and large surface have led to the minimization of the corrections associated to the background subtraction, application of the PHWT, multiple scattering, and sample alignment.

The capture yield of ^{242}Pu has been extracted from 1 eV to 500 keV after the careful data reduction process described in this thesis, which includes:

- Assesment of the correlation of different beam monitors.
- Time-of-flight to energy calibration including the shift associated to the Resolution Function of the facility.
- Efficiency assesment via the PHWT with help of a detailed MonteCarlo simulation of the detection set-up.
- Corrections for the efficiency requiring the simulation of realistic capture cascades.
- Assesment of the individual background contributions from ancilliary measurements or simulations.

- Development of an alternative method for the PHWT using an average weighting factor to avoid the enhancement of the statistical fluctuations, hence increasing the number of analyzed resonances; and to improve the capture to background ratio in the URR.
- Absolute normalization of the ^{242}Pu(n,γ) yield using the Saturated Resonance Method for the 4.9 eV resonance of ^{197}Au.
- Detailed discussion on the systematic uncertainties in the obtained capture yield.

9.3 Results of the ^{242}Pu(n,γ) cross section

The results in this thesis are divided in three neutron energy regions, in which the cross section has been determined using different neutron beam facilities, experimental techniques, analysis methods and theoretical formalisms.

9.3.1 Thermal capture cross section

The succesful measurements and the use of different experimental and analysis techniques have lead to three independent values for the thermal capture cross section of ^{242}Pu:

- **Activation**: Capture cross section from the decay of the produced ^{243}Pu relative to the capture cross section of ^{197}Au: 18.7(9) b.
- **PGAA single-line**: Capture cross section from the partial cross section of the most intense ^{242}Pu(n,γ) secondary γ-ray of 287 keV and its absolute emmission probability: 17(3) b,
- **PGAA unfolding method**: Capture cross section using the energy-weighted sum rule with internal calibration applied to the unfolded ^{242}Pu(n,γ) spectrum (i.e. only full energy deposition): 19.2(13) b.

The weighted average of the values for the thermal capture cross section in this work, 18.8(7) b, presents an excellent agreement with the previous measurements from Butler et al., Durham et al. and Bendt & Journey. On the other hand, the large value of Marie et al. can be regarded as an outlier with respect to to all other measurements. A recent experiment by Genreith et al. was carried in the same facility using the same two techniques. Their activation result, after renormalized with the new intensity for the 84 keV decay line proposed by Leconte et al. yields 20.0(14) b, compatible to our value.

The weighted average of all the available data sets for the thermal ^{242}Pu(n,γ) cross section yields 18.8(4) b if we exclude the outlier result of Marie et al. This is in very good agreement with the result of our work. Regarding the evaluated values, the results in this work supports the evaluated cross section in JEFF-3.2 (18.79 b), while the ENDF-VII.1 (21.28 b) evaluation, that gives significantly more weight to the result by Marie et al., and JENDL-4.0 (19.98 b) seem to overestimate the cross section by 13 and 6%, respectively.

9.3.2 Resolved Resonance Region from 1 eV to 4 keV

The capture cross section of ^{242}Pu has been extracted in its resonace region with a systematic uncertainty of only 5%, which meets the requirements of the NEA-HPRL. The good energy resolution of the facility and the large accumulated statistics have allowed to observe individual resonances and determine their parameters up to 4 keV, while resonance parameters from capture measurements were previously reported only up to 1.3 keV. The individual resonance parameters of 251 resonance have been extracted, 180 of which had never been reported before in any neutron capture measurement. Our analysis indicates a ∼4% higher capture cross section compared to JEFF-3.2 in terms of weighted average of resonance kernels ratio (∼6% higher compared to the recent measurement at DANCE). In particular, for the 2.67 eV resonance our radiative kernel is 4.2% larger than in the evaluations, and 1.8% higher than the value at DANCE.

Statistical model calculations, validated with different experimental observables, have allowed us to estimate the number of missed s-wave and visible p-wave resonances, based in reduced neutron widths. This statistical study has enable to tag several resonances as p-wave candidates, ten of which are below 500 eV and were already considered as such in ENDF/B-VII.1.

The large set of analyzed s-wave resonances has led to a value of S_0 more accurate than in previous experiment and compatible with the values in the literature. A higher value of $\langle\Gamma_\gamma\rangle$, compatible just with JEFF-3.2 and RIPL, was extracted from our analysis. Statistical simulations indicate that the low threshold for observation allows the strongest p-wave resonances to be observed, especially below 2 keV, while obviously some of s-wave resonances remain unobservable. The analysis of the observed number of resonances using such simulations leads to a value of D_0 consistent with JEFF-3.2 and with the value proposed by Rich et al., but significantly larger than the value in ENDF/B-VII.1 and RIPL.

9.3.3 Unresolved Resonance Region from 1 to 500 keV

The average capture cross section in the URR, obtained from the same measurement at n_TOF, becomes the data set to cover the energy range from 1 to 250 keV in a single measurement and the the first capture measurement beyond 250 keV. The achieved systematic uncertainty meets the target accuracy of 8-12% for the design of innovative nuclear systems in the energy range from 1 to 250 keV. At higher energies, our systematic uncertainty ranges from 15 to 25%, still below the current 35%.

Our result shows a good agreeement with the two measurements by Wisshak and Kaeppeler for neutron energies between 10 an 250 keV. On the other hand, the strong reduction of the cross section suggested by the recient measurement in LANSCE is not confirmed by our results. The comparison to the evaluations indicate a ∼10-14% smaller average capture cross section compared to JEFF-3.2 in the energy range from 1 to 250 keV and a good agreement above this energy, in line with the interpretation of the PROFIL and PROFIL2 post-irradiation experiments.

Last, the measured cross section has been described in terms of average resonance parameters by means of a Hauser-Feshbach calculation allowing width fluctuations with the SAMMY/FITACS code. The fitted values of S_0 and $\langle\Gamma_\gamma\rangle_0$ are consistent with those extracted from the statistical analysis of the resonances below 4 keV. On the other hand, the parameterized cross section suggests a significant increase in the partial p-wave cross section (S_1 and $\langle\Gamma_\gamma\rangle_1$) compared to the values in the literature. It must be mentioned that the accuracy of the fitted parameters is limited by the sizable correlation among them and the lack of total cross section data to constrain the fit.

In summary, the new ^{242}Pu capture data at n_TOF-EAR1 provide the first data set in the URR covering in a single measurement the full energy range up to 500 keV and supports the trend indicated by the PROFIL experiments to reduce the capture cross section in JEFF-3.2. This shall lead to a consistent re-evaluation of the URR together with the resonance parameters from the RRR.

Part V

Bibliography

Bibliography

[1] *Key world energy statistics*, IEA Publications, International Energy Agency(2017)

[2] *IPCC, 2014: Climate Change 2014: Synthesis Report*, Contribution of Working Groups I, II and III to the Fifth Assessment Report of the Intergovernmental Panel on Climate Change (Core Writing Team, R.K. Pachauri and L.A. Meyer (eds.)), Geneva, Switzerland (2014)

[3] *Energy Technology Perspectives 2017*, IEA Publications, International Energy Agency (2017)

[4] *World Energy Outlook 2016*, IEA Publications, International Energy Agency (2016)

[5] *World Energy Outlook 2017*, IEA Publications, International Energy Agency (2017)

[6] *The Role of Nuclear Energy in a Low-carbon Energy Future* Nuclear Energy Agency, OECD (2012) ISBN 978-92-64-99189-7

[7] E. Fermi, L. Szilard, *NEUTRONIC REACTOR*, United States Patent Office, Patent Nr. 2708856, May 17 (1955)

[8] *Technology Roadmap Update for Generation IV Nuclear Energy Systems*, OECD Nuclear Energy Agency for the Generation IV International Forum (2014)

[9] J.C. Wagner et al., *Categorization of Used Nuclear Fuel Inventory in Support of a Comprehensive National Nuclear Fuel Cycle Strategy*, ORNL/TM-2012/308, FCRD-FCT-2012-000232 (2012)

[10] *Physics and Safety of Transmutation Systems: A Status Report*, OECD-NUCLEAR ENERGY AGENCY, NEA No. 6090 (2006)

[11] W. Maschek, X. Chen, F. Delage, A. Fernandez-Carretero, D. Haas, C. Matzerath-Boccaccini, A.Rineiski, P. Smith, V. Sobolev, R. Thetford, J. Wallenius, *Accelerator driven systems for transmutation: fuel development, design and safety.*, Prog. Nucl. Energy **50**, 333 (2008).

[12] *Research Group for Nuclear Transmutation Systems, Nuclear Science and Engineering Center, JAEA*, https://nsec.jaea.go.jp/ndre/ndre3/trans/objective-e.html

[13] *International Atomic Energy Agency, Status and advances in Mox fuel technology*, IAEA Technical Reports Series **415** (2003)

[14] *GIF R&D Outlook for Generation IV Nuclear Energy Systems*, OECD Nuclear Energy Agency for the Generation IV International Forum (2014)

[15] *The European Strategic Energy Technology Plan Towards a low carbon future*, European Union, (2010) ISBN 978-92-79-15667-0

[16] Michal Herman, *Overview of Nuclear Data*, Brookhaven Science Associates, Berkeley, May 17-19 (2015)

[17] *Experimental Unevaluated Nuclear Data List (XUNDL)*, Available from http://www.nndc.bnl.gov/xundl.

[18] V.Semkova, N.Otuka, M.Mikhailiukova, B.Pritychenko, O.Cabellos for the International Network of Nuclear Reaction Data Centres (NRDC), *EXFOR - a global experimental nuclear reaction data repository: Status and new developments*, EPJ Web Conf. **146** 07003 (2017)

[19] *Evaluated Nuclear Structure Data File*, National Nuclear Data Center, Brookhaven National Laboratory.

[20] A. Santamarina, D. Bernard, P. Blaise, M. Coste, A. Courcelle, T.D. Huynh, C. Jouanne, P. Leconte, O. Litaize, S. Mengelle, G. Nogure, J-M. Ruggiri, O. Srot, J. Tommasi, C. Vaglio, J-F. Vidal, *The JEFF-3.1.1 Nuclear Data Library*, JEFF Report **22**, OECD/NEA Data Bank (2009)

[21] M.B. Chadwick et al. *ENDF/B-VII.1*, Nucl. Data Sheets **112**, 2887 (2011)

[22] K. Shibata et al. *JENDL-4.0: A New Library for Nuclear Science and Engineering*, J. Nucl. Sci. Technol. **48** 1 (2011)

[23] S.V. Zabrodskaya et al., *RUSFOND RUSSIAN NATIONAL LIBRARY OF EVALUATED NEUTRON DATA*, Problems of Atomic Science and Technology. Series: Nuclear Constants, issue 1-2 (2007)

[24] Z. Ge, H. Wu, G. Chen and R. Xu, *CENDL project, the chinese evaluated nuclear data library*, EPJ Web Conf. **146**, 02002 (2017)

[25] A. J. Koning, S. Hilaire, and M. C. Duijvestijn, *TALYS: Comprehensive Nuclear Reaction Modeling*, AIP Conference Proceedings **769**, 1154 (2005)

[26] R. Capote et al., *Reference Input Parameter Library (RIPL-3)*, Nucl. Data Sheets **110**, Issue 12, 3107 (2009)

[27] R. E. MacFarlane, A. C. Kahler, *Methods for Processing ENDF/B-VII with NJOY*, Nucl. Data Sheets **111**, 2739-2890 (2010)

[28] N. Colonna et al, *Advanced nuclear energy systems and the need of accurate nuclear data: The n-TOF project at CERN*, Energy Environ. Sci. **3**, 1910 (2010)

[29] M. Salvatores and R. Jacqmin, *Uncertainty and target accuracy assessment for innovative system using recent covariance data evaluations*, ISBN 978-92-64-99053-1, NEA/WPEC-26 (2008)

[30] *NEA High Request Priority List* http://www.nea.fr/dbdata/hprl/

[31] P. R. Fields, G. L. Pyle, M. G. Inghram, H. Diamond, M. H. Studier and W. M. Manning, *Pile Neutron Cross Sections of the Heavier Plutonium Isotopes*, Nucl. Sci. and Eng. **1**(1), 62-67 (1956)

[32] J. P. Butler et al., *THE NEUTRON CAPTURE CROSS SECTIONS OF Pu238, Pu242, AND Am243 IN THE THERMAL AND EPICADMIUM REGIONS*, Can. Jour. of Physics, **35**(2), 147-154 (1957)

[33] R.W. Durham et F. Molson, *Capture cross section of* ^{242}Pu, Can. Jour. of Physics, **48**(6), 716-724 (1970)

[34] P.J. Bendt et E.T. Jurney, *Thermal-neutron capture-gamma spectrum of* ^{242}Pu, Los Alamos Scientific Lab. Reports, **7853** (1979)

[35] F. Marie, et al. *Thermal neutron capture cross-section measurements of* ^{243}Am *and* ^{242}Pu *using the new mini-INCA* α*- and* γ*-spectroscopy station*, Nucl. Instrum. Methods A **556**, 547-555 (2006)

[36] C. Genreith et al., *Measurement of thermal neutron capture cross sections of* ^{237}Np *and* ^{242}Pu *using prompt gamma neutron activation*, J. Radioanal. Nucl. Chem. **296**, 699 (2013)

[37] M. Rossbach et al., *TANDEM: a mutual cooperation effort for transactinide nuclear data evaluation and measurement*, J. Radioanal. and Nucl. Chem. **304**, (2015)

[38] R.F. Casten, W.R. Kane, J.R. Erskine, A.M. Friedman and D.S.Gale, *States in* ^{243}Pu *from the (n,*γ*), (d,p), and (d,t) reactions*, Phys. Rev. C **14**, 912 (1976)

[39] Y. Akovali et al, *Nuclear data sheets for A = 243*, Nucl. Data Sheets **103**, 515 (2004)

[40] F. Poortmans et al., *Neutron resonance parameters of* ^{242}Pu, Nucl. Phys. A **207**, 342-352 (1973)

[41] M.Q. Buckner et al., *Absolute measurement of the* ^{242}Pu *neutron-capture cross section*, Phys. Rev. C **93**, 044613 (2016)

[42] E. Rich et al., *Modeling of the n + 242Pu Reactions for Fast Reactor Applications*, Nucl. Sci. Eng. **162**, 178 (2009)

[43] R.W. Hockenbury et al., *keV capture cross section of* ^{242}Pu, SP425, 584-586 (1975)

[44] K. Wisshak and F. Kaeppeler, *Neutron Capture Cross-Section Ratios of* ^{240}Pu, ^{242}Pu, ^{238}U, *and* ^{197}Au *in the Energy Range from 10 to 90 keV*, Nucl. Sci. Eng. **66**, 363 (1978)

[45] K. Wisshak and F. Kaeppeler, *Neutron Capture Cross-Section Ratios of Plutonium-240 and Plutonium-242 Versus Gold-197 in the Energy Range from 50 to 250 keV*, Nucl. Sci. Eng. **69**, 39 (1979)

[46] G. Noguere, E. Dupont, J. Tommasi and D. Bernard, *Nuclear data needs for actinides by comparison with post irradiation experiments*, Technical note CEA Cadarache, NT-SPRC/LEPH-05/204 (2005).

[47] J. Tommasi, E. Dupont and P. Marimbeau, *Analysis of Sample Irradiation Experiments in Phénix for JEFF-3.0 Nuclear Data Validation*, Nucl. Sci. Eng. **154**, 119-133 (2006)

[48] J. Tommasi and G. Noguere, *Analysis of the PROFIL and PROFIL-2 Sample Irradiation Experiments in Phnix for JEFF-3.1 Nuclear Data Validation*, Nucl. Sci. Eng. **160**, 232-241 (2008)

[49] https://www.nuclear-power.net/neutron-cross-section

[50] , N. Bohr, *Neutron Capture and Nuclear Constitution*, Nature **137**, 344 (1936).

[51] N. Bohr and J. A. Wheeler, *The mechanism of nuclear fission*, Phys. Rev. **56**, 426-450 (1939)

[52] G. Breit and E. Wigner, *Capture of slow neutrons*, Phys. Rev. **49**, 519531 (1936)

[53] E. Wigner, *Resonance reactions*, Phys. Rev. **70**, 606-618 (1946)

[54] E. Wigner and L. Eisenbud, *Higher angular momenta and long range interaction in resonance reactions*, Phys. Rev. **72**, 29-41 (1947)

[55] A. M. Lane and R. G. Thomas, *R-matrix theory of nuclear reactions*, Rev. Mod. Phys. **30**, 257-353 (1958)

[56] F. Gunsing, *Introduction to neutron-induced reactions and the R-matrix formalism*, Neutron Resonance Analysis School, Geel, Belgium 15-19 December (2014)

[57] F. H. Fröhner, *Evaluation and Analysis of Nuclear Resonance Data*, JEFF Report **18**, NEA/OECD (2000)

[58] J. M. Blatt and L. C. Biedenharn, *The angular distribution of scattering and reaction cross sections*, Rev. Mod. Phys. **24**, 258-272 (1952)

[59] J. E. Lynn, *The Theory of Neutron Resonance Reactions*, Clarendon Press, Oxford, (1968).

[60] P. L. Kapur and R. Peierls, *The dispersion formula for nuclear reactions*, Proc. Roy Soc.,A **166**, 277-295 (1938)

[61] D. B. Adler and F. T. Adler, *Uniqueness of R-matrix parameters in the analysis of low energy neutron cross sections of fissile nuclei*, Phys. Rev. C, **6**, 986-1001 (1972)

[62] N. M. Larson, *Updated Users' Guide for SAMMY: Multilevel R-Matrix Fits to. Neutron Data Using Bayes' Equations*, ORNL/TM-9179/R8, ORNL, Oak Ridge, TN, USA (2008)

[63] J. Heyse, *From experimental observables to resolved resonance parameters*, Neutron Resonance Analysis School, Geel, Belgium 15-19 December (2014)

[64] M. C. Moxon, T. C. Ware, C. J. Dean, *REFIT-2009: A Least-Square Fitting Program for Resonance Analysis of Neutron Transmission, Capture, Fission and Scattering Data*, Users' Guide for REFIT-2009-10 (UKNSF(2010)P243, April 2010)

[65] C.E. Porter (ed.) *Statistical Theory of Spectra: Fluctuations*, Acad. Press, New York (1965)

[66] A. Gilbert and A. G. W. Cameron. *A composite nuclear-level density formula with shell corrections*, Canad. Jour. Phys. **43**, 1446-1496 (1965)

[67] H.A. Bethe, *Nuclear Physics B. Nuclear Dynamics, Theoretical*, Rev. Mod. Phys.**9**, 69 (1937)

[68] E. P. Wigner, *Results and Theory of Resonance Absorption*, Proc. Int. Conf. Neutron Physics by Time-of-Flight, Gatlinburg Tennessee, ORNL-2309 (1956)

[69] C. E. Porter and R. G. Thomas, *Fluctuations of Nuclear Reaction Widths*, Phys. Rev., **104**, 483 (1956)

[70] W. Hauser and H. Feshbach, *The inelastics scattering of neutrons*, Phy. Rev. **87**, 366 (1952)

[71] F. Froehner, *Evaluation of the Unresolved Resonance Range of* ^{238}U, Nucl. Sci. Eng. **103**, 119 (1989)

[72] L. C. Gomes, *Imaginary Part of the optical Potential*, Phys. Rev. **116** 1226-1229 (1959)

[73] D. Wilmore and P.E. Hodgson, *THE CALCULATION OF NEUTRON CROSS-SECTIONS FROM OPTICAL POTENTIALS*, Nucl. Phys. **55**, 673-694 (1964)

[74] E. Rich et al., *Generalization of the SPRT method: application to* ^{242}Pu *cross sections in the Unresolved Resonance Range*, Proc. Int. Conf. Nuclear Data for Science and Technology, Nice, France, April 2227, 2007, EDP Sciences (2008)

[75] F. Froehner, B. Goel and U. Fischer, *FITACS*, computer code Report ANL-83-4, Argonne National Laboratory (1983)

[76] *International Status and Prospects of Nuclear Power*, IAEA Report GOV/INF/2017/12-GC(61)/INF/8 (2017)

[77] G. Aliberti et al., *Impact of Nuclear Data Uncertainties on Transmutation of Actinides in ADS*, Nucl. Sci. Eng. **146**, 13 (2004).

[78] G. Wallerstein et al., *Synthesis of the elements in stars: forty years of progress*, Rev. Mod. Phys. **69**, 995 (1997)

[79] F. Käppeler, R. Gallino, S. Bisterzo, Wako Aoki, *The s process: Nuclear physics, stellar models, and observations*, Rev. Mod. Phys. **83**, 157 (2011)

[80] *Compendium of Neutron Beam Facilities for High Precision Nuclear Data Measurements*, IAEA-TECDOC series **1743**, International Atomic EnergyAgency, Vienna (2014)

[81] Tran Tuan Anh et al, *Characteristics of Filtered Neutron Beam Energy Spectra at Dalat Reactor* World Jour. Nucl. Sci. and Tech., **4**, 96-102 (2014)

[82] O. Gritzay, *Neutron spectra after the interference neutron filters at Kyiv research reactor*, Summary Report of the Consultants Meeting on Neutron Sources Spectra for EXFOR, IAEA Headquarters, Vienna, 13-15 April (2011).

[83] L. Rosta and R. Baranyai, *Budapest Research Reactor – 20 Years of International User Operation*, Neutron News, **22**, 31-36 (2011)

[84] H. Guyon and P. Geltenbort, *The high flux research reactor at the Laue-Langevin Institute (ILL)*, Atw Internationale Zeitschrift fuer Kernenergie **58**(10), 607-608 (2012)

[85] *IBR-2 Pulsed Reactor at Frank Laboratory of Neutron Physics, Joint Institute for Nuclear Research, Dubna, Russian Federation* http://flnp.jinr.ru/34/

[86] J. Praena et al., *Measurement of the MACS of ^{181}Ta(n,γ) at kT=30 keV as a test of a method for Maxwellian neutron spectra generation*, Nucl. Instrum. Methods A **727**, 1-6 (2013)

[87] S. Oberstedt et al., *Nuclear Research with Mono-Energetic Neutrons at the JRC Monnet Facility*, Individual Reports Compendium of Neutron Beam Facilities for High Precision Nuclear Data Measurements

[88] Feinberg, G. et al. *LiLiT – a Liquid-Lithium Target as an Intense Neutron Source for Nuclear Astrophysics at the Soreq Applied Research Accelerator Facility*, Nucl. Phys. A **827**, 590-592 (2009)

[89] S. Alzubaidi, U. Bartz, M. Basten et al., *The Frankfurt neutron source FRANZ*, Eur. Phys. J. Plus **131**, 124 (2016)

[90] *KADoNiS: Karlsruhe Astrophysical Database of Nucleosynthesis in Stars*, http://exp-astro.physik.uni-frankfurt.de/kadonis1.0/

[91] D. Ene, C. Borcea, S. Kopecky, W. Mondelaers, A. Negret, A. J. M. Plompen, *Global characterisation of the GELINA facility for high-resolution neutron time-of-flight measurements by Monte Carlo simulations*, Nucl. Instrum. Methods A **618**, 54 (2010)

[92] K. H. Guber, T. S. Bigelow, C. Ausmus, D. R. Brashear, J. A. Harvey, P. E. Koehler, D. Wiarda, R. B. Overton, J. A. White and V. M. Cauley, *Recent refurbishment of the Oak Ridge Electron Linear Accelerator neutron source*, Int. Conf. on Nucl. Data for Sci. and Tech., 441-443 (2007)

[93] C. Guerrero et al. (The n_TOF Collaboration), *Performance of the neutron time-of-flight facility n TOF at CERN*, Eur. Phys. J. A 49, 27 (2013)

[94] C. Weiss et al., *The new vertical neutron beam line at the CERN n_TOF facility: design and outlook on the performance*, Nucl. Instrum. Methods A 799, 90-98 (2015)

[95] P. Koehler et al., *Measurement of the LANSCE neutron flux from 0.025 eV to 100 keV*, Nucl. Instrum. Methods A **292**, 541 (1990)

[96] K. Kino et al., *Measurement of energy spectra and spatial distributions of neutron beams provided by the ANNRI beamline for capture cross-section measurements at the J-PARC/MLF*, Nucl. Instrum. Methods A **626**, 58 (2011)

[97] S. Peggs for ESS/AD and the ESS/ADU Collaboration, *The European Spallation Source*, Proceedings of IPAC2011, San Sebastián, Spain

[98] J. Lerendegui-Marco, S. Lo Meo, C. Guerrero et al., *Geant4 simulation of the n_TOF-EAR2 neutron beam: Characteristics and prospects*, Eur. Phys. J. A **52**, 100 (2016)

[99] J. Alvarez et al., *Laser Driven Neutron Sources: Characteristics, Applications and Prospects*, Phys. Procedia **60**, 29 (2014).

[100] G.A. Mourou, G. Korn, W. Sandner, J. L. Collie (ed.), *ELI: Extreme Light Infrastructure Science and Technology with Ultra-Intense Lasers Whitebook*, THOSS Media GmbH, (2011)

[101] C. Guerrero et al., *Prospects for direct neutron capture measurements on s-process branching point isotopes*, Eur. Phys. J. A **53**, 87 (2017)

[102] B. Pritychenko, S.F. Mughabghab, *Neutron Thermal Cross Sections, Westcott Factors, Resonance Integrals, Maxwellian Averaged Cross Sections and Astrophysical Reaction Rates Calculated from the ENDF/B-VII.1, JEFF-3.1.2, JENDL-4.0, ROSFOND-2010, CENDL-3.1 and EAF-2010 Evaluated Data Libraries*, Nucl. Data Sheets **113**, 3120 (2012)

[103] Q. Ducasse et al., *Neutron-induced Cross Sections of Actinides via the Surrogate-reaction Method*, Nucl. Data Sheets **119**,233-236 (2014)

[104] J. I. Hoover, W. H. Jordan, C. D. Moak, L. Pardue, and H. Pomerance, *Measurement of neutron absorption cross sections with a pile oscillator*, Phys. Rev **74**,864-870 (1948)

[105] L. Seren, H. N. Fried, and S. H. Turkel, *Thermal neutron activation cross sections*, Phys. Rev. **72**, 888-901 (1947)

[106] C. Tuniz, *Accelerator mass spectrometry: ultra-sensitive analysis for global science*, Rad. Phys. and Chem. **61**, 317-322 (2001)

[107] D. Beauchemin. *Inductively Coupled Plasma Mass Spectrometry*, Anal. Chem. **82** (12),4786-4810 (2010)

[108] T. Belgya, *Prompt Gamma Activation Analysis at the Budapest Research Reactor*, Physics Procedia **31**, 99-109 (2012)

[109] M.C. Moxon, E.R. Rae, *A gamma-ray detector for neutron capture cross-section measurements*, Nucl. Instrum. Methods A **24**, 445455 (1963)

[110] R.L. Macklin, J.H. Gibbons, *Capture-Cross-Section Studies for 30-220-keV Neutrons Using a New Technique*, Phys. Rev. **159**, 1007 (1967)

[111] C.Guerrero et al., *The n_TOF Total Absorption Calorimeter for neutron capture measurements at CERN*, Nucl. Instrum. Methods A **608** 424 (2009)

[112] C.Guerrero et al.,

[113] H. D. Choi et al., *Database of prompt gamma rays from slow neutron capture for elemental analysis*, International Atomic Energy Agency, Vienna (2007).

[114] Z. Révay, R. B. Firestone, T. Belgya and G. L. Molnár G. L., *Prompt Gamma-Ray Spectrum Catalog*, chapter in *Handbook of Prompt Gamma Activation Analysis with Neutron Beams*, G. L. Molnár (Ed), Kluwer Academic Publishers, Dordrecht, Boston, London, 173-366 (2004).

[115] M. Krtika, R. B. Firestone, D. P. McNabb, B. Sleaford, U. Agvaanluvsan, T. Belgya, Z. S. Revay, *Thermal neutron capture cross sections of the palladium isotopes*, Phys. Rev. C **77**, 054615 (2008)

[116] G. Schramm, R. Massarczyk, A. R. Junghans, T. Belgya, R. Beyer, E. Birgersson, E. Grosse, M. Kempe, Z. Kis, K. Kosev, M. Krtika, A. Matic, K. D. Schilling, R. Schwengner, L. Szentmiklsi, A. Wagner, and J. L. Weil, *Dipole strength in ^{78}Se below the neutron separation energy from a combined analysis of ^{77}Se(n,γ) and ^{78}Se(γ,γ') experiments*, Phys. Rev. C **85**, 014311 (2012)

[117] R. Massarczyk, G. Schramm, A. R. Junghans, R. Schwengner, M. Anders, T. Belgya, R. Beyer, E. Birgersson, A. Ferrari, E. Grosse, R. Hannaske, Z. Kis, T. Kgler, K. Kosev, M. Marta, L. Szentmiklsi, A. Wagner, and J. L. Weil, *Electromagnetic dipole strength up to the neutron separation energy from ^{196}Pt(γ,γ') and ^{195}Pt(n,γ) reactions*, Phys. Rev. C **87**, 044306 (2013)

[118] T. Belgya et al., *High-resolution study of the 113Cd(n,γ) spectrum by statistical decay model with discrete levels and transitions* , EPJ Web of Conferences **146**, 05009 (2017)

[119] G.L. Molnaŕ, T. Belgya et al., *The new prompt gamma-activation analysis facility at Budapest*, J. Radioanal. Nucl. Chem. **215**, 111115 (1997)

[120] Zs. Rvay, T. Belgya, Zs. Kasztovszky, J. L. Weil, G. L. Molnár, *Cold neutron PGAA facility at Budapest*, Nucl. Instrum. Methods B **213**, 385-388 (2004)

[121] L. Szentmiklósi et al., *Upgrade of the prompt gamma activation analysis and the neutron-induced prompt gamma spectroscopy facilities at the Budapest Research Reactor*, J. Radioanal. Nucl. Chem. **286**, 501-505 (2010)

[122] J. Füzy, *Direct measurement of cold neutron moderator spectra*, Nucl. Instrum. Methods A **586**, 41-45 (2008)

[123] *CHANDA:solving CHAllenges in Nuclear DAta*, Project funded by FP7-EURATOM-FISSION, EC (Grant No. 605203)

[124] A. Vascon et al., *Toward large-area targets for TRAKULA*, Nucl. Instrum. Methods A **655**, 72-79 (2011)

[125] G. Sibbens et al., *Preparation of ^{240}Pu and ^{242}Pu targets to improve cross-section measurements for advanced reactors and fuel cycles*, J. Radioanal. Nucl. Chem. **299**, 1093-1098 (2014)

[126] A. Vascon et al., *Quantitative molecular plating of large-area ^{242}Pu targets with improved layer properties*, Appl. Rad. Isot. **95**, 36-43 (2015)

[127] K. Eberhardt et al., *Chemical purification of plutonium and preparation of ^{242}Pu-targets by Molecular Plating*, CHANDA-Workshop, PSI (Villigen, Switzerland), November 23-25 (2015)

[128] https://www.sketchandcalc.com/area-calculator

[129] C. Genreith, *Partial Neutron Capture Cross Sections of Actinides using Cold Neutron Prompt Gamma Activation Analysis*, Schriften des Forschungszentrums Jülich, Energy & Environment Band / Volume 250, ISBN 978-3-95806-036-4

[130] L. Szentmiklósi, T. Belgya, M. Boglarka, Z. Kis, *Characterization of HPGe gamma spectrometers by geant4 Monte Carlo simulations*, J. Radioanal. Nucl. Chem. **300**, 553-558 (2014)

[131] Fazekas B., Molnr G., Belgya T., Dabolczi L. and Simonits A. *Introducing HYPERMET-PC for automatic analysis of complex gamma-ray spectra*, J. Radioanal. Nucl. Chem. **215**, 271-277 (1997)

[132] Rvay Z., Belgya T., Ember P. P. and Molnr G. L. *Recent developments in HYPERMET PC*, J. Radioanal. Nucl. Chem. **248**, 401-405 (2001)

[133] Rvay Z., Belgya T. and Molnr G. L. *Application of Hypermet-PC in PGAA*, J. Radioanal. Nucl. Chem. **265**, 261-265 (2005)

[134] Z. Kis, P. Voölgyesi and Z. Szabó, J., *DÖME: Revitalizing a low-background counting chamber and developing a radon-tight sample holder for gamma-ray spectroscopy measurements*, Radioanal. Nucl. Chem. **298**, 2029-2035 (2013)

[135] P. R. Fields et al., *Alpha decay of ^{247}Cm*, Nucl. Phys. A **103**, 160 460-470 (1971)

[136] P. Leconte et al., *Measurement of gamma-ray emission probabilities using a combination of activation and oscillation techniques: applications to ^{171}Er, ^{181}Hf, ^{233}Pa and ^{243}Pu*, International Conference on Nuclear Data for Science and Technology, 521-524 (2007)

[137] J. Allison et al., *Geant4 developments and applications*, IEEE Trans. on Nucl. Sci. **53**, Issue:1, 270 (2006)

[138] J. Allison et al., *Recent developments in GEANT4*, Nucl. Instrum. Methods A **835**, 186 (2016)

[139] Zs. Révay and G. L. Molnár, *Standardisation of the prompt gamma activation analysis method*, Radiochim. Acta, **91**, 361369 (2003).

[140] C.D. Nesaraja, E.A. McCutchan, *Nuclear Data Sheets for A = 243*, Nucl. Data Sheets **121**, 695 (2014)

[141] T. Belgya, G. L. Molnár, Zs. Rèvay, and J. L. Weil, *Determination of Thermal Neutron Capture Cross Sections using Cold Neutron Beams*, AIP Conference Proceedings **769**, 744 (2005)

[142] T. Belgya et al., *New gamma-ray intensities for the $^{14}N(n,\gamma)^{15}N$ high energy standard and its influence on PGAA and on nuclear quantities*, J. Radioanal. Nucl. Chem. **276**, 609-614 (2008)

[143] T. Belgya, *Determination of thermal radiative capture cross section*, EFNUDAT Slow and Resonance Neutrons, Proceedings of the Scientific Workshop on Nuclear Data Measurements, Theory and Applications, Budapest, Hungary 2325 September (2009)

[144] M. Guttormsen, T.S. Tveter, L. Bergholt, F. lngebretsen, and J. Rekstad, *The unfolding of continuum y-ray spectra*, Nucl. Instrum. Methods A **374**, 37 (1996)

[145] T. Belgya et al., *Strengh function from the $^{113}Cd(n,\gamma)$ reaction*, Proceedings of the European Research Infrastructures for Nuclear Data Applications (ERINDA) workshop, CERN, Geneva, 119126 CERN-Proceedings-2014-002, ISBN: 978-92-9083-403-8, (2014)

[146] T. Kibédi, T.W. Burrows, M.B. Trzhaskovskaya, P.M. Davidson, C.W. Nestor, *Evaluation of theoretical conversion coefficients using BrIcc*, Nucl. Instrum. Methods A **589**, 202-229 (2008)

[147] T. Laplace et al, *Statistical properties of ^{243}Pu, and $^{242Pu}(n,\gamma)$ cross section calculation*, Phys. Rev. C **93**, 014323 (2016)

[148] J.P. Burnet et al., *Fifty Years of the CERN Proton Synchrotron: Volume 1*, CERN-2011-04,2011.

[149] C. Rubbia, et al., *A high Resolution Spallation driven Facility at the CERN-PS to Measure Neutron Cross Sections in the Interval from 1 eV to 250 MeV*, CERN/LHC/98-002-EET, 1998

[150] *The CERN Accelerator Complex*, https://home.cern/about/accelerators

[151] J. P. Revol and the TARC collaboration, *THE TARC EXPERIMENT (PS211): NEUTRON-DRIVEN NUCLEAR TRANSMUTATION BY ADIABATIC RESONANCE CROSSING*, CERN-Service d'information scientifque-RD/996-2000-decembre 1999. ISBN: 92-9083-156-1

[152] C.Borcea et al., *Results from the commissioning of the n_TOF spallation neutron source at CERN*, Nucl. Instrum. Methods A **513**, 524537 (2003)

[153] *Neutron TOF Facility (PS 213)*, Technical Design Report,CERN/INTC/2000-004, 2000.

[154] E. Chiaveri et al., *Proposal for n_TOF Experimental Area 2 (EAR-02)*, CERN-INTC-2012-029 (2012)

[155] A. Nuttin et al., *Comparative analysis of high conversion achievable in thorium-fueled slightly modified CANDU and PWR reactors*, Ann. Nucl. Energy **40**, 171 (2012).

[156] R. Reifarth, C. Lederer and F. Kppeler, *Neutron Reactions in Astrophysics*, J. Phys. G: Nucl. Part. Phys. **41**, 053101 (2014)

[157] S.M. Qaim, *Nuclear data for medical radionuclides*, J. Radioanal. Nucl. Chem. **305**, 233 (2015)

[158] R.F. Barth, J.A. Coderre, M.G.H. Vicente and T.E. Blue, *Boron neutron capture therapy of cancer: current status and future prospects*, Clin. Cancer Res. 11, 3987 (2005)

[159] I. Porras et al., *^{33}S for neutron capture therapy: nuclear data for monte carlo calculations*, Nucl. Data Sheets **120**, 246 (2014)

[160] F. Gunsing et al., *Nuclear data activities at the n_TOF facility at CERN*, Eur. Phys. J. Plus **131**, 371 (2016)

[161] F. Gunsing et al., *The measurement programme at the neutron time-of-flight facility n_TOF at CERN*, EPJ Web of Conferences **146**, 11002 (2017)

[162] S. Lo Meo, M.A. Cortés-Giraldo, C. Massimi et al., *GEANT4 simulations of the n_TOF spallation source and their benchmarking*, Eur. Phys. J. A **51**, 160 (2015)

[163] G.J. Russell, *Spallation Physics - An Overview*, ICANS-XI International Collaboration on Advanced Neutron Sources KEK. Tsukuba. October 22-26, 1990.

[164] D. Mancusi, S. Lo Meo , N. Colonna, A. Boudard, M. A. Cortés-Giraldo, J. Cugnon, J.-C. David, S. Leray, J. Lerendegui-Marco, C. Massimi, and V. Vlachoudis, *On the role of secondary pions in spallation targets*, Eur. Phys. J. A **53**, 80 (2017)

[165] R. Plag et al., *An optimized C6D6 detector for studies of resonance-dominated (n,γ) cross-sections*, Nucl. Instrum. Methods A **496**, 425 (2003)

[166] J. Balibrea-Correa, E. Mendoza, D. Cano-Ott et al. and the n_TOF Collaboration, *Measurement of the neutron capture cross section of the fissile isotope 235U with the CERN n_TOF total absorption calorimeter and a fission tagging based on micromegas detectors*, EPJ Web of Conferences **146** , 11021 (2017)

[167] M. Bacak et al. and the n_TOF Collaboration, *A compact multi-plate fission chamber for the simultaneous measurement of 233U capture and fission cross-sections*, EPJ Web of Conferences **146**, 03027 (2017)

[168] D.L. Prez Magn, L. Caballero, C. Domingo-Pardo, J. Agramunt-Ros, F. Albiol, A. Casanovas, A. Gonzlez, C. Guerrero, J. Lerendegui-Marco, A. Tarifeo-Saldivia, *First tests of the applicability of γ-ray imaging for background discrimination in time-of-flight neutron capture measurements*, Nucl. Instrum. Methods. A **823**, 107119 (2016)

[169] M. Calviani et al., *High-accuracy $^{233}U(n,f)$ cross-section measurement at the white-neutron source n_TOF from near-thermal to 1 MeV neutron energy*, Phys. Rev. C 80, 044604 (2009).

[170] D. Tarrio et al., *Measurement of the angular distribution of fission fragments using a PPAC assembly at CERN n_TOF*, Nucl. Instrum. Methods A 743, 79 (2014)

[171] F. Belloni et al., *Experimental studies of a Micromegas neutron detector*, Mod. Phys. Lett. A 28, 1340023 (2013)

[172] A.J. Pollitt et al., *Measurements of γ-ray Energy and Multiplicity from ^{235}U (ν thermal) using STEFF*, EPJ Web of Conferences 93, 02018 (2015)

[173] M. Sabaté-Gilarte et al., *Measurement of the $^{33}S(n,\alpha)$ cross-section at n_TOF(CERN): Applications to BNCT*, Rep. Pract. Oncol. Radiother. **21**, 113 (2016)

[174] J. Praena et al. (n_TOF Collaboration), *Measurement and resonance analysis of the $^{33}S(n,\alpha)^{30}Si$ cross section at the CERN n_TOF facility in the energy region from 10 to 300 keV*, Phys. Rev. C **97**, 064603 (2018)

[175] C. Weiss et al., *(n,α) Reaction in the s-process Branching Point ^{59}Ni*, Nucl. Data Sheets 120(0), 208 (2014)

[176] L Cosentino et al. and the n_TOF Collaboration, *Experimental setup and procedure for the measurement of the $^{7}Be(n, \alpha)\alpha$ reaction at n_TOF*, Nucl. Instrum. Methods. A **830**, 197-205 (2016)

[177] M. Barbagallo, J. Andrzejewski, M. Mastromarco, J. Perkowski, L.A. Damone and the n_TOF Collaboration, *Experimental setup and procedure for the measurement of the $^{7}Be(n, p)^{7}Li$ reaction at n_TOF*, Nucl. Instrum. Methods. A **887**, 27-33 (2018)

[178] M. Barbagallo et al., *High-accuracy determination of the neutron flux at n_TOF*, Eur. Phys. J. A **49**, 156 (2013)

[179] M. Sabaté, M. Barbagallo et al., (the n_TOF Collaboration), *High-accuracy determination of the neutron flux in the new experimental area n_TOF-EAR2 at CERN*, Eur. Phys. J. A **53**, 210 (2017)

[180] A. D. Carlson, *The neutron cross section standards, evaluations and applications*, Metrologia **48**, S328 (2011)

[181] *International Evaluation of Neutron Cross-Section Standards*, International Atomic Energy Agency (2007)

[182] S. Marrone et al., *A low background neutron flux monitor for the n_TOF facility at CERN*, Nucl. Instrum. Methods A **517**, 389 (2004)

[183] I. Giomataris et al., *MICROMEGAS: a high-granularity position-sensitive gaseous detector for high particle-flux environments*, Nucl. Instrum. Methods A **376**, 29 (1996)

[184] S. Andriamonje et al., *A Transparent Detector for n_TOF Neutron Beam Monitoring*, J. Kor. Phys. Soc. **559**, 1597 (2011)

[185] D.B. Gayther, *International Intercomparison of Fast Neutron Fluence-Rate Measurements Using Fission Chamber Transfer Instruments*, Metrologia 27, 221 (1990)

[186] C. Paradela et al., *Neutron-induced fission cross section of ^{234}U and ^{237}Np measured at the CERN Neutron Time-of-Flight (n_TOF) facility*, Phys. Rev. C **82**, 034601 (2010)

[187] D. Tarrío, *Neutron-induced fission cross section of ^{nat}Pb and ^{209}Bi from threshold to 1 GeV: An improved parametrization*, Phys. Rev. C **83**, 044620 (2011)

[188] *GEANT4 Physics Reference and User Manuals*, available at http://geant4.cern.ch

[189] A. Boudard et al., *New potentialities of the Lige intranuclear cascade model for reactions induced by nucleons and light charged particles*, Phys. Rev. C **87**, 014606 (2013).

[190] A. Ferrari et al., *FLUKA: A Multi-Particle Transport Code*, CERN-2005-10, INFN/TC_05/11, SLAC-R-773 (2005)

[191] D. B. Pelowitz, ed., *MCNPX User's Manual, Version 2.7.0*, Los Alamos National Laboratory report, LA-CP-11-00438 (2011)

[192] G. Lorusso et al., *Timeenergy relation of the n TOF neutron beam: energy standards revisited*, Nucl. Instrum. Methods A **532**, 622 (2004)

[193] C. Guerrero et al., *Monte Carlo simulation of the n_TOF Total Absorption Calorimeter*, Nucl. Instrum. Methods A **671**, 108117 (2012)

[194] C. Guerrero et al., *Measurement and resonance analysis of the ^{237}Np neutron capture cross section*, Phys. Rev. C **85**, 044616 (2012)

[195] T. Wright et al., *Measurement of the 238U(n,) cross section up to 80 keV with the Total Absorption Calorimeter at the CERN n_TOF facility*, Phys. Rev. C **96**, 064601 (2017)

[196] R. L. Macklin, J. H. Gibbons and T. Inada, *NEUTRON CAPTURE CROSS SECTIONS NEAR 30 keV USING A MOXON-RAE DETECTOR*, Nucl. Phys. **43**, 353-362 (1963)

[197] K. Wisshak, F. K.appeler, G. Reffo, F. Fabbri, *Neutron Capture in s-Wave Resonances of Iron-56, Nickel-58, and Nickel-60*, Nucl. Sci. Eng. **86** 168 (1984)

[198] F. Rau, *Entfaltung des mit einem Szintillationsspektrometer beobachteten Impulshöhenspektrums zum Energiespektrum der γ- Strahlung*, Nukleonik 5 **191** (1963)

[199] J.L. Taín et al., *Accuracy of the Pulse Height Weighting Technique*, Nucl. Sci. and Tech.**2**, 689-692 (2002)

[200] U. Abbondanno et al., *New experimental validation of the pulse height weighting technique for capture cross-section measurements*, Nucl. Instrum. Methods A **521**, 454 (2004)

[201] B. Leugers, *Neutron Capture Cross-Sections Of Krypton Isotopes And Their Astrophysical Implications*, Kernforschungszentrum Karlsruhe Reports, No. 2895 (1979)

[202] P. Mastinu et al., *New C_6D_6 detectors: reduced neutron sensitivity and improved safety*, CERN-n_TOF-PUB-2013-002 (2013)

[203] P. Zugec, N. Colonna, D. Bosnar et al., *GEANT4 simulation of the neutron background of the C6D6 set-up for capture studies at n_TOF*, Nucl. Instrum. Methods A **760**, 57 (2014)

[204] J. Lerendegui-Marco, *Report of the project during Summer Student stay*, CERN-STUDENTS-Note-2014-033, http://cds.cern.ch/record/1749924.

[205] C. Domingo, *i-TED: A novel concept for high-sensitivity (n,γ) cross-section measurements.*, Nucl. Instrum. Methods A **825**, 78-86 (2016)

[206] D. B. Everett, J. S. Fleming, R. W. Todd, J. M. Nightingale, *Gamma-radiation imaging system based on the Compton effect*, Proc. IEEE **124**, 995 (1977)

[207] R. Pani, M. N. Cinti, R. Scafè, R. Pellegrini, F. Vittorini, P. Bennati, S. Ridolfi, S. Lo Meo, M. Mattioli ,G. Baldazzi ,F. Pisacane ,F. Navarria ,G. Moschini ,P. Boccaccio, V. Orsolini Cencelli, D. Sacco, *Energy resolution measurements of LaBr3:Ce scintillating crystals with an ultra-high quantum efficiency photomultiplier tube*, Nucl. Instrum. Methods A **610**, 41 (2009)

[208] P.Conde, A. J. Gonzlez, L. Hernndez, P. Bellido, A. Iborra, E. Crespo, L. Moliner, J. P. Rigla, M. J. Rodrguez-lvarez, F. Snchez, M. Seimetz, A. Soriano, L. F. Vidal, J. M. Benlloch, *Results of a combined monolithic crystal and an array of ASICs controlled SiPMs*, Nucl. Instrum. Methods A **734** 132 (2014).

[209] C. Massimi et al., *Resonance neutron-capture cross sections of stable magnesium isotopes and their astrophysical implications*, Phys. Rev. C **85**, 044615 (2012)

[210] R. Macklin, J. Halperin, and R. Winters, *Absolute neutron capture yield calibration*, Nucl. Instrum. Methods A **164**, 213 (1979)

[211] C. Lederer et al., *^{197}Au(n,γ) cross section in the unresolved resonance region*, Phys. Rev. C **83**, 034608 (2011)

[212] F. Mingrone et al., *Neutron capture cross section measurement of 238U at the CERN n_TOF facility in the energy region from 1 eV to 700 keV*, Phys. Rev. C **95**, 034604 (2017)

[213] C. Domingo et al., *Resonance capture cross section of ^{207}Pb*, Phys. Rev. C **74** (2006)

[214] J. Lerendegui-Marco et al., *Geant4 Simulations for the Analysis of (n,γ) Measurements at n_TOF*, Basic Concepts in Nucl. Phys.: Theory, Experiments and Applications: La Rbida. Springer Proceedings in Physics (2016)

[215] Shen, V.K., Siderius, D.W., Krekelberg, W.P., and Hatch, H.W., Eds., *NIST Standard Reference Simulation Website*, NIST Standard Reference Database Number **173**,National Institute of Standards and Technology, Gaithersburg MD, 20899, http://doi.org/10.18434/T4M88Q

[216] *Geant4 Reference Physics Lists*, https://geant4.web.cern.ch/node/628

[217] C. Guerrero, J. Lerendegui-Marco et al., *On the use of stacks of fission-like targets for neutron capture experiments*, Nucl. Instrum. Methods A (submitted) (2018)

[218] E. Mendoza et al., *Measurement and analysis of the ^{243}Am neutron capture cross section at the n_TOF facility at CERN*, Phys. Rev. C **90**, 034608 (2014)

[219] E. Mendoza et al., *Measurement of the ^{241}Am and the ^{243}Am Neutron Capture Cross Sections at the n_TOF Facility at CERN*, Nucl. Data Sheets **119**, 65 (2014)

[220] *Wall Current Monitors*, http://psring.web.cern.ch/psring/psring/misc/wcm.html

[221] U. Abondanno et al., *The data acquisition system of the neutron time-of-flight facility n_TOF at CERN*, Nucl. Instrum. Methods A **538**, 692 (2005)

[222] *CERN Advanced STORage manager*, castor.web.cern.ch.

[223] P. Žugec et al., *Pulse processing routines for neutron time-of-flight data*, Nucl. Instrum. Methods A **812**, 134 (2016)

[224] P. Žugec, *User's guide through Pulse Shape Analysis routines*, Internal Report n_TOF Collaboration, October 2016

[225] R.Brun *ROOT: An object oriented data analysis framework*, Proceedings AIHENP'96 Workshop, Nucl. Instrum. Methods A **389** (1997)

[226] I. Antcheva et al., *ROOT – A C++ framework for petabyte data storage, statistical analysis and visualization*, Comput. Phys. Commun, **180**, 2499-2512 (2009)

[227] C. Guerrero et al., *Analysis of the BC501A neutron detector signals using the true pulse shape*, Nucl. Instrum. Methods A **597**, 212 (2008)

[228] F. Gunsing et al., ,

[229] K. Fraval et al., *Measurement and analysis of the $^{241}Am(n,\gamma)$ cross section with liquid scintillator detectors using time-of-flight spectroscopy at the n_TOF facility at CERN*, Phys. Rev. C 89 (2014) 044609

[230] A. Casanovas, C. Domingo-Pardo et al., *Measurement of the radiative capture cross section of the s-process branching points ^{204}Tl and ^{171}Tm at the n_TOF facility (CERN)*, EPJ Web of Conferences **178**, 03004 (2018)

[231] C. Guerrero, J. Lerendegui-Marco et al., *Neutron capture on the s-process branching point ^{171}Tm via time-of-flight*, Submitted to Phys. Rev. Lett. (2018)

[232] W. R. Leo, *Techniques for Nuclear and Particle Physics Experiments*, Springer Verlag, (1987)

[233] G. Aerts et al., *Neutron capture cross section of ^{232}Th measured at then_TOF facility at CERN in the unresolved resonance region up to 1 MeV*, Phys. Rev. C **73**, 054610 (2006)

[234] E. Mendoza, D. Cano-Ott, C.Guerrero, E.Berthoumieux, *Pulse pile-up and dead time corrections for digitized signals from a BaF_2 calorimeter*, Nucl. Instrum. Methods A **768**, 55-61 (2014)

[235] J.L. Taín and D. Cano-Ott, *The influence of the unknown de-excitation pattern in the analysis of -decay total absorption spectra*, Nucl. Instrum. Methods A **571** 719 (2007)

[236] J.Kopecky and M. Uhl, *Test of gamma-ray strength functions in nuclear reaction model calculations*, Phys. Rev. **41** 1941 (1990)

[237] C. Massimi, C. Domingo-Pardo, G. Vannini, et al., *$^{197}Au(n,\gamma)$ cross section in the resonance region*, Phys. Rev. C **81**, 044616 (2010)

[238] K. H. Schmidt, B. Jurado and C. Schmitt, *General description of fission observables: The GEF code*, EPJ Web of Conferences **146**, 04001 (2017)

[239] *Neutron-induced fission cross sections of ^{242}Pu from 0.3 MeV to 3 MeV*, P. Salvador-Castieira et al., Phys. Rev. C **92**, 044606 (2015)

[240] V. McLane, C. L. Dunford, P. F. Rose (Ed.), *ENDF-102, Data Formats and Procedures for the Evaluated Nuclear Data File, ENDF-6*, BNL-NCS-4495, Brookhaven National Laboratory, April 2001. Updated BNL-NCS-4495/04-Rev, ed. M. Herman, June 2005

[241] N. M. Larson, M. C. Moxon, L. C. Leal, and H. Derrien, *Doppler Broadening Revisited*, ORNL/TM-13525, Oak Ridge National Laboratory (1998)

[242] D. G. Naberejnev, C. Mounier, and R. Sanchez, *The Influence of Crystalline Binding on Resonant Absorption and Reaction Rates*, Nucl. Sci. Eng. **131**, 222-220 (1999)

[243] J. Ullmann et al., *Constraining the calculation of $^{234,236,238}U(n,\gamma)$ cross sections with measurements of the γ-ray spectra at the DANCE facility*, Phys. Rev. C **96**, 024627 (2017)

[244] G.F. Auchampaugh et al., *Parameters of the Subthreshold Fission Structure in Pu-242*, Phys. Rev. C **7**, 5 (1973)

[245] H. Weigmann et al., *Neutron-induced fission cross section of ^{242}Pu*, Nucl. Phys A **438**, 333 (1985)

[246] J. Lerendegui-Marco, C. Guerrero et al., *Radiative neutron capture on ^{242}Pu in the resonance region at the CERN n_TOF-EAR1 facility*, Phys. Rev. C **97**, 024605 (2018)

[247] F. H. Frohener, *SESH*, computer code GA-8380, Gulf General Atomic (1968)

[248] P. Axel, *Electric Dipole Ground-State Transition Width Strength Function and 7-Mev Photon Interactions*, Phys. Rev. **126**, 671 (1937)

[249] F. Corvi, G. Fioni, F. Gasperini, P. B. Smith, *The weighting function of a neutron capture detection system*, Nucl. Sci. Eng.. **107** 272 (1991)

[250] S. F. Mughabghab, *Atlas of Neutron Resonances*, 5th ed., Elsevier Science, New York (2006)

Part VI

Appendices

Appendix A

Nuclear structure data

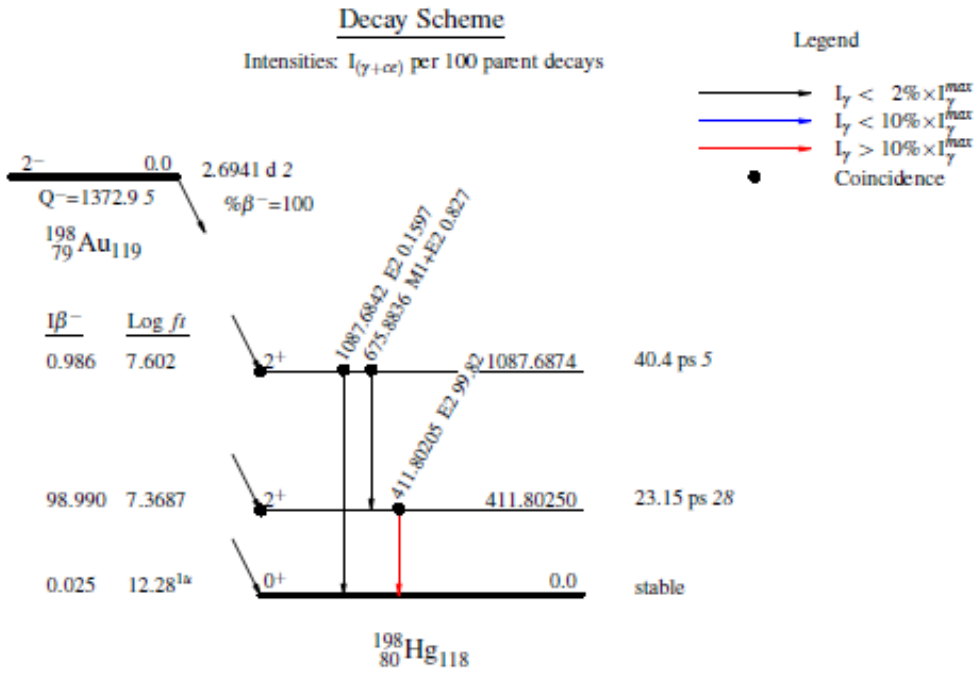

Figure A.1: Scheme of the β^- decay of ^{198}Au to ^{198}Hg. (from Ref. [19]).

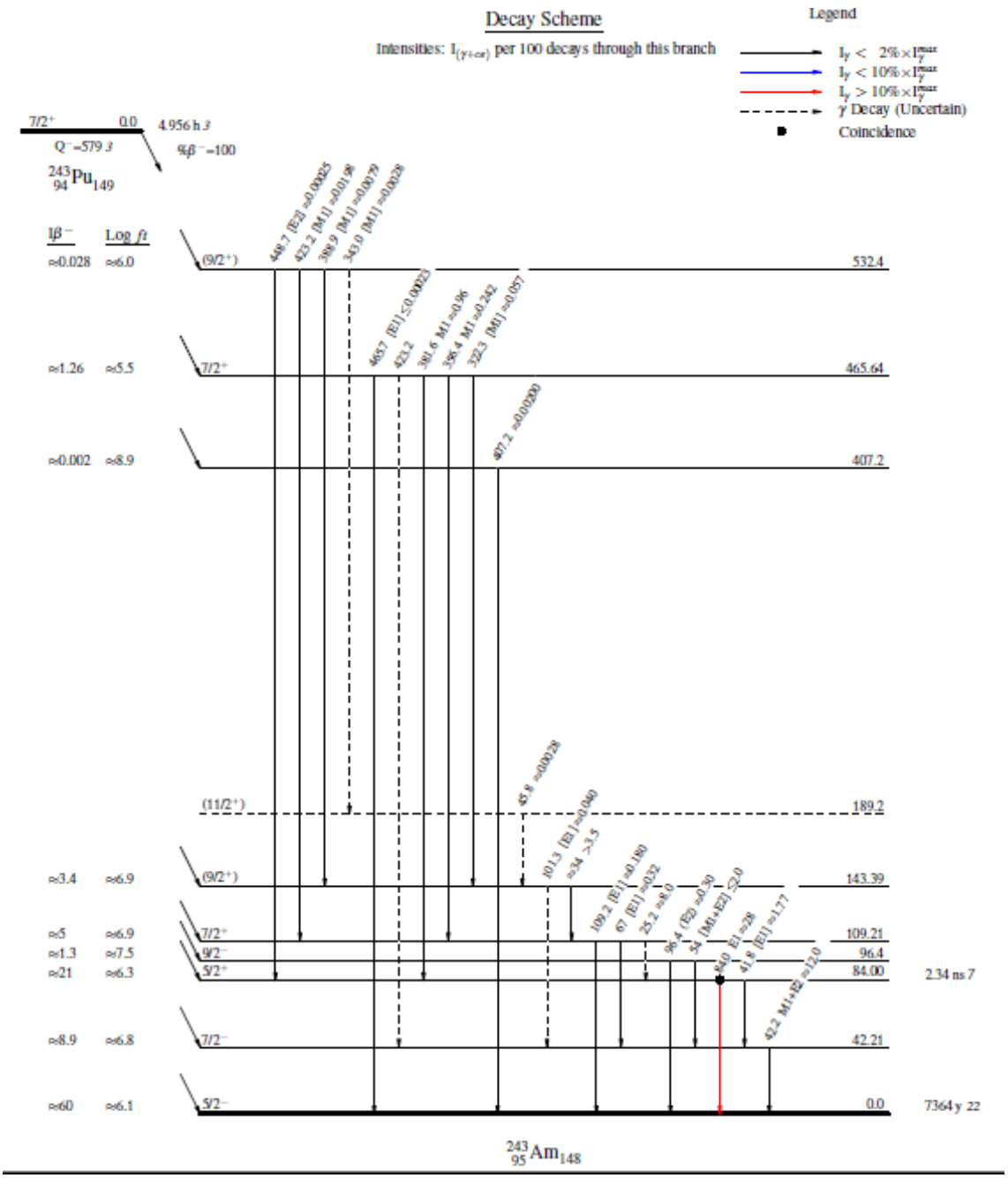

Figure A.2: Scheme of the β^- decay of 243Pu to ^{243}Am (from Ref. [19]).

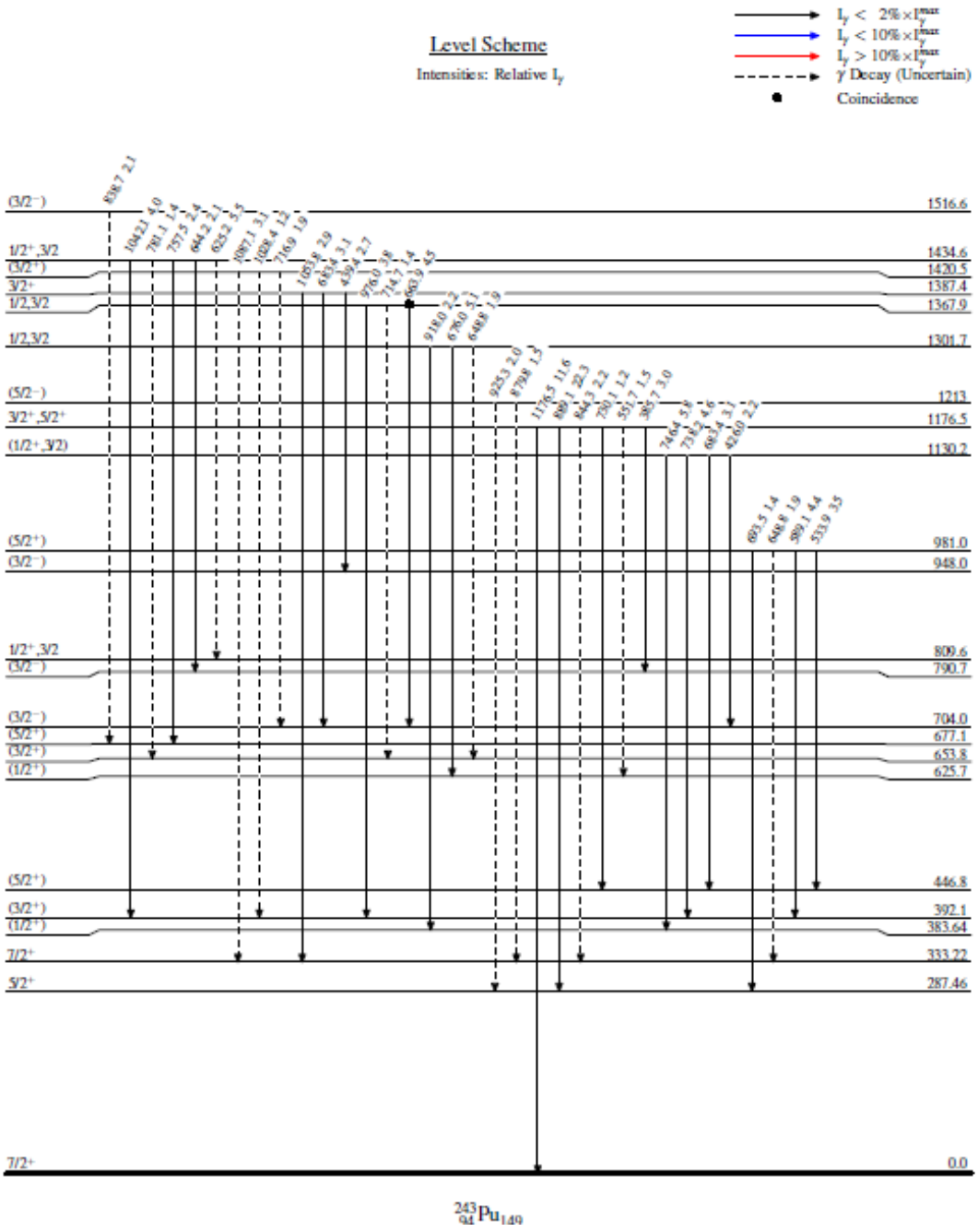

Figure A.3: Nuclear scheme of ^{243}Pu showing the ^{242}Pu(n,γ) secondary γ-ray transitions with initial states above 1 MeV (from Ref. [19]).

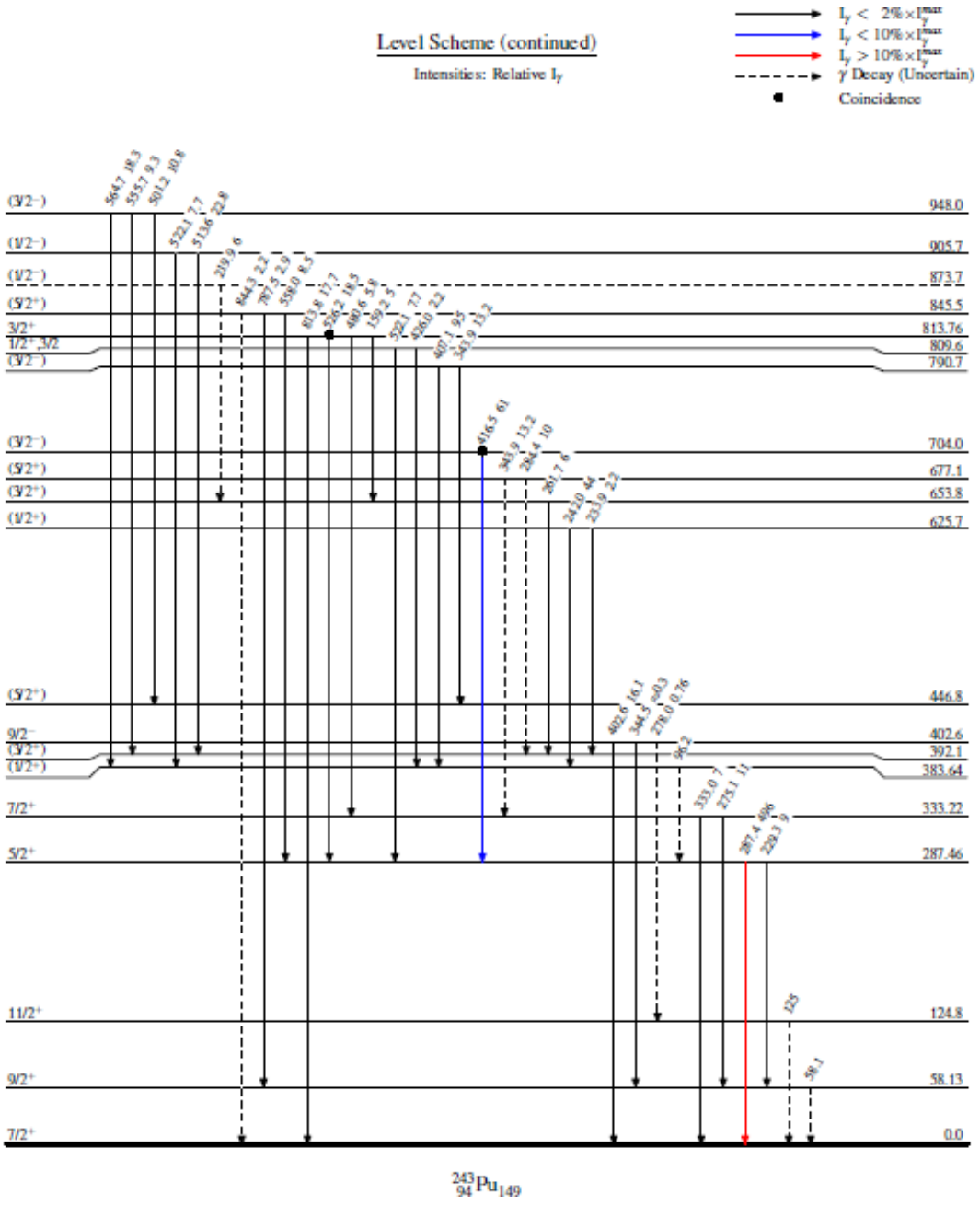

Figure A.4: Nuclear scheme of ^{243}Pu showing the ^{242}Pu(n,γ) secondary γ-ray transitions with initial states below 1 MeV (from Ref. [19]).

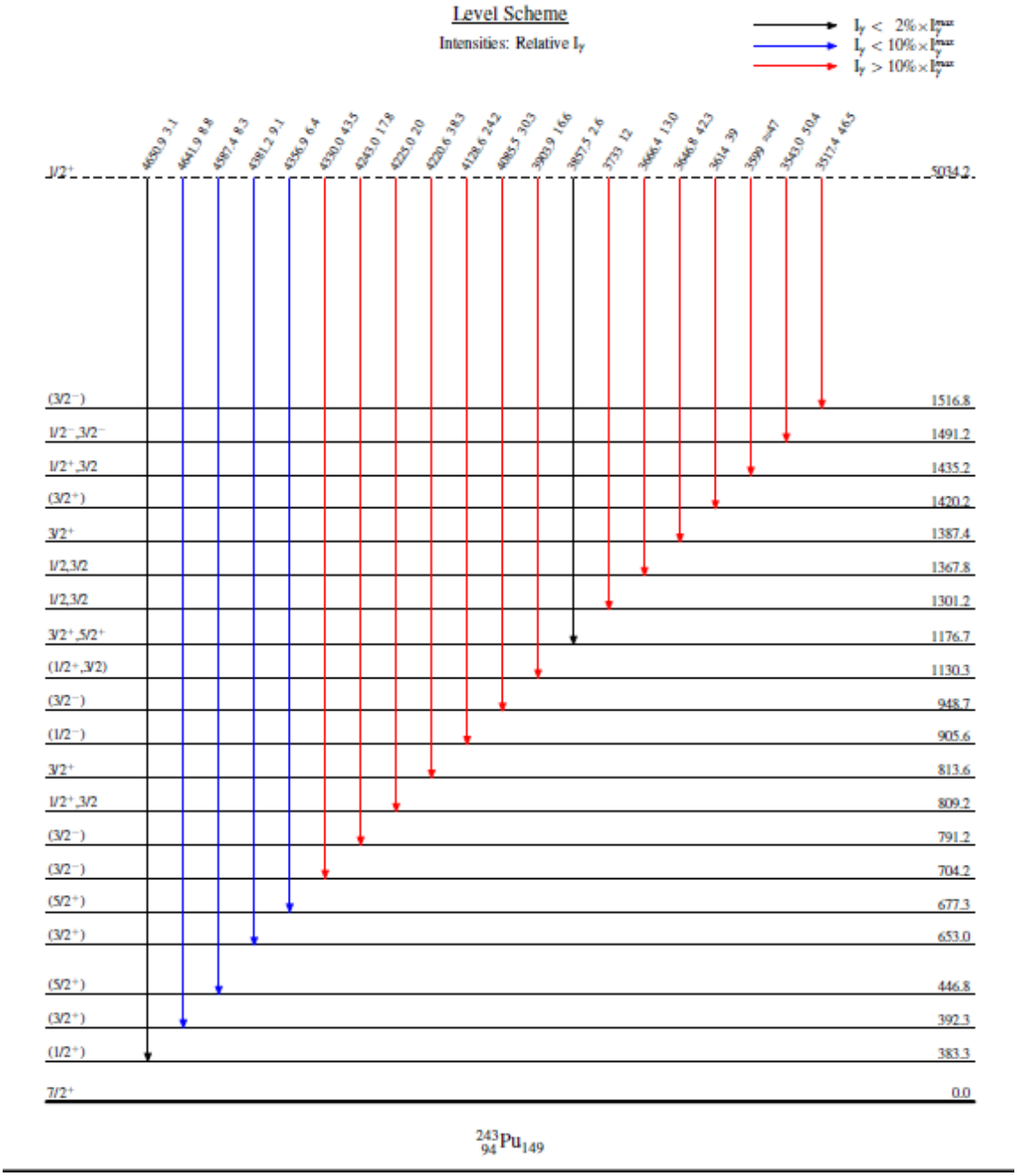

Figure A.5: Nuclear scheme of ^{243}Pu showing the ^{242}Pu(n,γ) primary γ-ray transitions (i.e. from the compound nucleus state) (from Ref. [19]).

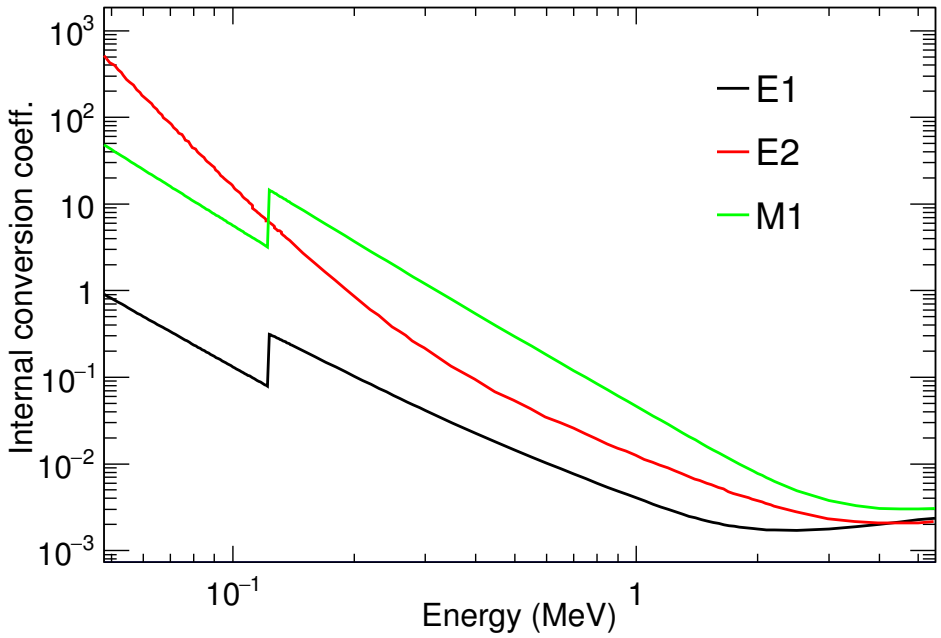

Figure A.6: Internal conversion coefficients of Pu as a function of the transition energy for E1, E2 and M1 multipolarities.

Appendix B

Pulse Height Weighting Technique (PHWT)

In order to acomplish the principles of the Total Energy Detection method, a mathematical manipulation of the detector response is needed to achieve the desired proportionality. The measured counts for each deposited energy must be weighted with an energy (pulse height) dependent weighting function (WF); this is known as the *Pulse Height Weighting Technique(PHWT)*[199, 200].

B.1 Principles of the PHWT

The efficiency of each detector for detecting a γ-ray of energy E_γ) can be defined as

$$\varepsilon(E_\gamma) \;=\; \int_0^\infty R(E_d, E_\gamma) dE_d, \tag{B.1}$$

where $R(E_d, E_\gamma)$ is the so-called response function of the detector, defined as the fraction of γ-rays of a given energy E_γ) that make an energy deposition of E_d. The right panel of Figure B.1 shows the detection efficiency as a function of E_γ) for a BICRON detector as a function of the γ-ray energy. From this figure, it is clear that the efficiency is far from being proportional to the γ-ray energy. In order to transform the efficiency so that it fulfills Eq. 5.8, the detector response $R(E_d, E_\gamma)$ must be weighted with a function dependent on the deposited energy.

The weighting function $W(E_d)$ is defined, in general, as a function of the energy deposited by a γ-ray E_d such that it fulfills the following expression:

$$\int_0^\infty R(E_d, E_\gamma) W(E_d) dE_d = k\ E_\gamma, \tag{B.2}$$

where the proportionality constant k (the same than in Eqs. 5.9 and 5.10) is forced to be 1 MeV^{-1}. The integral in this expression represents the weighted efficiency, which after the inclusion of the WF becomes equal numerically to the γ-ray energy E_γ.

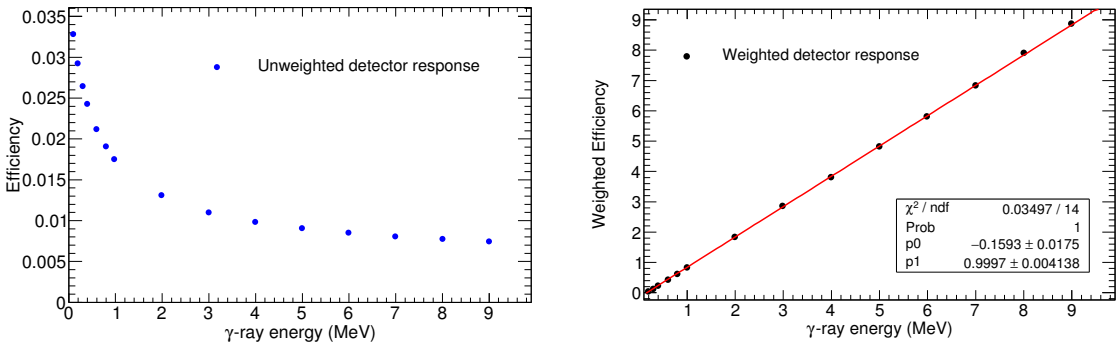

Figure B.1: Left: Unweighted efficiency of the (BICRON) detector #1 placed a 10 cm from the sample as a function of the γ-ray energy. Right: Efficiency of the same detector after the Weighting Function is applied to the detector response, showing a very good proportionality with the γ-ray energy.

Since the real spectra of γ-ray energy deposition are not continous and we will work with response functions of the detector for discrete energies, the following discrete variables can be introduced

$$\begin{aligned} E_d &\rightarrow E_j, \\ E_\gamma &\rightarrow E_i, \\ R(E_d, E_\gamma) &\rightarrow R_{ij}, \\ W(E_d) &\rightarrow W_j, \end{aligned} \tag{B.3}$$

and discrete sums over j will replace the integrals in Eqs. (B.1) and (B.2) hereafter.

If we replace Eq. B.2 in Eq. 5.10, the total weighted efficiency to detect a γ-ray cascade ϵ_c^w becomes proportional to the total energy of the cascade, which is the sum of the neutron separation energy of the target nucleus S_n plus the neutron energy E_n

$$\epsilon_c^w = \sum_i \sum_j W_j \cdot R_{ij} = \sum_i E_i = E_c = S_n + E_n, \tag{B.4}$$

and thus the principle of the TED is succesfully acomplished.

In a Time-of-Flight experiment, the time-of-flight corresponding to an energy deposition in the detectors is registered together with the deposited energy E_j. From the original distribution of counts as a function of the TOF and the energy deposited $C(TOF, E_j)$, the weighted distribution of counts for a given time of flight is calculated with the following energy-weighted sum

$$C^w(TOF) = \sum_j W_j \; C(TOF, E_j). \tag{B.5}$$

In order to calculate the appropiate WF, one must find a function that satisfies Eq. (B.2) for all the γ-ray energies in the energy range of interest for capture measurements (0-10 MeV). This implies, first, knowing the response functions R_{ij} for a large number of

γ-ray energies. In the past, R_{ij} were derived experimentally through careful measurement of responses of the detection system to mono-energetic γ-rays [249]. However, the lack of monoenergetic γ-ray sources in the whole energy range of interest (0-10 MeV) and the difficulties to include the detector and sample dependence of R_{ij} generated large systematic uncertainties. Later, it was proofed that Monte Carlo simulations, using codes such as MCNP [191] or Geant4 [137, 138], improved significantly the accuracy of the extracted WFs [200].

B.2 Geant4 application for the analysis of (n,γ) measurements at n_TOF

In order to obtain the response distribution of the C_6D_6 detectors for the calculation of the WF a detailed implementation of the geometry model of the capture setup in the MC code is necessary. The details in the implementation should include

- The detector geometry, which must be implemented as detailed as possible (active volume and surrounding materials).
- The dimensions and compositions of the materials, both of the sample and of the experimental setup, since they can have a non-negligible influence in the detector response.
- An accurate positioning of the detectors in the simulated setup is one of the main factors to reproduce the real efficiencies of the detectors in our measurement.

Different Geant4 applicattions had been used for the analysis of measurements carried out with C_6D_6 detectors during n_TOF Phase #2. However, the new features of the C_6D_6 capture set-up were still not included. The main changes had been:

- The new Legnaro detector model with reduced neutron sensitivity.
- New detector holders made of Al (2014-2015) and CF (since 2016).
- Two experimental areas, with slightly different geometries of the capture set-up but very similar if we forget about the orientation.

The idea behind the upgrade of the Geant4 application carried out in this work was to develop a useful tool not only for our own use for the analysis of the ^{242}Pu(n,γ) but for every member of the n_TOF collaboration that wants to calculate the Weighting Functions for any measurement performed in the future with C_6D_6 detectors.

Concerning the detector geometries, several previous works were devoted to implement in Geant4 the geometry of the long-existing C_6D_6 models (Bicron and FZK) [213]. An accurate implementation in Geant4 of the new Legnaro detector geometry, shown in the right panel of Figure B.2, was the first item of the the application upgrade carried out in this work. The Geant4 geometries of the three detector models are displayed in the left panel of Figure B.2, where the active C_6D_6 volumes are highlighted in green.

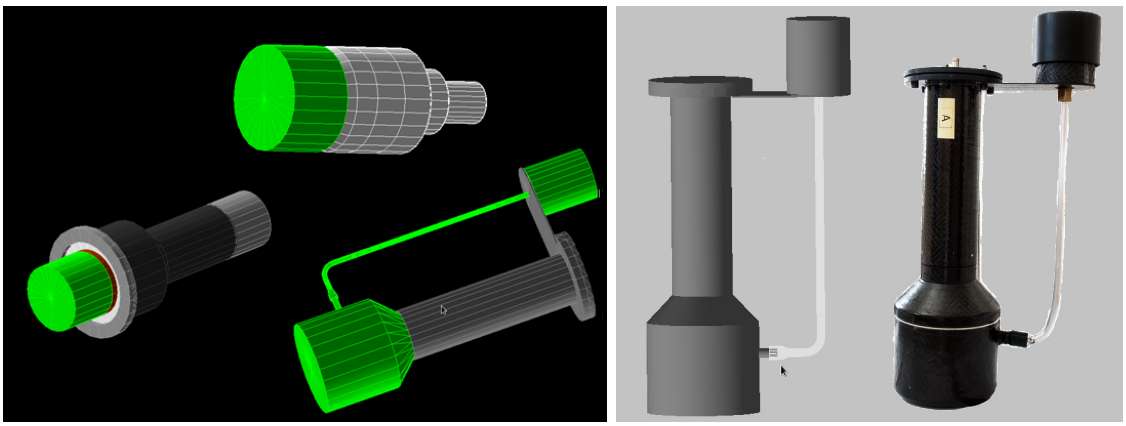

Figure B.2: Left: Geometry models for the different models of C_6D_6 detectors used at n_TOF, where the active volume is shown in green. Right: Comparison between the actual view of the new Carbon Fiber made Legnaro detector and its geometry model, developed as part of the Geant4 application upgrade in this work.

The new holding systems for the C_6D_6 detectors made of Al (2014) and carbon fiber (CF) (2016) replaced the previous and simpler detector holders used in n_TOF Phase #2. The new holders have been also included in the upgraded Geant4 application [204] (see Figure B.3).

Last, none of the previoulsly developed applications to simulate the C_6D_6 detector response allowed easy modification of the parameters, that were mostly hard-coded. In what concerns to the positioning of the capture detectors, just one of the angular positions was initially possible, placing the detectors facing the sample with and angle with the beam axis of 55 . In addition, the distance of the sample to the detectors was fixed for all of them and it was a hard-coded parameter. Furthermore, the Geant4 application was not able to register the deposited energy in all four detectors separately.

The main features of the released Geant4 application [214] are:

- **User friendly parameter file**: All the following features can be adjusted by modifiying only one anotated parameter file.
- **Choice of detectors**: Allows any number of detectors from 1 to 4 with the possibility to combine different models (BICRON, FZK and Legnaro)
- **Choice of detector holder**: The two different detector holding systems (Al, used for the ^{242}Pu(n,γ) measurement and all the measurements of 2014 and 2015) and the CF setup installed in EAR1 since 2016 (see Figure B.3).
- **Choice of detector holder**: Allows any number of detectors from 1 to 4 with the possibility to combine the different models of (BICRON, FZK and Legnaro).
- **Flexible positioning**: Each detector can be positioned at the desired distance from the center of the capture target and the angle at which the detectors face the sample can be set to 55° (as it has been usually the case in the setups used since 2014) or at

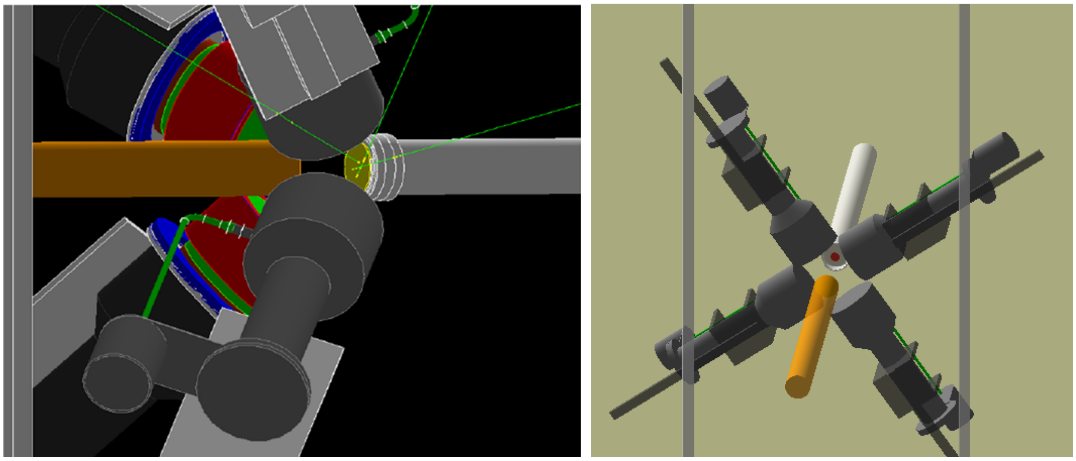

Figure B.3: Examples of geometry models simulated with the Geant4 application: The left side shows a capture setup combining BICRON and Legnaro C_6D_6 detectors on the aluminum support and several γ-ray tracks emmitted from a gold sample. The right side presents the implementation in Geant4 of the new carbon fiber structure holding four Legnaro detectors placed perpendicular to the neutron beam.

90°, as it was the case in n_TOF phase #1 and #2 (and also during 2016).

- **Sample dimensions, material and position**: Circular samples of different materials in the NIST database [215] available in Geant4 and with adjustable thickness and radius can implemented. A detailed view of the sample emmitting γ-rays is shown in the left panel of Figure B.3.
- **Self-shielding for strong resonances**: The capture cross section and atomic density of the sample is given as an input if one chooses to calculate the attenuation of the neutron flux for strong resonances.
- **Energy, type and number of particles**: The number of γ-rays as well as their energy can be adjusted. Additionally, in order to carry out studies of the direct neutron induced background or the neutron sensitivity, the application uses suitable Geant4 PL included the High Precision package for neutron transport *G4NeutronHP* [216] when neutrons are selected as primary particle.
- **Individual output**: The histograms of deposited energy are registered individually for each detector. The binning and energy range of the latter can be easily adjusted.

Appendix C

Simulation of detector response to (n,γ) cascades

The deviation of the real capture cascades from the simulated response to individual γ-rays used to calculate the Weighting Functions (WF), leads to uncertainties in the application of the PHWT. In order to assess the accuracy of this method and calculate the correction factors introduced in Section 6.8.2, accurate simulations of the detector response to realistic capture cascades, are the best solution. These simulations consist of two separated steps:

- First, the capture cascade data must be generated. This will be performed with help of the Captugens Code, developed by J.L. Tain et al. [235].
- Second, the simulated cascade energies must be read by the PrimaryGeneratorAction.cc class of thee Geant4 tool developed for the simulation of the response of the C6D6 Detectors to capture γ-rays.

C.1 Generation of cascades: the Captugens code

The Captugens Code, developed by J.L. Tain et al., combines two different approaches to describe the nuclear level properties (energies, spins, transition probabilities, etc...). This division of the Compound Nucleus nuclear scheme is sketched in Figure C.1:

- The low energy part, up to a certain cut energy E_{cut}, is described according to the properties of known levels, extracted from ENSDF [19].
- The high energy levels (i.e from E_{cut} to the neutron separation energy S_n)associated γ-ray transitions are determined from Level Density Parameterizations (LDP) and Photon Strenght Functions (PSF).

The energy-dependence of the level densities can be obtained from the Back-shifted Fermi Gas (BSFG) Model, Constant Temperature (CT) Model or a combination of both (CT+BSFG) known as Gilbert-Cameron Formula. The γ-ray strenghts for E1, M1 and

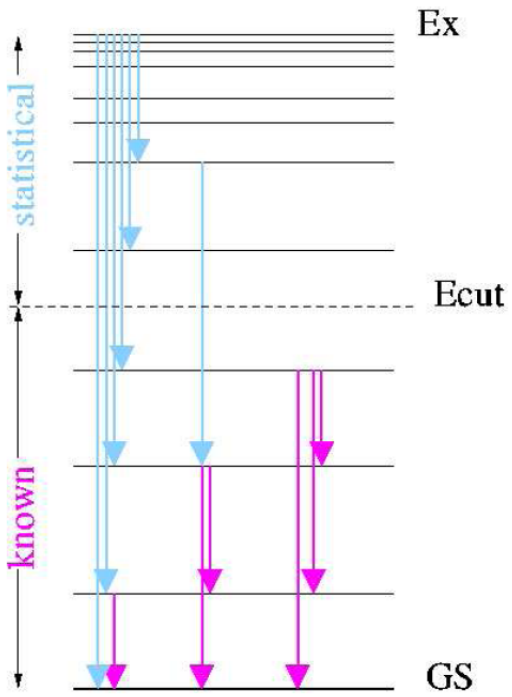

Figure C.1: *Description of the nuclear level scheme in the CAPTUGENS code: known levels are considered up a threshold energy beyond which the nucleus is treated as an statistical system characterized by statistical model parameters.*

E2 transitions can be parameterized with a Single Particle, Lorentzian or a Generalized Lorentzian.

In addition, the conversion electron (CE) process for the transitions between known levels is included, being especially relevant in the very low energy levels. Last, the code allows the inclusion of known isomeric levels (i.e. long-lived excited levels where a fraction of the cascades end).

The output of the Captugens code consists of a list of number including:

1. One line with two numbers corresponding to the number of γ-rays and conversion electrons emitted in that cascade.
2. A list of energies corresponding to the energies of the particles in the cascade.

C.2 MC simulation of the capture cascades

Second, the simulated cascade energies must be coupled to the *PrimaryGeneratorAction* class of the Geant4 application developed for the simulation of the response of the C_6D_6

detectors to capture γ-rays (see Appendix B.2). Different read-out methods were developed in the application to acomplish the goals of these simulations:

- **Single particle emmision**: The γ-rays are emmited sequentially to avoid the summing effect, as it is required by the PHWT.
- **Full cascade emission**: All the γ-rays of a given cascade are emmited in a single event, thus enabling the possibility of summing. This approach resembles the actual (n,γ) process, hence providing the deviation between reality and the single-detection required by the PHWT.
- **Inclusion of conversion electrons**: Aiming at studying the impact of conversion in the detection efficiency for a capture event, we

The same Geant4 applications was also coupled with minor changes in the *PrimaryGeneratorAction* class to simulate the response of our detection setup to the distribution of γ-rays from neutron induced fission on ^{242}Pu, generated with the GEF code [238]. This study aimed as assessing the background associated to the in our capture measurement, as it is explained in Section 6.7.2.

C.3 Optimization and validation of the (n,γ) cascades

Two different neutron capture reactions were simulated with Captugens, ^{242}Pu(n,γ) and ^{197}Au(n,γ). The latter is required to extract the correction factors for the absolute normalization of ^{242}Pu(n,γ) by means of the Saturated Resonance Method (SRM). The ^{197}Au(n,γ) cascade was generated using the statistical parameters from Ref. [236], without any additional adjustments. The validation of the simulated cascade with the experimental data is presented in the right panel of Figure 6.28. For the generation of the cascades, the cut energy in the ^{198}Au level scheme was set at 1600 keV, assumming that all the levels below this energy are known [19].

For the case of ^{242}Pu(n,γ), the experimental and theoretical knowledge of the Compound Nucleus (^{243}Pu) is more scarce and a systematic adjustment of the critical parameters in Captugens was carried out aiming at reproducing the experimental shape of the detector response to the ^{242}Pu(n,γ) cascade:

- **Setting** E_{cut}: According to Ref. [147], the level density is just completely known up to 0.4MeV. Above this energy, the known levels do to fully reproduce the level density extracted from (d,p) measurements. Indeed, our results showed that the generated cascades generated with E_{cut} values from 0.4 MeV to 0.750MeV were very similar (in terms of end point and multiplicity) and as a consequence the detector response was very similar. The final choice was E_{cut}=0.4 MeV to be consistent with the observations in [147].
- **Choosing a parameterization for LDP**: By default we have used the BSFG models with the parameters suggested in the recent paper on statistical properties

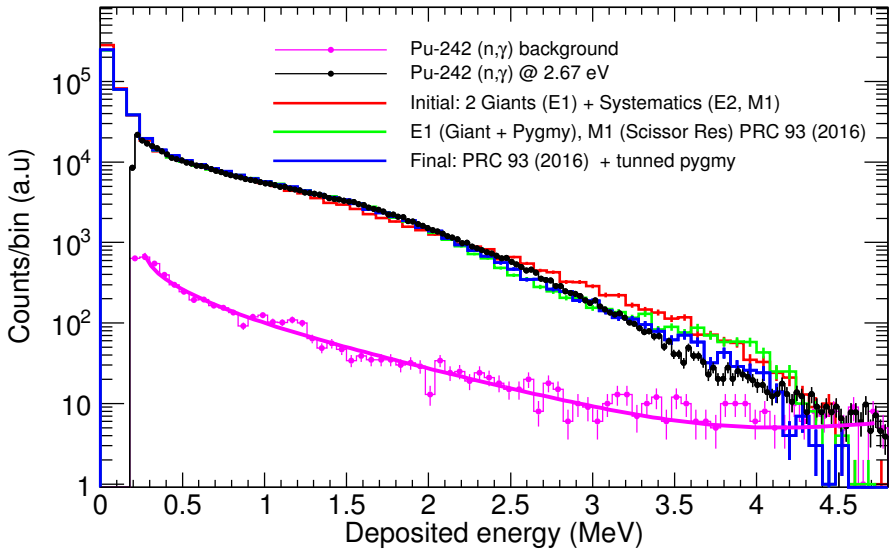

Figure C.2: *Experimental response of the C_6D_6 to a capture cascade (2.67eV resonance)compared to the results from simulations following a progressive adjustment of the PSF parameters.*

of ^{242}Pu(n,γ) [147] In this paper, the LDP parameters are extractee from systematic studies of neighbouring nuclei. A different set of parameters for the same model was obtained from RIPL3 [26] and from the Atlas of Neutron Resonances [250] The CT model was also tested with the parameterization, and was the final choice, following the recommendation of Ref. [147]. However, all the studied parameterizations for the level density lead to results of the corrections within 0.8%, hence the choice of LDP is not critical for our purpose.

- **Adjusting the possition and width of the PSF resonances**: In order to reproduce the shape of the experimental respose between 1.5 and 2 MeV, a Single Lorentzian resonance at 2.42 MeV was included for the M1 PSF, to reproduce the effect of the scissor resonances proposed in Ref. [147]. In addittion, the E1 component was described with a Generalizzed Lorentzian (one giant at 11.1 MeV and one pigmy at 4.2 MeV). The E2 contribution was described with a Single Lorentzian at 10.1 MeV. The inclusion of the average scission resonance and the fine tunning of the position and widths of the pigmy resonance to reproduce the experimental shape wer implemented in a proggressive approach illustrated in Figure C.2.

Appendix D

Individual resonance parameters

Table D.1: Individual resonance parameters and radiative kernels of the ^{242}Pu(n,γ) cross section obtained in this work. The uncertainties listed in the table are only statistical and have been obtained from the SAMMY calculations.

Energy (eV)	J	Γ_γ (meV)	$g_J\Gamma_n$ (meV)	Γ_f (meV)	R_K (meV)	n_TOF/JEFF	n_TOF/DANCE
2.67625(3)*	0.5	25.4(6)	2.0965(19)	0.002	1.936(4)	1.0428(21)	1.036(19)
22.569(10)*	0.5	24.8	0.297(3)	0.01	0.293(3)	1.041(10)	1.14(4)
32.952(17)+•	(0.5)	24.8	0.0199(22)	0.01	0.0199(22)	-	-
40.951(20)*	0.5	24.8	0.47(6)	0.01	0.461(6)	1.038(14)	1.12(4)
53.4649(8)*	0.5	24.1(3)	56.1(14)	0.0019	16.86(20)	1.029(12)	1.07(3)
67.628(12)*	0.5	24.8	4.68(4)	0.0445	3.95(3)	1.04(8)	1.11(3)
88.469(6)*	0.5	24.8	0.591(19)	0.0382	0.577(18)	0.93(3)	0.81(7)
107.3824(15)*	0.5	24.8	17.48(20)	0.0494	10.36(7)	1.093(7)	0.95(6)
131.446(3)*	0.5	24.8	6.39(9)	0.0635	5.1(6)	0.994(11)	0.87(7)
141.34(5)*•x	(0.5)	24.8	0.124(21)	0.01	0.123(21)	1.04(17)	1.04(21)
149.838(3)*	0.5	24.8	13.71(20)	0.0554	8.9(8)	0.983(9)	1.19(10)
163.69(21)*	0.5	24.8	0.49(4)	0.01	0.48(4)	0.91(7)	0.93(11)
205.022(3)*	0.5	23.7(3)	52.0(19)	0.0548	16.29(24)	1.093(16)	1.10(6)
210.24(5)*	0.5	24.8	0.3(4)	0.01	0.29(4)	0.7(10)	0.71(12)
215.488(7)*	0.5	24.8	5.48(14)	0.184	4.48(9)	0.991(21)	0.89(7)
219.54(6)*•x	(0.5)	24.8	0.28(4)	0.01	0.28(4)	0.97(15)	1.10(9)
232.942(8)*	0.5	24.8	5.61(17)	0.131	4.58(11)	1.09(3)	1.19(21)
264.7(7)*•x	(0.5)	24.8	0.36(6)	0.01	0.36(6)	0.95(16)	1.00(19)
272.41(8)*•x	(0.5)	24.8	0.32(6)	0.01	0.32(6)	1.9(4)	2.0(4)
273.786(7)*	0.5	24.8	14.8(5)	0.102	9.35(19)	1.001(20)	0.97(7)
275.07(9)*•x	(0.5)	24.8	0.27(6)	0.01	0.27(6)	1.6(4)	1.6(4)
281.2(13)*•x	(0.5)	24.8	0.16(5)	0.01	0.16(5)	1.3(4)	1.2(4)
298.873(10)*	0.5	24.8	9(3)	0.01	6.65(18)	1.06(3)	1.04(9)
303.727(8)*	0.5	26.6(13)	17.8(5)	0.067	10.6(3)	1.09(3)	1.04(7)
317.53(11)+•	(0.5)	24.8	0.33(9)	0.01	0.33(8)	-	-
320.096(7)*	0.5	26.7(4)	230(16)	0.017	23.9(4)	1.121(17)	1.36(5)
328.97(14)+•	(0.5)	24.8	0.2(8)	0.01	0.2(8)	-	-
332.642(8)*	0.5	28.5(7)	70(5)	0.018	20.3(6)	0.95(3)	0.97(8)
341.97(13)+•	(0.5)	24.8	0.39(1)	0.01	0.39(11)	-	-
374.484(19)*	0.5	24.8	6.2(3)	0.01	5(19)	0.99(4)	0.96(9)
380.52(19)*•x	(0.5)	24.8	0.18(7)	0.01	0.18(7)	0.7(3)	0.7(3)
382.548(10)*	0.5	22.7(6)	50(4)	0.085	15.6(5)	1.02(3)	0.98(7)
400.19(4)*	0.5	24.8	1.97(18)	0.01	1.83(16)	1.21(10)	1.10(14)
410.845(18)*	0.5	24.8	8.7(4)	0.01	6.47(23)	1.15(4)	1.05(9)
424.27(3)*	0.5	24.8	4.6(3)	0.18	3.86(19)	1.11(5)	1.11(11)
425.68(17)*•x	(0.5)	24.8	0.31(11)	0.01	0.31(11)	1.1(4)	1.1(4)
468.42†@•	0.5	24.2	0.03	30	-	-	-
473.73(9)*x	0.5	24.8	1.2(19)	0.32	1.13(17)	1.24(19)	1.20(22)
482.896(16)*	0.5	28.2(17)	23.5(12)	0.42	12.7(5)	1.16(5)	1.13(9)
486.97(19)+•	(0.5)	24.8	0.34(12)	0.01	0.34(12)	-	-
495.11(21)*•x	(0.5)	24.8	0.29(12)	0.01	0.29(11)	1.1(4)	1.08(4)
504.033(21)§	0.5	24.8	29(6)	0.19	13.6(13)	-	-
504.749(16)§+	0.5	24.8	60(10)	0.19	17.9(9)	-	-
536.81(14)*	0.5	25.9(8)	96(11)	0.043	20.4(7)	1.18(4)	-
548.81(17)*	0.5	22.3(9)	74(10)	0.077	17.1(8)	0.92(4)	-
576.532(16)*	0.5	24.8	44(4)	0.01	16.2(5)	1.21(4)	-
591.02(15)+•	(0.5)	24.8	1.02(24)	0.01	0.98(22)	-	-

Energy (eV)	J	Γ_γ (meV)	$g_J\Gamma_n$ (meV)	Γ_f (meV)	R_K (meV)	n_TOF/JEFF	n_TOF/DANCE
595.427(20)*	0.5	28.2(17)	38(3)	0.021	16.2(8)	1.28(6)	-
598.65(18)+•	(0.5)	24.8	0.95(25)	0.021	0.92(23)		-
600.21(3)*	0.5	24.8	10.4(8)	0.102	7.3(4)	1.11(6)	-
604.48(16)+•	(0.5)	24.8	0.99(24)	0.1	0.95(22)	-	-
611.14(3)*	0.5	24.8	13.1(10)	0.064	8.6(4)	1.08(6)	-
639.44(7)*	0.5	24.8	4.3(4)	0.04	3.7(3)	0.98(9)	-
660.27(13)+•	(0.5)	24.8	0.78(22)	0.066	0.76(20)	-	-
670.28(3)*	0.5	24.8	15.5(13)	0.051	9.6(5)	1.14(6)	-
693.56(3)*	0.5	29.1(20)	40(4)	0.24	16.8(9)	1.25(7)	-
712.18(3)*	0.5	25.9(11)	121(29)	0.163	21.3(12)	1.27(7)	-
713.9(16)+•	(0.5)	24.8	1.6(4)	0.01	1.5(3)	-	-
727.71(9)*	0.5	24.8	3.8(5)	0.05	3.3(4)	1.17(14)	-
737.23(3)*	0.5	26.1(12)	105(20)	0.45	20.8(11)	1.06(6)	-
748.04(19)+•	(0.5)	24.8	1.3(3)	0.05	1.2(3)	-	-
755.75(3)*@	0.5	21.5	130	1.6	-	-	-
762.8(5)*@	0.5	24.2	5.6	440	-	-	-
789.28(4)*@	0.5	24.2	64	1.6	-	-	
794.52(3)*	0.5	24.7(11)	201(78)	0.043	22(13)	1.02(6)	-
825.28(9)*	0.5	24.8	6(8)	0.21	4.8(5)	1.24(14)	-
831.91(21)+•	(0.5)	24.8	1.4(4)	0.01	1.3(4)	-	-
838.45(4)*	0.5	25.3(21)	39(5)	0.041	15.3(11)	1.17(8)	-
857.09(4)*	0.5	27(3)	34(4)	0.093	15.2(11)	1.13(8)	-
866.38(6)*	0.5	24.8	12.5(14)	0.043	8.4(6)	1.16(9)	-
873.74(11)+	0.5	24.8	6.1(9)	0.043	4.9(6)	-	-
879.64(4)*	0.5	23.2(17)	59(10)	0.027	16.6(12)	0.97(7)	-
887.31(5)*	0.5	28(4)	23.0(24)	0.0155	12.6(11)	0.99(8)	-
908.4(3)+•	(0.5)	24.8	0.8(3)	0.01	0.8(3)	-	-
913.31(21)+•	(0.5)	24.8	1.8(5)	0.01	1.7(4)	-	-
923.73(5)*	0.5	21.4(17)	59(12)	0.029	15.7(12)	1.14(9)	-
936.76(8)*	0.5	24.8	10.8(15)	0.01	7.6(7)	1(9)	-
950.35(8)*	0.5	24.8	12.4(16)	0.01	8.4(7)	0.92(8)	-
978.81(8)*	0.5	24.8	12.9(18)	0.01	8.6(8)	0.94(9)	-
1005.34(5)*	0.5	31(3)	43(6)	0.01	18.0(15)	1.16(9)	-
1024.04(25)+•	(0.5)	24.8	2.2(7)	0.01	2(6)	-	-
1031.36(5)*	0.5	23.4(23)	46(8)	0.01	15.5(14)	0.98(9)	-
1046.19(6)*	0.5	20.6(15)	118(47)	0.01	17.5(15)	0.87(8)	-
1063.55(6)*	0.5	24.8	44(8)	0.01	16.2(10)	1.16(7)	-
1088.99(6)*	0.5	27.4(16)	200(77)	0.01	24.1(17)	1.12(8)	-
1130.47(12)*	0.5	24.8	12.7(20)	0.01	8.5(9)	1.2(13)	-
1148.96(7)*	0.5	23.4(14)	300(146)	0.01	21.7(14)	0.97(6)	-
1185.47(13)*	0.5	24.8	11.4(19)	0.01	7.9(9)	0.93(11)	-
1198.78(7)*	0.5	23.2(20)	95(33)	0.01	18.6(18)	0.97(9)	-
1207.75(7)*	0.5	24.8	49(10)	0.01	16.7(12)	1.11(8)	-
1229.92(15)+	0.5	24.8	8.8(18)	0.01	6.6(10)	-	-
1239.1(3)+•	(0.5)	24.8	2.3(8)	0.01	2.1(7)	-	-
1249.31(14)*	0.5	24.8	11.1(20)	0.01	7.8(10)	1.18(15)	-
1268.96(10)*	0.5	24.8	26(5)	0.01	12.9(11)	1.01(9)	-
1288.33(9)*	0.5	23(3)	59(16)	0.01	16.6(18)	0.97(10)	-
1330.64(9)+	0.5	24.8	67(20)	0.01	18.5(15)	-	-
1342.22(10)+	0.5	24.8	33(7)	0.01	14.3(13)	-	-
1351.5(4)+•	(0.5)	24.8	1.7(8)	0.01	1.6(7)	-	-
1354.03(14)+	0.5	24.8	18(4)	0.01	10.5(13)	-	-

Energy (eV)	J	Γ_γ (meV)	$g_J\Gamma_n$ (meV)	Γ_f (meV)	R_K (meV)	n_TOF/JEFF	n_TOF/DANCE
1368.19(8)$^{+}$	0.5	24.8	210(95)	0.01	22.7(11)	-	-
1393.75(25)$^{+}$	0.5	24.8	6.2(16)	0.01	5.0(10)	-	-
1405.81(25)$^{+}$	0.5	24.8	6.5(16)	0.01	5.2(10)	-	-
1414.3(4)$^{+\bullet}$	(0.5)	24.8	2.1(8)	0.01	2(7)	-	-
1433.3(14)$^{+}$	0.5	24.8	19(4)	0.01	10.9(14)	-	-
1455.55(9)$^{+}$	0.5	24.8	103(40)	0.01	20.4(16)	-	-
1503.71(17)$^{+}$	0.5	24.8	17(4)	0.01	10.3(14)	-	-
1509.97(19)$^{+}$	0.5	24.8	12(3)	0.01	8.2(13)	-	-
1527.4(3)$^{+\bullet}$	(0.5)	24.8	3.9(14)	0.01	3.4(10)	-	-
1540.04(21)$^{+}$	0.5	24.8	12(3)	0.01	8(13)	-	-
1560.5(3)$^{+\bullet}$	(0.5)	24.8	4.6(16)	0.01	3.9(12)	-	-
1567.35(12)$^{+}$	0.5	24.8	499(195)	0.01	24.3(5)	-	-
1578.5(3)$^{+\bullet}$	(0.5)	24.8	5.1(15)	0.01	4.3(11)	-	-
1598.4(4)$^{+}$	0.5	24.8	7.2(22)	0.01	5.6(13)	-	-
1623.39(12)$^{+}$	0.5	24.8	106(42)	0.01	20.5(16)	-	-
1642.26(13)$^{+}$	0.5	24.8	62(21)	0.01	18.1(17)	-	-
1654.26(22)$^{+}$	0.5	24.8	15(4)	0.01	9.6(15)	-	-
1675.8(3)$^{+}$	0.5	24.8	7.1(20)	0.01	5.6(12)	-	-
1687.7(3)$^{+}$	0.5	24.8	8.4(24)	0.01	6.3(13)	-	-
1696.7(14)$^{+}$	0.5	24.8	55(18)	0.067	17.4(18)	-	-
1708.93(13)$^{+}$	0.5	24.8	199(85)	0.001	22.6(11)	-	-
1723.9(4)$^{+\bullet}$	(0.5)	24.8	3.7(14)	0.1	3.2(11)	-	-
1739.9(4)$^{+\bullet}$	(0.5)	24.8	7(3)	0.1	5.3(17)	-	-
1740.7(3)$^{+}$	0.5	24.8	9(3)	0.1	6.4(18)	-	-
1752.6(3)$^{+}$	0.5	24.8	8.6(25)	0.51	6.3(13)	-	-
1763.6(18)$^{+}$	0.5	24.8	37(10)	0.017	15.1(17)	-	-
1779(4)$^{+\bullet}$	(0.5)	24.8	6.3(21)	0.51	4.9(13)	-	-
1807.4(3)$^{+}$	0.5	24.8	7.6(23)	0.13	5.9(13)	-	-
1838.1(4)$^{@}$	0.5	-	-	-	-	-	-
1845.8(3)$^{+}$	0.5	24.8	11(3)	0.01	7.6(15)	-	-
1863.11(20)$^{+}$	0.5	24.8	34(10)	0.49	14.4(17)	-	-
1882.81(17)$^{+}$	0.5	24.8	303(130)	0.056	23.5(8)	-	-
1892.2(3)$^{+}$	0.5	24.8	15(4)	0.96	9.4(16)	-	-
1897.3(4)$^{+\bullet}$	(0.5)	24.8	7(3)	1	5.6(15)	-	-
1906.05(22)$^{+}$	0.5	24.8	33(11)	0.01	14.4(20)	-	-
1914(4)$^{+\bullet}$	(0.5)	24.8	5.6(21)	0.01	4.6(14)	-	-
1928.82(18)$^{+}$	0.5	24.8	361(159)	0.01	23.8(7)	-	-
1947.2(4)$^{+\bullet}$	(0.5)	24.8	6.3(24)	0.01	5.1(15)	-	-
1953.2(4)$^{+\bullet}$	(0.5)	24.8	5.5(21)	0.01	4.5(14)	-	-
1974.6(3)$^{+}$	0.5	24.8	10(3)	0.01	7.2(18)	-	-
1983.85(19)$^{+}$	0.5	24.8	71(27)	0.01	18.8(19)	-	-
2006.25(20)$^{+}$	0.5	24.8	86(35)	0.01	19.6(18)	-	-
2018.2(4)$^{+\bullet}$	(0.5)	24.8	9(3)	0.01	6.6(18)	-	-
2023.35(19)$^{+}$	0.5	24.8	187(88)	0.01	22.4(13)	-	-
2038.41(20)$^{+}$	0.5	24.8	99(41)	0.01	20.3(17)	-	-
2057.21(19)$^{+}$	0.5	24.8	183(86)	0.01	22.4(13)	-	-
2068.1(4)$^{+}$	0.5	24.8	9(3)	0.01	6.7(19)	-	-
2074.5(4)$^{+}$	0.5	24.8	12(4)	0.01	8(19)	-	-
2082.2(4)$^{+}$	0.5	24.8	13(4)	0.01	8.5(20)	-	-
2115.71(23)$^{+}$	0.5	24.8	77(31)	0.01	19.1(20)	-	-
2121(3)$^{+}$	0.5	24.8	18(6)	0.01	10.4(21)	-	-

Energy (eV)	J	Γ_γ (meV)	$g_J\Gamma_n$ (meV)	Γ_f (meV)	R_K (meV)	n_TOF/JEFF	n_TOF/DANCE
2141.1(4)$^+$	0.5	24.8	11(4)	0.01	7.6(20)	-	-
2166.5(3)$^+$	0.5	24.8	21(7)	0.01	11.6(22)	-	-
2186.8(23)$^+$	0.5	24.8	120(53)	0.01	21(16)	-	-
2209.9(3)$^+$	0.5	24.8	47(18)	0.01	16.6(22)	-	-
2223.3(3)$^+$	0.5	24.8	28(10)	0.01	13.2(23)	-	-
2229.6(4)$^+$	0.5	24.8	12(5)	0.01	8(22)	-	-
2265.2(3)$^+$	0.5	24.8	37(14)	0.01	15.1(23)	-	-
2271(4)$^+$	0.5	24.8	13(5)	0.01	8.4(22)	-	-
2276.5(3)$^+$	0.5	24.8	226(108)	0.01	22.9(11)	-	-
2291.8(5)$^{+\bullet}$	(0.5)	24.8	8(3)	0.01	6.3(19)	-	-
2303.7(3)$^+$	0.5	24.8	36(14)	0.01	14.8(24)	-	-
2311.3(3)$^+$	0.5	24.8	239(119)	0.01	23(11)	-	-
2315(4)$^+$	0.5	24.8	18(7)	0.01	10.4(25)	-	-
2338.6(3)$^+$	0.5	24.8	86(39)	0.01	19.7(21)	-	-
2351.9(5)$^+$	0.5	24.8	43(22)	0.01	16(3)	-	-
2359.9(4)$^+$	0.5	24.8	14(6)	0.01	9.1(23)	-	-
2366.9(5)$^+$	0.5	24.8	12(5)	0.01	8.1(22)	-	-
2384.6(4)$^+$	0.5	24.8	19(7)	0.01	11(24)	-	-
2401.6(4)$^+$	0.5	24.8	33(13)	0.01	14.4(25)	-	-
2424.7(4)$^+$	0.5	24.8	14(6)	0.01	9.2(25)	-	-
2431.1(4)$^+$	0.5	24.8	17(7)	0.01	10.1(24)	-	-
2446.4(4)$^+$	0.5	24.8	34(14)	0.01	14.7(25)	-	-
2459.7(4)$^+$	0.5	24.8	21(8)	0.01	11.6(25)	-	-
2471(4)$^+$	0.5	24.8	41(17)	0.01	15.8(24)	-	-
2497.9(3)$^+$	0.5	24.8	88(39)	0.01	19.8(20)	-	-
2525.7(5)$^+$	0.5	24.8	12(5)	0.01	8.3(23)	-	-
2538.9(4)$^+$	0.5	24.8	18(7)	0.01	11(3)	-	-
2549.4(5)$^+$	0.5	24.8	19(7)	0.01	10.7(24)	-	-
2563.7(3)$^+$	0.5	24.8	178(83)	0.01	22.3(13)	-	-
2605.2(4)$^+$	0.5	24.8	39(16)	0.01	15.5(24)	-	-
2623(4)$^+$	0.5	24.8	17(8)	0.01	10(3)	-	-
2637.4(3)$^+$	0.5	24.8	230(108)	0.01	23(11)	-	-
2702.6(5)$^+$	0.5	24.8	167(82)	0.11	22.1(14)	-	-
2703.6(5)$^+$	0.5	24.8	147(71)	0.11	21.7(15)	-	-
2736.2(4)$^+$	0.5	24.8	163(73)	0.094	22(13)	-	-
2745.5(6)$^{+\bullet}$	(0.5)	24.8	11(4)	1.5	7.3(19)	-	-
2758.7(4)$^+$	0.5	24.8	124(61)	0.031	21.1(18)	-	-
2794.2(5)$^+$	0.5	24.8	28(11)	0.01	13(3)	-	-
2811.1(5)$^+$	0.5	24.8	14(7)	0.01	9(3)	-	-
2816.8(5)$^+$	0.5	24.8	23(10)	0.01	12(3)	-	-
2871.6(4)$^+$	0.5	24.8	494(237)	0.01	24.2(6)	-	-
2889.5(5)$^+$	0.5	24.8	19(9)	0.01	11(3)	-	-
2904.8(5)$^+$	0.5	24.8	21(10)	0.01	12(3)	-	-
2916.5(4)$^+$	0.5	24.8	249(118)	0.01	23.1(10)	-	-
2931.7(5)$^+$	0.5	24.8	44(19)	0.01	16(3)	-	-
2941.3(4)$^+$	0.5	24.8	63(28)	0.01	18.1(23)	-	-
2947.7(4)$^+$	0.5	24.8	68(31)	0.01	18.6(23)	-	-
2974.3(4)$^+$	0.5	24.8	86(39)	0.01	19.7(20)	-	-
2993.9(4)$^+$	0.5	24.8	68(30)	0.01	18.5(22)	-	-
3002.7(4)$^+$	0.5	24.8	115(57)	0.01	20.9(19)	-	-

Energy (eV)	J	Γ_γ (meV)	$g_J\Gamma_n$ (meV)	Γ_f (meV)	R_K (meV)	n_TOF/JEFF	n_TOF/DANCE
3012.6(5)$^{+}$	0.5	24.8	34(15)	0.01	15(3)	-	-
3045.6(5)$^{+}$	0.5	24.8	21(10)	0.01	11(3)	-	-
3058.4(5)$^{+}$	0.5	24.8	60(28)	0.01	18(3)	-	-
3076.8(5)$^{+}$	0.5	24.8	89(41)	0.01	19.8(20)	-	-
3137.3(5)$^{+}$	0.5	24.8	62(28)	1.2	17.8(24)	-	-
3145(5)$^{+}$	0.5	24.8	340(167)	1.22	23.6(8)	-	-
3159.1(5)$^{+}$	0.5	24.8	143(67)	0.01	21.6(15)	-	-
3178.6(5)$^{+}$	0.5	24.8	85(39)	0.01	19.6(21)	-	-
3192.5(6)$^{+\bullet}$	(0.5)	24.8	16(7)	0.01	10(3)	-	-
3197(5)$^{+}$	0.5	24.8	37(17)	0.01	15(3)	-	-
3215.8(6)$^{+}$	0.5	24.8	40(19)	0.01	16(3)	-	-
3219.5(5)$^{+}$	0.5	24.8	112(55)	0.01	20.8(19)	-	-
3228.5(5)$^{+}$	0.5	24.8	62(29)	0.01	18.1(24)	-	-
3250.6(5)$^{+}$	0.5	24.8	68(31)	0.01	18.5(23)	-	-
3270.1(5)$^{+}$	0.5	24.8	52(24)	0.01	17(3)	-	-
3282.5(5)$^{+}$	0.5	24.8	55(26)	0.01	17(3)	-	-
3326.3(5)$^{+}$	0.5	24.8	188(90)	0.01	22.5(13)	-	-
3378.8(5)$^{+}$	0.5	24.8	72(34)	0.01	18.8(23)	-	-
3408.7(6)$^{+}$	0.5	24.8	25(12)	0.01	13(3)	-	-
3416.9(5)$^{+}$	0.5	24.8	187(97)	0.009	22.4(14)	-	-
3426.3(6)$^{+}$	0.5	24.8	51(24)	0.01	17(3)	-	-
3442.4(6)$^{+}$	0.5	24.8	31(14)	0.01	14(3)	-	-
3456.7(5)$^{+}$	0.5	24.8	233(116)	0.13	23(11)	-	-
3477.7(5)$^{+}$	0.5	24.8	118(57)	0.11	21(18)	-	-
3491.7(6)$^{+}$	0.5	24.8	105(52)	0.28	20.5(20)	-	-
3501.4(6)$^{+}$	0.5	24.8	236(115)	0.36	23(11)	-	-
3513.1(5)$^{+}$	0.5	24.8	127(60)	0.01	21.2(17)	-	-
3524.8(5)$^{+}$	0.5	24.8	157(76)	0.2	21.9(15)	-	-
3533.6(6)$^{+}$	0.5	24.8	59(28)	0.01	18(3)	-	-
3545.5(6)$^{+}$	0.5	24.8	28(14)	0.01	13(3)	-	-
3560.8(6)$^{+}$	0.5	24.8	43(20)	0.01	16(3)	-	-
3586.8(6)$^{+}$	0.5	24.8	321(156)	0.18	23.6(8)	-	-
3624.9(7)$^{+\bullet}$	(0.5)	24.8	12(6)	0.29	8(3)	-	-
3656.1(6)$^{+}$	0.5	24.8	161(79)	0.67	21.9(15)	-	-
3664.8(6)$^{+}$	0.5	24.8	40(20)	0.01	16(3)	-	-
3674.2(6)$^{@}$	0.5	-	-	-	-	-	-
3705.3(7)$^{+\bullet}$	(0.5)	24.8	14(7)	0.01	9(3)	-	-
3727.9(6)$^{+}$	0.5	24.8	200(180)	0.05	22.7(15)	-	-
3742.3(6)$^{+}$	0.5	24.8	76(36)	0.01	19.1(23)	-	-
3764.1(6)$^{+}$	0.5	24.8	48(23)	0.01	17(3)	-	-
3777.4(7)$^{+}$	0.5	24.8	370(182)	0.21	23.8(8)	-	-
3794.7(6)$^{+}$	0.5	24.8	84(40)	0.07	19.5(22)	-	-
3806.3(6)$^{+}$	0.5	24.8	70(34)	0.07	18.7(24)	-	-
3816.5(7)$^{+}$	0.5	24.8	115(55)	0.015	20.9(18)	-	-
3818.6(6)$^{+}$	0.5	24.8	452(229)	0.015	24.1(7)	-	-
3841.3(7)$^{+\S}$	0.5	24.8	37(25)	0.05	15(4)	-	-
3843.7(6)$^{+\S}$	0.5	24.8	57(35)	0.05	18(3)	-	-
3882.5(6)$^{+}$	0.5	24.8	88(42)	0.01	19.8(21)	-	-
3909.3(7)$^{+}$	0.5	24.8	25(12)	0.01	13(3)	-	-

Energy (eV)	J	Γ_γ (meV)	$g_J\Gamma_n$ (meV)	Γ_f (meV)	R_K (meV)	n_TOF/JEFF	n_TOF/DANCE
$3926.2(6)^+$	0.5	24.8	64(31)	0.01	18.3(25)	-	-
$3938.3(6)^+$	0.5	24.8	57(27)	0.01	18(3)	-	-
$3959.6(6)^+$	0.5	24.8	72(37)	0.01	19(3)	-	-

$*$) Included in JEFF-3.2.
+) Not included in JEFF-3.2.
@) Large (Non-negligible) fission width: Not analyzed, parameters in the table from JEFF-3.2 (E_n <1.3 keV).
•) p-wave candidate: Spin could not be assigned.
x) p-wave resonance in ENDF/B-VII.1.
†) Resonance in JEFF-3.2 below the experimental threshold in Γ_0: Neither confirmed nor rejected.
§ Doublet. Just one resonance in JEFF-3.2 or in previous measurements.